

Far offshore wind conditions in scope of wind energy

Holtslag, Maarten

DOI

[10.4233/uuid:3c66f401-6cff-4273-aa49-df4274ba767f](https://doi.org/10.4233/uuid:3c66f401-6cff-4273-aa49-df4274ba767f)

Publication date

2016

Document Version

Final published version

Citation (APA)

Holtslag, M. (2016). *Far offshore wind conditions in scope of wind energy*. [Dissertation (TU Delft), Delft University of Technology]. <https://doi.org/10.4233/uuid:3c66f401-6cff-4273-aa49-df4274ba767f>

Important note

To cite this publication, please use the final published version (if applicable).
Please check the document version above.

Copyright

Other than for strictly personal use, it is not permitted to download, forward or distribute the text or part of it, without the consent of the author(s) and/or copyright holder(s), unless the work is under an open content license such as Creative Commons.

Takedown policy

Please contact us and provide details if you believe this document breaches copyrights.
We will remove access to the work immediately and investigate your claim.

FAR OFFSHORE WIND CONDITIONS IN SCOPE OF WIND ENERGY

FAR OFFSHORE WIND CONDITIONS IN SCOPE OF WIND ENERGY

Proefschrift

ter verkrijging van de graad van doctor
aan de Technische Universiteit Delft,
op gezag van de Rector Magnificus prof. ir. K. C. A. M. Luyben,
voorzitter van het College voor Promoties,
in het openbaar te verdedigen op vrijdag 17 juni 2016 om 12:30 uur

door

Maarten Christiaan HOLTSLAG

natuurkundig ingenieur
geboren op 10 juli 1985 te Zoetermeer, Nederland.

Dit proefschrift is goedgekeurd door de promotor en copromotor:

Prof. dr. G. J. W. van Bussel
Dr. W. A. A. M. Bierbooms

Samenstelling promotiecommissie:

Rector Magnificus,	voorzitter
Prof. dr. G. J. W. van Bussel	Technische Universiteit Delft
Dr. W. A. A. M. Bierbooms	Technische Universiteit Delft

Onafhankelijke leden:

Prof. dr. R. J. Barthelmie	Cornell University, Verenigde Staten
Prof. dr. J. Peinke	Oldenburg University, Duitsland
dr. S. E. Gryning	Danish Technical University, Denemarken
dr. G. J. Steeneveld	Wageningen University
Prof. dr. H. J. J. Jonker	Technische Universiteit Delft
Prof. dr. D. G. Simons	Technische Universiteit Delft, reservelid



Keywords: meteorology, wind energy, far offshore, wind turbine performance

Printed by: Gildeprint drukkerijen Enschede

Front & Back: Photo by T.E. Holtslag-Nieuwenhuizen, design by Gildeprint drukkerijen Enschede

Copyright © 2016 by M. C. Holtslag

ISBN 000-00-0000-000-0

An electronic version of this dissertation is available at

<http://repository.tudelft.nl/>.

*Everything should be made as simple as possible
but not any simpler.*

Albert Einstein

SUMMARY

Far offshore atmospheric conditions are favourable for wind energy purposes since mean wind speeds are relatively high (i.e., high power production) while turbulence levels are relatively low (i.e., less fatigue loads) compared to onshore conditions. Offshore wind energy, however, is still expensive compared to onshore wind energy. There is little known about exact offshore wind conditions due to the costs involved in far offshore atmospheric measurement campaigns. This causes unnecessary conservatism in wind turbine design and suboptimal wind turbine performance, which subsequently results in an increase in the cost of energy of offshore wind energy.

The aim of this PhD research is twofold. First far offshore atmospheric conditions relevant for wind energy are studied from a meteorological point of view, which should result in a comprehensive, accurate and implementable description of offshore atmospheric conditions for wind energy purposes. Second, the influence of the specified atmospheric description on wind turbine performance is studied in more detail. This should result in fundamental insight how offshore wind turbines are influenced by atmospheric conditions. Results can then aid in reducing the cost of offshore wind energy if they are implemented correctly.

Atmospheric conditions relevant for wind energy have been studied, and known theoretical relations have been validated, based on measurements from a recently constructed meteorological mast sited 85 km offshore in the Dutch North Sea. In this thesis it is decided to emphasize on frequently occurring conditions that are relevant for wind energy, namely wind shear (the change in wind speed with height) and turbulence (the change in wind speed in time).

It is found that a general framework can be used in which wind shear and turbulence characteristics are coupled as a function of atmospheric stability, which is a measure of the vertical temperature gradient. The resulting wind profile however, is only valid relatively close to the surface, which poses problems given the size of state of the art wind turbines. A new wind profile that is valid for the entire atmospheric boundary layer has therefore been derived based on theoretical grounds and it has been validated with observation data. The proposed wind profile is found to provide a better representation of offshore wind shear, especially if the atmosphere is stably stratified.

It is recognised that the majority of shear profiles used in wind energy are not capable of describing situations with a local wind maximum. Such phenomena, called low-level jets, are known to occur often onshore at night, but the offshore occurrence is not studied frequently in absence of detailed offshore observation data. The occurrence and characteristics of low-level jets offshore have therefore been studied with aid of the new offshore meteorological mast. It is found that low-level jets occur frequently and with characteristics relevant for wind energy purposes (with respect to the maximum wind speed and height of the wind maximum).

The atmospheric knowledge obtained is used for wind energy applications with the aid of numerical simulation software and a reference wind turbine frequently used in research. Adopting the general framework including atmospheric stability in wind turbine fatigue load assessment shows that guidelines, which typically do not consider atmospheric stability, cause an overestimation of simulated wind turbine fatigue loads. This is not necessarily caused by conservatism in either wind shear or the amount of turbulence, but by the lack of a coupling between both conditions. This coupling, which occurs in reality, should be adopted in wind turbine design as well. In wind energy resource assessment one thus also has to observe atmospheric stability conditions accurately. Next, the impact of wind shear and turbulence on wind turbine performance is assessed separately. Although this approach is not representative for actual offshore conditions, in which wind shear and turbulence are coupled, it does provide fundamental insight in wind turbine performance as a function of specific atmospheric conditions.

With respect to wind shear, it is found that the validated boundary layer wind shear profile substantially influences wind turbine power production as well as fatigue loads experienced by wind turbine blades. Especially for stable conditions, where the boundary layer profiles deviate most from simple diabatic wind profiles, fatigue loads are reduced by more than 10%. At the same time power production is reduced by up to 2% for stable conditions.

In absence of a simple model that can be used to describe low-level jets, it is decided to first formulate a new empirical low-level jet wind model that can easily be implemented for wind energy purposes. Subsequently the influence of low-level jets on wind turbine performance is assessed, where it is found that low-level jets can have a substantial influence depending on the jet characteristics. If the jet occurs exactly at hub height, both power production as well as blade root bending moments reduce substantially.

Finally, the influence of specific turbulence scales is studied in detail with aid of numerical simulations. In these simulations turbulence is filtered in such a way that only specific scales remain present. This allows a detailed study in which turbulence scales are relevant for wind energy performance. The results provide insight in modelling of wind conditions and show which turbulence scales have to be incorporated into wind turbine simulations. It is found that the reference wind turbine is hardly influenced by turbulence kinetic energy present in very large and very small scales. The structures with a similar order of magnitude as the turbulence length scale contain a lot of turbulence kinetic energy, and the reference wind turbine is able to convert part of the turbulence kinetic energy into power. Out of all turbulence scales, those structures with a similar order of magnitude to the turbulence length scale also contribute most to wind turbine fatigue loads.

The results obtained in this research are primarily theoretical, and they provide more fundamental insight into offshore atmospheric conditions and the subsequent performance of a wind turbine. If properly implemented however, it is possible that wind turbines can be designed with less conservatism, which directly reduces the cost of offshore wind energy. Besides, numerous results are useful to improve the accuracy of resource assessment and wind power forecasting, both contributing to the cost of energy as well. It shows the need to approach offshore wind energy as an interdisciplinary field in which meteorologists and engineers collaborate to optimize wind turbine performance.

SAMENVATTING

In het algemeen wordt aangenomen dat windcondities ver op zee gunstig zijn voor wind-energie doeleinden, enerzijds omdat de gemiddelde windsnelheid relatief hoog is (dus een hoge stroomproductie) en anderzijds omdat er relatief weinig turbulentie is (dus een een lagere vermoeiingsbelasting) ten opzichte van windcondities op land. Windenergie op zee is momenteel nog duur ten opzichte van windenergie op land. Er is weinig bekend over exacte windcondities op zee vanwege de hoge kosten van meetcampagnes op zee. Dit kan er toe leiden dat windturbines op zee ontworpen worden met onnodig conservatisme, en dat ze niet optimaal functioneren. Dit zorgt er vervolgens voor dat de kostprijs van windenergie op zee hoog is.

Het doel van dit promotieonderzoek is tweeledig. Ten eerste worden atmosferische condities ver op zee die relevant zijn voor windenergie doeleinden bestudeerd vanuit meteorologisch perspectief. Dit resulteert in een begrijpelijke, nauwkeurige en toepasbare beschrijving van atmosferische condities op zee. Ten tweede wordt in detail onderzocht wat de invloed is van de beschreven atmosferische condities op het functioneren van windturbines. Dit geeft fundamenteel inzicht in de wijze waarop windturbines op zee beïnvloed worden door atmosferische condities. Daarnaast kunnen de resultaten, indien correct toegepast, bijdragen aan het verlagen van de kostprijs van windenergie op zee.

De relevante windcondities voor windenergie die bestudeerd zijn in dit proefschrift zijn windschering (de verandering van de windsnelheid met hoogte) en turbulentie (de verandering van de windsnelheid in de tijd). Daarnaast zijn bestaande theoretische relaties gevalideerd die gebruikt kunnen worden om deze windcondities te beschrijven. Hiervoor is gebruik gemaakt van observatiedata die verkregen is met behulp van een meteorologische meetmast die 85 km uit de kust in de Nederlandse Noordzee geplaatst is.

Als eerste blijkt dat een beknopte set vergelijkingen gebruikt kan worden om relevante atmosferische condities op zee te beschrijven. Met behulp van deze vergelijkingen zijn windschering en turbulentie karakteristieken gekoppeld als functie van atmosferische stabiliteit. De stabiliteit van de atmosfeer is een maat voor de verticale temperatuurgradiënt. Daarnaast is een nieuw theoretisch windprofiel afgeleid en gevalideerd met observatiedata. Dit windprofiel is geldig voor de gehele atmosferische grenslaag. Het blijkt dat het nieuwe windprofiel vooral voor stabiele condities nauwkeuriger is en windschering beter beschrijft.

Het merendeel van de windprofielen die gebruikt worden ten behoeve van windenergie zijn niet in staat om situaties te beschrijven waarbij een lokaal windmaximum voorkomt. Zulke condities worden low-level jets genoemd en het is bekend dat deze veelvuldig voorkomen boven land gedurende de nacht. Er is echter weinig bekend over het voorkomen van low-level jets op zee vanwege de afwezigheid van gedetailleerde lokale observatiedata. Zowel het voorkomen als ook de karakteristieken van low-level jets

op zee zijn daarom bestudeerd met behulp van de eerder genoemde meteorologische meetmast. Het blijkt dat low-level jets inderdaad regelmatig voorkomen op zee, en de eigenschappen van deze low-level jets lijken relevant te zijn voor windenergie doeleinden (met betrekking tot de maximum windsnelheid en de hoogte van het lokale windmaximum).

In het tweede gedeelte van dit proefschrift zijn de verkregen meteorologische resultaten toegepast op windenergie met behulp van numerieke simulatie software en een referentie windturbine die vaak gebruikt wordt in onderzoek. Het gebruik van de bekende set vergelijkingen inclusief atmosferische stabiliteit in vermoeiingsberekeningen van de referentie windturbine laat zien dat richtlijnen, exclusief atmosferische stabiliteit, resulteren in een overschatting van de gesimuleerde vermoeiingsbelasting van windturbine componenten. Deze overschatting wordt niet veroorzaakt door conservatisme in ofwel windschering ofwel de hoeveelheid turbulentie, maar door het missen van een koppeling tussen beide condities. Deze koppeling komt in werkelijkheid wel voor en moet dan ook meegenomen worden in de noodzakelijke ontwerpsimulaties van windturbines. Daarnaast is het van belang dat de stabiliteit van de atmosfeer nauwkeurig bepaald worden in resource assessment. Vervolgens is in detail gekeken naar de impact van enerzijds windschering en anderzijds turbulentie, apart van elkaar, op de respons van de referentie windturbine. Deze benadering is niet representatief voor de werkelijkheid waarin windschering en turbulentie gekoppeld zijn, maar resulteert wel in fundamenteel inzicht in de respons van een windturbine op specifieke windcondities.

Met betrekking tot windschering blijkt dat het gevalideerde windprofiel van de grenslaag een substantiële invloed heeft op zowel de stroomproductie van een windturbine als ook op de vermoeiingsbelasting van de bladen van een windturbine. Vooral voor stabiele condities is er een sterke invloed omdat de grootste verschillen optreden tussen het grenslaag windprofiel en eenvoudige diabatische windprofielen. Uit de simulaties blijkt dat de bladwortel vermoeiingsbelasting afneemt met meer dan 10% en de stroomproductie met maximaal 2%. Omdat een eenvoudig model van low-level jets ontbreekt, is besloten om een nieuw empirisch model te formuleren, dat eenvoudig toegepast kan worden voor windenergie doeleinden. Vervolgens is de impact van low-level jets op de stroomproductie en vermoeiingsbelasting van een windturbine onderzocht. Hieruit blijkt dat low-level jets een enorme impact kunnen hebben, afhankelijk van de exacte jet karakteristieken. Zowel de stroomproductie als de bladwortel belasting nemen substantieel af als de low-level jet exact op ashoogte van de windturbine voorkomt.

Als laatste is gekeken naar de invloed van specifieke turbulentieschalen op een windturbine met behulp van numerieke simulaties. De turbulente windvelden die gebruikt zijn in deze simulaties zijn bewust gefilterd. Hierdoor blijven specifieke turbulentieschalen in de windvelden behouden in de simulaties en kan in detail bekeken worden welke turbulentieschalen relevant zijn voor een windturbine. Dit geeft ook fundamenteel inzicht in het modelleren van de wind en het laat zien welke turbulentieschalen zeker meegenomen moeten worden in windturbinesimulaties. Het blijkt dat zowel zeer kleine als ook zeer grote turbulentiestructuren amper invloed hebben op de windturbine. Juist de structuren in de orde van de turbulente lengteschaal bevatten veel turbulente kinetische energie, en een deel van deze turbulente kinetische energie kan door een windturbine in stroom omgezet worden. Tegelijkertijd dragen van alle turbulente structuren speci-

fiek de structuren in de orde van de turbulente lengteschaal ook het meeste bij aan de vermoeiingsbelasting van de windturbine.

Resultaten uit dit onderzoek zijn voornamelijk theoretisch van aard en verschaffen fundamenteel inzicht in atmosferische condities op zee en de resulterende invloed op een windturbine. De verwachting is echter dat onnodig conservatieve zekerheidsmarges van windturbines aangepast kunnen worden als de verschillende bevindingen uit dit proefschrift correct geïmplementeerd worden. Dit kan direct resulteren in een afname van de kostprijs van windenergie op zee. Daarnaast zijn een aantal resultaten bruikbaar om de nauwkeurigheid van zowel resource assessment als wind power forecasting te verhogen. Beide processen dragen bij aan de kostprijs van windenergie. Dit laat ook zien dat het noodzakelijk is om windenergie op zee interdisciplinair te benaderen. Ondanks het feit dat meteorologie en windenergie twee aparte onderzoeksvelden zijn, moeten meteorologen en ingenieurs samen werken om het functioneren van windturbines te optimaliseren.

CONTENTS

Summary	vii
Samenvatting	ix
1 Introduction	1
1.1 Motivation	1
1.2 An introduction to boundary layer meteorology	2
1.2.1 Atmospheric Stability	3
1.2.2 Turbulence, fluxes and wind shear	4
1.2.3 The offshore boundary layer	6
1.3 An introduction to wind turbine research	7
1.3.1 Power production	7
1.3.2 Fatigue loads	8
1.4 Outline of this thesis	9
2 A coupled framework to define atmospheric conditions offshore	11
2.1 Introduction	12
2.2 Theory	13
2.2.1 Wind shear	14
2.2.2 Second-order moments	15
2.2.3 Turbulence spectra	16
2.3 Mast characteristics and data post processing	18
2.3.1 Meteorological mast IJmuiden	18
2.3.2 Data post processing	21
2.4 Results	24
2.4.1 Wind Shear	24
2.4.2 Second order moments	26
2.4.3 Turbulence Spectra	30
2.5 Conclusions	34
3 Extending the surface layer wind shear profile	37
3.1 Introduction	38
3.2 Derivation and parametrization of the wind shear model	39
3.2.1 Theoretic derivation of the wind shear profile	39
3.2.2 Parametrization of the resistance functions A and B	42
3.2.3 Parametrization of surface roughness and boundary layer height	45
3.2.4 Parametrization of c	47
3.3 Validation of the theoretic wind profile	50
3.3.1 Validation with stability classes	50
3.3.2 Validation for stability as a continuous parameter	53

3.4	Discussion	56
3.5	Conclusions.	56
4	The occurrence and characterization of low-level jets offshore	59
4.1	Introduction	60
4.2	Theory	61
4.2.1	Inertial Oscillation	61
4.2.2	Baroclinicity	61
4.2.3	Coastal surface changes	62
4.3	Data and Methodology	62
4.3.1	Data description	62
4.3.2	Methodology and terminology	63
4.4	Results	66
4.4.1	Primary jet characteristics	66
4.4.2	Exploration of formation causes	67
4.4.3	Case Study	71
4.5	Conclusions.	75
5	Wind turbine fatigue loads as a function of atmospheric conditions	77
5.1	Introduction	78
5.2	Simulation conditions	79
5.3	Prescribing atmospheric conditions	83
5.3.1	Wind shear.	83
5.3.2	Turbulence intensity	84
5.3.3	Turbulence spectrum	87
5.3.4	Probability distributions	87
5.4	Fatigue load assessment	90
5.4.1	Sensitivity of fatigue loads to atmospheric stability	90
5.4.2	Spectral analyses of bending moments.	93
5.4.3	Lifetime fatigue loads	96
5.5	Discussion	99
5.6	Conclusion	100
6	The impact of deviating shear profiles on wind turbine performance	103
6.1	Introduction	104
6.2	Wind shear models	105
6.2.1	Diabatic shear profiles	105
6.2.2	Derivation of an empirical LLJ-model	106
6.3	Equivalent wind speed and hub height wind speed	111
6.3.1	Kinetic energy flux for diabatic wind profiles.	113
6.3.2	Kinetic energy flux for LLJ wind profiles	114
6.3.3	Equivalent wind speed for diabatic wind profiles	116
6.3.4	Equivalent wind speed for LLJ wind profiles	117

6.4	Simulation results	117
6.4.1	Diabatic wind profiles and power production	118
6.4.2	Diabatic wind profiles and fatigue loads	120
6.4.3	Low-level jet wind profiles and power production	121
6.4.4	Low-level jet wind profiles and fatigue loads	125
6.5	Discussion	125
6.6	Conclusions.	126
7	Wind turbine performance as a function of turbulence scales	129
7.1	Introduction	130
7.2	Theory	130
7.3	Methodology	132
7.3.1	Simulation set-up	132
7.3.2	Filtering for eddy sizes	134
7.4	Results	135
7.4.1	Case description	135
7.4.2	Effect of turbulence scales on power production.	137
7.4.3	Effect of turbulence scales on blade root bending moment	141
7.5	Discussion	143
7.5.1	Implications for operating wind turbines	143
7.5.2	Design of simulations and experiments	144
7.6	Conclusions.	144
8	Conclusions and Recommendations	147
8.1	Conclusions.	147
8.1.1	Offshore atmospheric conditions	147
8.1.2	Implications for wind energy purposes	148
8.2	Recommendations	150
8.2.1	Offshore meteorology for wind energy purposes.	150
8.2.2	Wind energy aspects	151
A	Surface layer wind profiles	155
A.1	The log-profile for unstable conditions	155
A.2	The log-profile for stable conditions	157
B	Scaling arguments for unstable conditions	159
B.1	Free Convective scaling with MO-theory	159
B.2	Directional scaling for unstable conditions	160
C	The relation between RI and ζ	165
D	Deriving the boundary layer wind profile	167
D.1	Derivation of the general wind profile.	167
D.2	Derivation of the resistance function B	168

Bibliography	173
Acknowledgement	181
List of Publications	183
Curriculum Vitae	185

1

INTRODUCTION

The beginning is the most important part of the work;

Plato

1.1. MOTIVATION

Offshore wind energy is currently still relatively expensive compared to onshore wind energy. To stimulate the development of new offshore wind farms, a consortium of 13 public research institutes and private companies initiated the research program FLOW (Far and Large Offshore Wind). The primary aim of the FLOW project is to reduce the costs of offshore wind energy by 20%, but also to increase the reliability and stimulate the development of offshore wind farms. It is recognised that the offshore environment poses challenges for the development of wind farms, and to overcome these challenges it is evident that an accurate description of offshore meteorological conditions is required. The atmosphere offshore differs substantially from the onshore atmosphere, and an additional uncertainty arises from the lack of available observation data offshore. As such it is deemed necessary within the framework of the FLOW project that research is initialised on the description of offshore wind conditions for wind energy purposes. To this end a new meteorological observation mast located 85 km offshore in the Dutch North Sea area was constructed in scope of the FLOW research program, hereafter named meteorological mast IJmuiden. Obviously the observation data retrieved from meteorological mast IJmuiden play a crucial role in this research since it is one of the few observations sites globally that is truly located far offshore in the marine environment.

It is necessary to emphasize that in this research offshore meteorological conditions are studied *for wind energy purposes*. As such important meteorological processes like for example convection, cloud formation, precipitation and large scale dynamics are not considered here. Besides, studying all possible relevant meteorological conditions in combination with the subsequent impact of these conditions on wind turbine performance is not possible in scope of the available time of this PhD research. It is therefore

decided to emphasize on conditions relevant for a wind turbine in normal operation, while extreme conditions (such as wind gusts) as well as specific operating conditions (such as an emergency shut down) are neglected. The resulting relevant atmospheric conditions are wind shear (the change of wind speed with height) and turbulence (the change of wind speed in time).

There is a fundamental difference in the approach to this research from either a meteorological or engineering perspective. Engineers typically prioritise that something is working effectively and efficiently while the underlying physics are less important. In contrary, meteorologists (or physicists in general) tend to answer research questions with the fundamental physical laws that govern the situation studied. In this research one might either adopt an engineering approach (empirical relations, with strong computational efficiency) or a physicist approach (starting off with the governing equations of fluid mechanics and the forces that drive the atmosphere). It should come to no surprise given my background that in this thesis the second approach is adopted over an engineering methodology that might be efficient but lack accuracy. Several examples throughout this research will show that in absence of a physical approach to the research, one will by definition introduce conservatism in wind turbine design, whereas with a fundamental approach one will reduce conservatism at the expense of a reduction in efficiency (typically in terms of computational demand). As such, a crucial aspect in this thesis is the assessment of whether one may incorporate physics in wind energy research and wind turbine design while keeping computational demand as low as possible.

Wind turbines are designed to conform to guidelines, which for the wind energy industry are the IEC guidelines (IEC 2005). It is common practice in wind energy research to assess the performance of a wind turbine as a function of a given hub height wind speed. Similarly, the IEC guidelines also tend to prescribe atmospheric conditions as a function of hub height wind speed. The change of wind speed with height for example is typically considered with an empirical power law

$$\overline{U}_h = \left(\frac{z}{z_h} \right)^\alpha \quad (1.1)$$

where \overline{U}_h is the hub height wind speed, z_h is the wind turbine hub height, z is the height above the surface and α is a power which for offshore sites is assumed to be 0.14 (IEC 2009). Whereas an engineer will likely say that the advantage of Equation 1.1 is its simplicity, a meteorologist will likely say that the equation does not consider the fundamental parameters or processes that influence wind shear. Such parameters are for example the roughness of the surface and the presence of vertical temperature gradients. In the following sections the basic physical processes in the atmosphere will be discussed and an introduction to relevant aspects of wind energy research for this thesis will be presented.

1.2. AN INTRODUCTION TO BOUNDARY LAYER METEOROLOGY

The earth's atmosphere can generally be divided into two main regions: the lower part of the atmosphere that is strongly influenced by surface conditions, and the upper part of the atmosphere that does not interact with the surface in any way. The lower part,

called the (atmospheric) boundary layer, is the atmosphere we tend to feel every day: it stretches out from the surface up to approximately 1 km height, depending on a variety of surface and atmospheric conditions. The free atmosphere above the atmospheric boundary layer is not discussed any further in this thesis since it is irrelevant for wind energy purposes most of the time. Wind energy engineers might associate a boundary layer with aerofoils and the blades of a wind turbine, however to put everything into perspective: whereas the atmospheric boundary layer has a thickness of approximately 1 km, the boundary layer of an aerofoil is typically several millimetres thick.

1.2.1. ATMOSPHERIC STABILITY

A crucial characteristic of the atmospheric boundary layer is its *stability*. For the explanation of atmospheric stability it is convenient to consider the *potential* temperature instead of the absolute temperature one is used to. Let us consider an air parcel with a given absolute temperature T . Temperature depends on air pressure as is known from thermodynamics

$$T = \rho R_d P \quad (1.2)$$

where ρ is the air density, R_d is the gas constant of dry air and P is the air pressure. If the air parcel ascends to higher altitudes (and thus the air pressure decreases), by definition the parcel's temperature will decrease. Besides, if an air parcel with a given air pressure is cold, it is relatively heavy compared to a warm air parcel due to the relation between temperature and air density. In the absence of condensation effects, the change in temperature with height in an adiabatic atmosphere equals 9.8 K/km. This given change in temperature is accounted for if one considers the potential temperature

$$\theta(z) = T(z) + 0.0098z \quad (1.3)$$

Similarly, humidity also has an impact on the temperature of an air parcel. Since water vapour has a molar mass of 18 g mol^{-1} and dry air (a combination of primarily nitrogen and oxygen) has a molar mass of 29 g mol^{-1} , the addition of water vapour to dry air will result in a reduction of the molar mass of air. A slightly humid air parcel that is advected to very dry air is thus a bit lighter compared to the environment, even if the temperature and air pressure of the air parcel and the environment are similar. The correction of temperature for humidity effects is adopted by introducing the virtual potential temperature, which assuming the air is not saturated can be approximated as

$$\theta_v = \theta [1 + 0.61r] \quad (1.4)$$

where r is the mixing ratio, the ratio of mass of water vapour to the mass of dry air. The correction for humidity effects is especially important for offshore environments where the surface has an abundance of water available for evaporation.

We can now differentiate between three specific situations or states of the atmosphere as a function of the temperature profile (see also Figure 1.1, but note that the profiles shown in Figure 1.1 are wind profiles)

- The virtual potential temperature *increases* with height. If an air parcel ascends upwards, it will be cool compared to its environment and thus relatively heavy. As

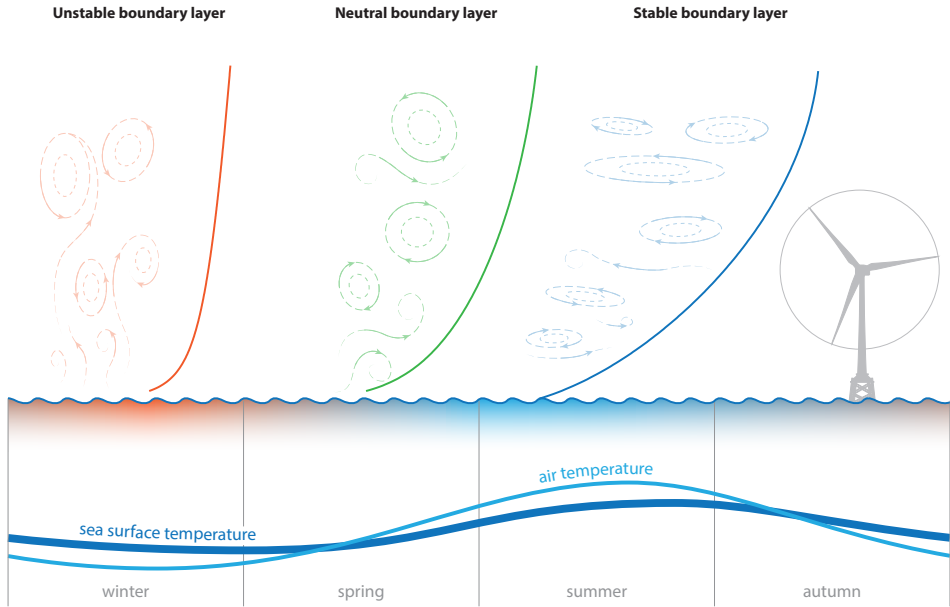


Figure 1.1: Impression of the seasonal cycle of stability offshore and the impact on wind shear (solid lines) and turbulence (dashed circles).

such it will descend back due to gravity effects. Such an atmosphere is called **stable** since vertical motions are suppressed by buoyancy effects. The stable boundary layer is characterised as a situation of warm air on top of a cool surface.

- The virtual potential temperature is *constant* with height. If an air parcel ascends upwards it will have the same temperature as its environment, and it will continue to ascend at the same speed as long as there is no force acting on the air parcel. This atmosphere is called **neutral**.
- The virtual potential temperature *decreases* with height. If an air parcel ascends upwards it will be warm compared to its environment and thus relatively light. As such the air parcel will accelerate and ascend further while the cool (and heavy) environment will slowly descend. Such an atmosphere is called **unstable** since vertical motions are enhanced by buoyancy effects. It is characterised as a situation with cold air over a warm surface.

The concept of static atmospheric stability is a crucial aspect of this research, and the impact of atmospheric stability on wind turbine performance will be studied in detail.

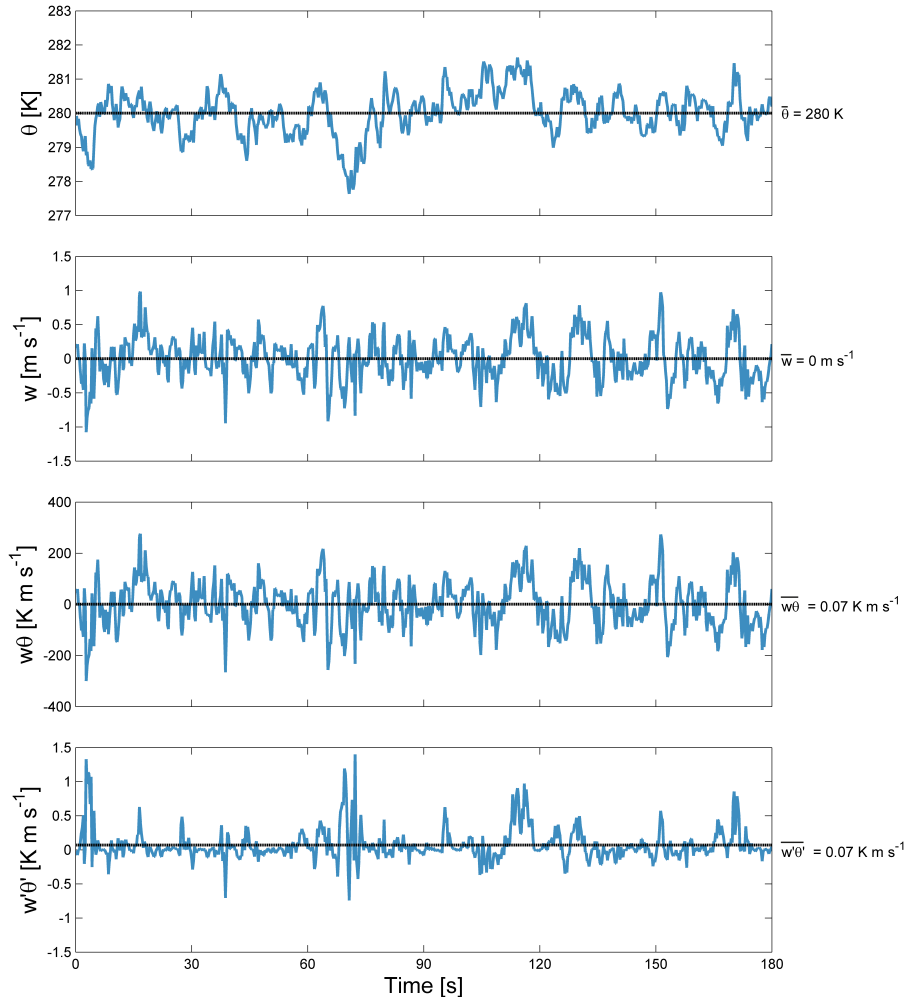


Figure 1.2: Artificial example of a temperature (first) and vertical wind speed (second) signal, and the corresponding total (third) and turbulent (forth) heat flux. The black lines correspond to the signal mean.

1.2.2. TURBULENCE, FLUXES AND WIND SHEAR

It has been shown that air parcels can randomly move vertically, but in reality this also occurs in the horizontal directions. The random movement of air parcels, deviating from the mean flow, is called turbulence. The mathematical notation of turbulence is typically done in terms of deviations from the mean state of a given variable. The upper two panels of Figure 1.2 show two artificial time signals of temperature and vertical wind speed. Both time signals can be decomposed at every time step into a mean and deviating component, which for respectively potential temperature and vertical wind speed equals

$$\theta(t) = \bar{\theta} + \theta'(t) \quad (1.5)$$

$$w(t) = \bar{w} + w'(t) \quad (1.6)$$

Here the overbars denote time averages and the primes denote fluctuating components. At each time step, there is some transport of heat by the vertical wind. The total flux of potential temperature, averaged with respect to time, is then computed as

$$\overline{w\theta} = \overline{\bar{w}\bar{\theta}} + \overline{w'\theta'} \quad (1.7)$$

since $\overline{w'\theta'} = \overline{w'\bar{\theta}} = 0$. This shows that over a given amount of time there is some heat transported by the *mean* flow and there is some heat transported by the *turbulent* flow. Besides, even if the mean vertical wind speed is 0 m s^{-1} , there might still very well be vertical transport of heat (see also the lower two panels of Figure 1.2). Similar reasoning can be applied for the transport of for example momentum and moisture.

In the atmosphere the mean wind speed normally increases with height. The change in wind speed with height, or wind shear, is a function of the stability of the atmosphere (see Figure 1.1). If the atmosphere is unstable, vertical transport of momentum is enhanced and as such momentum is redistributed more evenly across the atmosphere. This results in a flattened wind profile in which the wind speed does only slightly change with height at heights relevant for wind energy. For stably conditions however there is little turbulence and vertical transport is suppressed, which prevents redistribution of momentum vertically. If the atmosphere is stable stratified there is thus strong wind shear. This simple reasoning directly indicates the flawed simplification of guidelines that prescribe Equation 1.1 as a valid shear profile.

1.2.3. THE OFFSHORE BOUNDARY LAYER

As mentioned in the motivation of this thesis, it is explicitly aimed to study offshore atmospheric conditions. Whereas the aspects discussed so far are valid and applicable both offshore as well as onshore, it is important to understand some fundamental differences and the importance of surface characteristics.

A commonly heard motivation to construct wind farms offshore is the fact that prevailing wind conditions offshore are beneficial for wind turbines since mean wind speeds are high, while turbulence levels are low compared to onshore sites. This is true, and can easily be understood by noting that the surface roughness is significantly reduced compared to land surfaces. At the same time however, there is a constant interaction between surface and atmospheric conditions offshore. Onshore the roughness of the surface is typically either constant (urban areas), or there is a seasonal variation (nature areas or crop fields). Offshore however the roughness of the surface is neither constant nor changing with the seasons. Instead there is a direct interaction between the wind speed and the surface roughness since strong winds result in high waves, thereby increasing the roughness of the surface. Since turbulence is to an extent driven by friction, this also means that turbulence levels offshore tend to increase for very high wind conditions. Despite the increase in surface roughness for high wind speeds in the offshore environment, even for very high wind conditions the offshore surface roughness is substantially less compared to onshore sites.

As mentioned before the offshore environment is also characterised by an excessive availability of water which has to be accounted for when assessing temperature and stratification effects. If one would not consider humidity effects and extrapolate surface observations to typical wind turbine hub heights, it can be shown that the wind speed at hub height is overestimated by approximately 4% for stable conditions (Barthelme et al. 2010). Besides, if one determines atmospheric stability from regular surface observations without taking into account humidity effects, there is a tendency to determine a reduced stability (that is, actual stable conditions will be classified as near neutral, and unstable conditions will be classified as very unstable).

Lastly, the stability of the atmosphere is directly related to the temperature gradient between the surface and lower atmosphere. Whereas onshore the surface temperature has a daily cycle due to heating of the surface during the day by radiation, the offshore surface temperature does not change significantly on a time scale of hours. Instead there is typically a seasonal cycle offshore and the water temperature lags behind the air temperature. Whereas onshore atmospheric stability has a daily cycle, offshore there is a seasonal cycle in atmospheric stability conditions (Figure 1.1).

Due to the various differences between the onshore and offshore environment, relations used onshore to describe the environment cannot simply be copied to offshore sites without proper validation. Taking into account these fundamental differences however should result in an accurate and physical based description of offshore atmospheric conditions.

1.3. AN INTRODUCTION TO WIND TURBINE RESEARCH

Wind energy on its own is a highly interdisciplinary field of research, but the scope of this thesis is on those aspects that are directly dependent on the state of the atmosphere: power production and loads induced by the wind. When a wind turbine is designed, one has to consider a variety of atmospheric conditions as well as various operating conditions (IEC 2005). Ideally the final design is efficient in power production and sufficiently strong to avoid malfunctioning within the expected lifetime of the turbine, however overdimensioning of the turbine should be avoided. Eventually it is unavoidable that some conservatism is incorporated in the design of a turbine, typically by introducing safety factors. It is my belief however that if one considers environmental conditions as accurately as possible in the design of a new wind turbine, safety factors can be kept at a minimum, thereby reducing the overdimensioning that typically occurs.

1.3.1. POWER PRODUCTION

It can be shown that when air is flowing through an area A , the power of the wind is proportional to the wind speed cubed

$$P_w = \frac{1}{2} \rho A \bar{U}^3 \quad (1.8)$$

where P_w is the power of the wind. The maximum theoretical power extracted by a wind turbine from the wind in case of an ideal wind turbine without any losses is 59.3%, also known as the Betz limit. In practice the efficiency of state of the art wind turbines is less than 59.3% due to various electrical and mechanical losses.

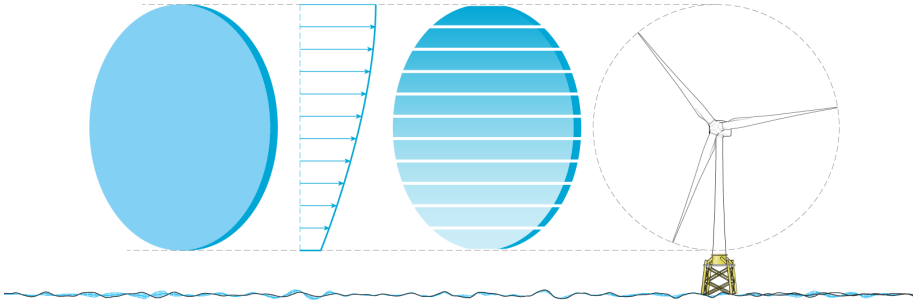


Figure 1.3: Representation of the kinetic energy flux through a wind turbine rotor disc. On the left side the assumption of a constant wind speed is visualised, while the impact of wind shear is shown in the middle sliced circle.

Any wind turbine is certified with a design power curve that relates the power production of the specified wind turbine to the wind speed experienced by the wind turbine. It is commonly assumed that the hub height wind speed \bar{U}_h is representative for the overall wind experienced by the wind turbine for power production calculations. In scope of previous equations however, it can easily be shown that for a circular rotor disc in combination with wind shear, the power of the wind in the upper half of the rotor disc is larger than the power of the wind in the lower half of the rotor disc (see Figure 1.3 for a visual clarification). As such, one can question if \bar{U}_h is indeed a representative wind speed for power curve certification and wind turbine performance assessment (Wagner et al. 2011). If it is assumed, for sake of simplicity, that \bar{U}_h is indeed representative, then one only has to obtain a distribution of \bar{U}_h over a given period of time to determine the expected lifetime power production of a turbine.

The expected lifetime power production of complete wind farms also strongly depends on prevailing wind directions, since wind turbines located in the wake of upstream turbines experience reduced mean wind speeds. This also has a significant impact on the fatigue of turbines since turbulence levels increase in the wake of a turbine. In this thesis, however, only the upstream (undistorted) wind conditions experienced by a single turbine and the resulting response of the turbine are considered.

1.3.2. FATIGUE LOADS

Wind turbines are typically designed to withstand forces exerted on the turbine for approximately 20 years. The loads experienced by a wind turbine can be separated into fatigue loads and extreme loads. Whereas extreme loads occur, hence the name, by rare events like extreme gusts reoccurring only once every few years, fatigue loads occur continuously. In this research only fatigue loads are considered since extremes and gusts are a study on its own.

Fatigue loads originate from the force exerted by the wind on the wind turbine. This force is variable in time, not only since for example the rotor rotates and experiences in one rotation high wind speeds and low wind speeds due to wind shear, but also due to the randomness of turbulent motions in the atmosphere. Due to the variability of the

force exerted by the wind on the turbine it is difficult to predict accurately how long wind turbine components will hold before breaking down. The strength of a turbine component is expressed in terms of a SN-curve in which the number of cycles before failure N is related to the stress S experienced by the component due to a constant cyclic load. For the majority of materials there is a minimum load below which fatigue is virtually negligible. This lower limit is called the fatigue strength ΔF_D which corresponds to N_D load cycles. For higher loads there is approximately a power law relation between the experienced load F_i and the corresponding cycles before failure N_i , which can be written as

$$N_i = N_D \left[\frac{\Delta F_D}{\Delta F_i} \right]^m \quad (1.9)$$

where m is the Wöhler exponent, a characteristic property of the material of which a turbine component is made of. Although some loads experienced by a wind turbine are periodic, part of the loads experienced by a wind turbine are random due to turbulence. It is common procedure in wind energy to use a rainflow counting algorithm to convert a random load signal into an estimate of the total fatigue load experienced by the turbine.

1.4. OUTLINE OF THIS THESIS

In this research the offshore atmosphere is studied primarily with the aid of observation data taken from the meteorological mast IJmuiden. This meteorological mast is located exceptionally far offshore compared to other offshore observation masts such as the meteorological mast OWEZ (located 15 km offshore), which provides a unique opportunity to assess far offshore atmospheric conditions for wind energy purposes. The impact of considering specific offshore atmospheric conditions on wind turbine design is analysed with the wind energy industry software package Bladed in combination with a reference 5 MW NREL wind turbine [Jonkman et al. \(2009\)](#). Bladed is used on purpose since it is widely used in both industry as well as academia, thus the results obtained in this study are directly implementable by industry as well. The 5 MW NREL wind turbine is considered since it is a frequently used reference turbine in literature, hence it is easy to compare results with other studies. This thesis consists of the following chapters:

Chapter 2 - A coupled framework to define atmospheric conditions offshore. In this chapter a framework is created in which all atmospheric conditions relevant for a wind turbine in standard operation are defined as a function of one fundamental dimensionless parameter, the stability parameter ζ . The framework follows Monin-Obukhov similarity theory, a scaling theory that has been validated onshore sufficiently close to the surface. If Monin-Obukhov theory is also valid offshore one can easily describe the offshore atmosphere with relations that have been validated onshore while taking into account the interaction between the wind and sea.

Chapter 3 - Extending the surface layer wind shear profile. In this chapter wind shear is studied in greater detail. Based on the work of [Gryning et al. \(2007\)](#) a wind shear profile is derived theoretically that should be valid for the entire boundary layer, this in contrast to the surface layer wind shear profile which is valid only in the lowest 10% of the boundary layer. The theoretic boundary layer wind shear profile is validated offshore with observation data, and the applicability of this wind shear profile for wind energy purposes is analysed showing potential difficulties.

Chapter 4 - The occurrence and characterization of low-level jets offshore. In this chapter the occurrence and characteristics of low-level jets (LLJs) offshore are analysed. LLJs are distinct wind shear profiles with a local wind maximum close to the surface, and there is a potential significant impact for wind turbines. These jets have been studied onshore frequently, but in absence of observation data up to a height of several hundreds of meters it has been difficult to assess LLJs offshore. With aid of LIDAR observation data, wind profiles up to 315 m height are studied showing the potential frequency of occurrence of LLJs offshore.

Chapter 5 - Wind turbine fatigue loads as a function of atmospheric conditions. This is the first chapter in which the obtained atmospheric results are directly put into perspective of wind energy. The framework derived in Chapter 2 is incorporated in the design software Bladed, and the impact of atmospheric stability on wind turbine fatigue loads is analysed. Besides, it is recognised that the framework has a disadvantage in terms of computational efficiency. As such a methodology is proposed that circumvents this disadvantage.

Chapter 6 - The impact of deviating shear profiles on wind turbine performance. In this chapter the impact of considering the boundary layer wind shear profile in contrast to the surface layer wind shear profile is analysed. Besides, an engineering model of a LLJ is presented that can easily be used for wind energy research. The impact of both of these wind profiles on wind turbine performance is studied with respect to wind turbine fatigue loads and wind turbine power production.

Chapter 7 - Wind turbine performance as a function of turbulence scales. In this chapter the influence of turbulence on wind turbine performance is studied in more detail. With aid of a special filter, turbulence structures are filtered out of numerical simulations, to assess specifically which scales of turbulence contribute most to wind turbine power production and wind turbine bending moments. This provides valuable insight how to define wind turbine simulations, but it also shows the necessity to consider turbulence in wind power forecasting.

Chapter 8 - Conclusions and Recommendations In this chapter the conclusions of the previous chapters are presented in combination with recommendations for future work.

As a final note it is pointed out that in scope of the funding of this project by the FLOW consortium, this thesis should not only meet academic criteria but also be understandable and usable by engineers and consultants working in industry. As such, it has been a challenge to write in depth meteorological and engineering research carried out for this thesis in an understandable but still academic way. In my opinion not only engineers and meteorologists should cooperate and find each other at an academic level, but wind energy as a whole should approach the remaining challenges in an interdisciplinary manner. This can only be achieved by incorporating knowledge of experts on various disciplines into the field of wind energy, thereby stepping outside the traditional boundaries of individual domains like aerodynamics, structural dynamics, meteorology, electrical engineering or policy making. In the end, wind energy can only successfully drive our future energy system if wind farms are designed taking into account all relevant disciplines in a multidisciplinary methodology.

2

A COUPLED FRAMEWORK TO DEFINE ATMOSPHERIC CONDITIONS OFFSHORE

*One can state, without exaggeration, that the observation of
and the search for similarities and differences
are the basis of all human knowledge.*

Alfred Nobel

For several decades meteorologists use Monin-Obukhov similarity theory (MO-theory) to describe the atmosphere relatively close to the surface. The relations that follow from MO-theory have been validated frequently on shore, however, offshore it has not been possible to perform a similar extensive validation due to the limited availability of observation data. With the construction of meteorological mast IJmuiden there is a unique possibility to validate MO-theory in a far offshore environment. If indeed MO-theory is valid offshore as well, then the knowledge obtained in the previous decades onshore can be used to describe the offshore atmosphere as well, taking into account specific surface conditions offshore.

In this chapter first of all MO-theory is explained, and the specifications of meteorological mast IJmuiden are presented. Next, it is aimed to validate MO-theory, since once can define a framework in which wind shear and turbulence characteristics are coupled as a function of atmospheric stability if MO-theory is applicable offshore. In this chapter the impact of MO-Theory on wind turbine performance is not discussed, and instead obtained results will be put into perspective of wind energy in Chapter 5.

Parts of this chapter are published as: Holtslag, M. C., Bierbooms, W. A. A. M. & van Bussel, G. J. W. (2015), 'Validation of surface layer similarity theory to describe far offshore marine conditions in the Dutch North Sea in scope of wind energy research', *Journal of Wind Engineering and Industrial Aerodynamics*, **136** 180-191.

2.1. INTRODUCTION

In wind energy the IEC guidelines (IEC 2005, 2009) are typically considered to prescribe atmospheric conditions for a variety of wind turbine operating conditions. If one would follow these guidelines strictly, then wind shear and the turbulence intensity would be a function of the hub height wind speed alone. For the turbulence spectra the guidelines consider either the Mann model (Mann 1994, 1998) or the Kaimal spectra Kaimal et al. (1972), and the spectral model parameters are assumed to be constant or a function of hub height wind speed as well. Thus for a given hub height wind speed the entire environment is defined according to these guidelines. As discussed in Section 1.2 this convenient simple representation of the atmosphere is incomplete. As such it is aimed to define a new framework in which the atmosphere is represented in a physical correct way.

In boundary layer meteorology, Monin-Obukhov similarity theory is generally applied to describe the atmosphere close to the surface (MO-theory, Monin & Obukhov (1954), Obukhov (1971)). In this theory it is assumed that the turbulent fluxes of heat, moisture and momentum are independent of height for a stationary atmosphere over horizontally homogeneous terrain. The assumption that turbulent fluxes are independent of height is typically used for the lowest 10% of the atmospheric boundary layer (Stull 1988), and it is expected that surface fluxes are representative for the atmosphere close to the surface. Validation of MO-theory has started in the 1960's, and ever since experimental studies have shown that MO-theory is applicable for a variety of surface conditions. A well-known example of such an experimental study is the Kansas experiment (Haugen et al. 1971, Businger et al. 1971), which was performed at a horizontally flat wheat-farming area of one square mile, with a uniform upstream fetch of 2.4 km. A detailed reflection on the Kansas and Minnesota experiments is given by Kaimal & Wyngaard (1990), in which also possible errors and distortions are discussed that might have influenced the experiments.

The various field experiments give confidence in the applicability of MO-theory in the lower parts of the atmosphere, but so far there is little validation performed for significantly far offshore (> 50 km offshore) sites due to the costs involved to conduct measurement campaigns far offshore. In scope of wind turbine design there is a growing interest in accurate methodologies to describe far offshore atmospheric conditions. The driving atmospheric conditions that are relevant here are wind shear and turbulence, which influence power production and wind turbine fatigue loads (Sathe & Bierbooms (2007), Mücke et al. (2011), Wagner et al. (2011)). Recent studies show that since atmospheric stability has a significant impact on wind shear (Sathe et al. 2011) and turbulence conditions (Sathe et al. 2013), both power production and fatigue loads of a wind turbine depend on atmospheric stability as well. Although atmospheric stability is generally neglected in wind turbine design (IEC 2005), it is well known that atmospheric stability influences wind turbine performance. Sathe & Bierbooms (2007) showed that for steady state conditions blade root fatigue loads in flapwise direction increase by a factor 6 to 24, depending on the distribution of atmospheric stability, if one considers stability in fatigue load assessment. For non steady state conditions, Sathe et al. (2013) showed that if one follows the IEC guidelines and neglects atmospheric stability fatigue loads of a wind turbine rotor are overestimated by 28 to 48%, and tower loads are even overestimated

up to 96%. With respect to power production, Wharton & Lundquist (2012) showed that wind turbines produce up to 15% more power for stable conditions compared to strongly convective conditions.

Due to the high heat capacity of water it is often assumed that the marine boundary layer is neutrally stratified. For the Dutch North Sea area however, Coelingh et al. (1996) showed that very unstable conditions are prevailing for all seasons. The unstable conditions occur primarily in winter and autumn when seawater is relatively warm compared to the atmosphere. Besides, for northerly winds one can expect advection of cold polar air over the relatively warm sea. Stable conditions are expected to occur for southerly winds for which warm air is advected. The dependence of atmospheric stability on wind direction for the Dutch North Sea is shown in Sathe et al. (2011) as well.

With the construction of meteorological mast IJmuiden 85 km off the Dutch coast, the opportunity has risen to assess the applicability of MO-theory to describe the far offshore marine boundary layer. If MO-theory is indeed valid far offshore, then it will be possible to define a framework of relatively simple equations that can be used to define wind shear, turbulence intensity and the turbulence spectra as a function of atmospheric stability. Besides, since in MO-theory wind shear and turbulence are mutually dependent on atmospheric stability (as is the case in reality as well), the resulting framework could include the coupling mechanism of atmospheric stability, which is not considered in guidelines typically considered in wind energy research.

2.2. THEORY

The explanation of Wyngaard et al. (1971) is followed to introduce Monin-Obukhov similarity theory. Similar as proposed by Obukhov (1946), it is expected that the wind and temperature profiles depend on four fundamental state variables: the surface heat flux H , the height above the surface z , the buoyancy parameter g/θ_v and the surface shear stress τ_0 . These four variables can be combined to form two temperature scales, two velocity scales and two length scales

$$\begin{aligned} \theta_{*0} &= -\frac{H}{\rho c_p u_{*0}} & u_{*0} &= \sqrt{\frac{\tau_0}{\rho}} & z & \\ \theta_f &= \left[\frac{\overline{\theta}_v}{gz} \left[\frac{H}{\rho c_p} \right]^2 \right]^{1/3} & u_f &= \left[z \frac{g}{\theta_v} \frac{H}{\rho c_p} \right]^{1/3} & L &= -\frac{u_{*0}^3 \rho c_p \overline{\theta}_v}{\kappa g H} \end{aligned} \quad (2.1)$$

Here c_p is the specific heat of air and κ is the Von Kármán constant. These velocity and temperature scales are not independent, since

$$-u_{*0}\theta_{*0} = u_f\theta_f = \frac{H}{\rho c_p} \quad (2.2)$$

And thus one is left with one independent temperature scale (typically θ_{*0} is chosen), one independent velocity scale (typically u_{*0} is chosen) and two independent length scales. As such there is only one dimensionless scale

$$-\frac{z\kappa g \left[\overline{w'\theta'_v} \right]_s}{u_{*0}^3 \overline{\theta}_v} = \frac{z}{L} = \zeta \quad (2.3)$$

where the surface heat flux H has been converted into the surface kinematic heat flux. In a neutral atmosphere by definition $\overline{w'\theta'_v} = 0$ and hence $\zeta = 0$. For unstable conditions $\overline{w'\theta'_v} > 0$ (and thus $\zeta < 0$) while for stable conditions $\overline{w'\theta'_v} < 0$ (and thus $\zeta > 0$). Following Buckingham Pi theory, all variables that are non-dimensionalized with the proper scaling variables should then be a function of ζ alone.

2

2.2.1. WIND SHEAR

In meteorology one typically considers the wind gradient $\partial\overline{U}/\partial z$ to describe wind shear, which can be made non-dimensional with the length scale z and velocity scale u_{*0} as

$$\frac{z}{u_{*0}} \frac{\partial\overline{U}}{\partial z} \quad (2.4)$$

The Von Kármán constant κ is typically included in the definition of the dimensionless wind gradient ϕ_M , which has to be a function of the dimensionless stability parameter ζ

$$\phi_M = \frac{\kappa z}{u_{*0}} \frac{\partial\overline{U}}{\partial z} = f(\zeta) \quad (2.5)$$

It has been the aim of numerous studies to first of all assess if indeed ϕ_M does depend on ζ , and to subsequently find proper relations between ϕ_M and ζ . An overview of experimentally obtained ϕ_M functions can be found in Högström (1988). With the aid of these functions one can obtain a wind shear profile after integration of ϕ_M

$$\overline{U}(z) = \frac{u_{*0}}{\kappa} \int_{z_0}^z \frac{\phi_M}{z} dz \quad (2.6)$$

where both u_{*0} and κ are assumed to be independent of height. The Von Kármán constant is defined in such a way that for neutral conditions, where $\zeta = 0$, $\phi_M = 1$. For neutral conditions it is thus found by definition

$$\overline{U}(z) = \frac{u_{*0}}{\kappa} \ln\left(\frac{z}{z_0}\right) \quad (2.7)$$

Equation 2.7 is known as the neutral logarithmic wind shear profile. For stable and unstable conditions the general expression of the wind shear profile is

$$\overline{U}(z) = \frac{u_{*0}}{\kappa} \left[\ln\left(\frac{z}{z_0}\right) - \Psi(\zeta) + \Psi(\zeta_0) \right] \quad (2.8)$$

where Ψ is a stability correction function of which the exact formulation depends on the formulation of ϕ_M , and $\zeta_0 = z_0/L$. Generally the last term on the right hand side is neglected since $\Psi(\zeta) \gg \Psi(\zeta_0)$. Equation 2.8 is known as the stability dependent logarithmic wind shear profile.

In this research two stability correction functions are considered for stable conditions, and two stability correction functions are considered for unstable conditions. The stability correction functions most frequently used in meteorology and wind energy are

the Businger-Dyer stability correction functions (BD-Functions, [Businger et al. \(1971\)](#), [Dyer \(1974\)](#))

$$\Psi(\zeta \leq 0) = 2 \ln\left(\frac{1+x}{2}\right) + \ln\left(\frac{1+x^2}{2}\right) - 2 \arctan(x) + \frac{\pi}{2} \quad (2.9)$$

$$\Psi(\zeta \geq 0) = -\beta\zeta \quad (2.10)$$

where $x = [1 - \gamma\zeta]^{1/4}$ and both γ and β are empirical parameters. In this research it is assumed that $\gamma = 19.3$ and $\beta = 6.0$ in agreement with [Högström \(1988\)](#). The derivation of Equations 2.9 and 2.10 is given in Appendix A.

It is recognised that the BD-functions may be incorrect for very unstable or very stable conditions. For very unstable conditions where $\zeta \rightarrow -\infty$, $u_{*0} \rightarrow 0$ and the friction velocity is thus no longer a valid state variable. Based on theoretically proposed dependencies it is expected that $\Phi_M \propto (-\zeta)^{-1/3}$ (see Appendix B for details on so called free convective scaling). This results for unstable conditions, as shown in Appendix A, in ([Carl et al. 1973](#))

$$\Psi(\zeta \leq 0) = 1.5 \ln\left(\frac{1+y+y^2}{3}\right) - \sqrt{3} \arctan\left(\frac{2y+1}{\sqrt{3}}\right) + \frac{\pi}{\sqrt{3}} \quad (2.11)$$

where $y = [1 - \gamma\zeta]^{1/3}$ and $\gamma = 12.87$ for the free convective formulation in line with [Fairall et al. \(1996\)](#) (note the difference compared to the value of 19.3 for the Businger-Dyer equation). True free convective conditions do not occur in reality, and Equation 2.11 has been validated in various studies for moderate unstable conditions ($-2 < \zeta < 0$, see [Högström \(1988\)](#) for details). In this chapter however Equation 2.11 is assumed to be valid for all unstable conditions. The validity of the -1/3 power proportionality for very unstable conditions is questioned by [Kader & Yaglom \(1990\)](#) who adopts directional scaling arguments, however the applicability of direction scaling for wind shear in the free convective limit is questionable as discussed in Appendix B. As such the commonly used -1/3 scaling is adopted for unstable conditions in this research, and the resulting wind shear profile is compared to the Businger-Dyer equations shown in Equation 2.9.

For stable conditions the linearity of Ψ in Equation 2.10 results in an overestimation of wind shear for strongly stable conditions (see [Holtslag \(1984\)](#), [Vickers & Mahrt \(1999\)](#), [Cheng & Brutsaert \(2005\)](#)). As such the formulation of [Holtslag & de Bruin \(1988\)](#) is considered in this research as well, which should be applicable up to at least $\zeta = 10$, defined as

$$\Psi_M(\zeta \geq 0) = -a\zeta - b\left[\zeta - \frac{c}{d}\right] \exp(-d\zeta) - \frac{bc}{d} \quad (2.12)$$

With coefficients $a = 1$, $b = 2/3$, $c = 5$, $d = 0.35$ ([Beljaars & Holtslag 1991](#)). The corresponding non-dimensional wind gradient is shown in Appendix A. The proposed theoretic wind shear profiles will be validated in Section 2.4.1 where 'Businger-Dyer' corresponds to Equations 2.9 and 2.10 (for unstable and stable conditions respectively), 'Free Convection' corresponds to Equation 2.11 and 'Holtslag' corresponds to Equation 2.12

2.2.2. SECOND-ORDER MOMENTS

In MO-theory the standard deviation of the wind is non-dimensionalized with the friction velocity. Similar as was found for wind shear, the non-dimensional second-order

moments are constant for neutral conditions (Stull 1988)

$$\frac{\sigma_x}{u_{*0}} = A_x \quad (2.13)$$

Where x denotes the three wind components. The constant coefficients A_x range from 1.7 to 2.9 for the horizontal components and from 1 to 1.6 for the vertical component (Busch 1973, Stull 1988).

As mentioned before u_{*0} is not a proper scaling parameter for very unstable conditions, and instead the velocity scale u_f is used to non-dimensionalize the second-order moments for such conditions. A 1/3 power law relation is therefore expected between the non-dimensional second-order moments and ζ for unstable conditions, as shown in Appendix B, which results in

$$\frac{\sigma_x}{u_{*0}} \propto [-\zeta]^{1/3} \quad (2.14)$$

Various relations that follow Equation 2.14 have been proposed and validated for moderate unstable conditions literature (Busch 1973, Stull 1988, Kader & Yaglom 1990, Hedde & Durand 1994). A formulation in line with

$$\frac{\sigma_x}{u_{*0}} = A_x [1 - B_x \zeta]^{1/3} \quad (2.15)$$

is expected to hold, to match the behaviour of the non-dimensional second-order moments for free convective and neutral conditions. Kader & Yaglom (1990) questioned the validity of a 1/3 power law relation for moderate unstable conditions based on directional scaling arguments. As shown in Appendix B, directional scaling might very well be adopted for moderate unstable conditions.

For stable atmospheric conditions the non-dimensional second-order moments are typically found to decrease with height within the boundary layer (Caughey et al. 1979, Stull 1988). In literature one can find various relations between the non-dimensional second-order moments and the relative height within the boundary layer as

$$\frac{\sigma_x}{u_{*0}} \propto \left[\frac{z}{h} \right]^p \quad (2.16)$$

where h is the boundary layer height and p is a power of approximately 0.5. Although a direct relation between the second-order moments and atmospheric stability is typically not shown in literature, do note that h does depend, amongst others, on atmospheric stability. Since it is difficult to accurately observe h in practice it is not aimed in this research to validate a relation in line with Equation 2.16. It is expected however that for increasing stable stratification the shear production of turbulence decreases while the suppression of turbulence by buoyancy increases, and therefore it is assumed that the non-dimensional second-order moments decrease with increasing stability.

2.2.3. TURBULENCE SPECTRA

For the expected turbulence spectra the derivation of Kaimal et al. (1972) is followed to define the Kaimal spectra. Note that the IEC guidelines for design load calculations (IEC 2005) recommend the use of the Mann uniform shear turbulence model (Mann 1994,

1998). Here however it is aimed to assess the applicability of similarity theory offshore to describe the relevant wind parameters for wind energy research. The Mann model, although possibly applicable offshore as well, is not derived on these scaling principles but is derived based on linearisation of the Navier-Stokes equations. One could argue that it is possible to fit the Mann model parameters to find stability dependences as is done for example in [Sathe et al. \(2013\)](#) but then one would no longer use methodologies based on surface layer similarity theory. As such the Kaimal spectra is considered to be a viable turbulence spectra for the far offshore environment.

Kolmogorov's similarity hypothesis for the inertial subrange states that the one dimensional spectrum of the longitudinal wind component scales as

$$F_u(k) = \alpha_k \epsilon^{2/3} k^{-5/3} \quad (2.17)$$

where F_u is the longitudinal wave number spectrum, k is the wave number, ϵ is the dissipation rate of turbulent kinetic energy and α_k is Kolmogorov's constant which according to [Högström \(1990\)](#) should be in the order of 0.5. Adopting Taylor's hypothesis of frozen turbulence, and relating the wave number k to the frequency n in Hz (since typically one measures frequency), Equation 2.17 can be written as

$$nS_u(n) = \alpha_k \epsilon^{2/3} \frac{2\pi n}{U}^{-2/3} \quad (2.18)$$

where S_u is the longitudinal frequency spectrum. Next, a dimensionless dissipation rate and a dimensionless frequency are introduced as respectively

$$\phi_\epsilon = \frac{\kappa z \epsilon}{u_{*0}^3} \quad (2.19)$$

$$f = \frac{nz}{U} \quad (2.20)$$

which allows Equation 2.18 to be written as

$$\frac{nS_u(n)}{\phi_\epsilon^{2/3} u_{*0}^2} = \frac{\alpha_k}{[2\pi\kappa]^{2/3}} f^{-2/3} \quad (2.21)$$

The advantage of this formulation is that the right hand side is independent of stability and a function of frequency alone. As such one would expect that for various stability conditions the turbulence spectra collapse onto one line in the inertial subrange. This is indeed found and shown in detail in Figures 4, 5 and 6 of [Kaimal et al. \(1972\)](#). The spectra separate at low frequencies however with an orderly decrease in the non-dimensional spectral energy for increasing stability at given non-dimensional frequencies. Similar results were found for the spectra of temperature fluctuations and the co-spectra of the Reynolds-Stress components and the turbulent heat flux.

Since the spectra are not uniform with the scaling applied here for all stability conditions, [Kaimal et al. \(1972\)](#) scaled the spectra with the variance of the corresponding signal. Clearly the spectra in the inertial subrange would no longer coincide for different stability conditions, however by introducing a modified frequency scale f/f_0 the collapse can be re-introduced. Here f_0 is the intercept of $nS_u(n)/\sigma_u^2 = 1$ and the extrapolated inertial subrange spectrum. For clarity reasons Figure 2.1 shows two examples of

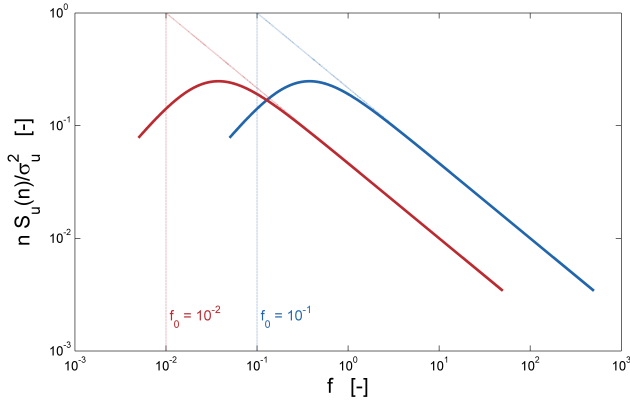


Figure 2.1: Dependence of the Kaimal spectra on the scaling frequency f_0 .

idealised spectra and the corresponding scaling frequencies f_0 . By including these scaling adjustments the spectra all have the same area of 1 (due to the scaling with σ_u^2), and all spectra have to collapse in the inertial subrange (due to the scaling with f_0). In [Kaimal et al. \(1972\)](#) it is shown that for stable conditions all spectra (that is, for the three wind components and temperature) satisfy

$$\frac{n S_x(n)}{\sigma_x^2} = \frac{0.164 f / f_0}{1 + 0.164 [f / f_0]^{5/3}} \quad (2.22)$$

In this chapter it is aimed to validate Equation 2.22 for both stable and unstable conditions. If indeed Equation 2.22 is found to be applicable, then it is aimed to parametrize f_0 as a function of ζ similar as for example [Kaimal \(1973\)](#), [Caughey \(1977\)](#). It should be noted that the coefficients of 0.164 used here are site specific and are found originally for onshore conditions. As such it is well possible that for offshore conditions these coefficients should change.

2.3. MAST CHARACTERISTICS AND DATA POST PROCESSING

In this section the specifics of meteorological mast IJmuiden are presented, including the precise sensor layout and sensor specifications, and possible sources of data distortion are explored as well. The observation data is filtered to reduce the possible distortion of data by the mast structure as much as possible. Besides, also the post-processing of the data for the validation of MO-theory is presented, since it is recognised that MO-theory is not valid for all conditions, and some crucial parameters have to be calculated from the standard observations.

2.3.1. METEOROLOGICAL MAST IJMUIDEN

The 92 m high meteorological mast IJmuiden is sited 85 km off the coast of IJmuiden (N 52°50.89' E 3°26.14'), and includes regular meteorological mast-equipment (anemom-

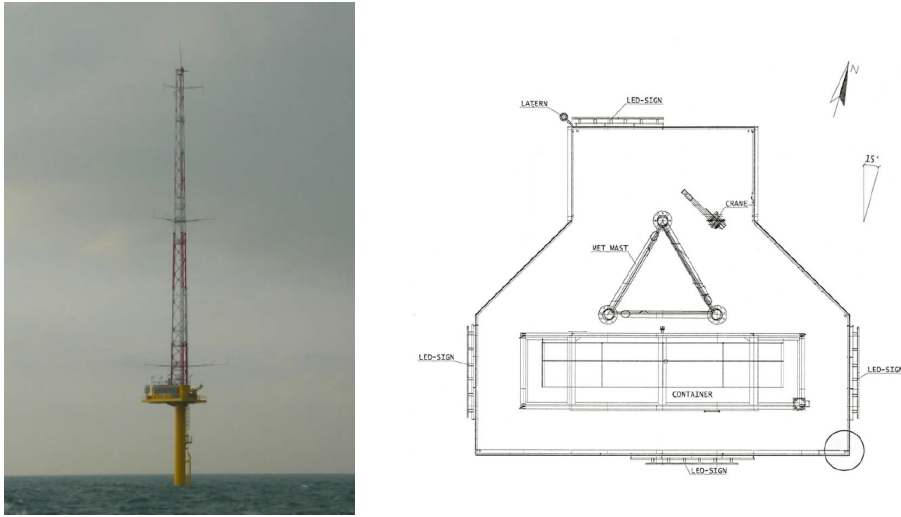


Figure 2.2: Photograph of meteorological mast IJmuiden, and an overview of the control platform, taken from [Werkhoven & Verhoef \(2012\)](#).

etry), a Zephir 300 LIDAR for observations up to 315 m height and a Triaxys wave buoy for wave and surface observations. A detailed description of the mast design, the sensor specifications and data collection procedure is found in the instrumentation report of the meteorological mast ([Werkhoven & Verhoef 2012](#)). The meteorological mast has a platform at 18 m height with a control room container, and horizontal booms have been installed at 25.5, 57 and 86.5 m height pointing outward of the mast in three directions (46.5° , 166.5° and 286.5° , called respectively NE, SSE and WNW from here on). In Figure 3 of [Wessels \(1983\)](#) it is shown that the ratio of the length of the horizontal booms to the radius of the meteorological mast is an important parameter to quantify flow distortion by the meteorological mast. This ratio equals respectively 9.1, 9.4 and 10.2 for the horizontal booms at 25.5, 57 and 86.5 m height. An impression of the mast itself and the layout of the platform with the control room is shown in Figure 2.2.

Several small wind turbines and solar panels are installed on top of the control room container for power production, which may lead to local flow distortion of wind sensors. A preliminary wind analysis showed that the wind observations at 25.5 m height from the SSE boom are indeed distorted, and these observations have thus not been included in subsequent analyses. Sensors are installed in the meteorological mast at the boom edges (to measure wind speed and wind direction), and both on top of the control room container as well as in the mast itself (pressure, temperature and relative humidity). The air pressure is measured at 21 and 90 m height with a Vaisala PTB210 air pressure sensor with an accuracy of 0.2 hPa, and the air temperature and relative humidity are observed at similar heights with a Vaisala HMP155D with an accuracy of respectively 0.1 K and 1%. At 85 m height the three components of the wind vector are observed with Metek USA-

1 sonic anemometers with an accuracy of 0.1 m s^{-1} , which are placed 1.5 m below the horizontal booms on a vertical spigot. At 27, 58.5 and 92 m height horizontal wind speed is measured with Thies first class advanced anemometers with an accuracy of 0.2 m s^{-1} , and at 26.2, 57.7 and 87.2 m height wind direction is measured with Thies first class wind vanes with an accuracy of 1° . The anemometers at 92 m height are placed on top of the mast itself, not on vertical spigots above horizontal booms. All sensors are calibrated according to ISO 17025. All wind, temperature, pressure and humidity observation operate at 4 Hz, and for each 10-minute interval the mean, minimum, maximum and standard deviation of the observations is stored. Besides, also the high frequency observation data of the sonic anemometers are available for analyses on turbulence characteristics.

The Zephir 300 LIDAR is a continuous wave LIDAR operating at 50 Hz, and measures the three components of the wind between 90 and 315 m height, with 10 observation heights equally spaced out every 25 m. The accuracy of the LIDAR is 0.5% for the wind speed observations and 0.5° for the wind direction. In this chapter LIDAR data are not used, however in following chapters the 10-minute mean observations are used for detailed assessment of wind profiles at higher altitudes.

The wave buoy measures specific wave characteristics like significant wave height and average wave period, current direction and current speed as well as water temperature. The buoy observations are stored as 1 hour averaged observations. In the remainder of this thesis only surface temperature observations of the wave buoy are used, and remaining observation data is discarded.

The fetch length to the shore is an important parameter to characterise the site, since for limited fetches one might experience the development of internal boundary layers (IBL) if the wind comes from land. The IBL is typically shallow if either the fetch length is limited, or if stable conditions occur. It can be shown (see Garratt (1990)) that for stable conditions and a fetch length of 85 km (which is the shortest fetch of the site, eastward of the tower), the IBL depth is in the order of 40 m or larger. Since neither easterly winds nor stable conditions prevail for the site considered, it is expected that internal boundary layers should not influence observation data to such an extent that Monin-Obukhov theory is no longer valid.

Flow distortion by the mast construction is expected to be less than 3% after carefully selecting sensors that are not distorted by the wake of the meteorological mast (Wessels 1983). The dynamic pressure in front of the mast however may result in a decrease of up to 4% of the observed wind speed. Similar, the wind direction observations are expected to be distorted by up to 2° by tower shadow effects.

One complete year of observation data is analysed in this research unless stated otherwise to assess representative site conditions that wind farms will experience in far offshore environments. As such seasonal effects should be accounted for. Unless stated otherwise the observation data of 2012 is used since this is the first year during which a complete yearly dataset is obtained.

2.3.2. DATA POST PROCESSING

Wind observations (speed and direction) are heavily distorted when the corresponding sensor is located in the wake of the meteorological mast. This can be shown if the average ratio of wind speed observations for two sensors at a given height are plotted against the

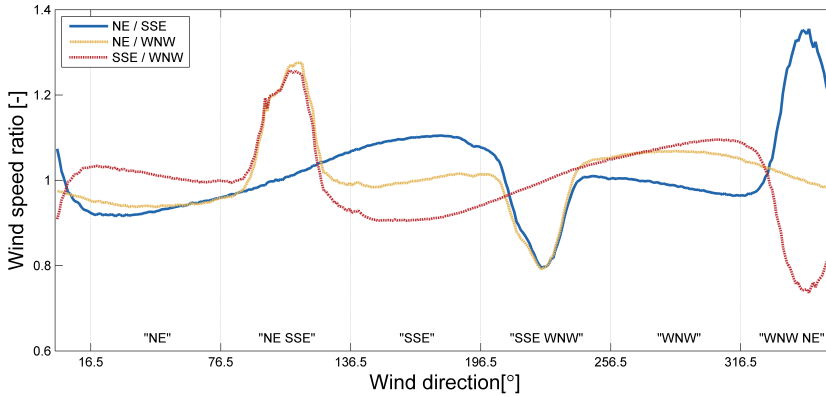


Figure 2.3: Average wind speed ratios at 27 m height for two adjacent sensors. Directions of horizontal booms are 46.5° (NE), 166.5° (SSE) and 286.5° (WNW). Vertical solid lines indicate the boundaries of wind sectors. The sensors used for wind speed determination are given in quotation marks.

average wind direction of the three wind vanes (or sonic anemometers). Based on Figure 2.3 it can be seen that these sensors experience significantly reduced wind speeds when located directly behind ($\pm 10^\circ$) the tower structure. Besides this, when one sensor is located directly in front of the tower, both remaining sensors located more to the side of the tower experience slightly increased wind speeds while the sensor in front of the tower experiences a reduced wind speed. The reduced wind speeds in front of the mast are caused by a static pressure increase that is formed due to the mast structure, and simultaneously the mast structure causes a tower shadow effect leading to a reduction in wind speeds observed behind the mast. The actual wind speed is determined either with two sensors (if one sensor is located downstream of the mast) or with one sensor (if two sensors are located slightly behind the mast at two opposing sides) since the main wind distortion is found downstream of the mast. A similar procedure is adopted to determine the actual wind direction. First the average wind direction is determined of all wind vanes (or sonic anemometers), and next the actual wind direction is calculated based on only those sensors that are in the free stream area.

The high frequency observation data (4 Hz) show that the turbulence spectra are strongly distorted by motion of the meteorological mast itself. The eigenfrequency of the meteorological mast is known to be 0.42 Hz (personal communication with RWE, the owner of the meteorological mast), which corresponds to the major peak in Figure 2.4. At a higher frequency of 1 Hz a second eigenfrequency is present, though this higher eigenfrequency is not known from structural analysis. All data in the bandwidth 0.33 to 0.50 Hz are removed to avoid contamination of the results, as is shown in Figure 2.4. Turbulent spectra are determined for each 10-minute interval, for which the trend of the data is removed. The scaling frequency f_0 is calculated as the intercept between the extrapolated inertial subrange spectra and the line $nS_u(n)/\sigma_u^2 = 1$, as described by Kaimal

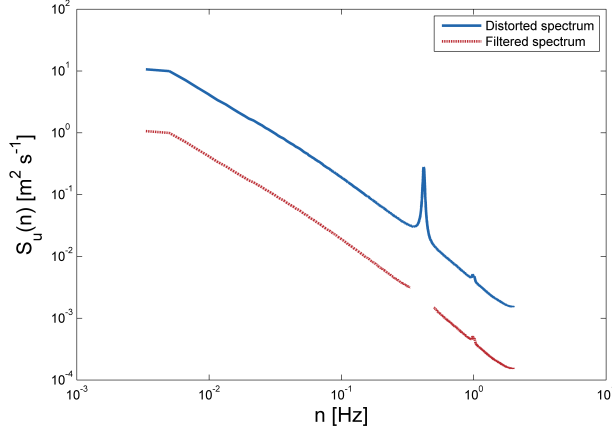


Figure 2.4: Average longitudinal turbulence spectrum as a function of frequency n (solid line), and the filtered (used) spectrum (dashed line). The filtered spectrum is reduced by a factor 10 and thus shifted vertically for clarity reasons.

et al. (1972) (see Figure 2.1 for clarification). Combining the following two equations

$$\frac{nS_u(n)}{\sigma_u^2} = sf^{-2/3} \quad (2.23)$$

$$\frac{nS_u(n)}{\sigma_u^2} = 1 \quad (2.24)$$

results in the scaling frequency

$$f_0 = s^{3/2} \quad (2.25)$$

where s is a constant determined per 10-minute interval in the inertial subrange of the turbulence spectrum. Figure 2.1 also shows that a change in f_0 results in a shift of the spectral peak along the non-dimensional frequency axes: if f_0 is large, the spectral peak is located at high frequencies (associated with small eddies), and vice versa if f_0 is small.

The Obukhov length cannot be determined with the eddy-covariance method close to the surface since turbulent fluxes of heat and momentum are not measured. Instead the Bulk-Richardson number (hereafter Rl) can be used to estimate ζ (Grachev & Fairall 1997) based on 10-minute mean observations of the surface temperature, and the temperature and wind speed observations at respectively 21 m and 27 m height. Both at the surface and at 21 m height the virtual potential temperature is calculated by combining Equations 1.3 and 1.4, which equals

$$\overline{\theta}_v(z) = \left[\overline{T}(z) + 0.0098z \right] [1 + 0.61r] \quad (2.26)$$

where the mixing ratio r is calculated as

$$r = \frac{\epsilon_R e}{P - e} \quad (2.27)$$

Here P is the air pressure, ϵ_R is the ratio of the gas constants for dry air to water vapour which equals 0.622, and e is the vapour pressure which can be calculated with the relative humidity and the Clausius-Clapeyron equation (Stull 2000). Note that in the conversion of temperature to potential temperature it is assumed that the air is unsaturated since the dry adiabatic lapse rate of 9.8 K km^{-1} is assumed to be valid. At the sea-air interface it is assumed that the air has a relative humidity of 100%.

One should determine RI with wind speed and temperature observations at similar heights, however, this is not possible since the wind speed and temperature sensors have not been installed at a similar height. It is therefore assumed that the virtual potential temperature calculated at 21 m height is representative for 27 m height as well. This results in

$$RI = \frac{g\Delta\bar{\theta}_v\Delta z}{\bar{\theta}_v\bar{U}^2} \quad (2.28)$$

And subsequently ζ is calculated as (Grachev & Fairall 1997)

$$\zeta = 10RI \quad \text{if } RI \leq 0 \quad (2.29)$$

$$\zeta = \frac{10RI}{1-5RI} \quad \text{if } RI \geq 0 \quad (2.30)$$

A derivation of the relation between ζ and RI is shown in Appendix C. The singularity at $RI = 0.2$ in Equation 2.30 causes $\zeta = \infty$ at $RI = 0.2$ and $\zeta < 0$ if $RI > 0.2$. This is incorrect, since both RI and ζ should have similar signs at all times (negative for unstable conditions and positive for stable conditions), hence for $RI > 0.2$ stability is not calculated (0.7% of all observations). Next L is calculated as

$$L = \frac{z'}{\zeta} \quad (2.31)$$

where z' is a reference height where the Richardson number is valid. One typically considers z' to be equal to the observation height, which in this study is at 27 m height and thus relatively far from the surface compared to for example ≈ 10 m height as considered in Fairall et al. (1996) and Grachev & Fairall (1997). In contrary, if one considers the gradient Richardson method (see for example Lange et al. (2004)) one can determine z' as

$$z' = \frac{z_1 - z_2}{\ln(z_1/z_2)} \quad (2.32)$$

where $z_1 > z_2$ are two observation heights above the surface. In this research $z_2 = 0$, and thus $z' = 0$ which is not feasible. As a compromise between the standard methodology ($z' = 27$) and Equation 2.32 ($z' = 0$), it is assumed that z' equals the average observation height, thus 13.5 m.

The aerodynamic roughness length is calculated with Charnock's equation for off-shore conditions (Charnock 1955)

$$z_0 = \alpha \frac{u_{*0}^2}{g} \quad (2.33)$$

Where α is Charnock's constant, taken as $1.2 \cdot 10^{-2}$ (Peña & Gryning 2008). The friction velocity is iteratively calculated by combining Equation 2.8 (neglecting the last term)

with Equation 2.33, which results in

$$u_{*0} \left[\ln \left(\frac{zg}{\alpha u_{*0}^2} \right) - \Psi(\zeta) \right] = \kappa \bar{U}(z) \quad (2.34)$$

All relevant parameters (L , u_{*0} , z_0) are thus calculated with observation data taken between 0 and 27 m height. As such relations that describe wind shear and turbulence relations will be validated above 27 m height to avoid self-correlation (Baas et al. 2006).

A sensitivity study is carried out to assess the accuracy of the determined parameters (L , u_{*0} , z_0) in scope of measurement errors. It is found that the stability determination is most sensitive to measurement errors of the temperature sensors, while the determination of u_{*0} and z_0 are most sensitive to flow distortion by the meteorological mast. A measurement error of 0.1 K for each temperature sensor, and hence a difference in ΔT of 0.2 K, would result in an error of ± 0.1 for z'/L for the majority of data used in this research (90% of the data considered). Similarly if the observed wind speed is underestimated by 4% due to the blockage effect of the meteorological mast, u_{*0} and z_0 are underestimated by respectively 6% and 11% for 90% of the data considered.

Data in which the wind speed, wind direction or temperature observations at time interval t differ substantially from those at time intervals $t-1$, $t+1$ and $t+2$ are neglected following Lange et al. (2004) since MO-theory assumes stationary atmospheric conditions. The maximum allowed differences are 20% for the wind speed, 15° for the wind direction, 0.5 K for the air temperature and 0.2 K for the sea temperature. The assumption of constant fluxes is only applicable in the lowest 10% of the boundary layer. Since for stable conditions the boundary layer can be shallow, the boundary layer depth is estimated as (Sathe et al. 2013)

$$h = c \frac{u_{*0}}{f_c} \quad (2.35)$$

Where h is the boundary layer height, f_c is the Coriolis parameter, and c is an empirical constant. It is recognised that c is a function of stability (as will be discussed in Chapter 3), and as mentioned in Peña et al. (2010a) and Sathe et al. (2013) c increases for unstable conditions and decreases for stable conditions. An exact relation however is still a matter of discussion, hence in this chapter the stability dependence of c is neglected. In line with Peña et al. (2010a) it is assumed that c is 0.15 for neutral conditions. Since $f_c \approx 10^{-4}$ for the given observation site and assuming c is 0.15 is found that h can be written as

$$h \approx 1.5 u_{*0} 10^3 \quad (2.36)$$

In practice, u_{*0} is nearly always less than 0.8 m s^{-1} , which would imply $h < 1200 \text{ m}$. The measurements at the top of the meteorological mast will fall outside of the surface boundary layer for the majority of observations. As such stable conditions where $u_{*0} < 0.2 \text{ m s}^{-1}$ are removed, since for such conditions the stable boundary layer is likely much more shallow than 300 m (this equals 9% of all observations). For unstable conditions h is generally large compared to stable conditions, hence no observation data is removed for unstable conditions beforehand. The impact of this minimum u_{*0} constraint will be shown in the results when shear profiles are validated. Due to the stationary and boundary layer height constraints 69% of the observation data remains for further analysis.

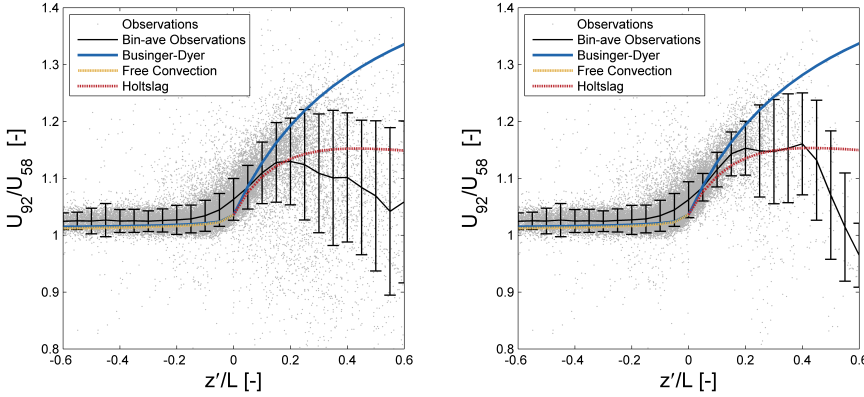


Figure 2.5: Wind shear ratio as a function of atmospheric stability (z'/L) according to observations and specific shear models (see legend). The thin solid line is showing the bin-averaged observations with error bars indicating one standard deviation within the bin. left panel: all data. Right panel: data filtered for stable conditions.

2.4. RESULTS

The validation of MO-theory is divided into three separate sections. First the accuracy of the stability corrected logarithmic wind profile is analysed by comparing observed wind shear with shear models incorporating the various Ψ -functions discussed in the theory. Next the non-dimensional wind variance is assessed for the three wind speed components separately. Finally the Kaimal spectra are validated, and the dependence of f_0 on ζ is assessed for the three wind components.

2.4.1. WIND SHEAR

Although it is preferred to assess the dependence of ϕ_M on ζ , the available data does not allow for determination of the local wind gradient $\partial\bar{U}/\partial z$. As such the wind shear ratio is analysed instead, which equals

$$\frac{\bar{U}(z_2)}{\bar{U}(z_1)} = \frac{\ln\left(\frac{z_2}{z_0}\right) - \Psi(z_2/L)}{\ln\left(\frac{z_1}{z_0}\right) - \Psi(z_1/L)} \quad (2.37)$$

Results are shown in Figure 2.5, where the wind speed ratio between 58 and 92 m height is plotted against z'/L . It is clear that wind shear is a function of stability, although there is a significant amount of scatter in the observations for stable conditions. The far majority of the observations (note the error bars) follow the theoretic wind profiles for unstable conditions and for stable conditions up to $z'/L = 0.2$. In the left panel of Figure 2.5 no constraint is placed on u_{*0} , and the observed wind shear shows increased scatter for near neutral and stable conditions mainly. It is found that wind shear is limited for unstable conditions, and increases for both neutral and stable conditions. For strongly stable stratifications however the scatter is very high, and on average the wind shear decreases compared to moderate stable conditions. This decrease is not captured by

the shear models. For unstable conditions differences between the Free Convection and Businger-Dyer formulations are too small to determine which formulation performs better, especially in scope of measurement errors. For weakly stable conditions the Holtslag and Businger-Dyer formulations differ little, and both perform well. For stable conditions around $z'/L \approx 0.25$ the formulation of Holtslag has better agreement with the bin-averaged observations, though scatter indicates that the exact wind shear strongly varies for a given atmospheric stability.

When u_{*0} is constrained for stable conditions by removing conditions where $u_{*0} < 0.2 \text{ m s}^{-1}$, scatter strongly reduces (right panel in Figure 2.5). For $0 < z'/L < 0.15$ both shear models used for stable conditions are in line with observations. For stable conditions up to $z'/L = 0.4$ the stability correction function of Holtslag seems to perform better than the Businger-Dyer formulation, but scatter in observation data becomes significant. For very strongly stable conditions wind shear again decreases, and it is expected that for such conditions the constraint on u_{*0} is not strong enough. Here local scaling might be more appropriate if one wants to define wind shear at a given height. The observations considered here, especially those at 92 m height, are likely taken above the surface layer where shear is less pronounced. Besides, it might very well be possible that low level jets occur as will be discussed in Chapter 4, especially for those situations where the wind speed ratio is less than 1 and the wind speed thus decreases with height.

In both panels wind shear is underestimated by the models for neutral conditions ($z'/L \approx 0$). This can at least be partially explained by the fact that in Figure 2.5 theoretical shear models with a constant surface roughness are considered. Following Equation 2.37 the wind speed ratio is a function of both stability and surface roughness. The constant surface roughness considered for the theoretical shear models is calculated with Equation 2.33 and using the average friction velocity for all observations. Since for neutral conditions wind speeds are generally high, it is found with Equation 2.34 that u_{*0} is high as well compared to the average of all observations. This is verified by the observation data in which the average u_{*0} is 0.39 m s^{-1} for near-neutral conditions, whereas the average u_{*0} of all observations is 0.31 m s^{-1} . Subsequently, wind shear between two heights also increases (as can be seen in Equation 2.37 by increasing z_0).

With respect to the measurement uncertainties, Section 2.3.2 shows that z'/L has an uncertainty of ± 0.1 , which would shift observations alongside the x-axes. This is not relevant for strongly unstable conditions since the mean observed wind shear and the theoretical wind shear are not sensitive to the exact value of z'/L . For neutral and stable conditions however part of the scatter might be related to measurement errors. The wind speed observations at 58 and 92 m height might also contain measurement errors up to 4% due to flow distortion, however, the wind speed ratio is not distorted significantly since the wind speed at both heights likely is distorted by a similar percentage. The accuracy of the wind speed sensors however might influence the results, and differences up to 5% of the wind speed ratio can occur if the sensor accuracy of $\pm 0.1 \text{ m s}^{-1}$ is considered. The uncertainty in wind speed observations therefore could have a significant impact on results, however, the mean observed wind shear follows the theoretic wind shear well for unstable and neutral conditions, hence it is expected that wind speed observations do not have a strong bias.

2.4.2. SECOND ORDER MOMENTS

The non-dimensional second-order moments of the three wind speed components are considered separately, that is in longitudinal (u), lateral (v) and vertical (w) direction. Analyses are performed for the wind speed observations at 85 m height since only at this height sonic anemometers are installed. For each 10-minute interval the coordinate system is aligned with the mean horizontal wind speed at 85 m height, and the wind vector is decomposed into three components. The artificial turbulence induced by meteorological mast movement has not been removed from the sonic observation data, hence the observed second-order moments of the horizontal wind components are slightly too high compared to the true atmospheric conditions. Results are shown in Figure 2.6. It is found that for unstable conditions the three non-dimensional second-order moments have two regimes: one for weakly to moderate unstable conditions where the non-dimensional second-order moments are constant (for $-z/L < 1$), and one for strongly unstable conditions where the non-dimensional second-order moments are a function of stability (for $-z/L > 1$). In order to meet both limiting conditions (constant for neutral conditions and proportional to $(-\zeta)^{1/3}$ for strongly unstable conditions), the non-dimensional second-order moments for unstable conditions are defined as

$$\frac{\sigma_x}{u_{*0}} = A_x (1 - B_x \zeta)^{1/3} \quad (2.38)$$

where A_x and B_x are empirical constants found from experimental data.

For weakly stable conditions similar results are found as for weakly unstable conditions as is expected from matching constraints, while the non-dimensional second-order moments tend to decrease with increasing stability for strongly stable conditions. Here weakly stable conditions correspond to $z/L < 0.5$ and strongly stable conditions correspond to $z/L > 1.5$. Note that for stable conditions the second-order moment of the vertical wind component starts to decrease for increasing stability earlier compared to both horizontal components, hence the difference between the definitions of weakly and strongly stable conditions as specified here. Similar as was found for wind shear, scatter becomes significant for strongly stable conditions. The median of the observed non-dimensional second-order moments for stable conditions can be approximated as

$$\frac{\sigma_x}{u_{*0}} = A_x (1 + C_x \zeta)^{-1/2} \quad (2.39)$$

This corresponds to the expected behaviour for neutral conditions, though, as mentioned in the theory, for strongly stable conditions the stability dependence of σ_x/u_{*0} is typically not considered.

The expressions 2.38 and 2.39 could be fitted to the observation data shown in Figure 2.6 to determine the various parameters A_x , B_x and C_x . Since the second-order moments are non-dimensionalized with u_{*0} , and u_{*0} is determined with Equation 2.34 (thus as a function of ζ), Figure 2.6 might be influenced by self-correlation between u_{*0} and ζ . To avoid this self-correlation, Equations 2.38 and 2.39 are multiplied with u_{*0} . For neutral conditions, where $\zeta = 0$, this results in $\sigma \propto u_{*0}$. A first estimate of A_x is based on approximately the 400 most near-neutral observations ($\approx 1\%$ of the data). With A_x known, B_x and C_x are found with regression analyses. As a final step, it is found from

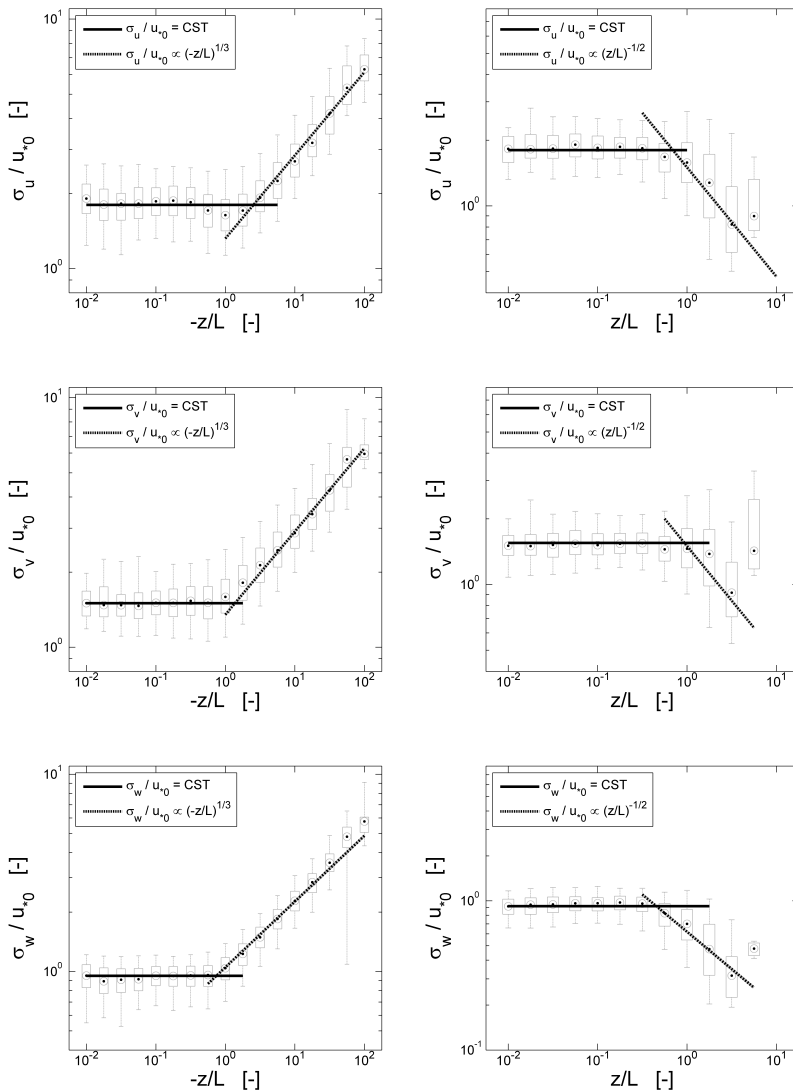


Figure 2.6: Normalised second-order moments as a function of z/L ($z = 85$ m) for unstable(left) and stable (right) conditions. From top to bottom the three wind components are shown separately (respectively u , v and w). Boxes correspond to the 25 and 75 percentile, error bars to the 5 and 95 percentile.

Table 2.1: Estimation of parameters A , B and C in Equations 2.38 and 2.39 and parameters D , E and F in Equations 2.40 and 2.41 for the three wind components.

Wind component	A	B	C	D	E	F
Longitudinal	1.99	0.33	1.32	0.01	0	0.03
Lateral	1.56	0.98	0.46	0.04	1.1	0.06
Vertical	1.09	1.18	2.83	0.1	2.9	0.2

the regression analyses that the first estimate of A_x is in general too high for stable conditions, and too low for unstable conditions. Matching constraints however prevent a change of A_x for stable and unstable conditions separately. The coefficient A_x is thus tuned in such a way that the average regression coefficient found for stable and unstable conditions is closest to 1. For clarification purposes the results are summarized in Table 2.1, and the regressions are shown in Figure 2.7.

Figure 2.7 shows that the equations obtained perform well to estimate the second-order moments, though there appear to be non-linearities in the scatter data for specific wind components. For the vertical wind component it is found that the obtained relations slightly underestimate the second-order moments for stable conditions, but overestimate the second-order moments for unstable conditions. This is related to the matching constraint for neutral conditions and the fixed constant A_x as explained previously. The constants shown in Table 2.1 indicate that for neutral conditions $\sigma_u > \sigma_v > \sigma_w$ (see A_x). The values found (respectively 1.99, 1.56 and 1.09 for the u, v, and w-component) are just in the range of values typically found in literature (respectively 1.7 to 2.9 for the horizontal components and 1 to 1.6 for the vertical component), except for the lateral wind direction. For unstable conditions the lateral and vertical second-order moments are more sensitive to ζ (see B_x). For stable conditions the second-order moments of the longitudinal and vertical components are most sensitive to ζ (see C_x). This last result was also found in Figure 2.6, where for the lateral component indeed the second-order moment is on average barely diminishing for strongly stable conditions except for one box at $z/L \approx 5$.

As mentioned before, the uncertainty in u_{*0} due to measurement errors is in the order of 6%, which directly results in an uncertainty of the parameter A_x of 6%. The uncertainty in the parameters B_x and C_x is proportional to the uncertainty in z/L . The presented uncertainty of z'/L in Section 2.3.2 corresponds to an accuracy in z/L of ± 0.6 . It is evident that if sensors indeed would have such a bias, the parameters B_x and C_x would differ substantially from the results presented in Table 2.1. A sensitivity study showed differences by a factor 3 in the determined parameters, and as such it is concluded that the estimation of A_x is significantly more reliable compared to the estimation of B_x and C_x .

2.4.3. TURBULENCE SPECTRA

The spectra are split in three components similar to the second-order moments, and observation data obtained with the sonic anemometers are considered. First the Kaimal spectrum is validated for the longitudinal wind component (the lateral and vertical components have been validated but showed similar results as the longitudinal turbulence

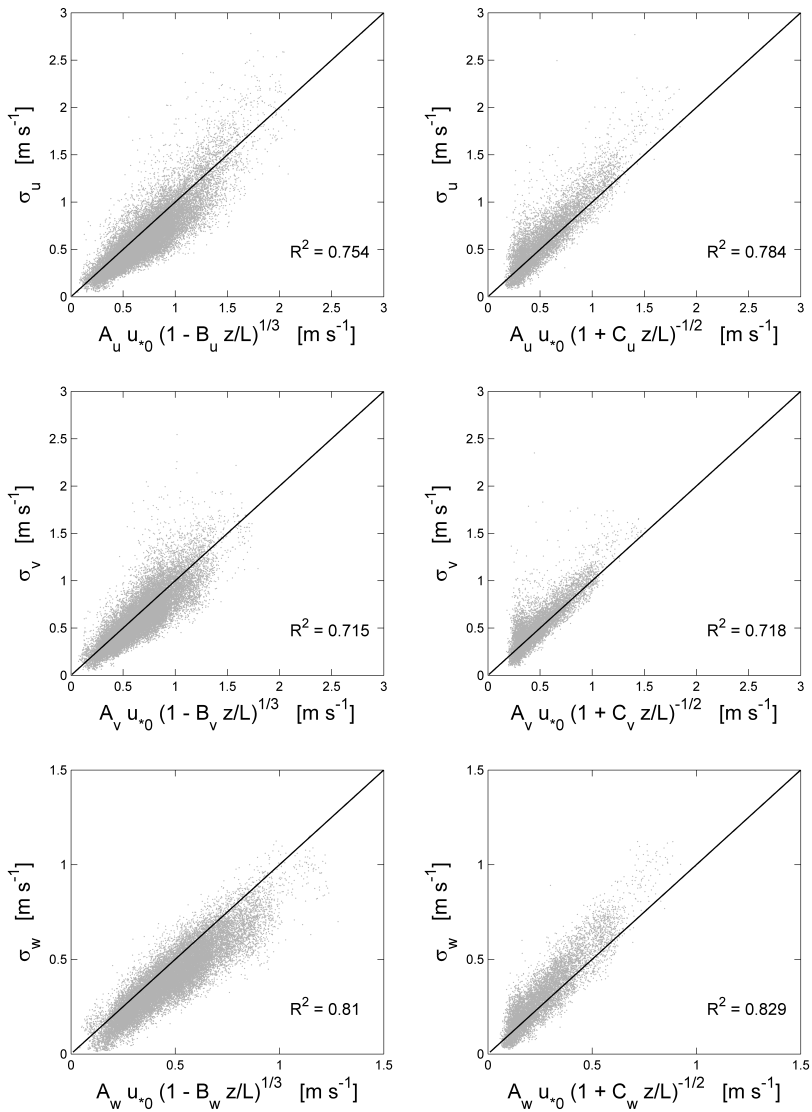


Figure 2.7: Second order moments as a function of $A_x u_{*0} (1 - B_x \zeta)^{1/3}$ (unstable conditions, left panels) and as a function of $A_x u_{*0} (1 + C_x \zeta)^{-1/2}$ (stable conditions, right panels). See Table 2.1 for coefficient values. From top to bottom the three wind components are shown, similar as Figure 2.6.

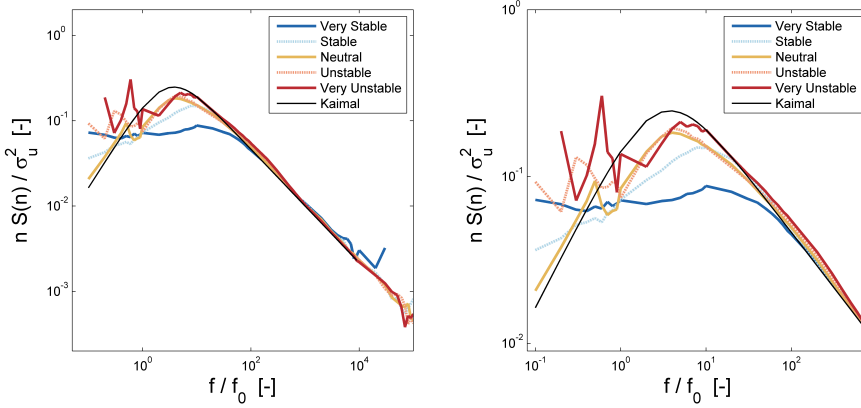


Figure 2.8: Median of the longitudinal turbulence spectra as a function of the normalised frequency f/f_0 . Stability classes are defined in the text, and the Kaimal spectrum corresponds to Equation 2.22. The right panel is similar as the left but emphasizes on the spectral peak.

spectrum). The median of observations is considered instead of the average of observations since the spectra are sensitive to outliers. Figure 2.8 shows the median of the longitudinal spectrum as a function of the normalised non-dimensional frequency f/f_0 for five stability classes. For every 10-minute time interval f , S_u and f_0 are calculated and per stability class the median of the non-dimensional spectral energy is plotted per normalised non-dimensional frequency f/f_0 .

The stability classes are defined such that the second-order moments have specific dependencies on stability (see Table 2.2 for an overview). First neutral conditions are defined such that σ_u differs no more than 10% from the neutral conditions according to Equations 2.38 and 2.39. This corresponds to $-1.01 \leq \zeta \leq 0.18$. The boundary is skewed to unstable conditions since B_x is small for the longitudinal wind component. Next, it is found that Equations 2.38 and 2.39 for the longitudinal and lateral conditions have intersects (for very stable and very unstable conditions $\sigma_u < \sigma_v$). The intersects serve as boundaries between unstable and very unstable conditions (located at $\zeta = -3.62$) and between stable and very stable conditions (located at $\zeta = 1.10$). An overview of the stability class characteristics is presented in Table 2.2, where the convention in wind energy is adopted to define stability classes in terms of L , not ζ (Peña & Gryning 2008, Sathé et al. 2011). Since the extreme class boundary for unstable conditions is 0, and u_{*0} is not constrained for unstable conditions, far more very unstable conditions are found compared to similar studies.

It is clear from Figure 2.8 that the Kaimal spectrum fits the median of the spectra in the inertial sub-range for all stability classes due to the frequency scaling applied here. The spectral peak however is located at too low normalised frequencies. This can be circumvented by altering the coefficients in Equation 2.22, and if both coefficients of 0.164 in the nominator and denominator are reduced to for instance 0.1, one would obtain a better fit. In this validation however the Kaimal spectrum is not fitted for each stability

Table 2.2: Stability class characteristics. For L-interval the boundaries are rounded to tens. The class characteristics (\bar{L} , $\overline{u_{*0}}$ and \bar{z}_0) are determined after data filtering and constraining data on u_{*0} for stable conditions. The mean Obukhov length for neutral conditions equals the mean absolute Obukhov length.

Stability class	L-interval [m]	\bar{L} [m]	$\overline{u_{*0}}$ [m s ⁻¹]	\bar{z}_0 [m]	Profiles
Very Unstable	-20 < L ≤ 0	-12	0.18	0.4*10 ⁻⁴	4666
Unstable	-80 < L ≤ -20	-45	0.28	1.0*10 ⁻⁴	10165
Neutral	480 ≤ L or L ≤ -80	1609	0.39	1.9*10 ⁻⁴	13415
Stable	80 ≤ L < 480	221	0.35	1.5*10 ⁻⁴	5682
Very Stable	0 ≤ L < 80	55	0.25	0.8*10 ⁻⁴	1797

class, and instead the original formulation as shown in Equation 2.22 is applied. For stable conditions the slope of the spectrum on the left hand side of the spectral peak (thus low frequencies) gradually decreases, and for very stable conditions the slope becomes approximately zero. Here the non-dimensional spectral energy is independent of the normalised non-dimensional frequency. Such spectra cannot be fitted by the traditional Kaimal spectrum, but may be obtained by altering the formulation more drastically than just changing coefficients. For very low frequencies scatter increases significantly since only few 10-minute intervals have such small scale frequencies (this depends on the mean wind speed and f_0). The median of all spectra shown here is thus sensitive to outliers for low frequencies specifically.

The dependence of f_0 on ζ is assessed in a similar way as was done for the second-order moments. Results can be seen in Figure 2.9. Despite the scatter (especially present for both horizontal wind components, see the length of the error bars) empirical relations are fitted to the median of the observations. The general pattern that emerges is that f_0 decreases when the atmosphere becomes more unstable, and increases when the atmosphere becomes more stable. Only for the longitudinal wind component it is found that f_0 is approximately constant for unstable conditions. Besides, the general pattern emerges that for a given stability ζ $f_{0-u} < f_{0-v} < f_{0-w}$. The empirical relations fitted to the median of the observations can be described by the following general equations

$$f_0 (\zeta \leq 0) = D_x (1 - E_x \zeta)^{-1/2} \quad (2.40)$$

$$f_0 (\zeta \geq 0) = D_x + F_x \zeta \quad (2.41)$$

where for the longitudinal component $E_x = 0$ since no stability dependence is found. An overview of the parameters is presented in Table 2.1. The linear dependence of f_0 on L for stable conditions corresponds reasonably well to the results obtained by Kaimal (1973), who found a non-linear dependence for near neutral conditions and a linear dependence for strongly stable conditions. It is found, similar as Kaimal (1973), that the coefficient F_x is highest for the vertical wind component and lowest for the longitudinal wind component.

These results show that the turbulence spectra, and the scaling frequency f_0 specifically, are a function of stability. Besides, the results can be used to assess the importance of large and small eddies for either unstable or stable conditions. If f_0 is large, most energy is present at high frequencies (thus small fluctuations, or eddies), while for small f_0 most energy is present at low frequencies (thus large fluctuations). From Figure 2.9 it

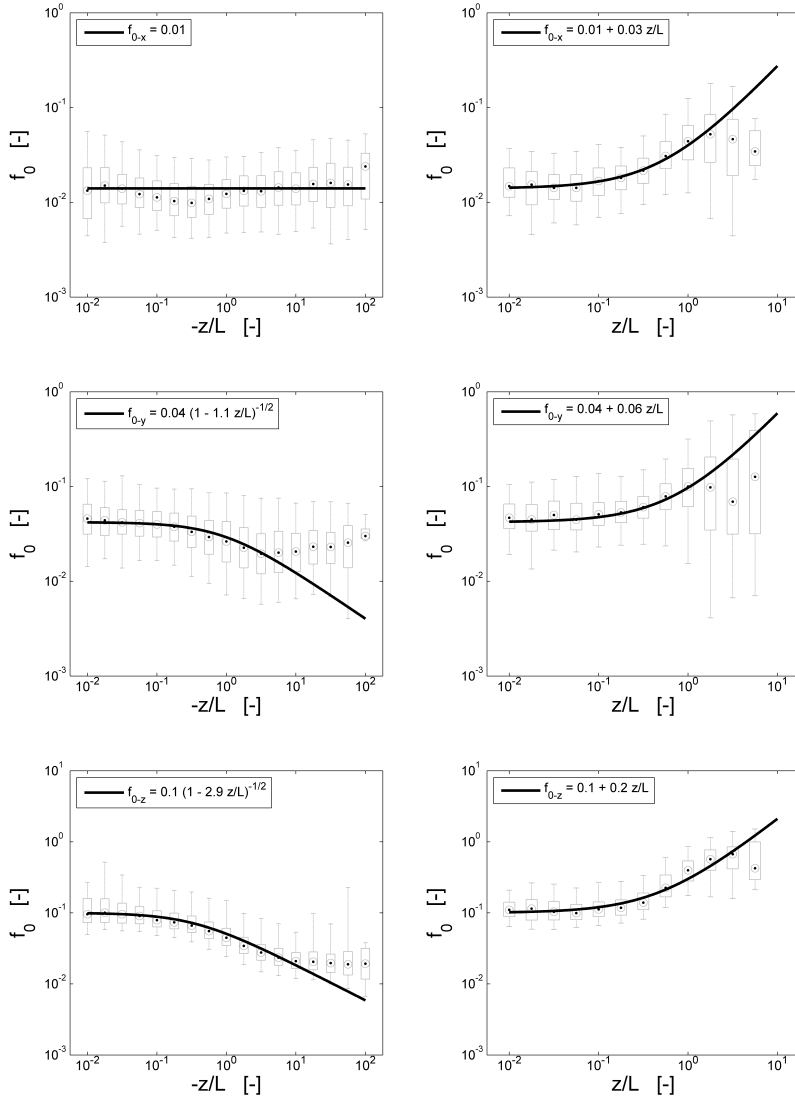


Figure 2.9: Scaling frequency f_0 as a function of stability. The figure layout is similar as Figure 2.6, and the dashed lines correspond to empirical fits.

is found that when the atmosphere becomes more stable, f_0 increases and more small turbulent structures occur. In contrary, when the atmosphere becomes more unstable f_0 decreases and the fluctuations have larger scales. Besides, since in general $f_{0-u} < f_{0-v} < f_{0-w}$ the fluctuations in the longitudinal component are typically larger than those in the lateral direction, and vertical fluctuations are smallest. This is all in agreement with general boundary layer theory (Stull 1988), and the Kaimal spectrum is applicable for far offshore conditions if one considers the stability dependence of f_0 .

Although the empirical relations of Equations 2.40 and 2.41 work reasonably well for neutral and moderate unstable and stable conditions, the relations do not seem to hold for very unstable and very stable conditions. For very unstable conditions it is found that the scaling frequency f_0 is very small and approximately constant, at least for the lateral and vertical wind component. The small f_0 value indicates that the eddies corresponding to the peak of the turbulence spectrum are very large, and it is recognised that the largest eddies in the atmospheric boundary layer are approximately as large as the depth of the boundary layer itself. As such there is an upper boundary to the size of the eddies, and thus also a lower boundary to the value of f_0 for very unstable conditions. This might very well explain the low constant f_0 value's for very unstable conditions. For stable conditions however this reasoning does not hold since f_0 becomes very large, corresponding to very small turbulent structures. It is possible however that in the determination of f_0 based on Equation 2.25, the slope s of the spectrum is not taken exactly within the inertial subrange of the turbulence spectrum but more to the left within the spectrum, including the spectral peak (see Figure 2.4). As a consequence the estimated slope s of the inertial subrange will be too low, and hence f_0 will be too low as well. In reality it might very well be that the scaling frequency for very stable conditions should have been higher then found in Figure 2.9 which might explain the deviation of f_0 from the empirical relations.

In scope of flow distortion and measurement errors, it is noted that in the determination of f_0 the considered variance is likely overestimated for all observations since any contribution of tower movement to the observed wind variance is not accounted for. As such there is likely a bias in the determined f_0 , and one can see in Figure 2.1 that an overestimation of the variance would result in an overestimation of f_0 . This would primarily influence the parameter D_x assuming the tower movement is independent of atmospheric stability. The parameters E_x and F_x are, similar as was found for the second-order moment parameters B_x and C_x , sensitive to the estimation of z/L . As such there is reasonable confidence in the estimation of D_x , but the exact values of E_x and F_x are uncertain and should be studied in more detail.

2.5. CONCLUSIONS

In this chapter observation data obtained from meteorological mast IJmuiden sited 85 km offshore has been analysed to assess if Monin-Obukhov similarity theory can be used to describe the far offshore marine atmosphere. It is concluded that MO-theory can be applied to describe wind shear and turbulence, unless the atmosphere has a strongly stable stratification. Both wind shear and turbulence depend strongly on stability, expressed as the non-dimensional stability parameter ζ .

For wind shear various stability correction functions are proposed in literature, and

for conditions where the boundary layer is sufficiently deep (characterized by u_{*0}), it is found that the Businger-Dyer functions hold. For unstable conditions there is no significant improvement if one adopts the Free Convection formulation. For stable conditions scatter is significant, and the formulation by [Holtslag & de Bruin \(1988\)](#) seems to perform better than the Businger-Dyer relations.

With respect to turbulence, it is found that the normalised second-order moments are proportional to $(-\zeta)^{1/3}$ for unstable conditions, and proportional to $\zeta^{-1/2}$ for stable conditions. For neutral conditions the non-dimensional second-order moments are small compared to results found in literature. The stability dependence for stable conditions is typically not found in literature, but is clearly present in the considered data.

For the turbulence spectrum the Kaimal spectrum can be used to describe the median of all spectra quite accurately. If one changes the specific coefficients of the original Kaimal spectrum one would increase the accuracy of the spectra in the low-frequency regime, left of the spectral peak. For (very) stable conditions the shape of the spectra differ and do not show the theoretical linear dependence on f/f_0 for low non-dimensional frequencies. The scaling frequency f_0 is found to be either constant (unstable, longitudinal component), proportional to $(-\zeta)^{-1/2}$ (unstable, lateral and vertical component) or proportional to ζ (stable conditions).

Combined, it is clear that for far offshore sites atmospheric stability is a crucial parameter, and one can approximate wind shear and turbulence with relative simple relations as a function of stability. The impact of atmospheric stability on wind turbine fatigue loads is assessed in [Chapter 5](#), where the relations obtained in this chapter will be considered to prescribe atmospheric conditions for wind turbine fatigue load assessment.

3

EXTENDING THE SURFACE LAYER WIND SHEAR PROFILE

The fundamental laws necessary for the mathematical treatment of a large part of physics (...) are completely known, the difficulty lies only in the fact that application of these laws leads to equations that are too complex to be solved.

Paul Dirac

In the previous chapter Monin-Obukhov similarity theory has been used to define a wind shear profile that is a function of atmospheric stability. The underlying assumptions however are only valid close to the surface, and with the ongoing trend to increase the size of wind turbines, there is a growing need to define a boundary layer wind shear profile for offshore sites. In recent work Gryning derived a wind shear profile based on theoretic arguments that should be applicable for the entire atmospheric boundary layer. The resulting wind shear profile has been validated onshore and at coastal sites, but offshore no validation has been carried out yet.

In this chapter it is aimed to derive a similar boundary layer wind profile, however, here the wind profile is defined as a continuous function of stability, instead of the commonly used approach to define conditions as a function of stability classes. The boundary layer wind shear profile has to be easily usable for wind energy purposes, which should result in a more accurate representation of atmospheric conditions in wind energy power production and fatigue load assessment. The impact of this specific boundary layer wind shear profile on wind turbine performance will be analysed in Chapter 6.

Parts of this chapter are incorporated in the publication: Holtslag, M. C., Bierbooms, W. A. A. M. & van Bussel, G. J. W. (2016), 'Extending the diabatic surface layer wind shear profile for offshore wind energy', *Submitted for publication to Renewable Energy*

3.1. INTRODUCTION

In the previous chapter it has been shown that Monin-Obukhov similarity theory (or surface layer similarity theory) works well to describe wind shear and turbulence properties in the lowest 100 m of the offshore atmosphere. State of the art multi-megawatt wind turbines however operate at heights well above what is typically called the surface layer. Since wind shear has a profound effect on both power production as well as on fatigue loads, it becomes increasingly important to accurately describe wind shear up to maximum blade tip heights of state of the art wind turbines. It is expected that in the near future wind turbines can reach maximum blade tip heights above 200 m, and in this chapter it is therefore aimed to define a wind shear profile that is accurate and applicable up to at least 200 m height.

The extrapolation of wind shear profiles to higher altitudes is not a novelty on its own, since already in the 1960's similar research was performed by Blackader (1962) and Blackader & Tennekes (1968). The wind profiles however were typically derived for simplified atmospheric conditions in absence of stratification effects. In a recent study, however, Gryning derived a theoretic wind shear profile that covers the entire boundary layer (Gryning et al. 2007), with specific parametrizations of the wind profile for stable and unstable stratifications. This profile has been validated in literature for onshore and coastal sites (Gryning et al. 2007, Peña et al. 2010a, Sathe et al. 2011). The offshore validation presented by Sathe et al. (2011) however is executed based on observations up to 116 m at most, which is too limited in scope of the dimensions of state of the art wind turbines. Besides, the two sites considered in Sathe et al. (2011) are located relatively close to the shore with a coastal distance of 18 km. Since in this thesis far offshore conditions are considered, it is questioned if Gryning's wind profile is applicable far offshore as well.

As a starting point Gryning's wind profile will be derived with slightly less simplifications as considered in Gryning et al. (2007). Next, it is recognised that the boundary layer height h is a crucial parameter in the shear profile, however, h is typically not available from regular observations. As such h will be parametrized in such a way that it can be estimated from surface observations. The resulting wind shear profile is derived analytically with physical based arguments, and the shear profile is completely defined with surface parameters that can be obtained from standard observation data. An added benefit is that with the proposed parametrization no new variables are introduced to the shear profile compared to the diabatic shear profile resulting from surface layer scaling. As such, there is no added complexity in terms of the amount of free variables in the shear profile, and it should be easily implementable for wind energy purposes.

In similar studies where atmospheric stability is considered in wind profiles, stability is typically defined into distinct but arbitrary classes. Examples found in literature show a division of stability in three (Hansen et al. 2014), four (Peña & Gryning 2008), five (van Wijk et al. 1990) or seven (Sathe et al. 2013) stability classes. In studies where Gryning's wind profile has been validated stability classes are also used (seven classes are considered in Gryning et al. (2007), Peña et al. (2010a) and Sathe et al. (2011)). Although the classification is convenient to simplify the analyses, here such a classification is discarded in the derivation and parametrization of the wind profile. The adopted classifications are typically subjectively chosen, and the boundaries between specific classes are thus arbi-

trarily defined. Similarly, in Chapter 2 turbulence spectra have been plotted for 5 distinct stability classes, however one could have used any classification set. To avoid this subjective classification, stability is considered here as much as possible as a continuous parameter. For visualisation purposes the validation of the derived shear profile will be performed with a classification of stability since this allows for simple visualisation of the results, however it is recognised that the arbitrary choice of stability classes might influence the outcome of the validation of the wind shear profile.

3.2. DERIVATION AND PARAMETRIZATION OF THE WIND SHEAR MODEL

The derivation of the boundary layer wind shear profile is based on theoretic and physics based arguments. The required mathematical integrals and derivatives are not elaborated upon explicitly here, but a more detailed assessment of the required mathematics can be found in Appendix D. The parametrization of the wind profile is based upon one year of observation data taken at meteorological mast IJmuiden, similar as used in Chapter 2. Besides the standard observations (i.e., wind speed, temperature, humidity and air pressure) also LIDAR observations up to 315 m height is considered. The LIDAR is set to determine the wind speed and wind direction between 90 m and 315 m height, with an equal spacing of 25 m in between, resulting in 10 LIDAR observation heights. Stability is calculated similar as discussed in Section 2.3.2, and the Obukhov length L will be one of the parameters of the wind profile. The derived wind profile will be validated with one independent year of observation data, which will be elaborated upon in Section 3.3.

3.2.1. THEORETIC DERIVATION OF THE WIND SHEAR PROFILE

Based on dimensional analysis, wind shear in terms of the gradient $\partial\bar{U}/\partial z$ depends on a velocity scale v and a local length scale l as

$$\frac{\partial\bar{U}}{\partial z} = \frac{v}{l} \quad (3.1)$$

Following Monin-Obukhov theory (Monin & Obukhov 1954, Obukhov 1971), one adopts the surface friction velocity u_{*0} as relevant velocity scale, assumed to be constant close to the surface, and the height z as relevant local length scale. Incorporating the definition of the dimensionless wind gradient ϕ_M to account for stability effects (see Businger et al. (1971) or Stull (1988)) one finds

$$\frac{\partial\bar{U}}{\partial z} = \frac{u_{*0}\phi_M}{\kappa z} \quad (3.2)$$

where κ is the Von Kármán constant, assumed to be 0.4 (Högström 1988). The principle arguments proposed by Gryning are that in the atmospheric boundary layer the friction velocity decreases linearly with height, and that the local length scale l can be decomposed into a summation of three specific length scales. These three specific length scales correspond to a local surface layer length scale (assumed to be ϕ_M / z , similar as in surface layer scaling), a local middle layer length scale (assumed to be $1 / l_{ML}$, which has to be parametrized) and a local upper layer length scale (assumed to equal $1 / [h - z]$, where

h is the boundary layer height). Incorporating these principle arguments in Equation 3.1, and taking into account the Von Kármán constant, results in

$$\frac{\partial \bar{U}}{\partial z} = \frac{u_{*0}}{\kappa} \left[1 - \frac{z}{h} \right] \left[\frac{\phi_M}{z} + \frac{1}{l_{ML}} + \frac{1}{h-z} \right] \quad (3.3)$$

The dependence of ϕ_M on stability has been studied extensively in literature, and the Kansas experiment is likely the most well-known study (Haugen et al. (1971), Businger et al. (1971)), though more recent studies are shown in Akylas & Tombrou (2005) and Cheng & Brutsaert (2005). For unstable conditions, one typically considers either the Businger-Dyer formulation (Businger et al. 1971) or the so called Free-Convection formulation (Paulson 1970), respectively

$$\phi_M = \left[1 - \gamma_{BD} \frac{z}{L} \right]^{-1/4} \quad (3.4)$$

$$\phi_M = \left[1 - \gamma_{FC} \frac{z}{L} \right]^{-1/3} \quad (3.5)$$

with $\gamma_{BD} = 19.3$ (Högström 1988) and $\gamma_{FC} = 12.87$ (Fairall et al. 1996). For stable conditions, one typically considers the Businger-Dyer formulation (Businger et al. 1971) or the formulation of Holtslag (Vickers & Mahrt 1999), respectively

$$\phi_M = 1 + \beta \frac{z}{L} \quad (3.6)$$

$$\phi_M = 1 + \frac{z}{L} \left[a + b \left[\exp \left(-d \frac{z}{L} \right) \left[1 + c - d \frac{z}{L} \right] \right] \right] \quad (3.7)$$

with $\beta = 6$ (Högström 1988), and the coefficients a , b , c and d are respectively 1, 2/3, 5 and 0.35 (Beljaars & Holtslag 1991). Integration of Equation 3.2 with respect to height results in the diabatic surface layer profile

$$\bar{U}(z) = \frac{u_*}{\kappa} \left[\ln \left(\frac{z}{z_0} \right) - \Psi(\zeta) + \Psi(\zeta_0) \right] \quad (3.8)$$

where z_0 is the aerodynamic roughness length, $\zeta_0 = z_0/L$ and Ψ is a stability correction function, which originates from (Paulson 1970)

$$- \int_{\zeta_0}^{\zeta} \frac{1 - \phi_M}{\zeta} d\zeta = -\Psi(\zeta) + \Psi(\zeta_0) \quad (3.9)$$

In agreement with Gryning et al. (2007) the Free-Convection formulation is adopted for unstable conditions, and the Businger-Dyer formulation for stable conditions, to derive the boundary layer wind shear profile. Note that the choice of adopting specific ϕ_M -functions has an impact on derived wind profile due to the required integration of Equation 3.3. Since two specific ϕ_M -functions are chosen for stable and unstable conditions, also the stability correction functions typically found in surface layer scaling shear profiles are set. For respectively stable and unstable conditions these are

$$\Psi \left(\frac{z}{L} \right) = -\beta \frac{z}{L} \quad (3.10)$$

$$\Psi \left(\frac{z}{L} \right) = \frac{3}{2} \ln \left(\frac{x^2 + x + 1}{3} \right) - \sqrt{3} \arctan \left(\frac{2x + 1}{\sqrt{3}} \right) + \frac{\pi}{\sqrt{3}} \quad (3.11)$$

where $x = [1 - \gamma_{FC} \frac{z}{L}]^{1/3}$. Due to the linearity of Equation 3.10 one can write for stable conditions

$$\Psi\left(\frac{z}{L}\right) = \frac{z}{h} \Psi\left(\frac{h}{L}\right) \quad (3.12)$$

Integration of Equation 3.3, and assuming $z_0/h = 0$, leads to the following shear profile for respectively stable and unstable conditions

$$\bar{U}(z) = \frac{u_{*0}}{\kappa} \left[\ln\left(\frac{z}{z_0}\right) + \frac{1}{2} \left[2 - \frac{z}{h} \right] \left[\frac{z}{h} \frac{h}{l_{ML}} - \Psi\left(\frac{z}{L}\right) \right] \right] \quad (3.13)$$

$$\bar{U}(z) = \frac{u_{*0}}{\kappa} \left[\ln\left(\frac{z}{z_0}\right) - \Psi\left(\frac{z}{L}\right) + \Psi\left(\frac{z_0}{L}\right) + \frac{z}{h} \left[1 - \frac{3}{2} \frac{x_z^2 - x_0^2}{x_z^3 - 1} \right] + \frac{1}{2} \left[2 - \frac{z}{h} \right] \frac{z}{h} \frac{h}{l_{ML}} \right] \quad (3.14)$$

where the subscripts z and 0 correspond to using respectively z and z_0 in x . Note that one could rewrite the term $z/h h/l_{ML}$ in these equations, but this is not done since a parametrization of h/l_{ML} will be derived. Besides, by incorporating Equation 3.12 in combination with the assumption that $z_0/h = 0$, there is no $\Psi(z_0/L)$ -term in the shear profile for stable conditions.

The parametrization will from here on deviate from the parametrization adopted by Gryning et al. (2007). The geostrophic wind speed at the top of the boundary layer is considered for the parametrization of l_{ML} . A common expression for the geostrophic wind is obtained for barotropic, stationary conditions as (Blackader & Tennekes (1968), Zilitinkevich & Deardorff (1974))

$$G = \frac{u_{*0}}{\kappa} \sqrt{\left[\ln\left(\frac{u_{*0}}{f z_0}\right) - B(\mu) \right]^2 + A^2(\mu)} \quad (3.15)$$

where G is the geostrophic wind speed, f is the Coriolis parameter, A and B are the resistance functions that will be parametrized in Section 3.2.2 and μ is the dimensionless stability parameter u_{*0} / fL . It is recognised however that Equation 3.15 is invalid if the boundary layer height h is not uniquely defined by μ alone, and in practice h also depends on other processes not taken into account in μ , such as entrainment and the vertical wind speed at the top of the boundary layer (Zilitinkevich & Deardorff (1974), Byun (1991)). As such, an alternative formulation of Equation 3.15 is proposed in Zilitinkevich & Deardorff (1974) where the boundary layer height h is a unique variable, which results in (see Equation 15 of Zilitinkevich & Deardorff (1974))

$$G = \frac{u_{*0}}{\kappa} \sqrt{\left[\ln\left(\frac{h}{z_0}\right) - B\left(\frac{h}{L}\right) \right]^2 + A^2\left(\frac{h}{L}\right)} \quad (3.16)$$

Since the resistance functions now depend on the dimensionless parameter h/L instead of μ , the parametrization of A and B will differ compared to using Equation 3.15 (Byun 1991). Evaluating Equations 3.13 and 3.14 at $z = h$ and combining with Equation 3.16

yields expressions for h/l_{ML}

$$\frac{h}{l_{ML}} = 2 \left[\sqrt{\left[\ln\left(\frac{h}{z_0}\right) - B\left(\frac{h}{L}\right) \right]^2 + A^2\left(\frac{h}{L}\right)} - \ln\left(\frac{h}{z_0}\right) \right] + \Psi\left(\frac{h}{L}\right) \quad (3.17)$$

$$\frac{h}{l_{ML}} = 2 \left[\sqrt{\left[\ln\left(\frac{h}{z_0}\right) - B\left(\frac{h}{L}\right) \right]^2 + A^2\left(\frac{h}{L}\right)} - \ln\left(\frac{h}{z_0}\right) + \Psi\left(\frac{h}{L}\right) - \Psi\left(\frac{z_0}{L}\right) - \left[1 - \frac{3}{2} \frac{x_h^2 - x_0^2}{x_h^3 - 1} \right] \right] \quad (3.18)$$

where the subscript h denotes the usage of h/L instead of z/L in x .

For sake of clarity, the shear profile is rewritten as

$$\bar{U}(z) = \frac{u_{*0}}{\kappa} \left[\ln\left(\frac{z}{z_0}\right) + \Upsilon + \Omega \right] \quad (3.19)$$

where the last term is similar in notation for stable and unstable conditions and given by

$$\Omega = \frac{z}{h} \left[2 - \frac{z}{h} \right] \left[\sqrt{\left[\ln\left(\frac{h}{z_0}\right) - B\left(\frac{h}{L}\right) \right]^2 + A^2\left(\frac{h}{L}\right)} - \ln\left(\frac{h}{z_0}\right) \right] \quad (3.20)$$

and all remaining terms are combined into a closing term. For stable conditions no terms remain due to the linearity of the stability correction function. This results for respectively stable and unstable conditions in

$$\Upsilon = 0 \quad (3.21)$$

$$\begin{aligned} \Upsilon = & \frac{z}{h} \left[2 - \frac{z}{h} \right] \left[\Psi\left(\frac{h}{L}\right) - \Psi\left(\frac{z_0}{L}\right) \right] - \left[\Psi\left(\frac{z}{L}\right) - \Psi\left(\frac{z_0}{L}\right) \right] \\ & + \frac{3}{2} \frac{z}{h} \left[\left[2 - \frac{z}{h} \right] \frac{x_h^2 - x_0^2}{x_h^3 - 1} - \frac{x_z^2 - x_0^2}{x_z^3 - 1} \right] - \frac{z}{h} \left[1 - \frac{z}{h} \right] \end{aligned} \quad (3.22)$$

Combined, this wind shear profile is a function of the same parameters as the surface layer wind shear profile (thus z , z_0 , L and u_{*0}), and three extra parameters: the boundary layer height h , and the two resistance functions A and B .

In reality z_0 is defined by the roughness of the surface, atmospheric stability is defined by temperature gradients in the atmosphere, and the wind speed at the top of the boundary layer (assumed to equal the geostrophic wind), is defined by horizontal pressure gradients. As a result u_{*0} will adjust to the other parameters, however, the wind profile is defined as a function of u_{*0} specifically for practical purposes, since this reduces the amount of variables that have to be specified when using the wind profile in simulations.

In the following two sections specific parametrizations are proposed, and the sensitivity of the resulting wind profile to remaining profile parameters is shown.

3.2.2. PARAMETRIZATION OF THE RESISTANCE FUNCTIONS A AND B

It is aimed in this study to define continuous functions for A and B , as opposed to choosing distinct values for a group of stability conditions as is done in Peña et al. (2010a). The

resistance functions A and B are parametrized following Byun (1991). Note that Byun (1991) has a reversed definition of A and B compared to Zilitinkevich & Deardorff (1974) and Gryning et al. (2007), and here the notation of Zilitinkevich & Deardorff (1974) is used in line with Equation 3.16. This results in

$$A = \frac{q+1}{q} \frac{\kappa u_{*0}}{fh} \quad (3.23)$$

$$B = \frac{p+1}{p} - \Psi\left(\frac{z_0}{L}\right) - \frac{\Psi\left(\frac{h}{L}\right)}{p} + \frac{p+1}{p \frac{h}{L}} \left[\Gamma\left(\frac{h}{L}\right) - \Gamma\left(\frac{z_0}{L}\right) \right] \quad (3.24)$$

where p and q are coefficients that vary between 1 and 3 (with $q = 1$ if the friction velocity decreases linearly with height and $p = 1.5$ for neutral conditions) and Γ is the integral of the stability correction function

$$\Gamma\left(\frac{h}{L}\right) = \int \Psi\left(\frac{h}{L}\right) d\frac{h}{L} \quad (3.25)$$

In absence of a proper parametrization of p as a function of stability it is assumed that $p = 1.5$. For stable and unstable conditions Γ equals respectively

$$\Gamma\left(\frac{h}{L}\right) = \frac{1}{2} \frac{h}{L} \Psi\left(\frac{h}{L}\right) \quad (3.26)$$

$$\Gamma\left(\frac{h}{L}\right) = \frac{h}{L} \left[\Psi\left(\frac{h}{L}\right) - 1 \right] - \frac{3}{2} \frac{x_h^2}{\gamma_{FC}} + \frac{31}{16\gamma_{FC}} \quad (3.27)$$

Combined this results for stable and unstable conditions respectively in

$$B = \frac{p+1}{p} + \frac{1}{2} \frac{p-1}{p} \Psi\left(\frac{h}{L}\right) - \Psi\left(\frac{z_0}{L}\right) \quad (3.28)$$

$$B = \frac{3}{2} \frac{p+1}{p} \frac{x_h^2 - x_0^2}{x_h^3 - 1} + \Psi\left(\frac{h}{L}\right) - \Psi\left(\frac{z_0}{L}\right) \quad (3.29)$$

where again it is assumed that $z_0/h = 0$. For neutral conditions these equations match, since

$$\lim_{L \rightarrow \infty} \frac{x_h^2 - x_0^2}{x_h^3 - 1} = \frac{2}{3} \quad (3.30)$$

It is thus found that for neutral conditions $B = 1.67$, and A is a function of the dimensionless parameter u_{*0}/fh .

With the above parametrization, the wind profile is a function of z_0 , h , L and u_{*0} . A brief sensitivity study is performed to assess the sensitivity of the theoretic wind shear profile to these four parameters. Results are shown in Figure 3.1, where the solid line in the four separate panels is the same reference wind profile for neutral conditions with $z_0 = 10^{-4}$ m, $h = 250$ m and $u_{*0} = 0.3$ m s⁻¹. With respect to the surface roughness it is found that obviously the magnitude of the wind speed changes as a function of the surface roughness (i.e., for a lower surface roughness the wind speed increases), but in

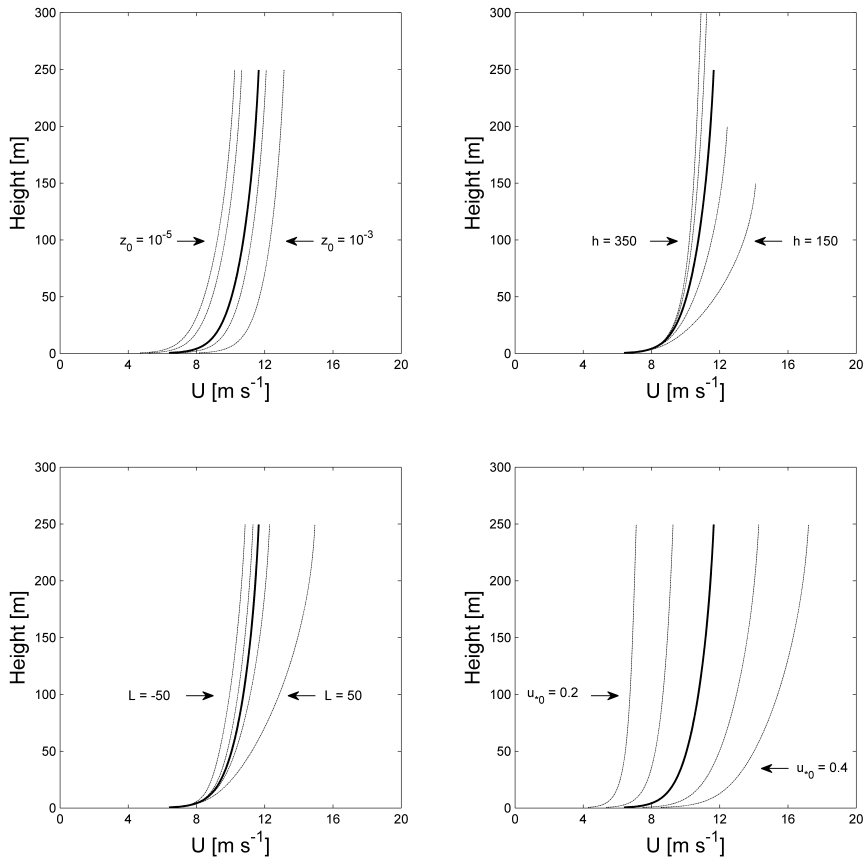


Figure 3.1: Sensitivity of the theoretic wind shear profile to the aerodynamic roughness z_0 (upper left panel), the boundary layer height h (upper right panel), the Obukhov length L (lower left panel) and the surface friction velocity u_{*0} (lower right panel). The solid black lines in the four panels are all similar as a reference profile with $z_0 = 10^{-4}$ m, $h = 250$ m, $L = \infty$ and $u_{*0} = 0.3$ m s⁻¹.

principle there is merely a shift in the profile along the x-axes with little change in the local wind gradient $\partial\bar{U}/\partial z$ at a given height. Notice that not only the wind speed close to the surface, but also at the top of the boundary layer (here at 250 m height) is influenced by z_0 , since the geostrophic drag law is a function of z_0 as well (see Equation 3.16). If the boundary layer height changes the wind profile will substantially change as well, and for shallower boundary layer the local wind gradient increases (i.e., the wind profile appears to be steeper at a given height). It is found that for increasing boundary layer heights (say from 250 to 350 m height) there is very little change in the wind profile, whereas the wind profile is very sensitive to reducing the boundary layer height below 200 m. Besides, close to the surface (say in the lowest 10 - 20 m) the wind profile is not sensitive to h since for $z \ll h$ the wind profile simplifies to the (adiabatic) surface layer wind profile.

The impact of stability is in line with the known stability dependence of the surface layer profile shown in Chapter 2: if the atmosphere becomes stably stratified wind shear increases. Besides, the wind speed at the top of the boundary layer is a function of stability as well due to the dependence of the resistance function B on stability. In Equation 3.28 it is found that if the atmosphere becomes more stably stratified B will become increasingly more negative, hence the geostrophic wind increases in Equation 3.16. The sensitivity of the wind profile to the friction velocity close to the surface (below 20 m height) is relatively straightforward, and the wind increases substantially with increasing u_{*0} . Since the diabatic wind profile is linearly dependent on u_{*0} (assuming other parameters of the wind profile are constant), close to the surface doubling u_{*0} will result in approximately twice as high wind speeds. For example, at 20 m height the wind speed approximately increases from 6 m s⁻¹ to 12 m s⁻¹ once u_{*0} increases from 0.2 m s⁻¹ to 0.4 m s⁻¹. This is no longer valid at the top of the boundary layer (at 250 m the wind speed increases from approximately 7 m s⁻¹ to 17 m s⁻¹) since the resistance function A depends on u_{*0} as well. Since A increases for increasing u_{*0} , Equation 3.16 shows that the geostrophic wind increases more than linear with increasing u_{*0} .

3.2.3. PARAMETRIZATION OF SURFACE ROUGHNESS AND BOUNDARY LAYER HEIGHT

In this section it is aimed to derive a parametrization of z_0 and h . Similar as in Chapter 2 z_0 is parametrized with Charnock's equation since offshore conditions are considered

$$z_0 = \alpha \frac{u_{*0}^2}{g} \quad (3.31)$$

with $\alpha = 0.012$ (Peña & Gryning 2008) and g is the gravitational acceleration of 9.81 m s⁻². The Rossby-Montgommery equation is used to estimate the boundary layer height h similar to Gryning et al. (2007) which equals

$$h = c \frac{u_{*0}}{f_c} \quad (3.32)$$

where c has to be parametrized, and f_c is the Coriolis parameter. Although, as mentioned in Byun (1991), h is in reality dependent on other parameters as well, here Rossby number similarity theory is adopted and it is assumed h is defined as a function of u_{*0} , f_c and L alone. Subsequently c is parametrized as a function of stability. First the sensitivity of the wind shear profile to c is assessed for stable and unstable conditions separately before c is parametrized.

Results are shown in Figure 3.2 where wind profiles are shown with $u_{*0} = 0.3$ m s⁻¹, the left and right plots corresponds to respectively unstable ($L = -200$ m) and stable ($L = 200$ m) conditions, and z_0 and h are parametrized with Equations 3.31 and 3.32. The solid lines in the left and right panels clearly do not correspond to similar conditions, and c is on purpose defined at smaller values for stable conditions in line with literature and subsequent analyses. Besides, notice that in the lower panels the non-dimensional wind speed is shown. The non-dimensional wind speed will as well be considered when validating the theoretic profile with observation data, hence it is sensible to know in advance how the non-dimensional wind speed changes as a function of relevant parameters.

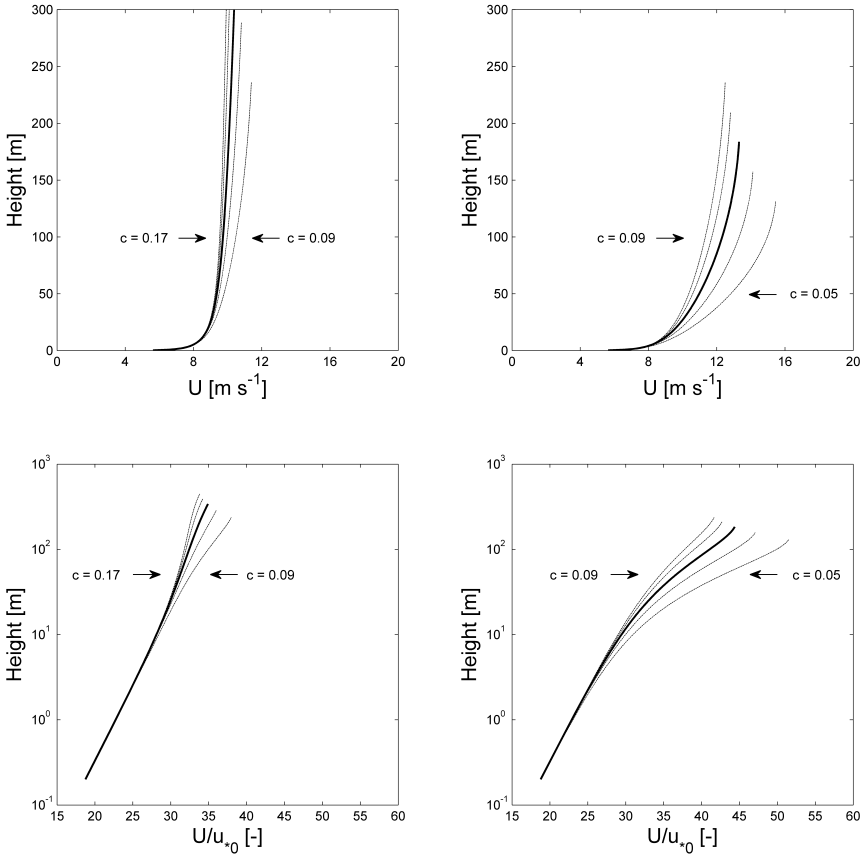


Figure 3.2: Sensitivity of the theoretic wind shear profile to the coefficient c for unstable (left panels) and stable (right panels) conditions. The upper panels show the wind profile, the lower panels show the non-dimensional wind profiles. Profiles are determined with $u_{*0} = 0.3 \text{ m s}^{-1}$ and L is -200 and 200 m for unstable and stable conditions respectively.

In general it is found that at a given height the wind speed (and non-dimensional wind speed) increases for decreasing c . This is in line with the upper right panel of Figure 3.1, where for a given stability and friction velocity a reduction in c results in a decrease of h . The change in wind speed is found to be small for unstable conditions, where c ranges in the shown profiles from 0.09 to 0.17. For stable conditions however the change in c from 0.05 to 0.09 is found to result in a substantial change in the wind profile. Again, this is in line with Figure 3.1, where the wind profile was found to be most sensitive to shallow boundary layers (i.e., small h and thus a small c), and stable conditions. Clearly the parametrization of c for stable conditions will be of importance for the accuracy of the shear profile.

To assess the behaviour of the non-dimensional wind profiles for stable and un-

stable conditions, it is recognised that for neutral conditions the diabatic surface layer wind profile would appear as a straight line on the lower panels of Figure 3.2. The non-dimensional wind profiles are found to differ substantially for unstable and stable conditions. For unstable conditions the non-dimensional wind profiles are found to curve leftwards from the surface to higher altitudes (i.e., the wind speed reduces compared to the neutral surface layer profile). For stable conditions there is a substantial curvature to the right with height (i.e., the wind speed increases compared to the neutral surface layer profile). Notice as well that at the top of the profile, the curvature is typically opposed to the remainder of the wind profile. For example, for unstable conditions and $c = 0.17$, the wind profile curves leftwards at $z \approx 20$ to 200 m height, however close to the top of the profile the curvature changes and there appears to be a sudden increase in the non-dimensional wind speed above $z \approx 200$ m. Similarly, for stable conditions and $c = 0.05$, the wind profile curves strongly rightwards, however near the top of the profiles around $z \approx 100$ m the profiles curves slightly back to the left. The behaviour of the wind profile at higher altitudes will be of importance when discussing the validation of the profile with observation data.

3.2.4. PARAMETRIZATION OF c

Based on the sensitivity analyses shown in Figure 3.2 it is clear that the parametrization of c can have a substantial impact on the accuracy of the boundary layer wind profile. As such literature parametrizations are not considered, and instead the derived theoretic wind shear profile is fitted to observation data to estimate c for each observed wind profile. This should result in a parametrization that is applicable for the offshore site considered in this research.

The same dataset is considered as used in Chapter 2, and any observation where data are missing in the wind profile observations up to 315 m height is discarded. Besides, also the filter for stationary conditions is adopted. After application of these filters a total dataset of 37623 observations remains, which equals approximately 71% of all data. The far majority of discarded data were not classified stationary following the criteria of Lange et al. (2004). The relative occurrence of unstable and stable conditions in the original and filtered dataset of 2012 is found to be similar (not shown in detail here), hence it is expected that the remaining data are representative despite the applied filter.

For each timestep only observation data at or below 27 m height are used to determine L and u_{*0} . The 27 m height wind speed observation is therefore not included when fitting the wind profile to observation data, since this could result in self correlation (Baas et al. 2006). Observations are grouped as a function of stability in terms of $100 / L$, ranging from -5 to 2 with a 0.1 binsize. For each stability group the derived extended wind shear profile is fitted to the observation data, where h is estimated with Equation 3.32. The procedure is done with $c = 0.01$ to 0.50 with increments of 0.001, to find an optimal fit for the given stability group. The quality of the fit is assessed by computing the root mean square error (RMSE) between the modelled and observed wind speed, where the RMSE is calculated as

$$RMSE = \sqrt{\frac{1}{n} \left[\sum [\bar{U}_{fit}(z) - \bar{U}_{obs}(z)]^2 \right]} \quad (3.33)$$

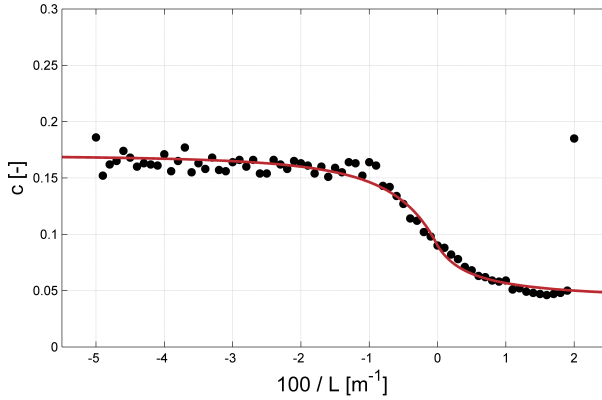


Figure 3.3: Value of coefficient c as a function of stability where the theoretic wind profile has an optimal fit to the observation data, as calculated with Equation 3.33.

in which $\bar{U}_{fit}(z)$ and $\bar{U}_{obs}(z)$ correspond to respectively the fitted and observed wind speed at height z , and n is the number of observation heights considered in the fit of the shear profile. It is assumed that c is optimal for a given stability if the average RMSE of the fitted wind profiles is smallest. The profile is fitted to observations up to 140 m height specifically. This is done since if either c or u_{*0} is very small, Equation 3.32 will estimate h to be low as well, which would prevent us from fitting the theoretic wind profile to several observations. This minimum boundary layer height could be raised up to 315 m height to cover all observations, however, it is recognised that for stable conditions the boundary layer can be shallow. The specified 140 m is thus a compromise, to fit the profile to several observations while also being able to parametrize c for (very) stable conditions. The same fitting procedure has also been done with a minimum boundary layer height of 250 m, which resulted in nearly the exact same parametrization for unstable and neutral conditions. The resulting optimal c -value as a function of stability is shown in Figure 3.3, including an empirical fit to the obtained results.

It is clear that c depends on stability, and c equals approximately 0.15 to 0.20 for strong unstable conditions, approximately 0.09 for neutral conditions and slightly less than 0.05 for strong stable conditions. For situations where $100/L > 2$ it was found that c increases significantly again up to values around 0.20, but due to a sharp increase in the RMSE these results are not considered to be appropriate. The empirical fit shown in Figure 3.3 for stable and unstable conditions corresponds to respectively

$$c = 0.04 + 0.05 \left(1 + 2 \frac{100}{L}\right)^{-1} \quad (3.34)$$

$$c = 0.17 - 0.08 \left(1 - 0.5 \frac{100}{L}\right)^{-3} \quad (3.35)$$

Which is forced to match for neutral conditions at $c = 0.09$. This provides a continuous parametrization of c as a function of stability, which has limiting values of 0.04 and 0.17

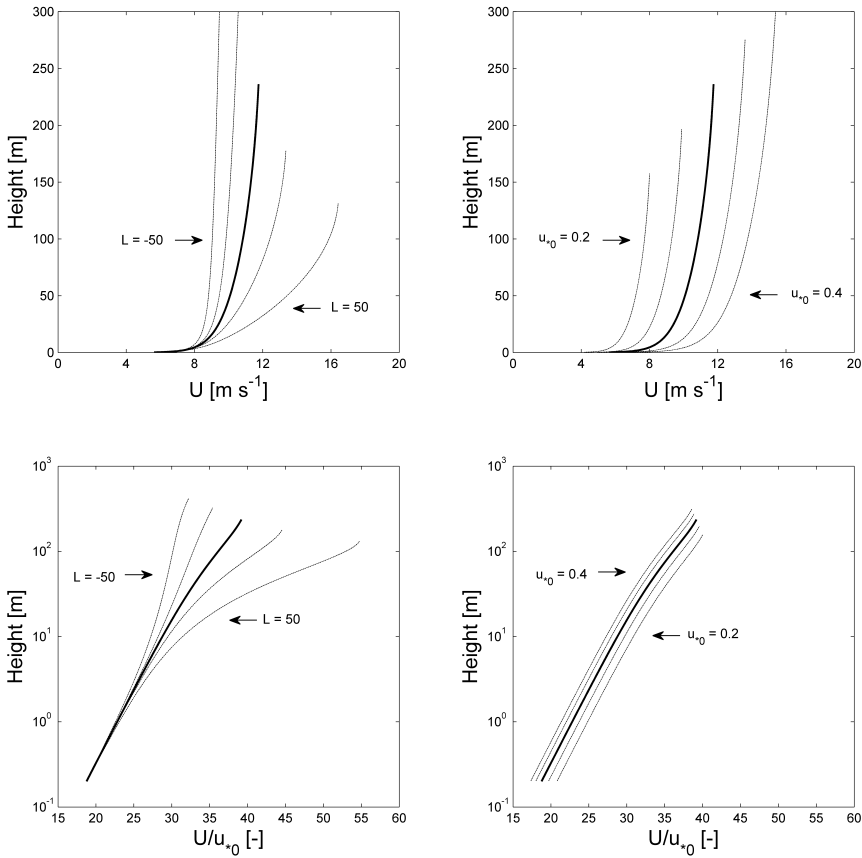


Figure 3.4: Sensitivity of the parametrized wind shear profile to stability (left panels) and u_{*0} (right panels), where upper panels show the wind profile and lower panels show the non-dimensional wind profiles. The solid black lines are similar for the four panels and correspond to a reference wind profile for neutral conditions with $u_{*0} = 0.3 \text{ m s}^{-1}$.

for extreme stable and unstable conditions. The results obtained for neutral and stable conditions are significantly smaller than proposed by [Sathe et al. \(2011\)](#), who used $c = 0.15$ and $c = 0.13$ for respectively neutral and very stable conditions. One possible explanation could be that offshore the boundary layer is more shallow compared to onshore, and thus for similar u_{*0} the boundary layer height will only decrease if a lower c is considered in the parametrization of h . Besides, the parametrization of A and B in this study differs from values considered by [Peña et al. \(2010a\)](#), and as such possibly also c has to change.

With a parametrization of c , the boundary layer height is a function of L , u_{*0} and f_c alone. As such, assuming a specific latitude, the boundary layer wind shear profile is thus defined as a function of L and u_{*0} alone. The resulting profile will be validated

Table 3.1: Overview of stability class characteristics used in Figure 3.5.

Class [-]	Regime [m]	L (prof) [m]	u_{*0} (prof) [m s ⁻¹]	Nr. of Obs. [-]
Very Unstable (VU)	$-100 \leq L < -50$	-69	0.33	5363
Unstable (U)	$-200 \leq L < -100$	-135	0.38	4412
Near Neutral Unstable (NNU)	$-500 \leq L < -200$	-284	0.38	2522
Neutral (N)	$\ L\ > 500$	-1336	0.35	2810
Near Neutral Stable (NNS)	$200 < L \leq 500$	296	0.34	1950
Stable (S)	$100 < L \leq 200$	141	0.26	1623
Very Stable (VS)	$50 < L \leq 100$	72	0.20	952

in Section 3.3, however, let us with the complete parametrization assess how the wind profile varies as a function of L and u_{*0} . Results are shown in Figure 3.4, in which the solid black lines all correspond to the same situation (i.e., neutral conditions with $u_{*0} = 0.3 \text{ m s}^{-1}$). With respect to stability it is found that for stable conditions the wind speed close to the surface increases, the local wind gradient increases and the boundary layer height decreases. This is in line with the expected behaviour of conditions in a stable atmosphere. With respect to the friction velocity it is primarily found that the wind speed and boundary layer height increase with increasing u_{*0} , however the local wind gradient shows little change as a function of u_{*0} . The non-dimensional wind profiles differ substantially as a function of stability as expected, however, for a given stability the wind profiles nearly collapse (i.e., the lower right panel in Figure 3.4 for neutral conditions). This is also the reason why in the validation non-dimensional wind profiles are considered, since the absolute wind speed differs substantially as a function of u_{*0} . The non-dimensional profiles do not perfectly collapse since various parameters of the wind profile are still a function of u_{*0} . As shown in Peña & Gryning (2008) this can be circumvented for the diabatic surface layer profile by introducing a stability-mean roughness length. Do note however that in the derived boundary layer wind profile both h and z_0 are a function of u_{*0} , hence a similar procedure is not applicable here.

Next it is aimed to validate the derived wind profile, and assess the performance of the boundary layer wind shear profile compared to commonly used wind profiles in meteorology and wind energy. Besides it is also analysed if part of the wind shear scatter for stable conditions shown previously in Chapter 2 Figure 2.5 can be explained by the new wind profile.

3.3. VALIDATION OF THE THEORETIC WIND PROFILE

A separate complete year of observation data is considered to avoid validating the parametrized theoretic wind profile with the same data as were used for the parametrization, which would result in an overestimation of the accuracy of the wind profile. From February 2013 until May 2014 the surface observation data of the buoy were not stored, hence a complete year of data starting at the first of June 2014 and lasting until the end of May 2015 is considered. Similar filters are used as described in the parametrization (i.e., no missing data in the observed wind profiles as well as stationary conditions), which results in 30469 observations (approximately 58% of all observations). This is substantially

less as was found for 2012, used in the parametrization of c , primarily due to an increase in missing LIDAR wind speed observations. As such more detailed information about the amount of unstable, neutral and stable observations considered is provided in the validation in Section 3.3.1. The various parametrizations proposed in the previous sections all allow the extended wind shear profile to be a continuous function of atmospheric stability. In principle there is thus no need to validate the wind profile for specific stability classes, however, for visualization purposes as well as for comparison purposes with literature, first the wind profile is validated for specific stability classes. Once done, the wind profile will also be validated for a continuous range of stability

3.3.1. VALIDATION WITH STABILITY CLASSES

For visualization purposes the observation data are grouped with respect to stability, and for comparison purposes the classification used by Peña et al. (2010a) is adopted with a slight modification of the stable and very stable classes (see Table 3.1). The stable and very stable classes are on purpose modified to have similar absolute class boundaries as used for unstable and very unstable conditions, since there is no physics based argument to adopt different class boundaries for stable and unstable conditions. The average observed non-dimensional wind profile is determined for each stability class for those observations where $0.1 \text{ m s}^{-1} \leq u_{*0} \leq 0.8 \text{ m s}^{-1}$. Besides, the average of the inverse of the Obukhov length is determined for each stability group, which is used to calculate theoretic wind profiles. The theoretic wind profiles are forced to match the observations at 27 m height for each stability class, which provides an estimate of u_{*0} used to calculate the theoretic wind profiles. With L and u_{*0} calculated, the theoretic wind profiles and the observed wind profiles are shown in Figure 3.5. The markers correspond to the average observed non-dimensional wind speed, the solid lines correspond to the boundary layer wind profile and the dashed lines correspond to the surface layer wind profile with the Businger-Dyer and Free-Convection stability correction functions.

For (very) unstable conditions it is found that the surface layer wind profile corresponds well to the observations up to 60 m height, but for higher altitudes the wind speed is underestimated. The boundary layer wind profiles overall has better agreement, especially for heights above 200 m, though in between 100 and 200 m height the boundary layer wind profile also appears to underestimate the observed wind speed. Do note however that the difference between the observed and modelled non-dimensional wind speed is in the order of $\bar{U}/u_{*0} \approx 0.5$ for the boundary layer wind profile, which should correspond to wind speed differences less than 0.5 m s^{-1} assuming $u_{*0} \leq 1 \text{ m s}^{-1}$ (which is correct for nearly all observations). For the surface layer wind profile, differences up to $\bar{U}/u_{*0} \approx 1$ are found around 300 m height, which thus corresponds to wind speed difference of approximately 1 m s^{-1} or less.

For (near) neutral conditions in general similar results are found as for (very) unstable conditions, though with different orders of magnitude. For neutral and slightly unstable conditions the surface layer wind profile underestimates wind speeds above 60 m height whereas the boundary layer wind profile has a substantial higher agreement with the average observed non-dimensional wind profile. For slightly stable conditions however the surface layer performs well up to 140 m height, and for higher altitudes there is an overestimation of the wind speed. The boundary layer wind profile again has high

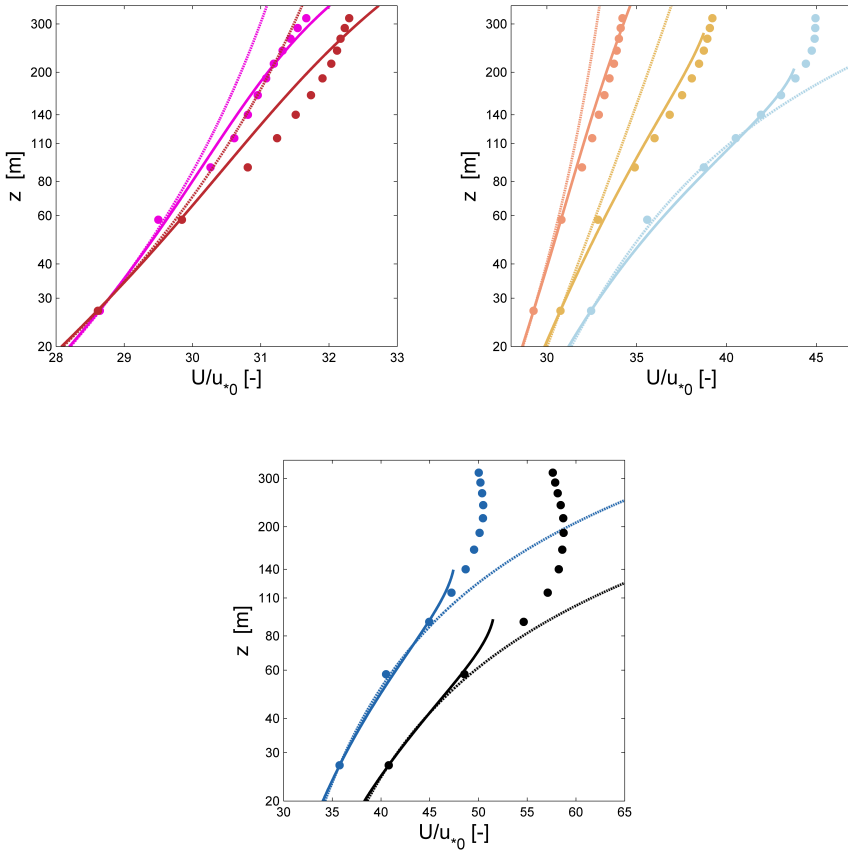


Figure 3.5: Validation of the non-dimensional boundary layer wind profile (solid lines) and the non-dimensional surface layer wind profile (dashed lines) compared to mean non-dimensional observed wind profile (markers) for various stability conditions. The upper left panel shows very unstable (VU, magenta) and unstable (U, dark red) conditions, the upper right panel shows near neutral unstable (NNU, light red), neutral (N, yellow) and near neutral stable (NNS, light blue) conditions and the lower panel shows stable (S, dark blue) and very stable (VS, black) conditions.

agreement with the observation data, though at 58 m height there seems to be a slight overestimation of the wind speed compared to the observations. It is found that at 190 m height, the boundary layer profile slightly underestimates the non-dimensional wind speed by $\bar{U}/u_{*0} \approx 0.5$. The surface layer wind profile however causes an underestimation of $\bar{U}/u_{*0} \approx 1$ to 2.5 for respectively near neutral unstable and neutral conditions, and an overestimation of $\bar{U}/u_{*0} \approx 2$ for near neutral stable conditions. Notice as well that for neutral and slightly stable conditions the boundary layer wind profile does not continue up to 315 m height since for the calculated values of L and u_{*0} the top of the boundary layer is determined below 315 m height. Besides, it is found that above 250 m height

the average observed non-dimensional wind profile no longer increases with height. Although one could interpret this as an indirect observation of the boundary layer height, do note that many observations are averaged, hence the observed boundary layer height is expected to vary a lot for the individual observations.

For (very) stable conditions result differ substantially compared to the previously discussed stability classes. First of all the average observations for both stable and very stable conditions show a wind maximum at respectively 200 and 160 m height. In [Peña et al. \(2010a\)](#) similar observations are shown for very stable conditions, which might be an indication of the occurrence of low-level jets. For stable conditions the boundary layer wind profile has a good agreement with the observation data, though there is a slight underestimation of the non-dimensional wind speed at 140 m height. For very stable conditions this underestimation is found at 90 m height all ready. The surface layer wind profile corresponds well to the observation data up to 90 m height for stable conditions, and up to 60 m height for very stable conditions, but there is a severe overestimation of the wind speed at higher altitudes. This agrees well to the results shown in Chapter 2. Especially at heights above 140 m the difference in the non-dimensional wind speed is in the order of $\overline{U}/u_{*0} \approx 5$ or larger, which can easily correspond to wind speed overestimations of more than 2.5 m s^{-1} .

For stable and very stable conditions it is found that the boundary layer wind profile does not perform as well as for other stability classes, hence these stable conditions are examined in more detail. The observations for stable and very stable conditions are further classified as a function of the friction velocity to assess if the wind profile performs better for specific conditions. Results are shown in Figure 3.6. It is found that the boundary layer wind profile typically performs poorly close to the top of the profile (i.e. for heights close to the estimations of h). For $u_{*0} > 0.35$ the boundary layer wind profile performs well for most observation heights, and substantially better compared to the surface layer wind profile at heights relevant for wind energy purposes. The poor performance of the wind profile for (very) stable conditions in the vicinity of h might have several causes, of which three possibilities are discussed.

First of all, as discussed in the parametrization of h , it is assumed that h is a function of three parameters (i.e., the Coriolis parameter, the friction velocity and atmospheric stability), while it is known that free atmosphere conditions are of influence as well. A more accurate estimate of h could result in better agreement with the observed wind profile. Second of all, it is mentioned in [Gryning et al. \(2007\)](#) that the length scale at the top of the boundary layer is assumed, for sake of simplicity, as $h - z$, which thus becomes 0 m in close proximity of the top of the boundary layer. In reality the length scale near the top of the boundary layer not necessarily has to become 0 m, as is shown for neutral conditions in [Peña et al. \(2010b\)](#). Finally, one also has to consider that the boundary layer wind profile will change substantially if c is small, but there is little change in the wind profile for large values of c . Since c decreases for stable conditions as found with Equation 3.34, it might very well be that a slight change in the parametrization of c would cause substantial different results. As shown in Figure 3.2, a slight decrease in c for stable conditions would result in an increase in wind speed (though consequently h also decreases).

The results presented here correspond well to those presented by [Peña et al. \(2010a\)](#),

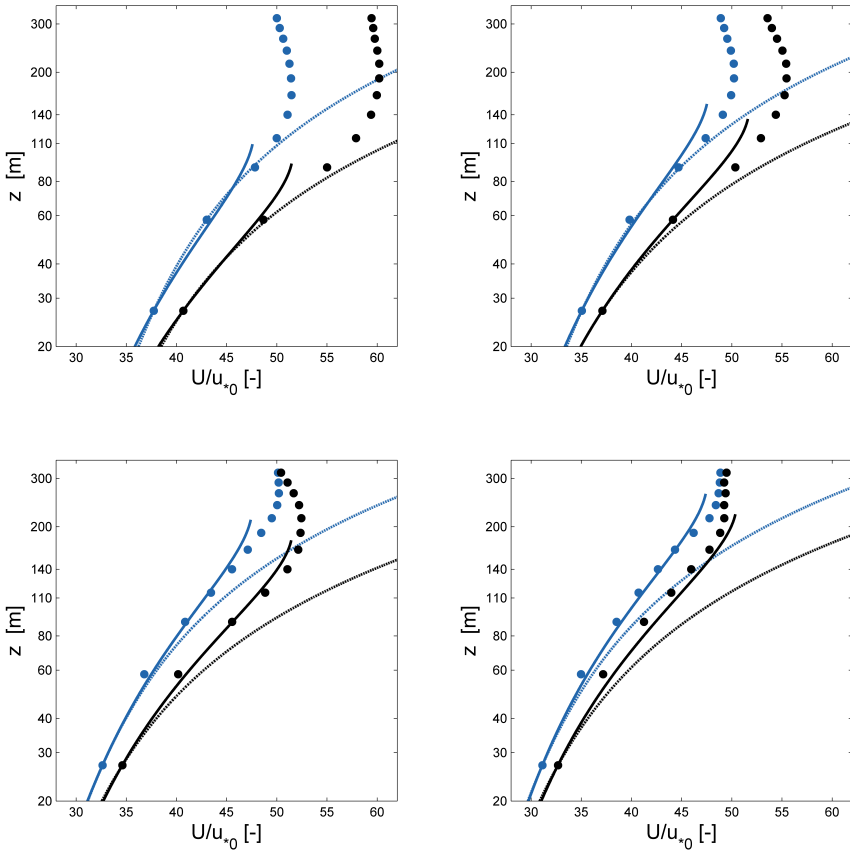


Figure 3.6: Similar wind profiles as shown in Figure 3.5 for stable (S, dark blue) and very stable (VS, black) conditions conditioned to u_{*0} . The panels corresponds to $0.15 \leq u_{*0} \leq 0.25$ (upper left panel), $0.25 \leq u_{*0} \leq 0.35$ (upper right panel), $0.35 \leq u_{*0} \leq 0.45$ (lower left panel) and $0.45 \leq u_{*0} \leq 0.55$ (lower right panel).

especially for unstable conditions, though the absolute values of \bar{U}/u_{*0} differ substantially since Peña et al. (2010a) considered onshore data with a higher surface roughness. Besides, whereas here it is found that for neutral and slightly stable conditions the gradient of the non-dimensional wind speed above 200 m height decreases with height, Peña et al. (2010a) shows wind profiles for similar stability classes where the gradient in the non-dimensional wind speed still increases at such heights. This differences is expected to be related to changes in the boundary layer height offshore and onshore, since close to the top of the boundary layer the non-dimensional wind speed becomes nearly constant with height (as shown both here and in Peña et al. (2010a) for (very) stable conditions).

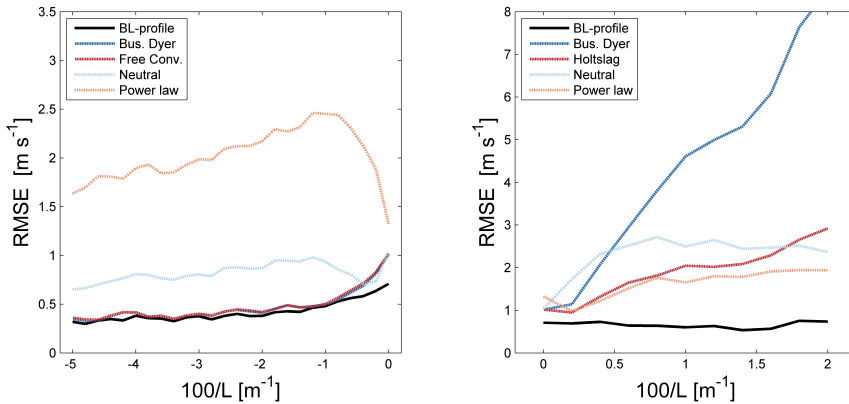


Figure 3.7: RMSE of various wind profiles for unstable (left panel) and stable (right panel) conditions. The wind profiles included here correspond to the derived boundary layer wind profile (BL-profile), the surface layer wind profile with specific stability correction functions (Bus. Dyer, Free Convection and Holtslag), the surface layer wind profile without stability correction (Neutral) and a power law wind profile with an exponent of 0.14 following IEC (2009).

3.3.2. VALIDATION FOR STABILITY AS A CONTINUOUS PARAMETER

The extended shear profile so far has been validated for seven specific stability classes, however, it is aimed to define a boundary layer wind shear profile that performs well for a continuous range of stability conditions, not for a group of stability conditions combined. As such the RMSE of the wind profile including the specified parametrization is assessed for a continuous range of stability conditions, and the performance of the extended wind profile is compared to other wind profiles commonly used in wind energy research. Results are shown in Figure 3.7. For unstable conditions it is found that the boundary layer wind profile performs approximately as good as the surface layer wind profiles with stability correction. Only for near neutral conditions the boundary layer wind profile starts to perform better compared to these specific surface layer wind profiles. The neutral surface layer wind profile performs less good for unstable conditions due to the absence of a stability correction. The power law performs very poor for unstable conditions since wind shear is strongly overestimated with the exponent of 0.14 considered here, assumed to be valid offshore following IEC (2009). For stable conditions however the boundary layer wind profile performs far better than any of the other shear profiles. Here it is found that the power law performs reasonably well, since wind shear is strong for stable conditions. Besides, the surface layer wind profile with the stability correction function of Holtslag performs substantially better compared to the Businger-Dyer correction function, in line with results shown in Chapter 2. It is remarkable that the neutral surface layer wind profile also performs quite well for stable conditions compared to the surface layer wind profile with the stability correction of Holtslag. It is expected here that the neutral wind profile underestimates wind shear for stable conditions (especially close to the surface), while the wind profile including the correction function of Holtslag

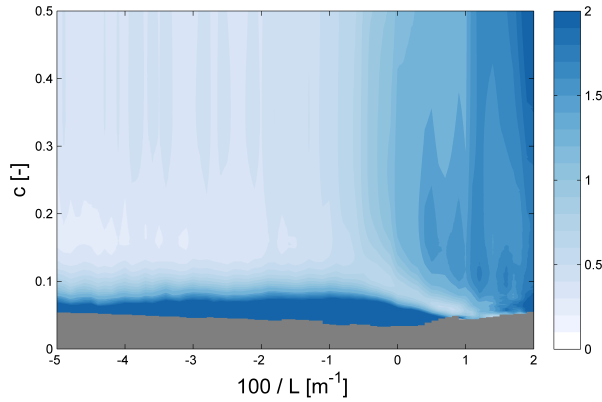


Figure 3.8: Average RMSE of the fitted boundary layer profile to observation data for a given stability (in terms of $100/L$) and the coefficient c . Grey shading corresponds to a combination of stability and c for which there are no observations found where h is estimated to be larger than 140 m.

overestimates wind shear (especially at higher altitudes).

Although it is clear that the derived boundary layer performs substantially better compared to other wind profiles considered for stable conditions, it is necessary to make a critical remark here that for such conditions the boundary layer profile frequently results in $h < 315$ m height. As such, the boundary layer wind profile does not determine a wind speed at higher altitudes whereas all other wind profiles considered do determine a wind speed. This results in a substantial reduction in the RMSE, but one could argue this also results in an incorrect comparison. The advantage here thus is that the boundary layer wind profile does not determine an incorrect wind speed at high altitudes, which results in an accurate wind profile. In scope of wind energy research however it is expected that this can pose a problem to define wind shear up to the maximum blade tip height of state of the art wind turbines. This will be elaborated upon further in Chapter 6.

3.4. DISCUSSION

The parametrization of c is discussed in more detail since the estimation of h is especially important for stable conditions. As mentioned previously c is parametrized specifically with observation data where the estimate of h is larger than 140 m. Observations with (very) stable conditions and small u_{*0} are thus not properly included in the parametrization of c . This is also shown in Figure 3.8, where the mean RMSE for a given stability and prescribed c -value is shown. For stable conditions, there clearly is an optimal c that decreases with increasing stability (See the light blue trace), however for $100/L > 1$ (i.e. very stable conditions) it is likely that c should become smaller than 0.05. The grey colours in Figure 3.8 however indicate that for stable conditions and $c < 0.05$ the corresponding RMSE cannot be calculated since there are no observations for which $h > 140$ m. Besides,

the parametrization of c is likely strongly dependent on stable observations where u_{*0} is large. This might explain why the boundary layer wind shear profile for (very) stable conditions performs substantially better for $u_{*0} > 0.35 \text{ m s}^{-1}$ compared to $u_{*0} < 0.35 \text{ m s}^{-1}$.

Note as well from Figure 3.8, although this is irrelevant for the discussion of the boundary layer wind profile for stable conditions, that for unstable conditions the optimal c value is not obvious at all. This not only explains why for unstable conditions in Figure 3.3 more scatter is found, but also shows that a value of $c = 0.3$ to 0.5 might as well have been chosen for unstable conditions without decreasing the accuracy of the wind profile substantially.

3.5. CONCLUSIONS

In scope of the size of state of the art wind turbines it is deemed necessary to define a wind shear profile that is valid for the whole boundary layer. As such in this Chapter a theoretic, physics based, boundary layer wind shear profile has been derived following the work of Gryning et al. (2007). The parametrization required to define various variables typically not observed directly during measurement campaigns is primarily based on literature. The theoretic profile is fitted to observation data for the parametrization of the boundary layer height (specifically for the coefficient c). Combined this has resulted in a wind profile that is accurate up to substantial higher altitudes than the surface layer wind profile, which is highly beneficial for wind energy purposes.

The average non-dimensional boundary layer wind shear profile is found to agree well with observations, and the performance is substantially better than the surface layer profile. This is especially the case for neutral and stable conditions. For stable conditions the profile does not accurately describe shear at higher altitudes. This might have various causes as discussed, and it is recommended to emphasize in future research specifically on the stable boundary layer wind shear profile. It might be required to alter the parametrization of h and c , or to consider a different approximation of the mixing length scale at the top of the stable boundary layer.

Based on the obtained results it is also possible to assess if some scatter found in Chapter 2 for wind shear can be explained with the newly derived profile. It is concluded based on the derivation of the boundary layer wind shear profile that the wind speed ratio between two specified heights is not only a function of stability, as considered in the assessment in Chapter 2, but also of u_{*0} , z_0 , h , A and B . It is therefore well possible that the scatter observed is related to other variables included in the shear profile. Besides, if the adopted parametrization of h is considered, then frequently it is found that $h < 500 \text{ m}$, thus the heights at which the wind speed ratio is determined in Chapter 2 (i.e., 58 and 92 m height) can often fall outside the surface layer.

Although the profile derived in this chapter provides some insight in the cause of variations in wind shear for stable conditions, the profile does not allow for a speed ratio less than one. The wind speed profile derived here will always result in a wind speed that increases with height, hence a wind speed ratio smaller than 1 is not explained with the boundary layer wind shear profile. As such in the following chapter specific situations are considered where the wind speed ratio can be less than 1.

4

THE OCCURRENCE AND CHARACTERIZATION OF LOW-LEVEL JETS OFFSHORE

I believe there are no questions that science cannot answer about a physical universe.

Stephen Hawking

The scatter in wind shear for stable atmospheric conditions found in Chapter 2 has, to an extent, been explained in Chapter 3: the boundary layer can be shallow for stable conditions. Especially for stable conditions wind shear profiles will deviate substantially from surface layer wind shear profiles. The second proposed cause of the scatter in wind shear, low-level jets, has not been discussed in detail yet. The wind speed profile during a low-level jet is characterized by a local wind maximum relatively close to the surface and decreasing wind speeds below and above the jet. Such conditions could have a substantial influence on wind turbine performance. However, before the impact of low-level jets on wind turbine performance is assessed, it is sensible to first study the occurrence and characteristics of low-level jets in the far offshore environment.

In this chapter it is aimed not only to assess if offshore low-level jet characteristics can be of influence for wind turbine performance, but also to explain what causes the occurrence of low-level jets offshore. These jets have been studied onshore frequently, but several specific causes of low-level jets onshore are not applicable offshore. This should aid in obtaining fundamental insight in the physical processes of offshore low-level jets. The results obtained in this chapter will be put into perspective of wind turbine performance in Chapter 6.

Parts of this chapter are incorporated in the publication: Holtslag, M. C., He, Y., Bierbooms, W. A. A. M. & van Bussel, G. J. W. (2016), On the occurrence and characteristics of low-level jets in the Dutch North Sea, Submitted for publication to *Journal of Wind Engineering and Industrial Aerodynamics*

4.1. INTRODUCTION

In Chapter 2 atmospheric conditions have been studied with aid of observation data collected at meteorological mast IJmuiden, and it is found that Monin-Obukhov theory can be used to describe offshore atmospheric conditions. With respect to wind shear, it was found that the diabatic surface layer wind shear profile coincides reasonably well with observations up to 90 m height for unstable and neutral conditions. For stable conditions scatter was found to increase substantially, and one possible cause of the scatter might be related to the occurrence of low-level jets. It is recognised that low-level jets might be of influence for offshore wind power (Nunalee & Basu 2014, Christakos et al. 2014), hence it is useful to assess if low-level jets also occur at the site considered in this thesis.

Low-level jets are characterized as wind conditions where the wind speed profile has a local maximum relatively close to the surface. Typically these wind maxima occur in the lowest 300 m of the atmosphere, though it is possible they occur at substantial higher altitudes (Stull 1988). In this chapter, however, only the lower parts of the atmosphere are considered where wind turbines operate due to the scope of this thesis. The occurrence of low-level jets onshore and at coastal sites has been studied frequently in previous decades, and an overview of commonly accepted causes of low-level jets is presented in Kraus et al. (1985). Well documented examples are for example the occurrence of jets onshore at Cabauw (Baas et al. 2009) or at the Great Plains (Whiteman et al. 1987). The majority of studies are executed either on shore, at coastal areas or relatively close to the shore. Offshore low-level jets have been studied with numerical models (Christakos et al. 2014, Nunalee & Basu 2014), but there have been few validations with observation data offshore, similar to for example Dörenkämper et al. (2015). This is primarily caused by the lack of far offshore observations sites where observations are done up to at least 300 m height, and lasting several years to assess seasonal dependences. This serves as an argument not to immediately assess the impact of low-level jets on wind turbine performance (which certainly would be a useful study for onshore sites due to the common concurrence of low-level jets on shore (Baas et al. 2009)), but first actually assess the occurrence and characteristics of low-level jets offshore.

In wind energy research wind shear is typically considered in terms of a power law or a diabatic logarithmic wind profile (IEC 2009). Since these profiles only describe wind speeds that gradually increases with height, which in reality is indeed commonly true, distinct phenomena such as low-level jets are not covered. Due to the significance of wind shear for wind energy purposes, and the possible benefits of increased wind speeds for wind power production, it is expected that the occurrence of low-level jets at a wind farm site might have a profound impact on wind turbines. With the ongoing development of offshore wind energy it is therefore questioned to what extent low-level jets occur offshore. In a previous study, He (2014) assessed the characteristics of offshore low-level jets, and derived an empirical low-level jet model based on a fourth order polynomial fit to observed low-level jet wind profiles. In this thesis the research of He (2014) is extended, and the meteorological aspects of low-level jets are assessed in much more detail.

The aim of this chapter is twofold. First, it is aimed to present an overview of the occurrence and characteristics of low-level jets offshore. Second, it is studied in more detail

for which physical conditions low-level jets have an increased likelihood of occurrence. This should aid in a more fundamental understanding what causes the occurrence of low-level jets far offshore. The quantification of the impact of low-level jets on wind turbine power production and wind turbine fatigue loads will be studied in Chapter 6.

4.2. THEORY

In this section the commonly accepted physical processes that can result in the development of a low-level jet are studied, however, specific conditions that by definition cannot occur offshore (i.e., sloping terrain) are not discussed. Besides, formation causes related to synoptic scales (i.e., related to weather patterns and frontal systems (Gerhardt 1963, Kotroni & Lagouvardos 1993)) are not elaborated upon in the theory since based on the observation data alone it is not possible to assess synoptic scale conditions in detail. As such three distinct situations that frequently result in the occurrence of low-level jets onshore and at coastal sites are elaborated upon. These are the inertial oscillation, baroclinicity and changing surface characteristics at coastal sites.

4.2.1. INERTIAL OSCILLATION

The Inertial oscillation is one of the primary causes of nocturnal low-level jets onshore. The rapid decay of turbulence at sunset causes frictional decoupling, and the wind close to the surface accelerates due to the force imbalance. The Coriolis force causes a deflection of the accelerating wind, and both the wind speed and wind direction will change in time after sunset. A simplified set of equations describing such conditions is presented in Stull (1988)

$$\overline{U} - \overline{U}_g = A \sin(f_c t) - B \cos(f_c t) \quad (4.1)$$

$$\overline{V} - \overline{V}_g = A \cos(f_c t) + B \sin(f_c t) \quad (4.2)$$

where \overline{U} and \overline{V} are the mean horizontal wind components, \overline{U}_g and \overline{V}_g are the mean horizontal geostrophic wind components, f_c is the Coriolis parameter, t is the time after sunset and A and B are parameters depending on initial conditions. As one can see, the resulting horizontal wind will oscillate in time around the geostrophic wind. More elaborate relations are presented in for example van de Wiel et al. (2010) and Shapiro & Fedorovich (2010). On shore, the inertial oscillation is triggered by the rapid decrease in turbulent mixing at sunset, however due to the absence of a diurnal cycle offshore it is not expected that the same phenomena occurs frequently offshore. Still, one can argue that the inertial oscillation might be the cause of offshore low-level jets since they can extend for hundreds of kilometres (Stull 1988). If winds are coming from shore, and if there is some diurnal variation present in the occurrence of offshore jets, then offshore low-level jets might well be related to the onshore inertial oscillation. Besides, as shown in Andreas et al. (2000), if stable conditions persist for a long time offshore, low-level jet wind profiles can occur even if the wind is not coming from shore. An overview of studies related to the inertial oscillation caused low-level jet can be found in Blackader (1957), Andreas et al. (2000), Baas et al. (2009) and van de Wiel et al. (2010).

4.2.2. BAROCLINICITY

The impact of baroclinicity on wind profiles is introduced by the thermal wind relations, which equal (Holton 1972)

$$\frac{\partial \overline{U}_g}{\partial z} = -\frac{g}{f_c T} \frac{\partial \overline{T}}{\partial y} \quad (4.3)$$

$$\frac{\partial \overline{V}_g}{\partial z} = +\frac{g}{f_c T} \frac{\partial \overline{T}}{\partial x} \quad (4.4)$$

where g is the acceleration due to gravity and T is the temperature. The geostrophic wind thus changes with height depending on horizontal temperature gradients. Temperature gradients can have various origins on small scales (i.e., local differential heating (Kottmeier et al. 2000)), large scales (i.e., orography, (Parish & Oolman 2010)) and synoptic scales (i.e., weather patterns and cyclones (Kotroni & Lagouvardos 1993)), however, sufficiently far offshore only synoptic scale causes are expected to be relevant since differential heating should not occur far offshore, and orography is absent. Example studies where the occurrence of low-level jets are related to baroclinicity can be found in Bonner (1968) and Doyle & Warner (2010).

4.2.3. COASTAL SURFACE CHANGES

Although far offshore conditions are considered in this research, one should not neglect on forehand the effect of coastal surface changes. It is found in various studies that coastal effects can cause low-level jets at least 80 km offshore (Smedman et al. 1995). The possible effect of coastal surface changes is twofold, and in principle both effects have been discussed previously. First, if the wind close to the surface is perpendicular directed to the shore (from land to sea), there will be a sudden reduction in surface roughness and thus turbulence levels will suddenly decrease. At the same time the wind close to the surface will accelerate since friction at the surface reduces. This frequently results in the development of an internal boundary layer (Garratt 1990, Galmarini & Attié 2010), however, if the speed up is sufficient one might get locally an overshoot: wind speeds close to the surface can become stronger than wind speeds at higher altitudes. A similar effect as the inertial oscillation can thus occur: a reduction in turbulence levels, and an increase in wind speed in the lower parts of the atmospheric boundary layer. Despite these similarities, the formation cause differs substantially, since there is no need for a sudden rapid decrease in incoming short-wave radiation or for a strong stable atmospheric stratification. Second, due to differences in heating at sea and onshore, horizontal temperature gradients can occur. If at the same time the geostrophic wind is directed parallel to the coast, Equations 4.3 and 4.4 shows that the geostrophic wind can decrease with height. These baroclinic conditions can trigger low-level jets at coastal sites, however it is questioned if this also can result in the development of a low-level jet far offshore. Various causes of coastal low-level jets are discussed in Hsu (1979), Zemba & Friehe (1987) and Nunalee & Basu (2014).

4.3. DATA AND METHODOLOGY

In this section an overview is provided of the data considered in this research. A more elaborate discussion on the observation data can be found in Chapter 2. Besides, the methodology and terminology adopted in this chapter will be discussed for clarification purposes.

4.3.1. DATA DESCRIPTION

Wind speed, wind direction, temperature, humidity and air pressure observations are considered to properly assess the characteristics and possible formation causes of low-level jets offshore. Wind speed and wind direction observations of the cup anemometers and wind vanes at 27, 58 and 92 m height are used in combination with the LIDAR observations up to 315 m height. Temperature, air pressure and relative humidity is observed at 21 m height, and surface temperatures are measured with the wave buoy. All observations are stored as 10-minute mean conditions, and anemometer wind observations are corrected for tower distortion effects as discussed in Chapter 2. Data has been collected since 2012, however there have been substantial periods where observation data were not stored. As such exactly two years of data are considered in this chapter, namely 2012 and the period from the first of June 2014 until the end of May 2015, similar as used in Chapter 3.

Atmospheric stability is considered in terms of the Obukhov length L , calculated with the bulk Richardson number, however, the filter for stationary conditions adopted in Chapter 2 is not used in this chapter. The filter for stationary conditions is discarded since a low-level jet is a dynamic condition and characteristics like shear and maximum wind speed are expected to change in time. The cup anemometer and LIDAR wind observations are nearly overlapping at 90 m height, hence wind speed and wind direction observed by the anemometers and LIDAR are compared. If either the wind speed differs more than 2 m s^{-1} or the wind direction differs by more than 30 degree, observations are discarded. The 2 m height difference will result in a minor difference in wind conditions, substantially smaller than the 2 m s^{-1} and 30 degrees considered here. It is known that a LIDAR at times can observe the wind direction at a 180 degree difference compared to inflow conditions. As such, those observations where the wind direction observed by the LIDAR and wind vane differs by 150 to 210 degree are not discarded.

For the subsequent wind profile analyses most observations at 27 and 58 m height are used in combination with LIDAR observations from 90 to 315 m height. The anemometer observations at 90 m height are thus only used to validate LIDAR observations, but not in the actual analyses of wind profiles. Only those specific observations where the wind profile observations between 27 and 315 m height has no missing values, and where stability could be calculated (i.e., no missing temperature, pressure and humidity observations, and $RI < 0.2$), are considered in the analyses. Besides, all data where at 90 m height there is too much discrepancy between the anemometer and LIDAR observations as discussed previously is discarded. This leaves us with 45554 observations in the first year considered, and 39290 observations in the second year considered, which equals respectively 86.4% and 74.8% out of all yearly observations.

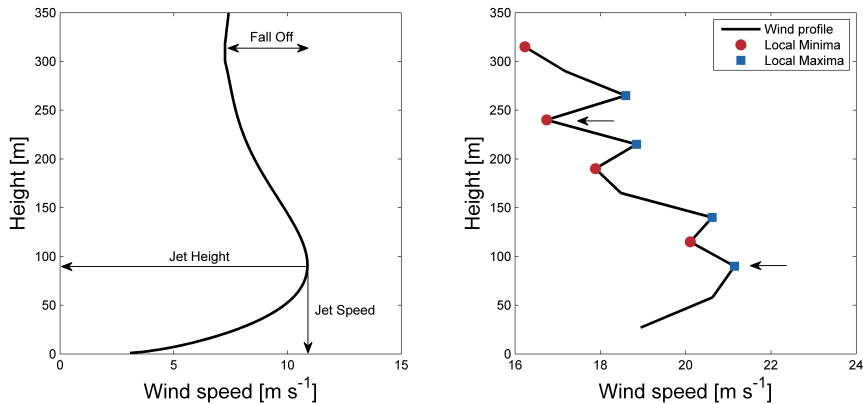


Figure 4.1: Low-level jet terminology used in this chapter (left panel), and an example observed low-level jet with local minima and local maxima (right panel). The black arrows in the right panel correspond to the jet height and jet falloff height determined based on specific detection criteria.

4.3.2. METHODOLOGY AND TERMINOLOGY

An overview of the adopted terminology used to describe a low-level jet is presented in Figure 4.1, where a simplified example jet profile is shown in the left panel in combination with the terms frequently used in the remainder of this chapter. The jet height corresponds to the height where the maximum wind speed in the wind profile is observed. The jet speed corresponds to the magnitude of the wind vector at the jet height. The jet falloff is defined as the difference between the jet speed and the minimum wind speed observed above the jet. The jet falloff is considered both as an absolute and relative value, where the relative jet falloff is calculated with respect to the jet speed (i.e., a falloff of 20% means the minimum wind speed above the jet is 20% less than the jet speed). The persistence of the jets is also considered by determining for how many consecutive observations the jet is present.

A set of criteria is used to detect the occurrence of jets in the observation dataset. As explained in Kraus et al. (1985) one could choose to define jets based on the physical origins, which provides more insight in the cause of jets, but less in the characteristics. Since it is aimed to assess if jets are of importance for offshore wind power, the cause of jets offshore is in this study less relevant than the characteristics. In scope of measurement errors it is important to set sufficiently strong detection criteria, primarily in terms of the jet falloff, however, setting these criteria too strict will result in discarding jets that might be of importance for wind energy purposes. In literature various criteria are considered, and in this chapter the effect of adopting various possible criteria is assessed as well. Examples of detection criteria used in literature are typically in terms of the observed jet falloff, either absolute, relative or a combination of both. Besides, there are often constraints specified that have to be fulfilled to consider the observed jets in subsequent analyses. Examples of these constraints are related to the jet height (i.e., within the lowest 100 or 500 m (Dörenkämper et al. 2015, Baas et al. 2009)), the wind minimum

above the jet (i.e., at least 3 m s^{-1} (Dörenkämper et al. 2015)) or a minimum persistence of the jet (i.e., 1.5 hour (Baas et al. 2009)).

The methodology of Baas et al. (2009) is followed to only consider a minimum to be representative if the wind speed directly above the local minimum increases by at least 1 m s^{-1} before decreasing again. The absolute jet falloff has to be at least 2 m s^{-1} , and the relative jet falloff has to be at least 20%. Also, if there is no local minimum found (the wind speed continuously decreases), the highest observation height will be assumed to correspond to the minimum. The example observed low-level jet shown in the right panel of Figure 4.1 has three local minimum in the wind speed profile. The minimum at 115 m height is not considered to be representative since the wind speed at 140 m height is less than 1 m s^{-1} stronger than the wind speed at 115 m height. The minimum detected at 190 m height is also not considered since the relative jet falloff is smaller than 20%. The minimum detected at 240 m height is for this low-level jet considered as the falloff height, since both the absolute and relative falloff at this height is in line with the set criteria, despite the fact that at 315 m a lower wind speed is observed.

It is recognised that in this research observation data are used of a substantial smaller part of the atmosphere compared to the studies of for example Andreas et al. (2000) and Baas et al. (2009). Since the LIDAR has a maximum observation height of 315 m, only jets can be detected that have a maximum wind speed in the lowest 290 m of the atmosphere, and for those jets a significant minima has to be present at or below 315 m as well. Numerous low-level jets will thus not be detected in this study that would be detected if one would observe up to higher altitudes. Similarly, not only the amount of jets and corresponding jet heights will be influenced by the observation setup, but also the jet falloff estimated with the observation data. For those wind profiles where the wind speed is gradually decreasing with height above the jet height, it is assumed that the observed wind speed at 315 m height is a minimum in the wind profile. In reality however, it might very well be that the wind speed decreases further above 315 m height. This will be briefly assessed when discussing jet characteristics in Section 4.4.1. Despite the limitations of the observation setup, it is expected that the results are still useful for wind energy purposes, since neither jets with a jet height above 290 m, nor the exact jet falloff above 315 m should be of substantial influence to offshore wind energy. For meteorological purposes however it is clear that not all low-level jets that occur offshore are detected.

In Table 4.1 it is shown how many jets are detected in the dataset considered in this study for various detection criteria in terms of the jet falloff. Here no constraints are considered with respect to the jet height, jet speed or persistence of the jets. The most strict detection criteria (upper row) corresponds to the criteria used by Baas et al. (2009) without a persistence criteria. There is an obvious increase in the amount of jets detected in both years considered once the detection criteria are relaxed. Whereas for the strict detection criteria approximately 3 - 3.5% of all observed wind profiles have jet characteristics, this increases to slightly more than 10% once the detection criteria are relaxed. The percentages shown in Table 4.1 are not extremely high (Baas et al. (2009) for example shows that at Cabauw low-level jets occur 30% of all nights), however, do note that the detected jets occur at many different days during the year, ranging from 130 (in line with Nunalee & Basu (2014)) to nearly 270 different days of the year. This is a first indication

Table 4.1: Influence of specific detection criteria (first two columns) on the amount of low-level jets observed per year.

Falloff [m s ⁻¹]	Falloff [%]	Jets (Y1) [-]	Jets (Y2) [-]	Jets (Y1) [%]	Jets (Y2) [%]	Days (Y1) [-]	Days (Y2) [-]
2.0	20	1417	1337	3.11	3.40	135	131
2.0	10	1738	1688	3.82	4.30	155	150
2.0	0	1739	1693	3.82	4.31	155	150
1.5	20	1878	1745	4.12	4.44	157	156
1.5	10	2651	2459	5.82	6.26	201	199
1.5	0	2706	2503	5.94	6.37	203	199
1.0	20	2380	2106	5.22	5.36	176	171
1.0	10	4065	3643	8.92	9.27	252	250
1.0	0	4561	4016	10.01	10.22	269	260

that offshore jets have a short persistence, which will be discussed in Section 4.4.2 as well

From here on the characteristics of the low-level jets detected in the dataset considered will be assessed. Although the detection criteria could be relaxed from here on to assess the characteristics of as many jets as possible, this is not done, since one would become more prone to incorporating jets that are influenced by measurement errors. As such only jets are considered that have at least an absolute jet falloff of 2 m s⁻¹, and a minimum relative jet falloff of 20%. Besides, from here on there is no longer a differentiation between the two years of data and instead simply the two years of data are simply combined.

4.4. RESULTS

The results are divided into three sections. First jet characteristics are discussed in combination with the frequency of occurrence of low-level jets as a function of time, wind direction and atmospheric stability. Next ambient conditions are analysed in more detail to explore possible causes of low-level jet occurrences offshore. Finally a specific case study is presented of a jet that persisted for approximately 20 consecutive hours. Although this specific jet alone might not be representative for the frequently occurring short lasting low-level jets, it does allow for a more complete analyses of atmospheric conditions during a long-lasting low-level jet.

4.4.1. PRIMARY JET CHARACTERISTICS

The jet characteristics analysed in more detail here are the jet speed and corresponding jet height as well as the absolute jet falloff and the corresponding height at which the minimum wind speed is observed. Results are shown in Figures 4.2 and 4.3. It is found that the majority of low-level jets have a maximum wind speed of 5 to 15 m s⁻¹. Besides, the maximum wind speed is typically observed in the lowest 165 m. The absolute jet falloff is found to be less than 4 m s⁻¹ for the majority of low-level jets, however, for nearly 1800 out of the 2754 jets considered here the height at which the wind minima is detected corresponds to the maximum observation height. The calculated jet falloff for these 1800 low-level jets might thus very well be an underestimation compared to

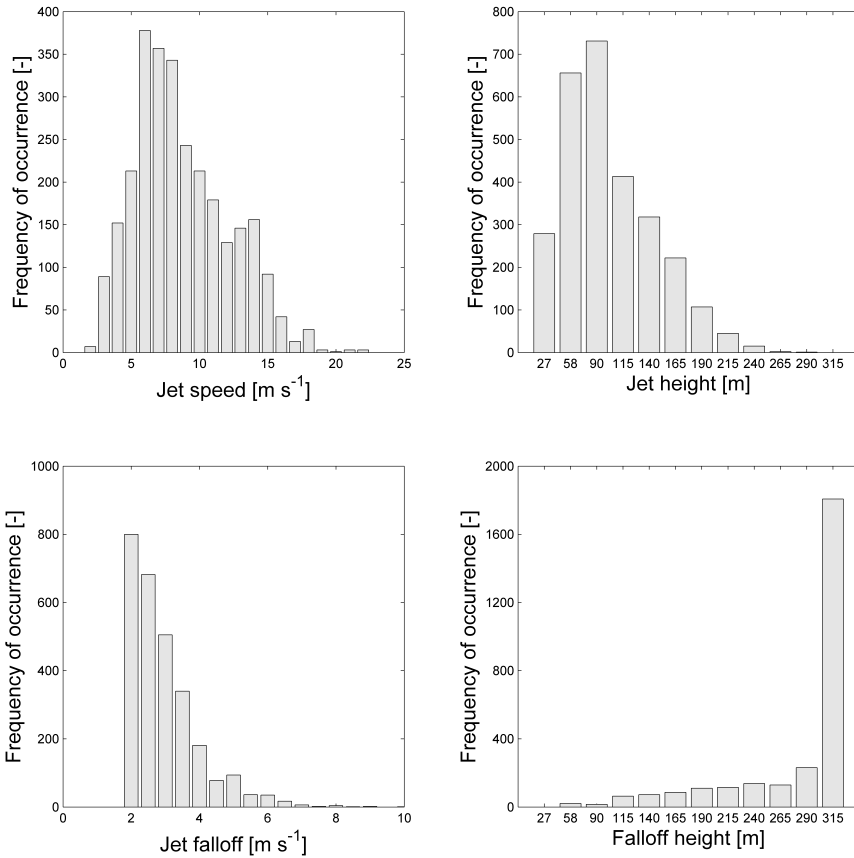


Figure 4.2: Frequency of occurrence of observed jet speed (upper left panel), jet height (upper right), absolute jet falloff (lower left) and jet falloff height (lower right).

the actual falloff, since the wind speed above 315 m height might as well decrease even further. Besides, it is likely that a number of low-level jets that have occurred in the years considered are not detected due to the limited maximum observation height, since the detection criteria are not met at or below 315 m height.

Figure 4.3 shows the jet speed and jet falloff as a function of the jet height. It is found, in agreement with Baas et al. (2009), that stronger low-level jets occur at higher altitudes. Similarly, also the stronger jet falloff is observed for jets that occur at higher altitudes. Since low-level jets that occur close to the surface are typically quite weak, the absolute falloff simply cannot be large. At higher altitudes, the low-level jets typically have higher jet speeds and thus also must have a larger absolute jet falloff due to the relative detection criteria of 20%. For the detected low-level jets above 250 m height results start to differ. There are however very few jets observed with a jet height above 250 m (see Figure 4.2), hence results are statistically uncertain. Besides, also the jet falloff is often

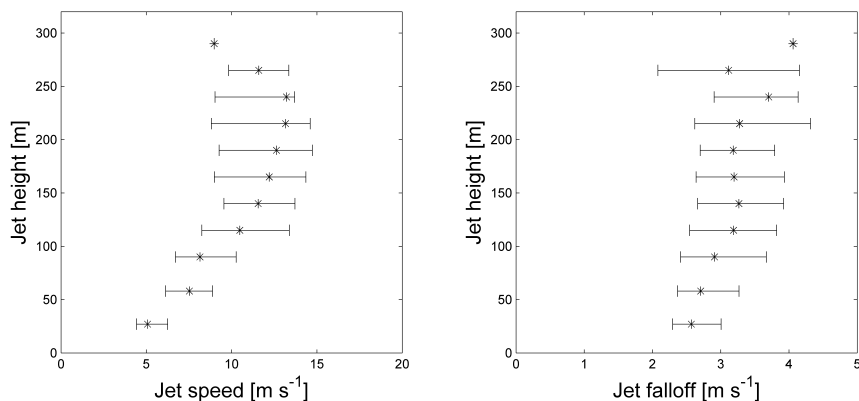


Figure 4.3: Jet speed (left panel) and absolute jet falloff (right panel) as a function of jet height. Marks indicate the median and error bars the 25 and 75 percentiles of observed jet characteristics.

determined at 315 m height, which might cause an underestimation of the jet falloff. It is expected that if observations at higher altitudes would be included, the results above 250 m height would be more in line with those of [Baas et al. \(2009\)](#), and both the jet speed and absolute jet falloff are expected to increase for increasing jet heights.

In scope of offshore wind energy the results obtained here indicate that the jets that do occur offshore may very well be of influence for wind turbine performance. Not only do the jets occur at heights where wind turbines operate (say, below 165 m height). Besides, the jet speed corresponds to wind speeds at which wind turbines operate, since most wind turbines are designed to operate at wind speeds up to 20 to 25 m s^{-1} .

4.4.2. EXPLORATION OF FORMATION CAUSES

The conditions for which low-level jets occur most frequently are studied to find a possible cause of the occurrence of low-level jets offshore. First the time when low-level jets occur is considered. Low-level jets that occur onshore due to the inertial oscillation show a strong diurnal occurrence. As shown in [Figure 4.4](#) this is not the case offshore, although there does appear to be a slight increase in the occurrence of low-level jets at night. One would also not expect a strong diurnal cycle of the occurrence of low-level jets offshore, due to the absence of a diurnal cycle of the surface temperature and thermal induced turbulence.

[Figure 4.4](#) also shows the seasonal variation in the occurrence of low-level jets, where it is found that in spring and summer there are far more low-level jets compared to autumn and winter. This seasonal cycle is distorted by a significant peak in the occurrence of low-level jets in March. A more detailed assessment of the data showed that in March 2015 the LIDAR was unavailable for the majority of time, and nearly all jets (and observations for that matter) in March are obtained in 2012. It appears that in March 2012 there were an unusual high amount of low-level jets, but statistically this does not indicate anything about the seasonal dependence, and it should thus be considered an outlier in

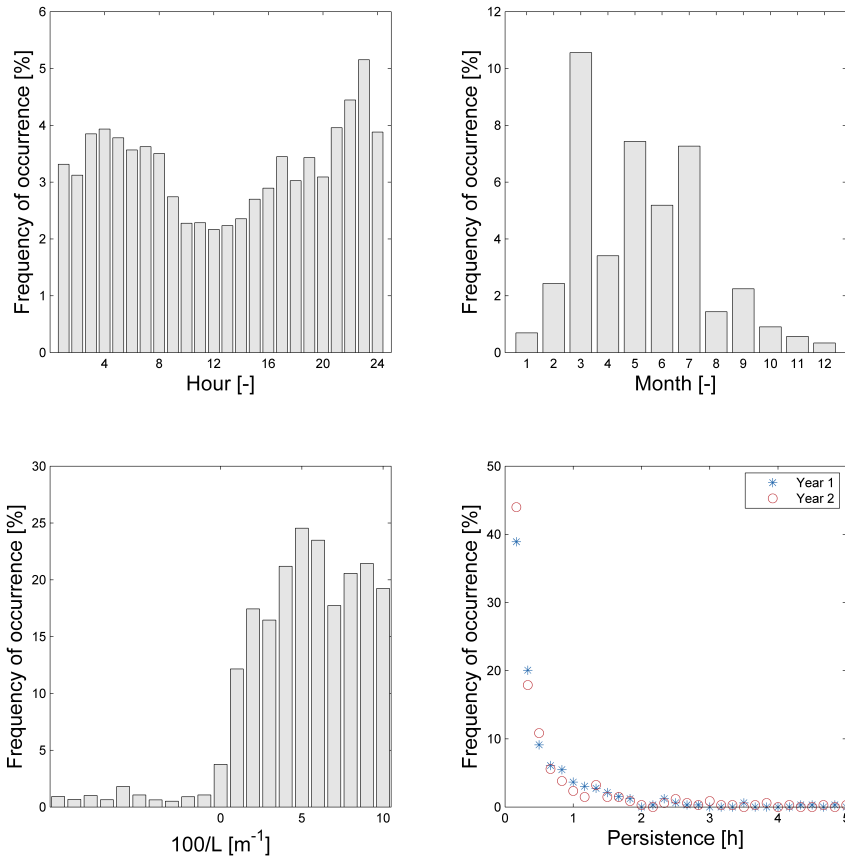


Figure 4.4: Frequency of occurrence of observed low-level jets as a function of the time of the day (upper left panel), month (upper right panel) and stability (lower left panel). The persistence of observed low-level jets for the two years analysed is shown in the lower right panel.

the upper right panel of Figure 4.4. It is known that offshore atmospheric stability has a seasonal cycle (Sathe et al. 2011), compared to the diurnal cycle of stability onshore. Besides, onshore low-level jets that originate due to the inertial oscillation are related to atmospheric stability as well. As such the frequency of occurrence of low-level jets as a function of atmospheric stability is analysed as well.

In the lower left panel of Figure 4.4 the relative occurrence of low-level jets for a given atmospheric stability is shown. It is found that there is a very clear relation between the occurrence of low-level jets and the stability of the atmosphere. There is little chance for the occurrence of low-level jets if the atmosphere is unstable, whereas for stable conditions there is approximately 20-25% chance that low-level jets occur. This might serve as a preliminary indication that the scatter in wind shear found in Chapter 2 is indeed partially related to the occurrence of low-level jets.

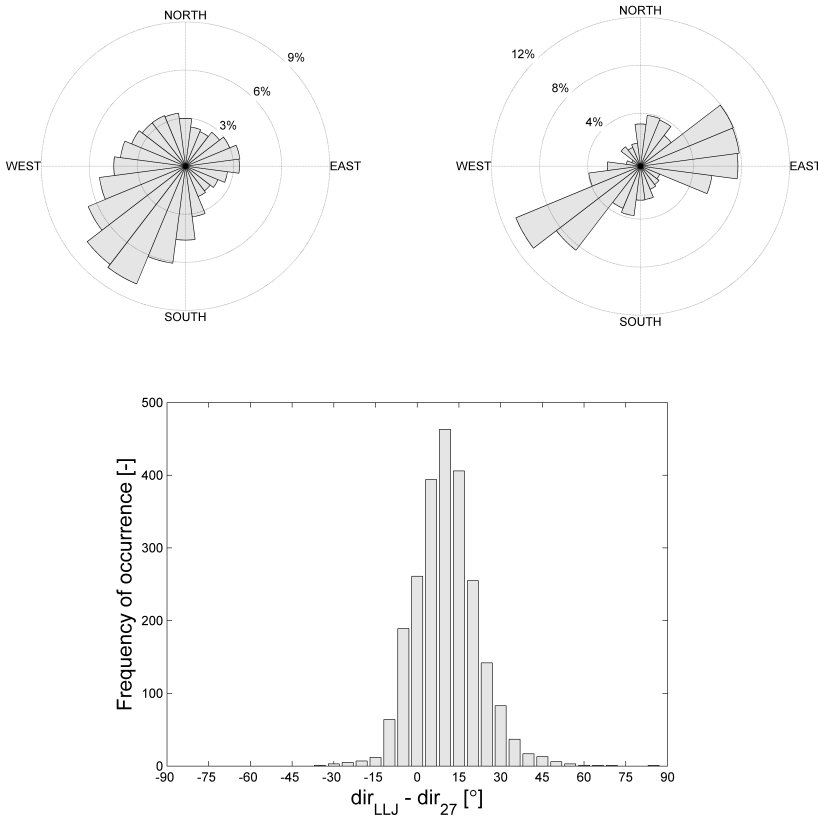


Figure 4.5: Wind rose of the 90 m height observed wind direction (upper left panel) and wind rose of the observed low-level jet wind direction at the jet height (upper right panel). The lower panel shows the difference in wind direction between the jet height and 27 m height.

The lower right panel of Figure 4.4 shows the persistence of low-level jets observed. Here it is clearly found that indeed, as suggested in Section 4.3.2, the far majority of observed low-level jets persist for very short times. Nearly half of the jets is present for a single 10-minute observation, and in fact 85% of all observed low-level jets has a persistence of 1 hour or less. This clearly shows a fundamental difference in the offshore low-level jet compared to the long-lasting nocturnal low-level jet observed onshore.

The occurrence of low-level jets as a function of wind direction is considered to further analyse for which conditions offshore low-level jets occur. Figure 4.5 shows the wind rose based on 90 m height observations in the upper left panel, with prevailing south-westerly winds. For most low-level jets (upper right panel) it is found that the wind direction at the jet height is either south-westerly or easterly. Note that since the wind rose at the jet height is considered, the upper right panel of Figure 4.5 has wind direction ob-

servations at varying altitudes, and one should be careful in comparing results with the 90 m height wind rose. Results are in line with the occurrence of low-level jets onshore at Cabauw, as shown by Baas et al. (2009). Since south-westerly wind directions prevail, it comes to no surprise that many low-level jets have a south-westerly wind direction at the jet height as well. The frequent occurrence of low-level jets for easterly wind directions does not coincide with prevailing wind directions, and it is found (not explicitly shown) that for approximately 20% of all easterly winds a low-level jet wind profile occurs. It is expected that the low-level jets with south-westerly and easterly wind directions have different causes, since the fetch length differs substantially for these directions. For easterly winds the change in surface roughness at the coast can enhance the formation of low-level jets (Smedman et al. 1995). Besides, since low-level jets can extend horizontally for more than 100 km (Stull 1988), it is well possible that jets that occur onshore due to the inertial oscillation are present offshore as well for easterly winds. For south-westerly winds however the fetch length is substantial longer, and inertial oscillations are not expected to occur as frequently as onshore. It is more likely that the south-westerly directed jets are related to synoptic scale baroclinicity and frontal systems, though it is not possible to make any definite conclusions due to the limitations of the available observation data.

Figure 4.5 also shows the wind veer between the jet height and the 27 m height wind (i.e., the wind turns clockwise with height), where jets with a jet height of 27 m height are discarded since one would obviously have a 0 degree wind veer for such conditions. It is found that the wind typically veers from the surface towards the core of the low-level jet, and results are quite similar to those presented by Andreas et al. (2000), in which it is proposed that Ekman dynamics control wind veer, and jet directions are related to the geostrophic wind direction if the wind veers with height. In contrast to Andreas et al. (2000) however, the direction of the core of the jet has strong prevailing origins (either south-west or east) and it is expected that the jets are, at least to an extent, surface controlled.

In scope of the theoretic causes of low-level jets presented in Section 4.2 and the previously discussed results, one cannot solely contribute the observed low-level jets to either the inertial oscillation, baroclinicity or coastal surface changes. Instead, it is likely that a variety of causes contributes to the formation of low-level jets offshore.

4.4.3. CASE STUDY

The far majority of detected low-level jets have a very short persistence as shown in Figure 4.4. In May 2012 however, a low-level jet has been observed that persisted for a consecutive 20 hours, and even just before these 20 hours the wind profile had low-level jet characteristics. Such a long persisting low-level jet provides a unique opportunity to assess atmospheric conditions during a low-level jet in more detail. The low-level jet considered here initiated at the 21th of May 2012 at 23:00 UTC. Weather maps provided by the KNMI (KNMI 2015) indicate that a warm front, preceded by an occlusion front, were present in the morning of the 21th of May 2012, and both frontal systems passed by the observation site well before the low-level jet was observed.

Observed atmospheric conditions are shown in Figures 4.6 and 4.7. For this case study on purpose atmospheric conditions well before the onset of the jet are considered,

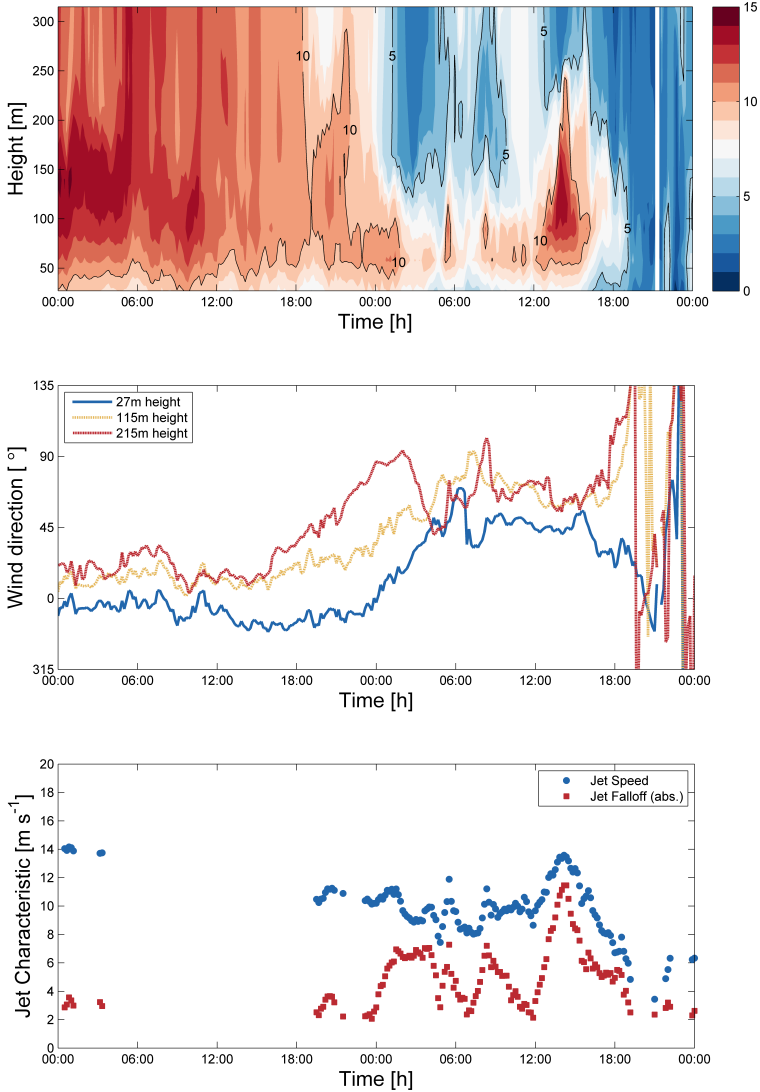


Figure 4.6: Characteristics of the examined 20 hour lasting low-level jet. The individual panels show observations starting at the 21th of May 2012 00:00 UTC until the 23th of May 2012 00:00 UTC. The individual panels show the wind speed as a function of height and time (upper panel), the wind direction at 3 specified heights (middle panel) and the jet speed and absolute jet falloff (lower panel).

to assess in more detail the change in atmospheric conditions well before the jet is actually present. The wind speed is plotted as a function of time and height to visualize the characteristic shape of the low-level jet: starting at approximately 23:00 on the 21th of May, there clearly is a separate high wind speed area close to the surface. For the ma-

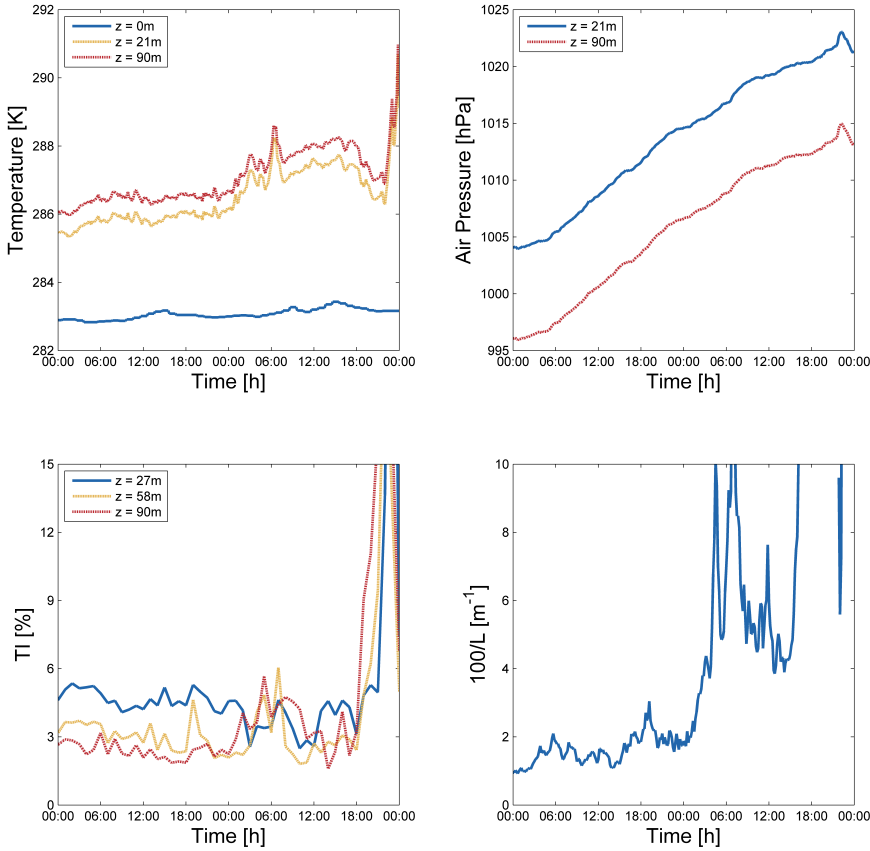


Figure 4.7: Observed air and sea virtual potential temperature (upper left panel), air pressure (upper right panel), hourly average turbulence intensity (lower left panel) and atmospheric stability (lower right panel) for the examined 20 hour lasting low-level jet. The time axes corresponds to the same time steps as shown in Figure 4.6.

For the majority of time the wind speed below 100 m height is more than 4 m s^{-1} stronger than the wind speed at higher altitudes, and maximum wind speeds exceed 10 m s^{-1} frequently. This shows not only that this specific low-level jet is long lasting, but also well developed, and the detection criteria earlier discussed are easily reached for the majority of time. For sake of clarity the lower panel of Figure 4.6 also shows the main jet characteristics (jet height and absolute jet falloff) as a function of time. This not only serves to easily convert wind speeds shown in the upper panel into jet characteristics, but also shows that in fact the jet is present for a longer period of time (i.e., after 19:00 on the 22nd of May). However, since there are several local observations where the detection criteria are not fulfilled, the jet does not, according to the adopted detection criteria, persist for more than 20 hours.

In the middle panel the wind direction observed at three heights is shown. The wind direction observed at higher altitudes is not shown to keep the panel as clear as possible, though it is found that above 215 m height the wind direction is nearly constant with height. For sake of clarity the wind direction is not shown in a similar height-time dependence as wind speed, since the wind direction during the last hours considered here rapidly changes. The change in wind direction in time is discussed first, and afterwards the change in wind direction with height will be discussed. The wind direction varies from north to east typically, and the wind initially slowly veers in time from the onset around 23:00 on the 21th of May until 06:00 on the 22nd of May. At 215 m height the wind veers in time all ready initiates at 15:00 UTC on the 21th of May, well before the low-level jet is first detected. Once the jet starts to devolve (around 16:00 on the 22nd of May), the wind direction close to the surface is backing (turning counter clockwise) from north-east to north, while at higher altitudes the wind veers from north-east to south-east. Afterwards, once the jet is no longer observed, the wind direction rapidly changes at all heights. With respect to the change in wind direction with height, it is found that the wind between 27 and 115 m height, which is often below the jet core, veers with height at all times considered. Between 115 and 215 m height the wind either veers or is constant with height for the majority of time.

Besides wind characteristics, also ambient conditions shown in Figure 4.7 are relevant to understand the formation of the specific low-level jet studied here. It is found that, in line with the analysed weather maps, air pressure is gradually increasing with time. The virtual potential air temperature is primarily slowly increasing in time, while the sea surface temperature is nearly constant in time. The atmosphere is found to be stable at all times considered, and before the low-level jet is detected the atmosphere has a relatively strong stable stratification with $50 \leq L \leq 100$ m. Once the low-level jet is formed, the stable conditions intensify with $0 \leq L \leq 50$ m. The peaks in stability observed between 04:00 and 00:00 on the 22nd of May are related to a combination of changing temperatures (i.e., larger temperature differences result in strong stability) as well as changing wind speeds close to the surface (for similar temperature gradients, the atmosphere is more stable if the wind gradient is low). The exact stability however is not as important as the fact that the atmosphere is continuously stable with $L \leq 100$ m. Similarly, the turbulence intensity in the first 36 hours considered is quite low, typically less than 6% with some short lasting exceptions, until the jet starts to vanish after 18:00 on the 22nd of May. Before the jet is formed the turbulence intensity is found to decrease with height, however once the low-level jet occurs there is variation in the turbulence intensity, especially at 58 and 90 m height. Once the low-level jet has dissipated, the turbulence intensity increases substantially since there is a strong decrease in mean horizontal wind speed (see also the upper panel of Figure 4.6).

With aid of the results presented, let us discuss the potential formation cause of this specific low-level jet. This jet should by no means be considered a representative jet offshore: not only does the jet persist for substantial longer periods of time compared to the majority of offshore low-level jets, the wind direction at the core of the low-level jet also corresponds neither to the prevailing south-westerly nor to the frequently seen easterly wind directions (Figure 4.5). Both the pressure and temperature change in time does not show any signs of the passing of fronts, and since cold fronts are also not shown on the

weather maps fronts are discarded as the possible cause of this specific low-level jet. It is possible this jet is related to decoupling and an inertial oscillation, however, if this would be the case it would be expected that a speed up of the wind speed close to the surface would occur. In the 48 hours considered, there is a speed up present around 14:00 on the 22nd of May with strong winds at 130 m height, however at the onset time of the jet the wind speed close to the surface is not increasing compared to previous hours. Besides, the decoupling at shore typically occurs around sunset when turbulence decays and vertical mixing of momentum by turbulence suddenly ceases, and this rapid decrease in turbulence is not observed in the hours (or even 24 hours) preceding the jet. Instead, it appears that the low-level jet is mainly the result of a sudden rapid decrease in the wind speed above approximately 100 m height. This decrease in wind speed at higher altitudes might be related to baroclinicity, where horizontal temperature gradients result in decreasing geostrophic winds with height as shown by the thermal wind relations. It has to be emphasized that in scope of the available observation data alone one cannot conclude if conditions are indeed baroclinic or not, this would require either a substantially more elaborate measurement campaign with temperature observation at various sites and altitudes across the sea, or one could rely on numerical weather models. The scope of this chapter however is to assess if low-level jets offshore could be relevant for wind energy purposes, hence these additional analyses are beyond the scope of this research.

4.5. CONCLUSIONS

Low-level jets are well studied onshore, and due to the limited amount of observation data offshore there have been few studies that deal with the occurrence of low-level jets far offshore. In this study it is shown that indeed low-level jets also occur frequently offshore, and the characteristics of these low-level jets might very well be of importance for wind turbine performance. Not only do many jets occur at or around typical wind turbine hub heights, the jet speed is also found to coincide with operating wind speeds of wind turbines. This serves as a first argument to assess the influence of low-level jets on wind turbine performance for offshore wind energy purposes.

For the site considered it is found that low-level jets persist for a very short time, in contrast to the onshore low-level jet. It is found that, depending on the detection criteria used, low-level jets occur in about 3 to 10% of all 10-minute mean observations, however, the jets have been observed approximately once or twice every 3 days (just with a short persistence). Besides, it is recognised that the limited maximum observation height considered in this study might result in an underestimation of the amount of low-level jets that occur offshore. Still, the frequent occurrence of low-level jets (which is possible higher than found in this study) serves as a second argument to assess the impact of low-level jets on offshore wind turbine performance.

It has been the aim of this study to also assess the cause of low-level jets offshore, however it is concluded that the available data are too limited for strong conclusions in this respect. It is found that, for the site considered, there is an increased chance for the occurrence of a low-level jet in summer and for stable atmospheric stratification. Besides, the majority of low-level jets occur when the wind direction corresponds to either prevailing or to the shortest fetch wind-directions (i.e., respectively south-westerly or easterly in this study). Combined, there are indications that a variety of physical pro-

cesses result in the development of low-level jets offshore. These processes include synoptic scale baroclinicity and possibly the presence of frontal systems, surface characteristics at the coast and the horizontal extent of low-level jets that are formed onshore due to the inertial oscillation.

A distinct long lasting low-level jet is detected in the dataset, which has been studied in more detail. This specific jet shows indications of inertial oscillations (i.e., strong stable conditions and wind veer close to the surface), but it is not accelerating in time. In contrary, the wind speed at higher altitudes above the jet rapidly diminishes at the onset of the jet. It is expected, in absence of frontal systems, that this jet is caused by baroclinicity, although it is emphasized that this is merely a hypothesis in absence of more elaborate data.

Based on the results presented in this chapter it is recommended not only to further study the occurrence and characteristics of low-level jets in the far offshore environment from a meteorological point of view, but also assess in more detail the impact of low-level jet on wind turbine performance. It is expected that the distinct shear characteristics influence both power production and fatigue loads experienced by a turbine. The impact of low-level jets on wind turbine performance will be further studied in Chapter 6

5

WIND TURBINE FATIGUE LOADS AS A FUNCTION OF ATMOSPHERIC CONDITIONS

*What we usually consider as impossible are simply engineering problems;
There's no law of physics preventing them.*

Michio Kaku

Wind turbines are designed to withstand forces that are exerted on turbine components for at least 20 to 25 years, and the extreme forces that may occur once every 50 years. Part of these forces originate from dynamic atmospheric conditions, which results in non-constant bending moments and subsequent fatigue loads that eventually will lead in component malfunctioning or break down. A correct prescription of wind conditions in wind turbine fatigue load assessment is thus of importance to ensure the design of a sufficiently strong wind turbine without over-dimensioning of individual components.

It is common procedure in fatigue load assessment to separately define a turbulent wind field that is superimposed onto a mean flow that contains wind shear. Turbulence and wind shear are usually defined as a function of hub height wind speed, neglecting atmospheric stability. In this chapter it is assessed if atmospheric conditions can be implemented in fatigue load assessment in a physically correct way. Due to the added complexity of prescribed atmospheric conditions, it is possible that computational expenses increase. As such it will also be explored if it is possible to implement atmospheric conditions in a computational efficient way.

Parts of this chapter are published as: Holtslag, M. C., Bierbooms, W. A. A. M. & van Bussel, G. J. W. (2014), 'Definition of the equivalent atmospheric stability for wind turbine fatigue load assessment', *Journal of Physics: Conference series*, 524 012110 and as: Holtslag, M. C., Bierbooms, W. A. A. M. & van Bussel, G. J. W. (2016), 'Wind turbine fatigue loads as a function of atmospheric conditions offshore', *Wind Energy* doi: 10.1002/we.1959.

5.1. INTRODUCTION

Wind turbine fatigue loads originate from variations in bending moments in time experienced by wind turbine components. In previous decades fatigue loads and the proper setup of load simulations in wind turbine design has been an important research topic since one does not want turbine components to malfunction or even break down, but one also does not want to over-dimension wind turbine components. The most simplified situation where a wind turbine experiences periodic loads is in a stationary atmosphere with wind shear. Similarly, one could also consider non-stationary conditions without wind shear. In either way, although such conditions are not representative to reality, it does provide fundamental insight in the impact of wind shear and turbulence separately on the fatigue loads experienced by specific wind turbine components. To no surprise such simplified conditions have been considered in literature. [Sathe & Bierbooms \(2007\)](#) for example assessed the importance of changing wind profiles as a function of atmospheric stability for stationary conditions, and found fatigue loads experienced by the blade root increase significantly if (very) stable conditions occur frequently at the site of interest. To study the impact of turbulence on wind turbine fatigue loads one first has to carefully consider how to incorporate turbulent conditions in fatigue load simulations. For a given hub height wind speed a range of turbulence intensities might occur, and for each combinations of hub height wind speed and turbulence intensity that is expected to occur at the site of interest one should in principle perform a fatigue load simulation. It is shown in [Hansen & Larsen \(2005\)](#) that if the standard deviation of the wind σ_u is log-normally distributed, one could define an equivalent turbulence (or more precise, an equivalent standard deviation of the wind, σ_{eq}) for which one will obtain the same fatigue load as if one would combine load simulations of all σ_u -values that occur weighted by the log-normal distribution. This conveniently reduces the amount of simulations required to assess the impact of turbulence on fatigue loads experience by a wind turbine. Besides, various studies have shown the non-Gaussianity of velocity increments (i.e. the difference in wind speed between two observations with a given timelag, see for example [Gontier et al. \(2007\)](#), [Morales et al. \(2011\)](#), [Mücke et al. \(2011\)](#)), which is typically neglected when turbulent conditions are prescribed for load simulations.

It would of course be more accurate to perform load simulations in which both wind shear and turbulence conditions are prescribed simultaneously. [Dimitrov et al. \(2014\)](#) used an empirical approach to conditionalise the power law wind shear profile to turbulence intensity, and found that the blade root flapwise loads are most influenced by wind shear. Besides, the effect of wind shear on extreme loads was found to be negligible. [Sathe et al. \(2013\)](#) performed a load simulation in which wind shear and turbulence were a function of atmospheric stability, and found that blade and rotor loads were highest for stable conditions while tower base loads were highest for unstable conditions. Both studies used the standard approach to use a stochastic model to create a 3-dimensional turbulent wind field that can be superimposed onto the mean wind conditions (i.e. wind shear). In contrary, one could also consider a Large-Eddy-Simulation (LES) numerical model to create a wind field. The advantage of a LES model, though being much more time consuming, is that the Navier-Stokes equations are solved and boundary layer characteristics are preserved in the wind field. Clearly such LES based wind fields are much more realistic than purely stochastic based wind fields. In a comparison [Sim et al. \(2010\)](#)

showed that for a neutral atmosphere the characteristics of blade root flapwise loads were similar, while spectral characteristics of tower base loads differed, depending on using either LES-based or stochastic-based inflow conditions. For a stable stratification it was shown with LES-based inflow conditions that blade root flapwise loads increase, and tower base loads decrease, when atmospheric conditions change from neutral to stable (Sim et al. 2009).

The use of LES models to define inflow conditions for wind turbine load simulations is promising but not considered in this thesis. Instead the importance of atmospheric stability on fatigue loads of specific wind turbine components is assessed in a more conventional way with stochastic wind fields. It is recognised however that in most studies where atmospheric stability is considered, stability is categorized into distinct classes. Examples found in literature show differences in the amount of stability classes adopted, for example Hansen et al. (2014) considered 3 stability classes, van Wijk et al. (1990) considered 5 stability classes and Peña et al. (2010a) considered 7 stability classes. A recurring problem is that any physical based argument for these exact boundaries of the adopted stability classes is missing. Atmospheric stability in terms of the Obukhov length L (Monin & Obukhov 1954) is in fact a continuous parameter which can range from $-\infty$ to $+\infty$, and in various studies (for example Sathe et al. (2013)) extreme stable ($0 < L < 10$) and extreme unstable ($-50 < L < 0$) conditions are neglected. As such one might question if adopting a specific distinct classification system for atmospheric stability is beneficial for wind energy purposes, besides giving general insight in the performance of a wind turbine for stable, neutral and unstable atmospheric conditions.

Although there is a fundamental flaw in how guidelines approach the description of the atmosphere, one has to acknowledge the practicality of reducing complexity when defining atmospheric conditions. In scope of the number of load cases that have to be addressed in wind turbine design (IEC 2005), adding more complexity (and thereby probably adding more required simulations) for each load case can quickly result in a significant computational burden. In terms of the classification system for atmospheric stability discussed previously, it can easily be shown that incorporating stability with 7 classes causes an increase in computation demand by a factor 7. Adding such a computational burden to industry standards can only be justified if there is a significant improvement in the accuracy of lifetime fatigue load estimations compared to simplifying the atmosphere.

In this chapter the dependence of fatigue loads of three turbine components (blade root, rotor and tower base) are considered for two directions per component (i.e. flapwise and edgewise or for-aft and side-side). Before load simulations are carried out a methodology is proposed how to prescribe atmospheric conditions based on relations presented in Chapter 2. Next, the impact of atmospheric stability on fatigue loads is determined. A comparison with guidelines is carried out to assess if following guidelines results in either an underestimation or overestimation of lifetime fatigue loads.

5.2. SIMULATION CONDITIONS

Due to the nature of this research simulation aspects are elaborated on before specific atmospheric conditions applied in the simulations are discussed in detail in Section 5.3. Wind turbine fatigue loads at three specific locations of the wind turbine are assessed.

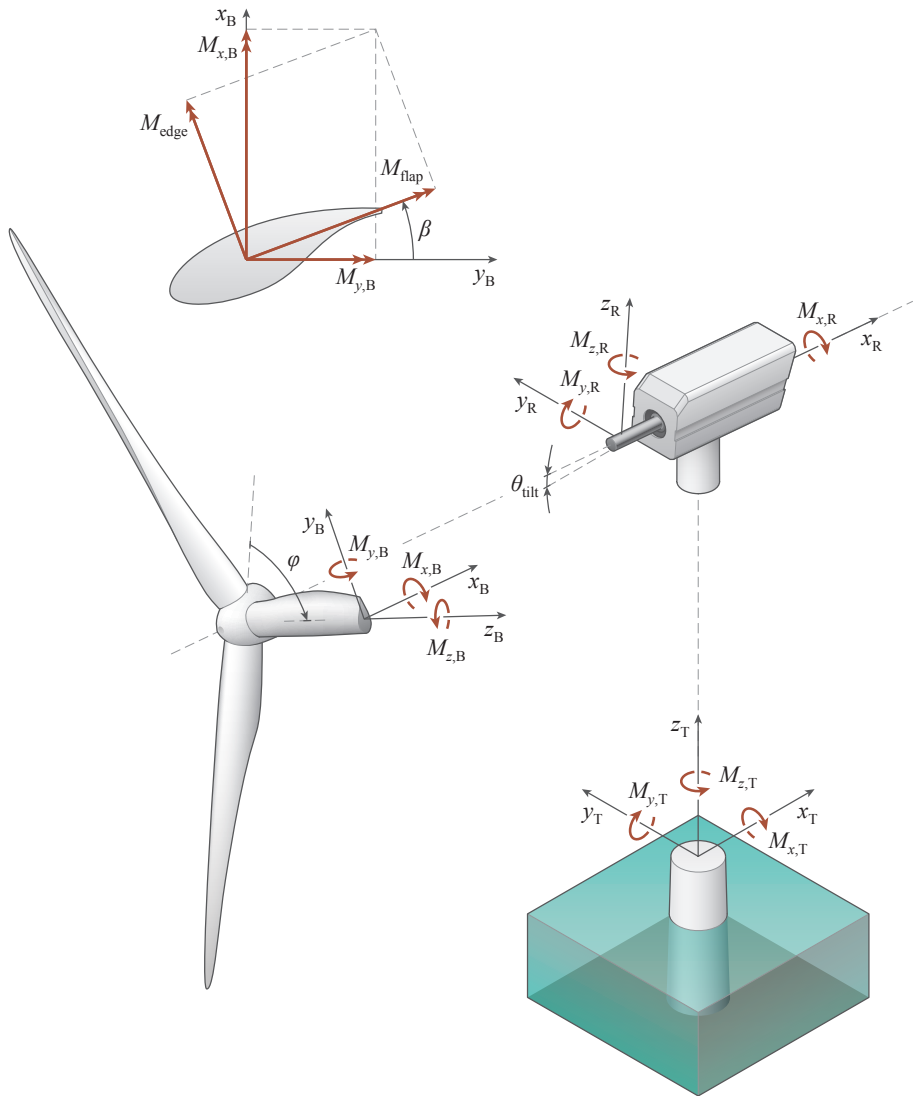


Figure 5.1: Coordinate system used in this research for the blades (left, subscript B), rotor (upper right, subscript R) and tower (lower right, subscript T). The bending moments around all three axes are shown as well.

The corresponding coordinate systems are shown in Figure 5.1, where for the blade root and rotor a rotating reference frame is considered. The blade root flapwise and edgewise loads correspond to respectively the bending moments $M_{y,B}$ and $M_{x,B}$ assuming the blades are not pitched. Once the blades are pitched both $M_{y,B}$ and $M_{x,B}$ contribute to the flapwise as well as the edgewise loads, and the relative importance of each bending moment depends on the pitch angle. The rotor out of plane loads correspond to $M_{y,R}$ and $M_{z,R}$, depending on the position of the coordinate system (i.e., rotor azimuth

Table 5.1: Overview of primary characteristics of the NREL 5MW machine.

Rated power	5.0 MW
Number of blades	3
Rotor diameter	126 m
Hub height	90 m
Cut-in wind speed	3 m s ⁻¹
Rated Wind speed	11.6 m s ⁻¹
Cut-Out wind speed	25 m s ⁻¹
Control	Variable speed, collective pitch

angle), while the rotor in plane loads correspond to $M_{x,R}$. For the tower loads a simple fixed coordinate system is used, and the fore-aft loads thus only correspond to $M_{y,T}$, and the side-side loads are caused by $M_{x,T}$.

The simulations are carried out for the 5 MW NREL reference turbine frequently used in research (Jonkman et al. 2009), with main characteristics being summarized in Table 5.1. Although waves cause fatigue as well, the scope of this chapter is purely on the influence of offshore atmospheric conditions on wind turbine fatigue loads. Hydrodynamic loads are thus not included in any of the simulations to keep the results as clear as possible. As such not the complete IEC standard for offshore conditions is considered, but only the sections that describe atmospheric conditions. The wind turbine tower below sea level is modelled as a monopile structure with constant diameter and the water depth equals 20 m. All simulations are carried out with the wind turbine design software Bladed version 3.85, and fatigue load simulations are carried out for typical operating wind speeds ranging from 4 to 25 m s⁻¹ with a 1 m s⁻¹ interval. To reduce problems with spin-up during which the wind turbine has to adjust to the ambient conditions, the simulations are run for 630 seconds from which the last 600 seconds are used for the load calculations. Besides, simulations are carried out in such a way that they are representative for regular operating conditions similar to IEC design load case 1.2 without sub-optimal turbine functioning (yaw misalignment, shut down or faults) or non-standard atmospheric conditions (extreme gusts or extreme shear). At all times simulations are carried out for a given prescribed mean hub height wind speed \bar{U}_h , and for each hub height wind speed 6 turbulence seeds are considered to reduce statistical uncertainty in agreement with IEC standards IEC (2005).

Lifetime fatigue loads are considered in terms of the lifetime equivalent load, which can be calculated as

$$F_{EQ-TOT} = \int_{\bar{U}_{in}}^{\bar{U}_{out}} \int_{-\infty}^{\infty} F_{EQ}(\bar{U}_h, \zeta_h) P(\bar{U}_h, \zeta_h) d\zeta_h d\bar{U}_h \quad (5.1)$$

Here F_{EQ-TOT} is the total lifetime equivalent load, F_{EQ} is the equivalent load for a given hub height wind speed \bar{U}_h and stability ζ_h , and $P(\bar{U}_h, \zeta_h)$ is the joint probability of hub height wind speed and stability. The stability parameter ζ_h equals z_h/L where z_h is the hub height of the wind turbine and L is the Obukhov length defined in Chapter 2. The

Table 5.2: Overview of case specifications for the fatigue load assessment. The number of simulations corresponds to the amount of simulations required for each wind turbine component as elaborated upon in Section 5.3.

Case number	Case 1	Case 2	Case 3
Atmosphere	IEC standards	stability dependent	stability dependent
Wind speed bins	22	22	22
Stability classes	-	7	34
Turbulence Seeds	6	6	6
Nr. of Simulations	132	924	4488

equivalent load F_{EQ} is calculated similar as shown in [Veldkamp \(2006\)](#)

$$F_{EQ} = \left(\frac{\sum F_i^m n_i}{n_{EQ}} \right)^{1/m} \quad (5.2)$$

with n_{EQ} is the number of equivalent cycles, taken as 10^7 , F_i and n_i are the fatigue load ranges and fatigue cycles and m is the Wöhler exponent. The fatigue load and fatigue cycles are obtained from a rainflow counting algorithm in Bladed. Since the 5 MW NREL turbine is a hypothetical reference turbine, there are no S-N curves available to obtain m for specific turbine components. As such [Veldkamp \(2006\)](#) is followed and m is assumed to be respectively 4, 8 and 12 for the tower, the hub and the blades. This corresponds to welded steel for the tower, cast iron for the hub and glass fibre for the blades.

To assess the impact of including a physical based representation of the atmosphere in wind turbine design, three separate cases are defined for which all load simulations are carried out (see Table 5.2 for a summary). These cases differ only in terms of prescribed environmental atmospheric conditions while turbine characteristics are kept constant. The first simulation case follows the IEC standards version 61400-3 for off-shore conditions as closely as possible. A thorough explanation of the exact relations used is presented in Section 5.3. With the considered wind speeds and turbulence seeds, one needs to carry out 132 simulations. The second case follows the traditional way of assessing the impact of atmospheric stability on wind turbine performance with arbitrary distinct stability classes. The classification system of [Peña et al. \(2010b\)](#) with seven stability classes is adopted, and for each stability class one characteristic stability condition is considered for which simulations are carried out. As such, the second case requires seven times more simulations (924). The stability class boundaries and the representative stability for each class is shown in Table 5.3, where the representative stability L for each stability class equals the mean of the corresponding class boundaries. The third case aims to approach the distribution of atmospheric stability as closely as possible. In practice it is an extension of case two, but with a significant increase in the amount of stability classes. To keep the computational time required for all simulations manageable, the continuous distribution of stability is approximated by 34 separate classes, which increases the amount of required simulations to 4488.

The observation data used in this chapter is the same as used in Chapter 2. It is found that the majority of observations have a stability within the range $L \leq -9$ and $L \geq 18$ (this covers at least 90% of all observations for a given hub height wind speed). As such $L = -9$

Table 5.3: Stability classification for simulation case 2, taken from Peña et al. (2010a). The stability class abbreviations correspond to those used in Chapter 3 Table 3.1.

Stability class	Stability regime (L)	Stability regime (ζ_h)	Characteristic L
VU	$-100 \leq L < -50$	$-1.8 < \zeta_h \leq -0.9$	$L = -75$
U	$-200 \leq L < -100$	$-0.9 < \zeta_h \leq -0.45$	$L = -150$
NNU	$-500 \leq L < -200$	$-0.45 < \zeta_h \leq -0.18$	$L = -350$
N	$\ L\ \geq 500$	$-0.18 < \zeta_h \leq 0.18$	$L = \infty$
NNS	$200 \leq L < 500$	$0.18 < \zeta_h \leq 0.45$	$L = 350$
S	$50 \leq L < 200$	$0.45 < \zeta_h \leq 1.8$	$L = 125$
VS	$10 \leq L < 50$	$1.8 < \zeta_h \leq 9$	$L = 30$

and $L = 18$ are in this research considered the most unstable and stable conditions in the simulations. As will be shown later, conditions within the range $L \leq -18$ and $L \geq 30$ cause by far most of the fatigue loads, thus those conditions that are not included specifically should not influence the outcome of the results significantly. The 34 classes are defined in terms of ζ_h , ranging from -10 to 5, with a stability class size of 1, and increased density of classes between $-1 \leq \zeta_h \leq 1$ where a class size of 0.1 is adopted. This increased density is adopted since for near neutral conditions atmospheric conditions change rapidly with only a slight change in atmospheric stability.

5

5.3. PRESCRIBING ATMOSPHERIC CONDITIONS

The atmospheric conditions that are of most importance for the lifetime fatigue loads for non-extreme conditions are wind shear and turbulence, where turbulence is characterized in terms of the turbulence intensity, the turbulence spectrum and the turbulence coherence. The atmosphere is defined following the IEC standards for simulations of case 1, and based on the framework defined in Chapter 2 for simulations of case 2 and 3. For case 1 wind shear and turbulence intensities are defined according to IEC (2009), and the turbulence spectra according to IEC (2005). The observation data shown in the following sections frequently include observations at 85 m height, which differs from the hub height of the 5 MW NREL wind turbine. Since only at 85 m height sonic anemometers are installed in the meteorological mast this is the only height at which three dimensional turbulence characteristics are observed (i.e. including the lateral and vertical characteristics).

5.3.1. WIND SHEAR

For wind shear it is common procedure to use either a power law (used for case 1) or a logarithmic shear profile (used for case 2 and 3), which can be written as

$$\frac{\overline{U}(z)}{\overline{U}_h} = \left[\frac{z}{z_h} \right]^\alpha \quad (5.3)$$

$$\frac{\overline{U}(z)}{\overline{U}_h} = \frac{\ln[z/z_0] - \Psi[\zeta]}{\ln[z_h/z_0] - \Psi[\zeta_h]} \quad (5.4)$$

to define the wind speed at a given height as a function of a reference wind speed. Here z_h is a reference height (here the hub height), α is the power of the power law (here 0.14) and z_0 and the Ψ -functions validated in Chapter 2 are used (Equations 2.11 and 2.12).

5.3.2. TURBULENCE INTENSITY

The turbulence intensity is determined at the hub height. For the turbulence intensity, the IEC offshore standards propose that the standard deviation of the wind σ_x is a function of the surface roughness and wind speed, and the lateral and vertical turbulence intensity equal respectively 0.7 and 0.5 times the longitudinal turbulence intensity. The turbulence intensity proposed by the IEC corresponds approximately to the 90% percentile of σ_x grouped to wind speed (Türk & Emeis 2010). This corresponds to the following equations

$$TI_x = \frac{1}{\ln(z_h/z_0)} + 1.84 \frac{I_{ref}}{\bar{U}_h} \quad (5.5)$$

$$TI_y = 0.7 TI_x \quad (5.6)$$

$$TI_z = 0.5 TI_x \quad (5.7)$$

Here I_{ref} is the reference turbulence intensity, which equals the mean turbulence intensity observed at a wind speed of 15 m s^{-1} (here found to be 5.66% for the site considered) and the subscripts x , y and z denote the longitudinal, lateral and vertical direction.

For the simulation cases that incorporate atmospheric stability, the concept of the equivalent turbulence (Veldkamp 2006) is considered. Application of this concept is only valid if the standard deviation of the wind is log-normally distributed for a given subset of observations considered. Hansen & Larsen (2005) show that for a given hub height wind speed σ_x is approximately log-normally distributed, and as such one can use the equivalent turbulence in fatigue load simulations if atmospheric conditions are grouped based on the mean observed hub height wind speed. In this research however fatigue simulations are executed as a function of hub height wind speed and atmospheric stability, hence it is questioned if σ_x for a given combination of \bar{U}_h and L is also log-normally distributed.

One can easily assess if a variable is normal distributed with a normal plot, where an ordered variable follows a straight line if the variable is normal distributed. Since σ_x is expected to follow a log-normal distribution, $\ln(\sigma_x)$ is expected to be normal distributed. The stability classification system used for case 2 is considered to group σ_x for similar wind speeds and stability to maintain sufficient observations for each group of observations. The normal distribution of $\ln(\sigma_x)$ is assessed with a normal plot. The assessment is shown for four specific wind speeds (6, 10, 14 and 18 m s^{-1}), and results are shown in Figure 5.2. It can be seen that for most wind speeds and stability classes considered, $\ln(\sigma_x)$ more or less follows a straight line on the normal plot thus σ_x is approximately log-normally distributed. Exceptions can be seen primarily for stable conditions where curvatures are found. One might argue that it is therefore inappropriate to consider an equivalent turbulence for stable conditions, however as will be shown stable conditions do not prevail for the site considered. Besides, as was shown in Chapter 2 theoretic relations used to describe wind shear, second order moments and turbulence spectra are

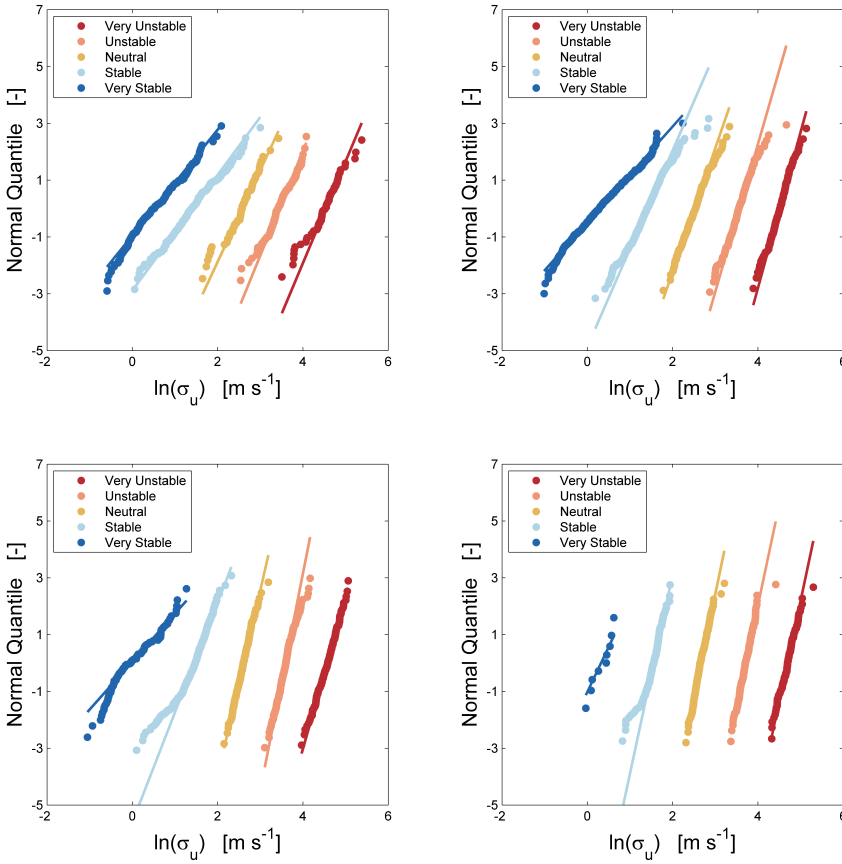


Figure 5.2: Normal distribution of $\ln(\sigma_x)$ grouped on stability (see legend) and wind speed for a wind speed of 6, 10, 14 and 18 m s^{-1} for respectively the upper left, upper right, lower left and lower right panel. The markers and lines are shifted horizontally to achieve better spacing for visibility reasons.

simplified compared to the significant scatter observed. The simplification to assume a log-normal distribution of σ_x is therefore assumed to be acceptable in consideration of representing the stable atmospheric conditions with Monin-Obukhov theory. Combined it is worthy to recognise that the simulated fatigue loads for stable conditions will be uncertain and results might deviate from reality due to the simplified representation of the stable atmosphere.

The equivalent turbulence can be calculated as follows. For a log-normally distributed variable x , the log-normal distribution parameters M and S are a function of the mean μ

and standard deviation σ of x as

$$F(x) = \Phi\left(\frac{\ln(x) - M}{S}\right) \quad (5.8)$$

$$M = \ln\left(\frac{\mu^2}{\sqrt{\mu^2 + \sigma^2}}\right) \quad (5.9)$$

$$S = \sqrt{\ln\left(\frac{\sigma^2}{\mu^2} + 1\right)} \quad (5.10)$$

Here Φ is the cumulative distribution function of the standard normal distribution and F is the cumulative distribution function of x . Hence if one knows σ_x is log-normally distributed, and the mean and standard deviation of σ_x are known, the distribution parameters M and S are easily calculated. The equivalent turbulence is a function of these distribution parameters (Veldkamp 2006)

$$\sigma_{EQ} = \exp(M + 0.5mS^2) \quad (5.11)$$

This can be written with aid of the shown definitions of M and S as

$$\sigma_{EQ} = \mu_\sigma \left(1 + \frac{\sigma_\sigma^2}{\mu_\sigma^2}\right)^{0.5m-0.5} \quad (5.12)$$

In Chapter 2 μ_σ (i.e. the mean of the standard deviation of the wind) has been defined with Equations 2.38 and 2.39. Here it is explored if σ_σ (i.e. the standard deviation of the standard deviation of the wind) has a similar dependence on stability as μ_σ . Both μ_σ and σ_σ are shown in Figure 5.3, where the non-dimensional standard deviation of the longitudinal wind component is shown as a function of $85/L$, where 85 coincides with the height of the observations of σ_u . Results for the lateral and vertical wind component are in fact found to be similar. It can be seen that in general both the mean and standard deviation of σ_x have a similar dependence on stability for all unstable conditions, and for stable conditions for $85/L \leq 1$. It is therefore assumed that the following relation holds between the mean and standard deviation of σ_x

$$\sigma_\sigma = \epsilon \mu_\sigma \quad (5.13)$$

Where ϵ is a constant of approximately 0.2 to 0.25 (found to be 0.23, 0.25 and 0.20 for the longitudinal, lateral and vertical wind components). This conveniently simplifies Equation 5.12 as

$$\sigma_{EQ} = \mu_\sigma (1 + \epsilon^2)^{0.5m-0.5} \quad (5.14)$$

Do note that for strong stable conditions σ_{EQ} is underestimated based on Figure 5.3. Incorporating Equations 2.38 and 2.39 and the diabatic surface layer wind profile provides an equation for the equivalent turbulence intensity

$$TI_x(\zeta_h < 0) = \frac{A_x \kappa (1 - B_x \zeta_h)^{1/3}}{\ln(z_h/z_0) - \Psi[\zeta_h]} [\epsilon_x^2 + 1]^{0.5m-0.5} \quad (5.15)$$

$$TI_x(\zeta_h > 0) = \frac{A_x \kappa (1 + C_x \zeta_h)^{-1/2}}{\ln(z_h/z_0) - \Psi[\zeta_h]} [\epsilon_x^2 + 1]^{0.5m-0.5} \quad (5.16)$$

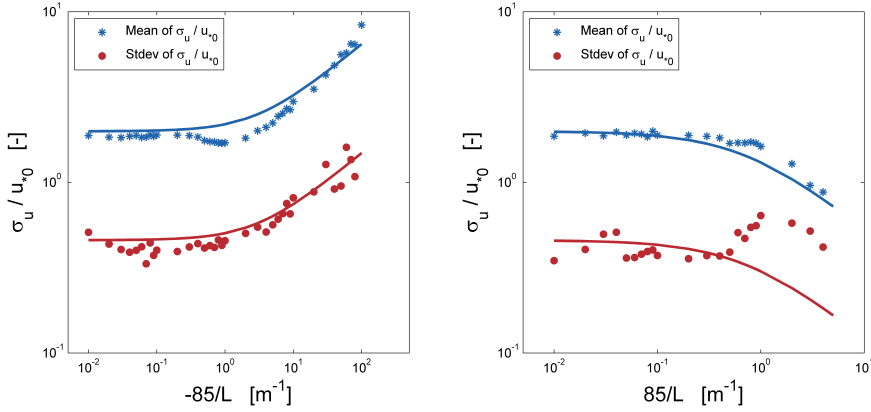


Figure 5.3: Mean and standard deviation of the non-dimensional second order moments of the longitudinal wind component for unstable (left) and stable (right) conditions.

which is used to prescribe the turbulence intensity for simulation cases 2 and 3. For the turbulence intensity of the lateral and vertical wind component only the constants A_x , B_x , C_x and ϵ_x change, the remainder of Equations 5.15 and 5.16 is kept constant. With Equations 5.15 and 5.16 it is assumed that the turbulence intensity is constant with height (i.e. a function of hub height, but constant across the rotor disc), which in practice is not true, however the simulation environment used does not allow for prescribing the turbulence intensity as a function of height. Also, because the turbulence intensity is a function of m , and m differs for the three turbine components considered, simulations cases 2 and 3 mentioned in Table 5.2 require additional simulations for each wind turbine component considered. As such, whereas the 132 simulations of case 1 suffice for all three wind turbine components, for case 2 and 3 respectively 2772 and 13464 simulations are needed to cover the three wind components.

5.3.3. TURBULENCE SPECTRUM

For the turbulence spectrum the three dimensional Kaimal spectrum (Kaimal et al. 1972) is considered, which is one of the suggested spectra of the IEC standards. The general form for the spectrum is given as (IEC 2005)

$$\frac{f S_x(f)}{\sigma_x^2} = \frac{4f L_x / \bar{U}_h}{\left[1 + 6f L_x / \bar{U}_h\right]^{5/3}} \quad (5.17)$$

where L_x is a turbulent length scale. The IEC standards propose that the turbulent length scale above 60 m height equals respectively 340.2, 113.4 and 27.7 m for the longitudinal, lateral and vertical direction. This notation differs from the notation used in Chapter 2, in which the scaling frequency f_0 is considered. After rewriting to confirm to the notation

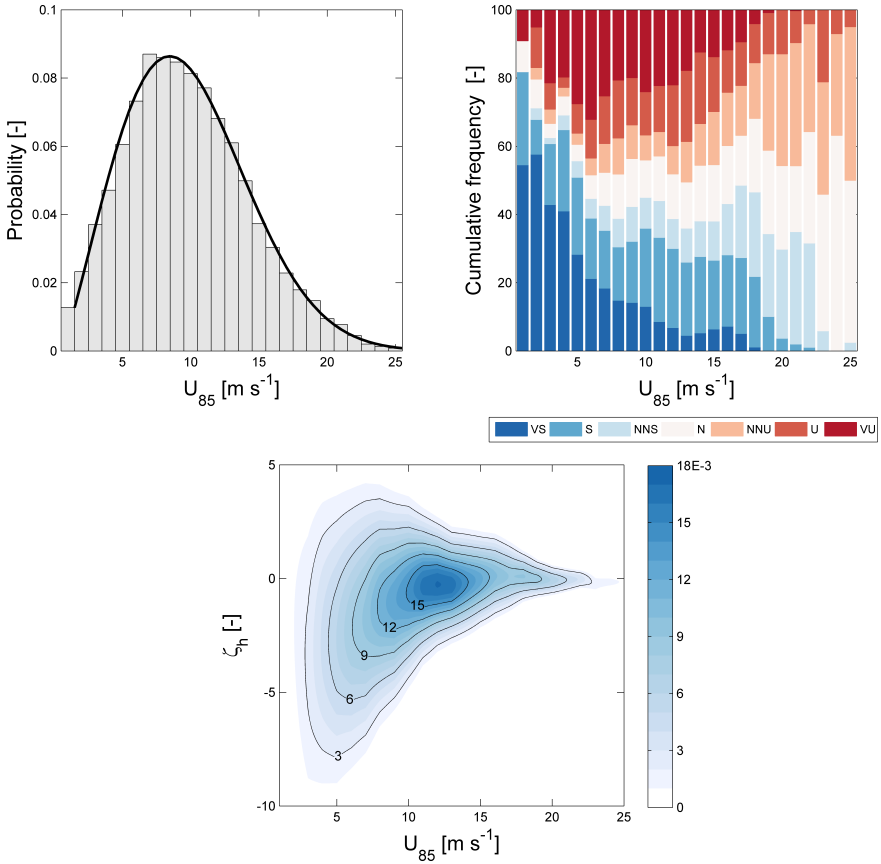


Figure 5.4: Weibull distribution (upper left panel), stability class distribution (upper right panel) and the joint probability distribution of wind speed and stability (lower panel).

of the Kaimal spectrum as shown in Equation 5.17, L_x is a function of stability as

$$L_x(L < 0) = 0.041 \frac{z_h}{D_x [1 - E_x \zeta_h]^{-1/2}} \quad (5.18)$$

$$L_x(L > 0) = 0.041 \frac{z_h}{D_x + F_x \zeta_h} \quad (5.19)$$

where the constants D_x , E_x and F_x are found in Chapter 2.

5.3.4. PROBABILITY DISTRIBUTIONS

As shown in Equation 5.1, the lifetime fatigue loads depend on the joint probability distribution of wind speed and stability, which is given by

$$P(\bar{U}_h, \zeta_h) = P(\bar{U}_h) P(\zeta_h | \bar{U}_h) \quad (5.20)$$

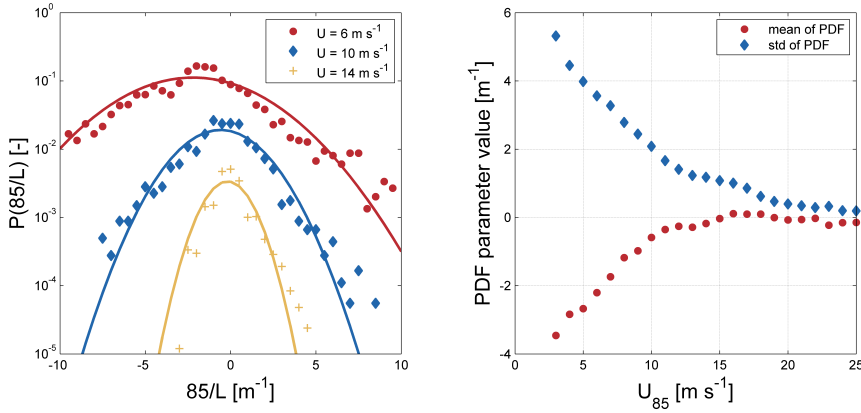


Figure 5.5: Probability density function of stability ($85/L$) for specific wind speeds (left panel) and the distribution parameters as a function of wind speed (right panel). The distributions on the left side for 10 and 14 m s^{-1} are shifted vertically by a factor 10 and 100 respectively for clarity reasons.

where $P(\bar{U}_h)$ is the distribution of the hub height wind speed and $P(\zeta_h|\bar{U}_h)$ is the distribution of stability conditionalized by hub height wind speed. If stability is neglected as is done for case 1, one does not consider the probability distribution of stability and hence the distribution of $P(\bar{U}_h)$ suffices. Based on the observation data presented in Chapter 2 it is found that the Weibull distribution at a height of 85 m has a scale parameter of 10.52 and a shape parameter of 2.18. For case 2 the joint probability distribution equals the multiplication of the probability distribution of the wind speed and the relative occurrence of each stability class. Figure 5.4 shows in the upper panels the distribution of the wind speed and the occurrence of stability conditions, which are used to determine $P(\bar{U}_h, \zeta_h)$ for case 1 and 2. For case 3 the joint probability distribution of stability equals the multiplication of the previously determined Weibull distribution $P(\bar{U}_h)$ and the probability distribution of stability conditionalized by wind speed $P(\zeta_h|\bar{U}_h)$ which has to be determined from observations. In recent work Kelly & Gryning (2010) modelled the distribution of L by separating the distribution into two tails, one for stable conditions and one for unstable conditions with distinct different characteristics. By definition their model has a peak in the PDF of L at neutral conditions. Although this is appropriate for various observation datasets (as shown in their validation), it is recognised that in this study the conditionalized distribution of L does not necessarily have a maximum in the distribution at neutral stratification. This is also found from observation data (see Figure 5.5), where the probability distributions shown in the left panel indeed do not necessarily have a maximum for $85/L = 0$. The observed distributions do follow a Gaussian distribution reasonably well, although for moderate to high wind speeds there are insufficient observations to properly assess the behaviour of the stability distribution for moderate to strong stable and unstable conditions. Despite this uncertainty it is assumed $P(\zeta_h|\bar{U}_h)$ is Gaussian distributed for all wind speeds, and the distribution parameters as a function of wind speed are shown in the right panel of Figure 5.5. It is found, as expected, that the

mean stability converges to neutral conditions for moderate to high wind speeds. Besides, for low wind speeds the variance of stability increases, and moderate to strong stable and unstable conditions occur more frequently for low wind speeds. Multiplication of the Weibull distribution with the modelled Gaussian distribution of $P(\zeta_h|\bar{v})$ results in the required joint probability distribution of stability and wind speed for case 3, shown in the lower panel of Figure 5.4.

Comparing the stability class distribution and the joint probability distribution of stability and wind speed, note that adopting the stability classification of Table 5.3 results in the classification of many stable and very stable conditions for wind speeds ranging from 1 to 10 m s⁻¹. In contrary, the joint probability distribution shows there are predominantly unstable conditions for these wind speeds. This difference is caused by the choice of class boundaries in Table 5.3, and conditions with $-50 \leq L \leq 0$ are neglected in the classification. It can be seen that such conditions (which equal $\zeta_h \leq -1.8$) in fact occur very frequently. It is expected that neglecting these unstable conditions in the classification system of simulation case 2 will have a significant impact on the simulated lifetime fatigue loads.

5.4. FATIGUE LOAD ASSESSMENT

To understand the importance of the dynamic coupling of wind shear and turbulence for fatigue load assessment, first the dependence of the fatigue load of various turbine parts on atmospheric stability is assessed. As will be shown in Section 5.4.1, the fatigue load of the various turbine components depend differently on atmospheric stability since the sensitivity of these components to respectively wind shear and turbulence differs. Next the bending moment spectra of the specific turbine components considered in this study are shown in Section 5.4.2 to assess if the variation of the bending moments occur primarily at multiples of the rotational frequency, at eigenfrequencies of the turbine components or at other frequencies. Since fatigue is caused by varying loads, the spectra can be used to reason if wind shear or turbulence is expected to cause the majority of turbine fatigue loads (although clearly the spectra cannot be substituted for fatigue loads directly, it serves as an indication). In Section 5.4.3 lifetime fatigue loads are compared for the three cases specified earlier, and a methodology is proposed how to incorporate stability in fatigue load assessment in a computational efficient way.

5.4.1. SENSITIVITY OF FATIGUE LOADS TO ATMOSPHERIC STABILITY

The results of case 3, including the continuous distribution of stability, are used for the sensitivity analyses to consider as much stability conditions as possible. Only the equivalent loads of the blade root flapwise, the rotor out of plane and tower base fore-aft bending moment are shown in detail since the remaining loads are predominantly caused by gravitational forces and turbulence. The coupling between wind shear and turbulence is thus far less relevant for the loads not shown in detail in this section. Figure 5.6 shows in the left panels the equivalent load as a function of hub height wind speed and atmospheric stability for the blade root, the rotor and the tower base. The right panels show the equivalent load multiplied with the joint probability distribution of hub height wind speed and atmospheric stability, indicating which combination of hub height wind

speed and atmospheric stability contributes most to the lifetime fatigue loads of the specific wind turbine components.

For the blade root flapwise equivalent load it is found that the highest loads occur for a combination of very strong wind speeds and strong unstable conditions. There is a clear tendency that for a given atmospheric stability the blade root equivalent load increases with increasing wind speed. The effect of atmospheric stability however is less straight forward, and for a given hub height wind speed there is typically a minimum in the blade root equivalent load for near neutral conditions. When the atmosphere changes from neutral to unstable conditions the equivalent loads increase. For a changing atmosphere from neutral to stable conditions a similar result is found (see mainly for the contour of 2600 kNm), though for low wind speeds the increase in equivalent load is limited. Note as well that for very strong stable conditions (where $\zeta_h > 3$) equivalent loads actually decrease with increasing stability (this is best seen for $\bar{U}_h > 20$ m s⁻¹). The included contour line of 2600 kNm also shows that the blade root equivalent loads obtained for strong unstable conditions (with $\zeta_h = -10$) and $\bar{U}_h = 12$ m s⁻¹ are equal to the equivalent loads experienced for stable conditions (with $\zeta_h = 5$) and a hub height wind speed of 21 m s⁻¹. This serves as an indication of the substantial influence of atmospheric stability on the equivalent loads experienced by the blade root, at least in flapwise direction. After multiplication of the equivalent load distribution with the joint probability distribution of wind speed and atmospheric stability it is found that those situations that result in the highest equivalent load hardly contribute to the lifetime equivalent loads experience at the blade root since such conditions do not occur frequently. Instead, those conditions that occur frequently (near neutral conditions with $10 < \bar{U}_h < 15$) contribute most to the lifetime equivalent loads. This is also shown by the similarity between the lower panel of Figure 5.4 and the upper right panel of Figure 5.6. It is expected based on these results that both wind shear and turbulence are significant for the blade root flapwise loads, since the equivalent loads tend to increase if the atmosphere changes from neutral to stable (here wind shear increases) and the equivalent loads also increase if the atmosphere changes from neutral to unstable (here turbulence levels increase).

For the rotor out of plane equivalent loads it is found, similarly as for the blade root flapwise loads, that highest loads occur for high wind speeds in combination with very strong unstable conditions, and the rotor loads also increase with increasing hub height wind speeds. It is also found that for a given hub height wind speed a minimum equivalent load is found for near neutral conditions, and loads increase if the atmosphere becomes either unstable or stable stratified. This increase in rotor equivalent loads for increasing stability is also found for low wind speeds (i.e. see the contour of 800 kNm), and it is found again that if the atmosphere becomes very stable stratified with $\zeta_h > 3$ equivalent loads decrease with increasing stability, though the decrease is minimal. After multiplication of the rotor equivalent loads with $P(\bar{U}_h, \zeta_h)$ similar results are found as where shown for the blade root loads, and those conditions that occur most frequently also contribute most to the lifetime loads. For the rotor loads however there is a slight increase in the contribution of stable conditions to the lifetime equivalent loads compared to the blade root loads. Based on these results there clearly is similarity between the dependence of blade root and rotor loads on atmospheric stability and hub height

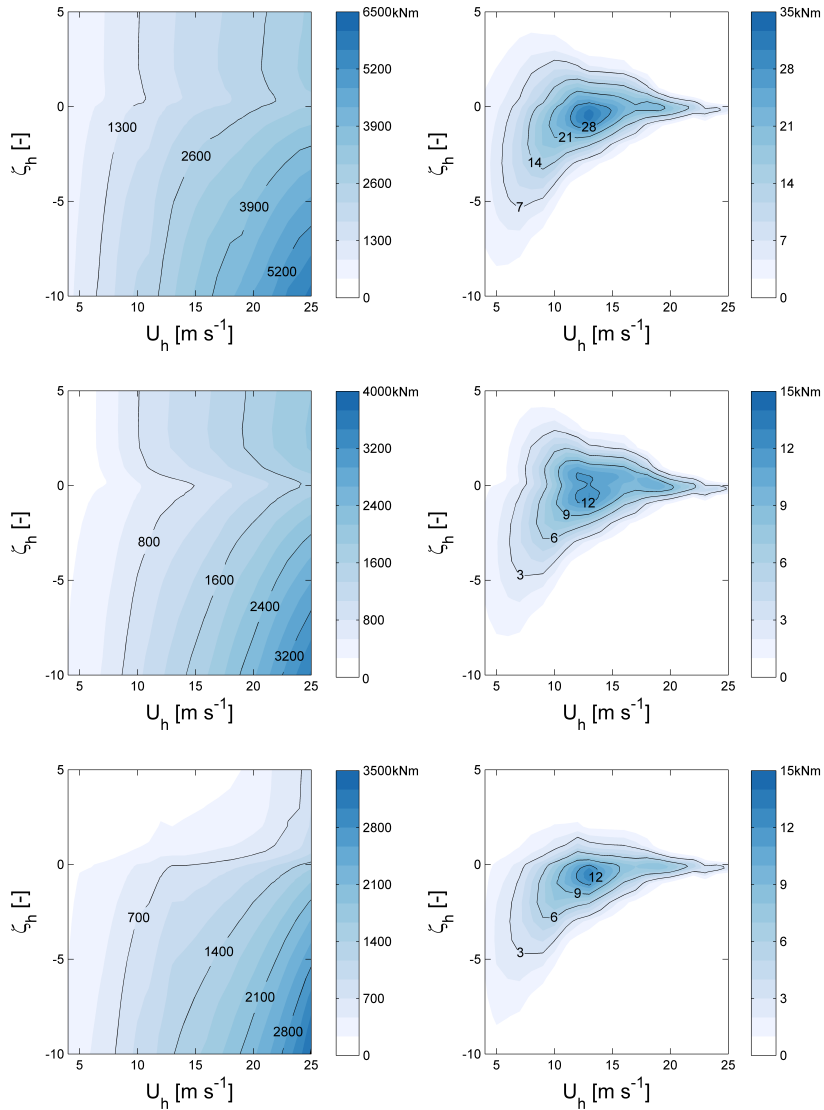


Figure 5.6: Equivalent load of the blade root (upper panels), rotor (middle panels) and tower base (lower panels) as a function of hub height wind speed and atmospheric stability (left panels, F_{EQ}) and the same equivalent load multiplied with the joint probability distribution of wind speed and stability (right panels, $F_{EQ}P(\bar{U}_h, \zeta_h)$).

wind speed.

The tower fore-aft equivalent loads show a similar dependence on hub height wind speed, and an increase in hub height wind speed tends to result in higher tower loads. It is also found in agreement with the previous results that for a given hub height wind speed the highest tower loads occur when the atmosphere is very unstable stratified, however the lowest loads do not occur for neutral conditions but for stable conditions. The decrease in loads is in fact so substantial that similar loads occur for strong unstable ($\zeta_h = -10$) and stable ($\zeta_h = 5$) conditions at hub height winds speeds of respectively 7 and 24 m s⁻¹. Based on this severe decrease in tower loads for increasing stable stratifications, and recognizing that for stable conditions wind shear increases substantially, it is concluded that wind shear has little impact on tower loads. This is in line with the hypothesis of [Sathe et al. \(2013\)](#), which states wind shear does not cause a dynamic moment at the tower base. Incorporating the joint probability distribution of wind speed and stability shows similar results as found for the blade root and rotor loads with the exception that stable conditions with $\zeta_h > 1$ hardly contribute to the lifetime tower base equivalent loads.

Overall it is found that highest loads for all turbine components considered occur for strong wind speeds and very unstable conditions, however, since such conditions hardly ever occur the relative contribution of these conditions to the lifetime fatigue loads is limited. Wind shear is expected to be important for the blade root and rotor loads, whereas turbulence is expected to be important for all three components considered, seeing that for all three components loads increase substantially if the atmosphere changes from neutral to unstable stratification. The site specific joint probability distribution of wind speed and stability has a significant impact on the estimated lifetime equivalent loads, and if one would consider a different site with more stable conditions results would likely also differ substantially. Results are in line with those presented in [Sathe et al. \(2013\)](#), who found qualitatively similar results using other turbulence and wind shear models. During resource assessment it is thus of importance that an accurate joint probability distribution of wind speed and atmospheric stability is obtained to estimate the lifetime loads experienced by various wind turbine components.

5.4.2. SPECTRAL ANALYSES OF BENDING MOMENTS

With the previous assessment it is clear for which conditions, in terms of hub height wind speed and atmospheric stability, highest equivalent loads occur for various components, and which conditions contribute most to the lifetime equivalent loads experienced by these turbine components. Previous results can be considered an indirect indication of the importance of wind shear and turbulence for the loads of these components, however, more insight can be obtained with spectral analyses of the bending moments experienced by the turbine components. Despite the fact that the spectra of the bending moments do not translate directly into equivalent loads, fatigue is caused by variation of the bending moment, and changes in the spectra can be used as an indication which physical processes (i.e. shear or turbulence) contribute to the fatigue of turbine components. An overview of relevant frequencies is shown in [Table 5.4](#). In the following analyses the same three components are considered as previously discussed, and spectral analyses are carried out for a hub height wind speed of 7 m s⁻¹ with an

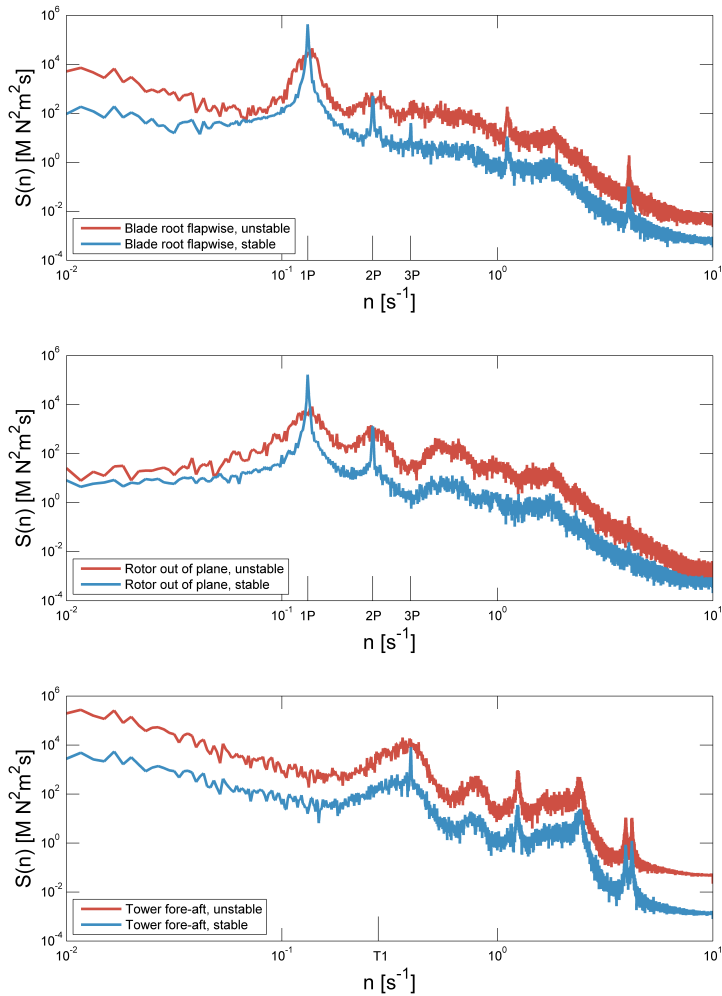


Figure 5.7: Spectra of the blade root flapwise bending moment (upper panel), the rotor out of plane bending moment (middle panel) and tower fore-aft bending moment (lower panel) determined for a hub height wind speed of 7 m s^{-1} . Stable corresponds to $\zeta_h = 2$, unstable to $\zeta_h = -5$.

Table 5.4: Rotational frequencies and eigenfrequencies of the turbine for $\bar{U}_h = 7 \text{ m s}^{-1}$.

Period/frequency type	Frequency [Hz]
1P rotational frequency	0.13
2P rotational frequency	0.26
3P rotational frequency	0.40
First flapwise blade eigenfrequency	1.10
Second flapwise blade eigenfrequency	4.07
First fore-aft tower eigenfrequency	0.28
Second fore-aft tower eigenfrequency	1.88

atmospheric stability of $\zeta_h = 2$ for stable conditions and $\zeta_h = -5$ for unstable conditions.

The following reasoning is considered for the interpretation of the turbulence spectra. It is expected that spectral peaks will be found at rotational frequencies (1P in a rotational frame, 3P in a fixed frame) as well as at eigenfrequencies of turbine components. If only the turbulence intensity is changed, it is expected that as a result the spectra of the bending moment will shift upward (for increasing turbulence levels) or downward (for decreasing turbulence levels), since turbulence acts on all frequencies. A change in wind shear however not necessarily influences the spectrum considered. If wind shear is of importance for the bending moment considered, than an increase in wind shear and decrease in turbulence levels (thus from unstable to stable conditions) will cause the spectral peak at rotational frequencies to become narrow and sharp defined. For such conditions the majority of variation in the bending moment occurs at the exact rotational frequency where a peak is observed. If however wind shear is not of importance for the component consider, then the variation in the bending moment will occur at all frequencies, not only at the rotational frequencies. This is expected to be valid even if there is high wind shear and little turbulence. The spectra can thus be used to make an interpretation of the importance of wind shear for the components considered. The turbulence spectra obtained from the simulations are shown in Figure 5.7.

For the blade root flapwise bending moment the spectra of stable and unstable conditions show distinct peaks at the 1P and 2P frequencies. The small peaks that occur at higher frequencies in fact correspond to two eigenfrequencies of the blade. For the rotor out of plane bending moment similar results are found, though the peaks at higher frequencies are limited. For both components the 1P and 2P peaks differ in shape (width and height) for the spectra corresponding to stable and unstable conditions. At the same time the spectra obtained for the unstable atmosphere are shifted vertically since the turbulence intensity increases for unstable conditions. The combined interpretation is that the blade root flapwise bending moment and the rotor out of plane bending moment are influenced substantially by both wind shear and turbulence.

The spectra of the tower fore-aft bending moment has a relatively broad peak at the 3P frequency. The majority of this 3P spectral peak does not differ substantially in shape for the stable and unstable spectra, in contrast to the pronounced 1P and 2P peaks of the blade root flapwise and rotor out of plane bending moments. There is however for stable conditions a slight narrow peak at the exact 3P frequency. This distinct small peak might be an indication of a minor shear effect, however the far majority of the tower fore-aft

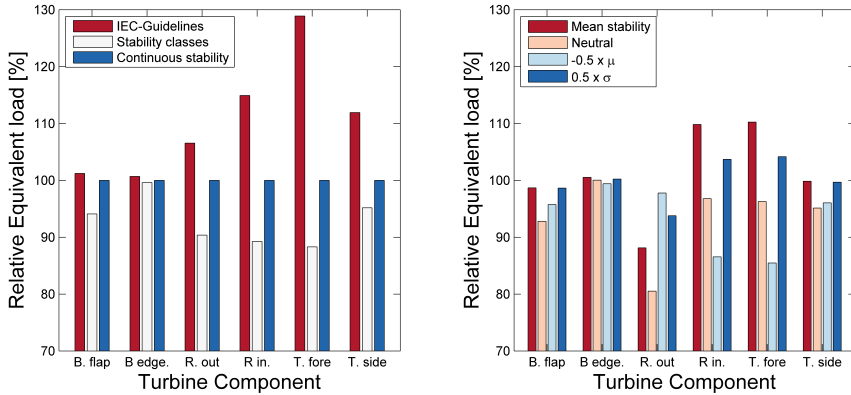


Figure 5.8: Relative lifetime equivalent loads of various wind turbine sections (left panel) based on the specified cases, and the sensitivity of the lifetime fatigue loads to the distribution of stability.

5

bending moment spectra is simply a vertical shift, which is caused by a substantial increase in turbulence intensity for unstable conditions. As such, while wind shear is of importance for blade root and rotor loads, it does not appear to be of significant influence for tower loads. This corresponds to previous results, where it was found that tower fore-aft equivalent loads significantly decrease if the atmosphere changes from unstable to stable stratification. Since turbulence is of importance for the tower fore-aft loads, it is surprising that there is no distinct peak visible at the first tower fore-aft eigenfrequency. In contrary, at approximately 1.1 Hz there is a spectral peak not related to any of the multiples of the rotational frequency. In scope of the presented eigenfrequencies in Table 5.4, it is unclear what causes the spectral peak specifically at 1.1 Hz, which should be studied in future research. Still it is clear that turbulence is the driving cause of the tower fore-aft loads.

The results obtained from the spectral analyses are in line with the preliminary interpretation discussed before: all three wind turbine components are substantially influenced by turbulence, but wind shear is only relevant for the blade root flapwise bending moment and the rotor out of plane bending moment.

5.4.3. LIFETIME FATIGUE LOADS

The lifetime fatigue loads that a 5 MW NREL wind turbine would experience for the wind speed and stability distribution is determined for the three specified cases. The left panel of Figure 5.8 shows the relative lifetime fatigue loads of all components considered, and the percentages are also shown in Table 5.5. The absolute numbers are not relevant since a hypothetical wind turbine is considered, and fatigue loads are converted to equivalent loads for comparison purposes. For each component the determined lifetime equivalent load is normalised with those obtained in case 3. It is found that lifetime equivalent loads of the blade root (both in flapwise and edgewise direction) are comparable for case 1 (IEC standards) and case 3 (continuous stability distribution). Using the dis-

Table 5.5: Equivalent load for various wind turbine components for the cases considered, relative to the loads obtained for case 3.

Case	B. flap	B. edge	R. out of plane	R. in plane	T. fore-aft	T. side-side
1	100.8	100.6	106.3	113.7	127.5	111.3
2	93.8	99.5	90.2	88.4	87.4	94.8
3	100.0	100.0	100.0	100.0	100.0	100.0
$\zeta_h = \bar{\zeta}_h$	99.0	100.6	88.4	109.8	110.6	100.0
$\zeta_h = 0$	92.4	100.0	80.3	95.8	95.2	94.6
-0.5μ	95.4	99.3	98.1	85.4	84.3	95.5
0.5σ	98.7	100.2	93.6	103.9	104.4	99.7

tinct stability classes results in an underestimations of the flapwise fatigue loads by 6%, while edgewise loads are similar as for both other cases. The similarity between the three cases for determining the lifetime blade root edgewise equivalent loads is caused by the dominant contribution of gravitational loads, and shows shear and turbulence have little effect on the lifetime blade root edgewise loads. The out of plane and in plane rotor loads are overestimated by the IEC by respectively 6% and 14%, while using the seven stability classes results in an underestimation of respectively 10% and 12%. The fore-aft tower loads are overestimated by 28% by the IEC, and underestimated by 13% following the stability classes, while the side-side tower loads are overestimated by 11% by the IEC, and underestimated by 5% following the stability classes. It is recognised that if hydrodynamic loads would be included differences in tower loads would likely be smaller between the three cases.

The lifetime equivalent loads depend strongly on the relative occurrence of stable and unstable conditions and as such the sensitivity of lifetime fatigue loads to the distribution of atmospheric stability is assessed briefly. For this assessment the distribution of stability for each hub height wind speed is adjusted artificially by either imposing pure neutral conditions, or by changing the mean or standard deviation of stability for each hub height wind speed. Results are shown in the right panel of Figure 5.8 and in Table 5.5. The bar in the right panel of Figure 5.8 corresponding to the mean stability will be elaborated upon in the next paragraph. It is shown that if one would consider a site with purely neutral conditions fatigue loads decrease by 4 to 8% for most turbine components besides the rotor out of plane loads. This decrease is caused by a typical reduction in turbulence levels compared to the conditions observed in reality, where unstable conditions occur most frequently (see the lower panel of Figure 5.4). If the mean stability for each hub height wind speed is multiplied by a factor -0.5 (thus from strong unstable to slight stable, indicated by $-0.5 \times \mu$ in the legend of Figure 5.8) loads decrease substantially for the rotor in plane and tower fore-aft loads. When the standard deviation of the stability distribution is multiplied by a factor 0.5 (indicated by $0.5 \times \sigma$ in the legend) loads differ by about 2 to 7% from those determined with the original observation data. Combined this shows that it is important to recognise the offshore atmosphere is not neutral stratified by default, and it is important to accurately determine probability distribution

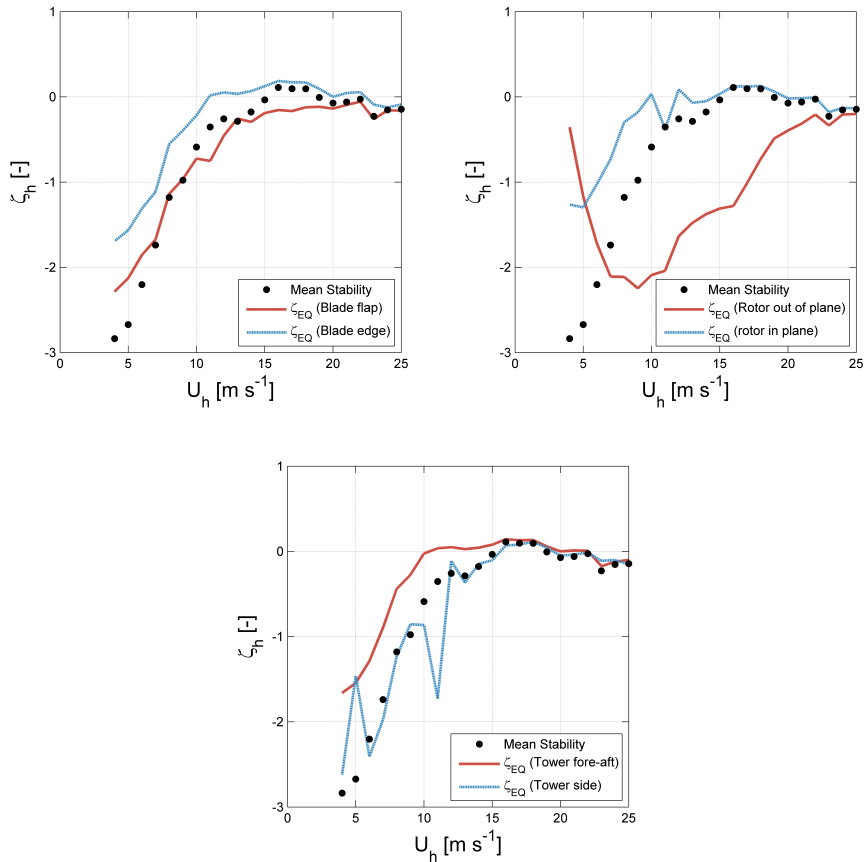


Figure 5.9: Equivalent stability as a function of hub height wind speed for the blade root loads (left panel), rotor loads (middle panel) and tower loads (right panel).

parameters of atmospheric stability.

For each hub height wind speed one can calculate based on the load simulations an equivalent stability ζ_{EQ} . The equivalent stability is defined as the stability for which one computes the exact same equivalent load as if one would perform a full set of load simulations, represented in this study with the 34 stability classes of case 3. The equivalent stability is thus a function of hub height wind speed and is expected to vary depending on wind turbine specifications and site conditions. It is questioned if the mean of the stability distribution for each wind speed resembles a good approximation of the equivalent stability for the blade root loads. Figure 5.9 shows the equivalent stability for the wind turbine components considered. As can be seen, the mean stability corresponds quite well to the equivalent stability for the blade root flapwise loads and the tower side-side loads, but not for the other components. For the rotor out of plane loads results deviate significantly, and the equivalent stability is much more unstable compared to

the mean stability, even for very strong wind speeds. For the remaining components the equivalent stability for wind speeds above 15 m s^{-1} corresponds well to the mean stability, with deviations of $\zeta_h = \pm 0.2$ at most. For wind speeds below rated the equivalent stability differs significantly more from the mean stability. As such, it is concluded that for each component assessed in a fatigue study one should consider a specific equivalent stability. For comparison purposes, the lifetime fatigue loads that one would obtain using the mean stability as a representative substitute for the equivalent stability is included in the right panel of Figure 5.8. As can be seen, for most components it would be an improvement to consider the mean stability instead of 7 distinct stability classes, and only for the rotor out of plane loads the results are worse. It therefore appears that for fatigue load assessment, one might be able to neglect the specification of stability classes and incorporate only the mean stability in the load assessment. This significantly reduces the computational demand of fatigue load assessment if one wants to incorporate atmospheric stability.

It is assumed in the analyses that since the representation of the atmosphere is most elaborate when considering a continuous distribution of stability, the resulting simulated equivalent loads of case 3 correspond best to equivalent loads experienced by a wind turbine in reality. It clearly is of importance to validate if this is indeed true, however this falls outside the scope of this research.

5.5. DISCUSSION

From the previous results it is clear that if one follows the IEC standards one will overestimate the fatigue loads for all wind turbine components considered in this study. Based on the used equations for wind shear and the longitudinal turbulence intensity one can find that the relations that incorporate stability frequently result in higher wind shear or turbulence intensity compared to the relations prescribed by the IEC. As such one cannot conclude that the IEC standards simply overestimate wind shear or turbulence levels. As a clarification, Figure 5.10 shows observations of wind shear and the turbulence intensity. One can see here that indeed the determined shear and turbulence levels following the IEC are not by definition too strong compared to either the observation data or the stability dependent relations. For stable conditions shear is frequently higher compared to IEC standards, and for unstable conditions turbulence is frequently higher compared to the IEC standards. For neutral conditions however (the intersection of the blue and red line in Figure 5.10), both wind shear and the turbulence intensity are less than the conditions prescribed by the IEC standards. Besides, whenever wind shear is high turbulence is low (upper left corner of Figure 5.10) and vice versa when turbulence levels are high wind shear is limited (lower right corner of Figure 5.10). There is never an occurrence of both high wind shear and high turbulence levels (upper right corner of Figure 5.10). This shows that indeed wind shear and turbulence are coupled, and by considering atmospheric stability this coupling can be included in wind turbine load assessment.

When adopting the stability classes the dynamic coupling is included, however for the majority of wind turbine components fatigue loads are underestimated compared to considering a continuous distribution of stability. This is primarily caused by the choice of class boundaries, since stable conditions up to $L = 10$ and unstable conditions up to

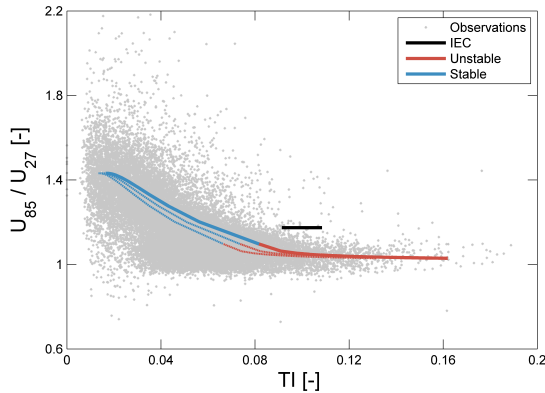


Figure 5.10: Observed and modelled wind shear and turbulence intensity. The solid blue and red lines correspond to Equation 5.4 (for wind shear) and respectively Equations 5.15 and 5.16 (for the TI) with $m = 12$, the dashed lines are determined with $m = 4$ and 8 . The black line corresponds to the IEC standards with wind speeds ranging from 3 to 25 m s^{-1} .

$L = -50$ are chosen as the stability limits. From the load figures shown in this research it is evident that unstable conditions of $-10 < \zeta_h < -1.8$ contribute significantly to the lifetime fatigue loads, while for very stable conditions with $\zeta_h > 2$ fatigue loads are limited. As such incorporating the arbitrary choice of class boundary limits causes an underestimation of lifetime fatigue loads, and it is recommended to include more significant unstable conditions in fatigue load assessment as well.

It is recognised that the results obtained are wind turbine specific, and results might differ if the wind turbine design is changed. Especially the material considered for the various wind turbine components are of crucial importance since the results are certainly dependent on the choice of the Wöhler exponent m . The equivalent load F_{EQ} obviously depends on m (see Equation 5.2), but the equivalent turbulence for cases 2 and 3 (i.e. the stability dependent cases) is a function of m as well (see Equations 5.15 and 5.16). If one would consider materials that correspond to a lower Wöhler exponent, for example welded steel instead of cast iron for the hub, then the equivalent turbulence would decrease. Since the equivalent load ranges are in first approximation linearly proportional to the standard deviation of the wind (Veldkamp 2006), the equivalent load would also decrease (besides the obvious change based on Equation 5.2). It would therefore be valuable to assess the sensitivity of the results presented in this study to the Wöhler exponent and specific wind turbine designs.

5.6. CONCLUSION

Wind turbine fatigue loads are predominantly caused by wind shear and turbulence levels, which both are influenced by atmospheric stability. It is shown that the offshore site considered is not neutral stratified by default, especially for low wind speeds. The impact of atmospheric stability on wind turbine fatigue loads is assessed for the 5 MW

NREL wind turbine for three wind turbine components. For all three components highest loads occur when the atmosphere is unstable stratified since for such conditions turbulence levels are high. Fatigue loads decrease when the atmosphere changes from an unstable to a neutral stratification since turbulence levels decrease and wind shear does not increase substantially. When the atmosphere becomes stable stratified, wind shear rapidly increases while turbulence levels rapidly diminish. The impact on fatigue loads differs for the three components considered. The tower loads decrease strongly when the atmosphere becomes stable stratified, which indicates shear is not contributing substantially to the tower loads. The blade root flapwise loads and rotor loads increase if the atmosphere becomes stable stratified, but if the atmosphere becomes very stable this increases in simulated fatigue loads stops.

The lifetime fatigue loads experienced by a wind turbine depend strongly on the joint probability distribution of hub height wind speed and atmospheric stability, and typically IEC standards are followed in which atmospheric stability is neglected, which has significant benefits in terms of computational demands for the load simulation. It is also possible not to adopt IEC standards, and instead consider a limited set of stability classes with arbitrary class boundaries. In this study both approaches are compared to a computational heavy set of simulations where the continuous distribution of stability is approximated. Here it is assumed that fatigue loads simulated with the continuous distribution of stability are most comparable to reality, however there clearly is a need for validation with fatigue load observations. It is found that if one neglects atmospheric stability following the IEC standards lifetime fatigue loads are overestimated, while adopting several stability classes results in an underestimation of lifetime fatigue loads. The overestimation by the IEC standards is not caused by conservatism in wind shear or turbulence levels. Instead, the coupling of wind shear and turbulence by atmospheric stability is missing. By incorporating atmospheric stability in the fatigue load assessment one prevents simulating an atmosphere with both high levels of wind shear and turbulence. This coupling is included in the load assessment when stability is considered in several stability classes, however the classification system used in this study neglected strong unstable conditions with $\zeta_h < -1.8$. Such conditions were found to occur frequently at the site considered here, and for such conditions typically highest fatigue loads occur. As such, neglecting strong unstable conditions in fatigue load assessment results in an underestimation of the lifetime fatigue loads experienced by a wind turbine.

If one approaches the continuous distribution of atmospheric stability with many small stability classes one approaches reality at the cost of heavy computational expenses. It is found that one can significantly reduce computational expenses by adopting one mean stability for each hub height wind speed. The error in lifetime fatigue loads does not increase substantially compared to using several stability classes. This approach has the same computational expenses as if one follows the IEC standards, but the error in lifetime fatigue loads is significantly reduced, especially for the tower loads. Combined, there are significant benefits in considering atmospheric stability in a smart and computational effective way in wind turbine fatigue load assessment.

6

THE IMPACT OF DEVIATING SHEAR PROFILES ON WIND TURBINE PERFORMANCE

Measure what is measurable, and make measurable what is not so.

Galileo Galilei

In the previous chapter it has been shown that atmospheric stability has a substantial influence on wind turbine fatigue loads. It is recognised, based on Chapters 3 and 4, that simple wind profiles no longer suffice to describe wind shear in the offshore environment for state of the art wind turbines. As such, it is questioned to what extent these deviating wind profiles influence wind turbine performance.

An extended boundary layer wind shear profile has been derived in Chapter 3 for standard conditions where the wind speed increases with height. So far no simple engineering model has been defined yet that can be used to assess the effect of low-level jets on wind turbines. As such, it is aimed in this chapter to derive a new simple empirical low-level jet wind profile. If a simple low-level jet model is obtained one can assess how both wind models (the extended boundary layer wind shear profile and the low-level jet wind profile) influence wind turbine performance. Although in the previous chapter only fatigue loads have been considered, one can also consider wind turbine performance in terms of power production. Considering both aspects of wind turbine performance provides valuable insight in how wind turbines will respond to various shear conditions that occur in reality, which are not necessarily covered in current resource assessment or wind turbine design.

This chapter is based on one paper that will be submitted for publication as: Holtslag, M. C., He, Y., Bierbooms, W. A. A. M. & van Bussel, G. J. W. (2016), 'Derivation and implementation of an empirical low-level jet wind shear model for wind energy purposes', and on the publication: Holtslag, M. C., Bierbooms, W. A. A. M. & van Bussel, G. J. W. (2016), 'Extending the diabatic surface layer wind shear profile for offshore wind energy', Submitted for publication to *Renewable Energy*

6.1. INTRODUCTION

It is well known that wind turbine loads are substantially influenced by wind shear, hence wind turbines are designed with specific shear conditions in mind following standards (IEC 2005, 2009). Not only does the fatigue of wind turbine components differ for varying shear conditions (Sathe & Bierbooms 2007), but the power production of a wind turbine also depends on the amount of wind shear (Wagner et al. 2011). For fatigue loads there is a clear relation between high shear conditions and high turbine loadings, at least for blade root and hub loads as shown in Chapter 5, hence wind shear is an undesirable characteristic of the atmosphere. Wagner et al. (2011) has shown with respect to power production that both low wind shear and high wind shear can result in an increase in inflow of kinetic energy through the rotor disc area. As such, potentially wind shear can be favourable for power production of wind turbines. The results presented in Chapter 5, in Sathe & Bierbooms (2007) and in Wagner et al. (2011) are all obtained assuming validity of simple wind profiles, either diabatic surface layer wind profiles or empirical power laws. Despite the simplification of wind shear, they do provide a qualitative relation between the amount of wind shear and the resulting fatigue loads and power production.

In Chapter 3 it has been shown that surface layer wind profiles do not represent offshore atmospheric conditions accurately for state of the art wind turbines. Especially for neutral and stable conditions, wind shear is incorrectly prescribed by the surface-layer wind profiles, and observed wind shear is much better represented with the proposed boundary layer wind shear profile. As such, it is investigated in this chapter if using diabatic surface layer wind profiles for wind energy purposes results in a correct representation of wind turbine fatigue loads and power production compared to considering more accurate boundary layer wind shear profiles. It is hypothesized that especially for stable conditions, where the boundary layer wind profile is found to be much more accurate, the diabatic wind profile will result in an overestimation of fatigue loads (and potentially a slight overestimation of power production).

In Chapter 4 low-level jets have been discussed, and the occurrence and characteristics of low-level jets offshore have been quantified. So far however there is little known on the impact of low-level jets on wind turbine performance. Recent studies have shown the impact of low-level jets on resource assessment (Nunalee & Basu 2014) and wake characteristics (Lu & Porté-Agel 2011, Bhaganagar & Debnath 2015). Besides, Kelley et al. (2004) assessed the potential impact of low-level jets on wind turbine performance qualitatively, but a similar quantitative study in terms of wind turbine power production and experienced fatigue loads as a function of low-level jet wind profiles is lacking. This is likely to an extent related to the complexity of existing low-level jet models, which are impractical to use in terms of time dependence and the need of specific input parameters (i.e., see the models of Shapiro & Fedorovich (2010) and van de Wiel et al. (2010)). A simple empirical low-level jet model has been proposed by He (2014), who also assessed the subsequent influence of the modelled low-level jets on wind turbine power production. It is found however that the proposed model has undesirable characteristics far above the low-level jet, and if a jet occurs close to the surface this can pose problems to accurately define wind shear at heights relevant for wind energy purposes.

In scope of the principle relations between wind shear and wind turbine performance described before, it is expected that low-level jets result in high fatigue loads and

high power production. Based on a to-be derived simplified model of a low-level jet, it will be explored in which way the primary characteristics of low-level jets (i.e., the jet speed and jet height, but also the width of the jet) influence wind turbine performance. Here again the impact of low-level jet characteristics on power production as well as wind turbine fatigue loads is considered.

It is noted that in this chapter a highly simplified representation of the atmosphere is adopted, in which turbulence is discarded. As such in Chapter 7 the effects on turbulence on a wind turbine will explicitly be studied. Combined, this should provide fundamental insight how specific meteorological processes influence wind turbine performance.

6.2. WIND SHEAR MODELS

In this chapter two shear conditions discussed previously are considered that deviate from the commonly used theoretic profiles used in wind energy research. These are the boundary layer wind shear profile (BL-profile) derived in Chapter 3, and the low-level jet wind profile (LLJ-profile) discussed in Chapter 4. The BL-shear profile has been fully derived and validated in Chapter 3, hence in this section only the exact relations used in subsequent analyses are provided without discussing the derivations. With respect to the LLJ-profile however so far only the characteristics of offshore low-level jets have been quantified and discussed. As such in Section 6.2.2 an empirical low-level jet model will be derived that can be used for wind energy purposes.

6.2.1. DIABATIC SHEAR PROFILES

As shown in Chapter 3, offshore wind profiles at heights relevant for wind energy purposes can deviate substantially from commonly used surface layer wind profiles. In this section the equations used to define the BL-profile and SL-profile (surface layer shear profile) will be briefly summarized.

The surface layer wind profile is taken from Chapter 2 Equation 2.8, and is defined as

$$\bar{U}(z) = \frac{u_{*0}}{\kappa} \left[\ln\left(\frac{z}{z_0}\right) - \Psi(\zeta) + \Psi(\zeta_0) \right] \quad (6.1)$$

in combination with Charnock's equation to parametrize z_0 , and the Businger-Dyer and Free Convection stability correction functions for respectively stable and unstable conditions

$$\Psi(\zeta \geq 0) = -\beta\zeta \quad (6.2)$$

$$\Psi(\zeta \leq 0) = 1.5 \ln\left(\frac{1+y+y^2}{3}\right) - \sqrt{3} \arctan\left(\frac{2y+1}{\sqrt{3}}\right) + \frac{\pi}{\sqrt{3}} \quad (6.3)$$

Combined, the SL-shear profile is defined as a function of u_{*0} and L , however, the wind profile can also be defined with a specified hub height wind speed and corresponding hub height in combination with L .

The boundary layer wind profile is taken from Chapter 3 Equation 3.19, and defined as

$$\bar{U}(z) = \frac{u_{*0}}{\kappa} \left[\ln\left(\frac{z}{z_0}\right) + \Upsilon + \Omega \right] \quad (6.4)$$

where Ω has a similar function for stable and unstable conditions

$$\Omega = \frac{z}{h} \left[2 - \frac{z}{h} \right] \left[\sqrt{\left[\ln\left(\frac{h}{z_0}\right) - B\left(\frac{h}{L}\right) \right]^2 + A^2\left(\frac{h}{L}\right)} - \ln\left(\frac{h}{z_0}\right) \right] \quad (6.5)$$

and Υ differs for stable and unstable conditions as respectively

$$\Upsilon = 0 \quad (6.6)$$

$$\begin{aligned} \Upsilon = \frac{z}{h} \left[2 - \frac{z}{h} \right] & \left[\Psi\left(\frac{h}{L}\right) - \Psi\left(\frac{z_0}{L}\right) \right] - \left[\Psi\left(\frac{z}{L}\right) - \Psi\left(\frac{z_0}{L}\right) \right] \\ & + \frac{3}{2} \frac{z}{h} \left[\left[2 - \frac{z}{h} \right] \frac{x_h^2 - x_0^2}{x_h^3 - 1} - \frac{x_z^2 - x_0^2}{x_z^3 - 1} \right] - \frac{z}{h} \left[1 - \frac{z}{h} \right] \end{aligned} \quad (6.7)$$

Besides, the parametrization of the resistance functions A and B is incorporated as

$$A = \frac{q+1}{q} \frac{\kappa u_{*0}}{fh} \quad (6.8)$$

$$B = \frac{p+1}{p} + \frac{1}{2} \frac{p-1}{p} \Psi\left(\frac{h}{L}\right) - \Psi\left(\frac{z_0}{L}\right) \quad (6.9)$$

$$B = \frac{3}{2} \frac{p+1}{p} \frac{x_h^2 - x_0^2}{x_h^3 - 1} + \Psi\left(\frac{h}{L}\right) - \Psi\left(\frac{z_0}{L}\right) \quad (6.10)$$

where Equations 6.9 and 6.10 correspond to respectively stable and unstable conditions. Charnock's equation is considered to parametrize z_0 , and the Rossby-Montgommery equation is used to parametrize h as $h = cu_{*0}/f_c$ with the parameter c a function of stability as

$$c = 0.04 + 0.05 \left(1 + 2 \frac{100}{L} \right)^{-1} \quad (6.11)$$

$$c = 0.17 - 0.08 \left(1 - 0.5 \frac{100}{L} \right)^{-3} \quad (6.12)$$

for respectively stable and unstable conditions. The stability correction functions used in the BL-shear profile are the same functions as used in the SL-shear profile. Combined, also the BL-shear profile is a function of either u_{*0} and L or a function of the hub height wind speed and corresponding hub height in combination with L .

From here on first a LLJ-model is derived before the impact of specific shear models on wind turbine performance is assessed.

6.2.2. DERIVATION OF AN EMPIRICAL LLJ-MODEL

It is aimed in this section to formulate a steady-state LLJ-model in which the main characteristics of the jet correspond to observed low-level jets characteristics. In wind energy research, one typically defines the wind speed at a reference height (usually at hub height), and wind shear is then defined as a function of this reference wind speed. A similar approach is adopted in the derivation of a LLJ-model, however, the hub height

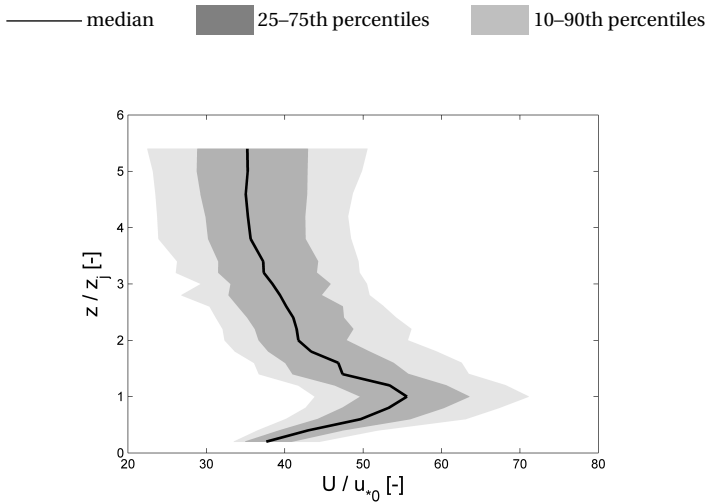


Figure 6.1: Non-dimensional wind speed as a function of the non-dimensional height of all observed low-level jet profiles.

wind speed is no representative wind speed since it can vary depending on jet characteristics. Instead it is aimed to consider the jet height and jet speed as primary input parameters to control the LLJ-profile. As a starting point, it is recognised that at least for low-level jets related to the inertial oscillation, the jet can be considered a speed-up of the wind in time. As such it is assumed that the low-level jet can be considered a superposition on top of a neutral wind profile, which will be used as a starting wind profile. Besides, as shown in Chapter 4 it can be convenient to assess wind profiles in terms of the non-dimensional wind speed. Clearly the observed non-dimensional wind speed of low-level jet wind profiles are not expected to collapse onto each other since the jet height differs for the observed jets. As such, the non-dimensional wind speed is considered as a function of the non-dimensional height $R = z/z_j$, where z_j is the jet height. The same observation data as used in Chapter 4 is used in this chapter, and the statistics of the 2754 low-level jet profiles detected in the two years of observation data are shown.

Results are presented in Figure 6.1, in which the clear shape of low-level jet profiles is shown with by definition a local maximum at $R = 1$. Besides, there is no local maximum observed above the jet for the specific percentiles shown. The width of the shaded area that corresponds to the specific percentiles indicate there is a substantial scatter in the non-dimensional wind speed for the observed low-level jets. It is expected that this is, at least partially, related to the various causes of low-level jets offshore discussed in Chapter 4. While for surface layer wind profiles one might expect a collapse of non-dimensional wind profiles onto each other, this is not found here for the low-level jet profiles. It is expected that the wind speed at the jet height is not only a function of u_{*0} , but also of atmospheric stability and possibly other parameters depending on the formation cause of specific low-level jets.

In scope of the previous assumption to consider a simplified model with the super-

position of a low-level jet on a neutral logarithmic wind profile, a principle model of the non-dimensional low-level jet wind profile is formulated as a function of the relative height z/z_j as

$$\frac{\bar{U}_{LLJ}(R)}{u_{*0}} = \frac{1}{\kappa} \left[\ln \left(\frac{R}{R_0} \right) + X(R) \right] \quad (6.13)$$

where $X(R)$ has to be modelled yet and $R_0 = z_j/z_0$. The following requirements of the model are specified that at all times have to be met

- Close to the surface ($z \ll z_j$) the wind profile has to coincide with the logarithmic wind profile. As such X will be defined in such a way that $\lim_{R \rightarrow 0} X(R) = 0$.
- Far above the jet ($z \gg z_j$) the wind profile has to coincide with the logarithmic wind profile. Note that this is not necessarily complying to observations, however it prevents that the LLJ-model far above the jet has unrealistic large or small (negative) non-dimensional wind speeds. As such X is defined in such a way that $\lim_{R \rightarrow \infty} X(R) = 0$.
- There has to be a local maximum specifically at the jet height, where the jet speed is obtained. As such the first and second derivatives of Equation 6.13 to R have to be respectively 0 and negative at $R = 1$.

To comply with the first two constraints a general model of $X(R)$ is defined with aid of a log-normal distribution, which can be written as

$$X(R) = \frac{c_1}{R} \exp(-c_2 [\ln(R) - c_3]^2) \quad (6.14)$$

Where the three coefficients c_1 , c_2 and c_3 originate either from constraints or parametrizations. Incorporating Equation 6.14 into Equation 6.13 provides a general LLJ wind profile

$$\frac{\bar{U}_{LLJ}(R)}{u_{*0}} = \frac{1}{\kappa} \left[\ln \left(\frac{R}{R_0} \right) + \frac{c_1}{R} \exp(-c_2 [\ln(R) - c_3]^2) \right] \quad (6.15)$$

Next, in line with the third constraint formulated, the first derivative of Equation 6.15 is considered, which equals

$$\frac{\partial}{\partial R} \frac{\bar{U}_{LLJ}(R)}{u_{*0}} = \frac{1}{R} - \frac{c_1 [2c_2 [\ln(R) - c_3] + 1] \exp(-c_2 [\ln(R) - c_3]^2)}{R^2} \quad (6.16)$$

and has to be 0 at $R = 1$. This subsequently results in

$$c_1 = \frac{1}{1 - 2c_2c_3} \exp(c_2c_3^2) \quad (6.17)$$

and it is thus found, based on the formulated constrains, that c_1 can be written as a function of c_2 and c_3 , which reduces the number of independent coefficients to two.

Here the equations are briefly rewritten for sake of convenience in the subsequent derivations and analyses. Incorporating Equation 6.17 into Equation 6.15, and defining $P_1 = 2c_2c_3$ and $P_2 = c_2$, results in

$$\bar{U}_{LLJ}(z) = \frac{u_{*0}}{\kappa} \left[\ln \left(\frac{z}{z_0} \right) + \frac{z_j}{z[1 - P_1]} \exp \left(P_1 \ln \left(\frac{z}{z_j} \right) \right) - P_2 \left[\ln \left(\frac{z}{z_j} \right) \right]^2 \right] \quad (6.18)$$

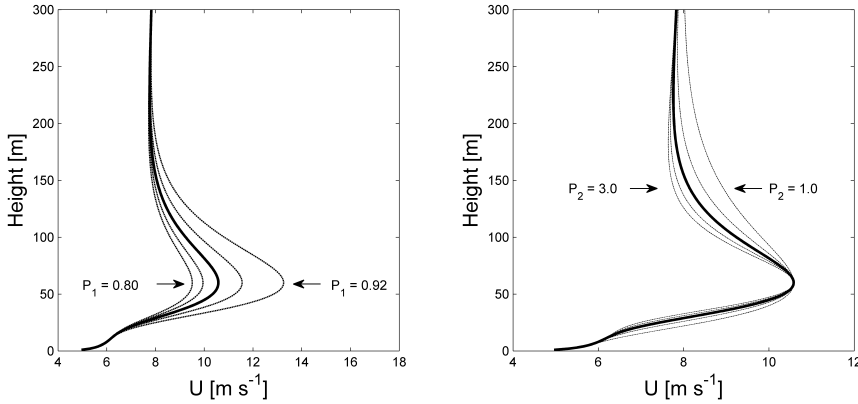


Figure 6.2: Sensitivity of the derived low-level jet model to the model parameters P_1 (left panel) and P_2 (right panel). All profiles are defined with $u_{*0} = 0.2 \text{ m s}^{-1}$ and $z_j = 60 \text{ m}$. The solid black line in both panels is the exact same profile with $P_1 = 0.86$ and $P_2 = 2$.

This will be the LLJ-model used in the remainder of this chapter. However, in line with the last constraint it is recognised that the second derivative of Equation 6.15 has to be negative at $R = 1$. The second derivative is found to equal

$$\frac{\partial^2 \bar{U}_{LLJ}(R)}{\partial R^2} = \frac{2c_1 [1 + 3c_2 [\ln(R) - c_3] - c_2 + 2c_2^2 [\ln(R) - c_3]^2] \exp(-c_2 [\ln(R) - c_3]^2)}{R^3} - \frac{1}{R^2} \quad (6.19)$$

and has to be negative at $R = 1$. This results in

$$-1 + 2c_1 [1 - 3c_2 c_3 - c_2 + 2c_2^2 c_3^2] \exp(-c_2 c_3^2) < 0 \quad (6.20)$$

and it is found, with the aid of Equation 6.17 and incorporating the newly proposed parameters P_1 and P_2 , that

$$-1 + \frac{[2 - 3P_1 - 2P_2 + P_1^2]}{1 - P_1} < 0 \quad (6.21)$$

The parameters P_1 and P_2 therefore have to be constrained as

$$2P_2 > [1 - P_1]^2 \quad (6.22)$$

Let us now place the various coefficients and terms of Equation 6.18 into perspective. First of all, the low-level jet is superimposed onto a neutral logarithmic wind profile that hereafter will be referred to as the background wind profile. It is assumed, similar to previous chapters, that the aerodynamic roughness length z_0 can be parametrized with Charnock's equation as a function of u_{*0} (see Equation 2.33). At the jet height, thus $R = 1$, it is found with Equation 6.18 that the difference between the low-level jet wind profile and the background wind profile is proportional to $1 / (1 - P_1)$. This can also be seen in the left panel of Figure 6.2, where for a given u_{*0} an increase in P_1 causes an increase

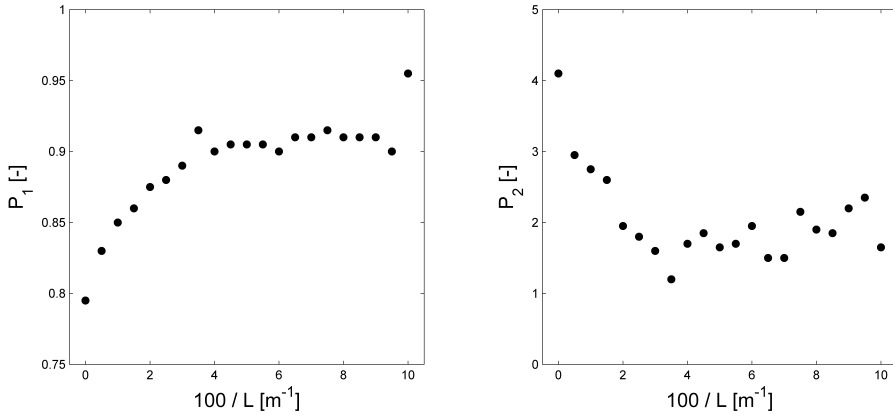


Figure 6.3: Dependence of the low-level jet model parameters P_1 (left) and P_2 (right) on atmospheric stability.

in the jet speed. One also has to specify the second coefficient P_2 which controls the width of the jet if P_1 has been specified as well. This is also shown in the right panel of Figure 6.2, where it is found that an increase in P_2 results in a narrow, or thin low-level jet. There can be peculiar shapes in the jet profile below the jet core since a superposition of a simple jet model onto a logarithmic wind profile is considered. For example, there is a slight bump in the wind profile in Figure 6.2 around 25 m height. Combined, an empirical model has been defined that can be used to assess the impact of low-level jets on wind turbine performance. It is a flexible model in which one can specifically adjust jet characteristics (speed, height, width and in principle the falloff indirectly) as preferred.

Although it is not aimed to formulate a parametrization that follows the underlying physics of low-level jets, it is expected that the shape and strength of low-level jets is influenced by the stability of the atmosphere. As such it is briefly assessed if a parametrization of the coefficients P_1 and P_2 could be formulated as a function of the Obukhov length L . This parametrization will not be used when assessing the impact of low-level jets on wind turbine performance. The number of free parameters in the LLJ-model could be further reduced if indeed the coefficients P_1 and P_2 are a function of stability. A similar approach as discussed in Section 3.2.4 is followed, and the derived model will be fitted to observation data to find for a given stability an ideal value of the coefficients P_1 and P_2 for which the root mean square error is smallest. For this assessment observation data obtained at the meteorological mast IJmuiden is used. All observation data starting at the first of January 2012 until the 31th of May 2015 are considered, and the terminology and detection criteria discussed in Chapter 4 is adopted. Next, only stable conditions with $0 < 100/L < 10$ are considered since the far majority of low-level jets occurs during stable conditions. The profile is fitted for values of P_1 of 0.6 to 0.99 (with a 0.005 spacing) and P_2 from 0.5 to 8 (with a 0.05 spacing). The resulting optimal values of P_1 and P_2 as a function of stability are shown in Figure 6.3. Here it is found that P_1

is approximately 0.8 for neutral conditions, and increases to values up to approximately 0.92 for very stable conditions. The exceptional high value of 0.96 at $100/L = 10 \text{ m}^{-1}$ is expected to be an outlier with high uncertainty due to the limited amount of observations with $100/L \approx 10 \text{ m}^{-1}$. For P_2 it is found that P_2 is approximately constant for the majority of stable conditions, varying typically between 1.5 and 2.5 for stable conditions, while for neutral conditions P_2 is higher (slightly higher than 4). As such, in scope of the sensitivity shown in Figure 6.2 it appears that for stable conditions the jets are at least stronger and more narrow.

It is possible to parametrize the dependence of P_1 and P_2 as a function of stability, but this is not done in this research. First of all, the proposed LLJ-model is empirical, and not based on theoretic arguments on the formation of low-level jets. Second of all, the low-level jets considered here originate from a variety of atmospheric conditions as discussed in Chapter 4, and not all these conditions are related to atmospheric stability. As such P_1 and P_2 are not parametrized as a function of stability explicitly, and instead the impact of the specific deviating wind profiles on wind turbine performance is assessed. First a theoretic assessment is done in terms of the flux of energy that flows through the wind turbine rotor disc for the diabatic wind profiles and the low-level jet model. Afterwards numerical simulation data are analysed to assess the impact of shear profiles on wind turbine performance in more detail.

6.3. EQUIVALENT WIND SPEED AND HUB HEIGHT WIND SPEED

The aim of this chapter is to assess the influence of various shear profiles on wind turbine performance, which will be assessed based on simulation data obtained with the simulation software Bladed (similar as used in Chapter 5) for the 5 MW NREL reference wind turbine. However, before the simulation data are analysed, it is recognised that for power production purposes the hub height wind speed might not be a representative wind speed experienced by the wind turbine. It is recognised in [Wagner et al. \(2011\)](#) that wind shear has a profound impact on the energy flux across the rotor disc of a wind turbine (i.e., the resource of a wind turbine for power production). This is also shown in [Wharton & Lundquist \(2012\)](#) implicitly, who found that power production increases if the atmosphere has a stable stratification. In contrary however, [Elliot & Cadogan \(1990\)](#) show that wind turbine power production decreases when turbulence levels are low (i.e., stable conditions), which they contribute to shear effects. Similarly, in [Vanderwende & Lundquist \(2012\)](#) it is found that wind turbine power production increases for unstable conditions and decreases for stable conditions compared to neutral conditions. In all these studies however, observation data of wind turbine power production are considered, and since in practice a wind turbine is influence by both turbulence and wind shear it unclear to what extent results are caused by wind shear specifically. Due to the conflicting conclusions of the studies mentioned here, it is worthwhile to perform an idealised simulation experiment in which solely wind shear is consider while turbulence is neglected, Though this is not representative for actual conditions, it does provide fundamental insight in the influence of wind turbine power production as a function of wind shear alone.

In absence of wind shear, the flux of kinetic energy across the rotor disc of a wind

turbine is defined as

$$KE = \frac{1}{2} \rho \bar{U}_h^3 A \quad (6.23)$$

Here ρ is the air density, A is the rotor disc area and \bar{U}_h is the mean hub height wind speed. Incorporating the effect of wind shear, one has to consider a height dependence of \bar{U} and a corresponding height dependent area A

$$KE_{sh} = \frac{1}{2} \rho \int \bar{U}(z)^3 A(z) dz \quad (6.24)$$

where KE_{sh} is the shear dependent flux of kinetic energy. Note that implicitly it is assumed that the air density is constant across the rotor disc, though in principle one could extend the derivation to include a height dependent air density as well. If one divides the rotor disc area into a finite number of areas to approximate the integral with a summation, one can determine at each height z the corresponding wind speed with the derived shear profile (as a function of stability). Since the segment of a circle above a horizontal line at a distance d of the centre of the circle can be analytically calculated as

$$A_{seg} = R^2 \operatorname{asin} \left(\frac{\sqrt{R^2 - d^2}}{R} \right) - d \sqrt{R^2 - d^2} \quad (6.25)$$

it follows that the area of a segment confined by two horizontal lines at a distance of respectively d_1 and d_2 of the centre of the circle equals

$$A(z) = R^2 \left[\operatorname{asin} \left(\frac{\sqrt{R^2 - d_1^2}}{R} \right) - \operatorname{asin} \left(\frac{\sqrt{R^2 - d_2^2}}{R} \right) \right] - d_1 \sqrt{R^2 - d_1^2} + d_2 \sqrt{R^2 - d_2^2} \quad (6.26)$$

In the following assessment the shear dependent energy flux is assessed relative to the uniform shear. Combing Equations 6.23 and 6.24, and approximating the integral with a summation, one finds

$$KE_{\%} = 100 \sum_z \frac{\bar{U}(z)^3}{\bar{U}_h^3} \frac{A(z)}{\pi R^2} \quad (6.27)$$

where the area in Equation 6.23 is rewritten as πR^2 and $KE_{\%}$ is the relative kinetic energy flux that is used in the following analyses.

With aid of the previous equations it is possible to define a representative equivalent wind speed \bar{U}_{eq} by combining Equations 6.23 and 6.24, which corresponds to (Wagner et al. 2011)

$$KE_{sh} = \frac{1}{2} \rho \bar{U}_{eq}^3 A \quad (6.28)$$

Hence the equivalent wind speed is defined as

$$\bar{U}_{eq} = \left[\bar{U}(z)^3 \frac{A(z)}{\pi R^2} \right]^{1/3} \quad (6.29)$$

Whether or not there is a need to consider the equivalent wind speed instead of the hub height wind speed for wind turbine power production assessment depends on the difference between both wind speeds.

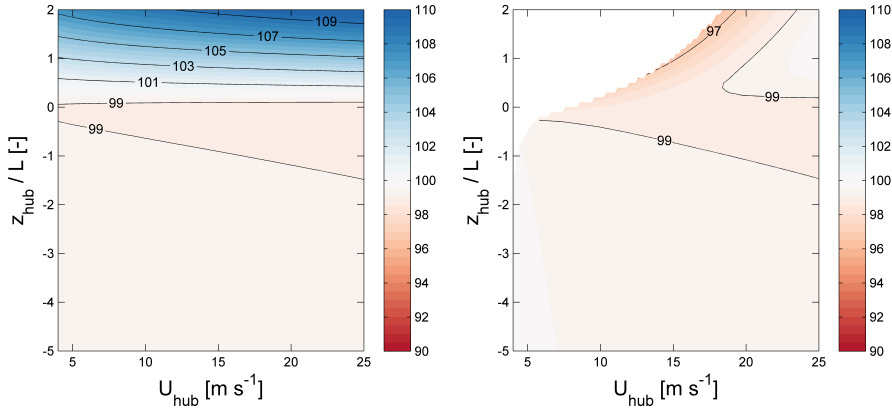


Figure 6.4: Relative kinetic energy flux assuming the conventional diabatic wind shear profile (left panel) and assuming the proposed boundary layer wind shear profile (right panel) for a given hub height wind speed and atmospheric stability.

The relative kinetic energy flux and the equivalent wind speed will be assessed in the following sections for the diabatic profiles previously discussed in Section 6.2.1 and for the low-level jet model previously discussed in Section 6.2.2.

6.3.1. KINETIC ENERGY FLUX FOR DIABATIC WIND PROFILES

For the diabatic wind profiles, the relative kinetic energy flux is assessed as a function of hub height wind speed and stability. Results are shown in Figure 6.4.

It is found that for unstable and neutral conditions there is a minor difference in the relative kinetic energy flux when using either of the considered shear profiles. For such conditions the relative kinetic energy flux is less than 100% for both diabatic wind profiles, ranging from 97.8 to 99.8% depending on stability. This is in agreement with the results found by [Wagner et al. \(2011\)](#) who showed that for low wind shear, which corresponds to unstable and neutral conditions, the relative kinetic energy flux is less than 100%.

For stable conditions however there is a significant difference in the results obtained depending on the shear profile considered. If one determines the relative kinetic energy flux with the diabatic surface layer shear profile, one finds that for stable conditions the relative kinetic energy flux is well above 100% with a maximum of 110% for high wind speeds. If one however considers the newly derived boundary layer wind shear profile, one finds a relative kinetic energy flux well below 100% with a minimum of 95%. Combined, this results in a difference of 15% in the relative kinetic energy flux depending on the shear profile considered.

For low wind speeds and stable conditions, the relative kinetic energy flux is not calculated for the boundary layer shear profile in Figure 6.4. For such conditions, Equation 6.11 determines h below the maximum blade tip height, hence the shear profile cannot be determined up to the maximum blade height. This is an obvious drawback of the

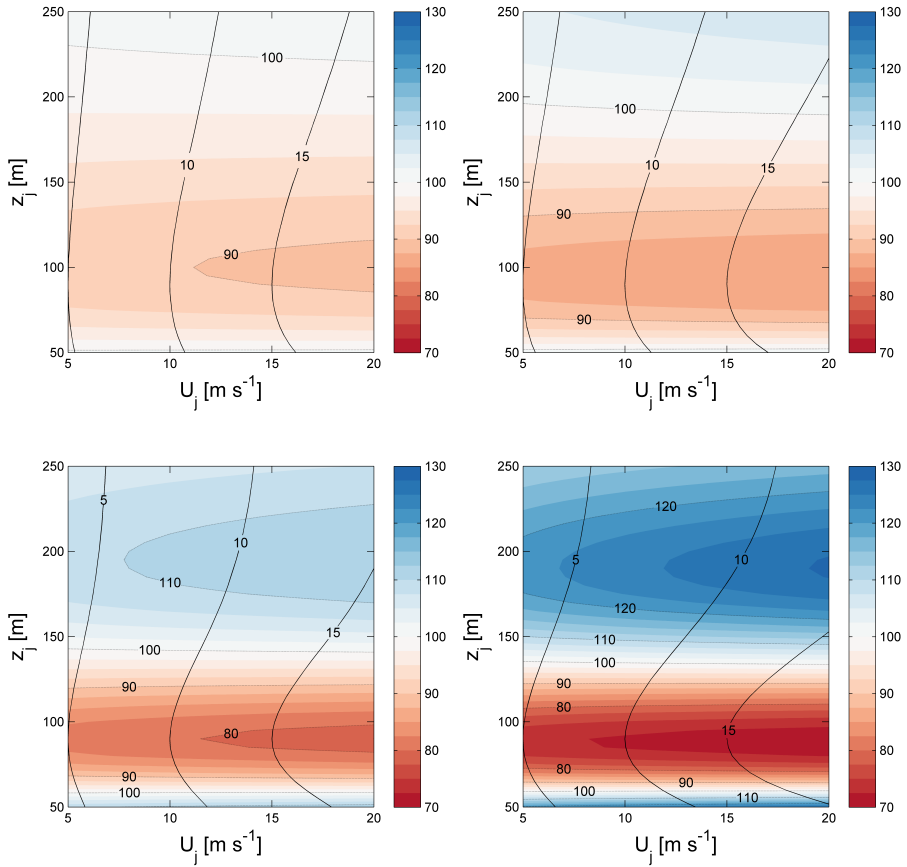


Figure 6.5: Relative kinetic energy flux using the low-level jet model for a given jet height and jet speed. The individual panels correspond to P_1 and P_2 are respectively 0.8 and 1 (upper left), 0.9 and 1 (upper right), 0.8 and 3 (lower left) and 0.9 and 3 (lower right).

BL-shear profile derived in Chapter 3, since for low wind speeds one cannot determine a representative wind shear profile, and thus power production and fatigue load assessment cannot be carried out. It thus shows that for offshore conditions it is necessary to consider the inversion layer at the top of the boundary layer, and possibly even free atmospheric conditions above the boundary layer.

6.3.2. KINETIC ENERGY FLUX FOR LLJ WIND PROFILES

For the low-level jet wind profiles the relative kinetic energy flux is assessed as a function of the jet speed and the jet height. Besides, it is also assessed how $KE_{\%}$ varies depending on model parameters. The hub height wind speed is included in solid contours since it is a common procedure in wind energy to assess wind turbine characteristics as a function of the hub height wind speed. Results are shown in Figure 6.5.

The influence of changing the model parameters P_1 and P_2 is shown in the four individual panels (see the caption of Figure 6.5 for details). It is found in all four panels that the relative kinetic energy flux is typically lowest when the jet height equals the hub height of the wind turbine. The decrease in the kinetic energy flux can be as large as 25%, which is an indication of the potential severe impact of low-level jets on wind turbine power production. In contrary, if the low-level jet is situated sufficiently far above wind turbine hub, the kinetic energy flux can be larger than 100%. For such situations a low-level jet might cause an increase in power production.

It makes sense to also specifically consider the change in kinetic energy flux for a given constant hub height wind speed, since the jet height does not correspond to the hub height wind speed. By following the contour of a fixed hub height wind speed, for example the 10 m s^{-1} contour, it is found that depending on the jet height there can be either an increase or decrease in the flux of kinetic energy through the rotor disc. The exact increase or decrease is highly dependent on the model parameters P_1 and P_2 . An increase in either of the parameters P_1 or P_2 has similar results: the low-level jet becomes sharper, either by increasing the distance between the jet speed and the background wind speed (i.e., through an increase in P_1), or the jet becomes narrow (i.e., through an increase in P_2). In either way, the change in the kinetic energy flux becomes larger.

It is interesting to note that if the jet height is located close to the surface (say, around 50 m in Figure 6.5), the relative kinetic energy flux can become larger than 100% again. The effect of a jet either far above or below the hub is similar: there is a substantial increase in the kinetic energy flux in either the upper or lower part of the rotor disc. The hub height wind speed is no longer representative for the kinetic energy flux through the rotor disc. Similarly, if the jet is positioned exactly at the hub, the hub height wind speed is also not representative. This provides an indication that it is sensible to assess if a representative wind speed that the wind turbine experiences can be defined for power production assessment.

6.3.3. EQUIVALENT WIND SPEED FOR DIABATIC WIND PROFILES

The assessment of the equivalent wind speed for the diabatic shear profiles is on purpose constrained to hub height wind speeds up to 16 m s^{-1} . This is done since for rated power production it is irrelevant whether or not there is a difference between both wind speeds. The results are shown in Figure 6.6, where positive values indicate hub height wind speed larger than the equivalent wind speed. It is expected that results are in line with previously shown kinetic energy flux (Figure 6.4), taking into account a possible sign change.

It is indeed found that for neutral and unstable conditions there is virtually no difference between the hub height wind speed and the equivalent wind speed (i.e., differences less than 0.1 m s^{-1}). One can thus safely assume the hub height wind speed to be representative in power production assessment for unstable and neutral conditions. For stable conditions differences increase, and in line with Figure 6.4 it is found that the hub height wind speed is smaller than the equivalent wind speed for the surface layer wind profile (i.e., one underestimates the amount of kinetic energy in the rotor disc area), and vice versa for the boundary layer wind profile. If the absolute differences between the equivalent wind speed and the hub height wind speed are considered, than in general

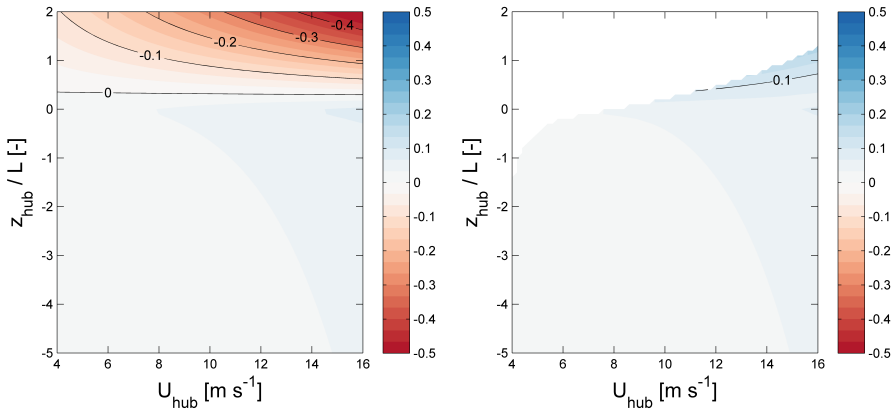


Figure 6.6: Difference between the hub height wind speed and the equivalent wind speed for the surface layer wind profile (left panel) and the boundary layer wind profile (right panel) as a function of hub height wind speed and atmospheric stability.

one finds differences to be less than 0.3 m s^{-1} . As such, it is expected that only in rare situations (very stable and near rated wind speeds) adopting the equivalent wind speed for power production assessment will be of influence.

6

6.3.4. EQUIVALENT WIND SPEED FOR LLJ WIND PROFILES

For the low-level jet model also the difference between the equivalent wind speed and the hub height wind speed is assessed. Results are shown in Figure 6.7. It is found that for the low-level jet wind profiles, the difference between the hub height wind speed and the equivalent wind speed is substantially larger as was found for the diabatic wind profiles. For low-level jets situated exactly at the hub height, the hub height wind speed can be up to 2 m s^{-1} larger than the equivalent wind speed (though one can question if the wind turbine does not operate at rated power for such conditions). For low-level jets situated far above the wind turbine however, the hub height wind speed can be up to 1 m s^{-1} smaller than the equivalent wind speed. If the results shown in Figure 6.7 are compared to those presented in Figure 6.6, then it is clear that in the case of a low-level jet the equivalent wind speed differs much more from the hub height wind speed than for diabatic wind profiles. It is therefore expected that the introduction of the equivalent wind speed is especially useful when assessing the influence of low-level jets on wind turbine power production.

The effect of the specific shear profiles on both wind turbine power production as well as blade root bending moments will be considered in the following analyses of simulation data. For the bending moment assessment it is not sensible to consider the equivalent wind as a representative wind speed (the loads experienced by a wind turbine component do not depend on the magnitude of the flux of kinetic energy, but on the change of the wind in space and time). As such the applicability of the equivalent wind speed is only considered when assessing wind turbine power production as a func-

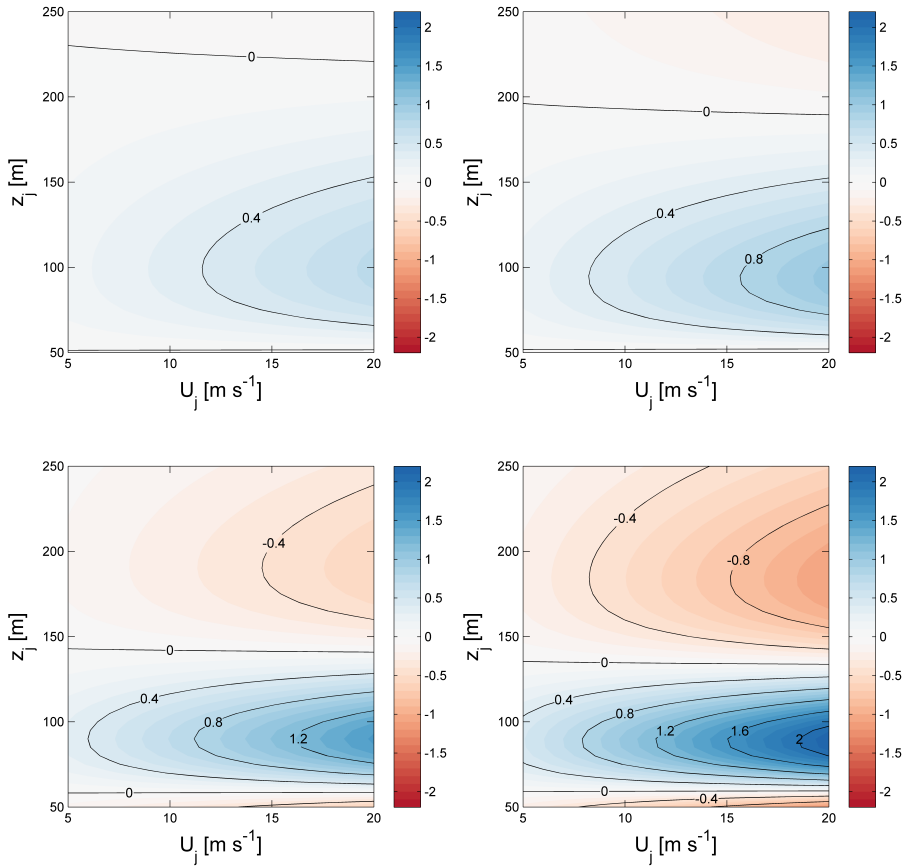


Figure 6.7: Difference between the hub height wind speed and the equivalent wind speed using the low-level jet model for a given jet height and jet speed. The individual panels correspond to the parameter settings similar as used in Figure 6.5.

tion of low-level jet characteristics.

6.4. SIMULATION RESULTS

Simulations are executed with the wind turbine design software Bladed and the reference 5 MW NREL wind turbine similar as described in Chapter 5. First the influence of diabatic shear profiles on wind turbine performance is discussed, and afterwards it is assessed how low-level jets influence wind turbine performance. Seven specific stability conditions are considered for the diabatic shear profiles as shown in Table 6.1 to reduce the computational expenses of the simulations. In Table 6.1 also the minimum wind speed at which the boundary layer wind shear profile computes a wind profile for the entire wind turbine can be found (i.e., up to 153 m height). Note that for stable con-

Table 6.1: Specific stability conditions used in the assessment of the influence of diabatic wind profiles on wind turbine performance.

Stability class	Specific stability	minimum \overline{U}_h
Very Unstable	$z_h / L = -2$	4.0 m s ⁻¹
Unstable	$z_h / L = -1$	4.2 m s ⁻¹
Near Neutral Unstable	$z_h / L = -0.5$	4.8 m s ⁻¹
Neutral	$z_h / L = 0$	7.5 m s ⁻¹
Near Neutral Stable	$z_h / L = 0.1$	8.5 m s ⁻¹
Stable	$z_h / L = 0.2$	9.5 m s ⁻¹
Very Stable	$z_h / L = 0.4$	11.1 m s ⁻¹

ditions, in comparison to the results presented in Chapter 3 very stable conditions are not considered, and the analyses are limited up to $z_h / L = 0.4$ (i.e., $L = 225$ m). This is on purpose done since for much stronger stable conditions the boundary layer profile shear profile only determines a wind profile up to the maximum blade tip height for above rated wind speeds. As such only above rated power production would be assessed for such strong strong stable stratifications, and it is not expected that there is a significant variation in power production for above rated wind speeds. For the low-level jet wind profiles the performance of a wind turbine will be assessed in a sensitivity study, by altering either the hub height or one of the the model parameters P_1 and P_2 .

6.4.1. DIABATIC WIND PROFILES AND POWER PRODUCTION

The influence of the diabatic wind shear profiles on wind turbine power production is shown in Figure 6.8. Both the absolute and relative difference in power production compared to a reference simulation in which the wind speed is constant with height is shown. For high wind speeds it is found that for all stability conditions considered wind shear does not influence power production, since the pitch controller limits power production to rated power.

For the surface layer wind shear profiles it is found that for the majority of stability conditions considered, the wind turbine power production is less than one would obtain assuming constant wind speed across the rotor disc. Only if the atmosphere becomes stable stratified with $z_h / L = 0.4$ the power production equals the power production assuming constant wind speed. It is expected that if stronger stable stratification would be considered, it would be found that the power production is higher compared to assuming constant wind speed. At first sight it is remarkable to find that the surface layer wind shear profile has a minimum power production for neutral stratification. If the results are placed in perspective of Figure 6.4 however, it is note that indeed the kinetic energy flux through the rotor disc has a minimum for near neutral conditions. If the atmosphere changes from neutral to very unstable, the power production for a given hub height wind speed slowly increases. In terms of the magnitude of the decrease in power production, it is found that for neutral conditions the surface layer wind profile results in a 1% decrease in wind turbine power production compared to using a constant wind speed across the rotor disc.

For the boundary layer wind shear profile it is found first of all that there is a larger

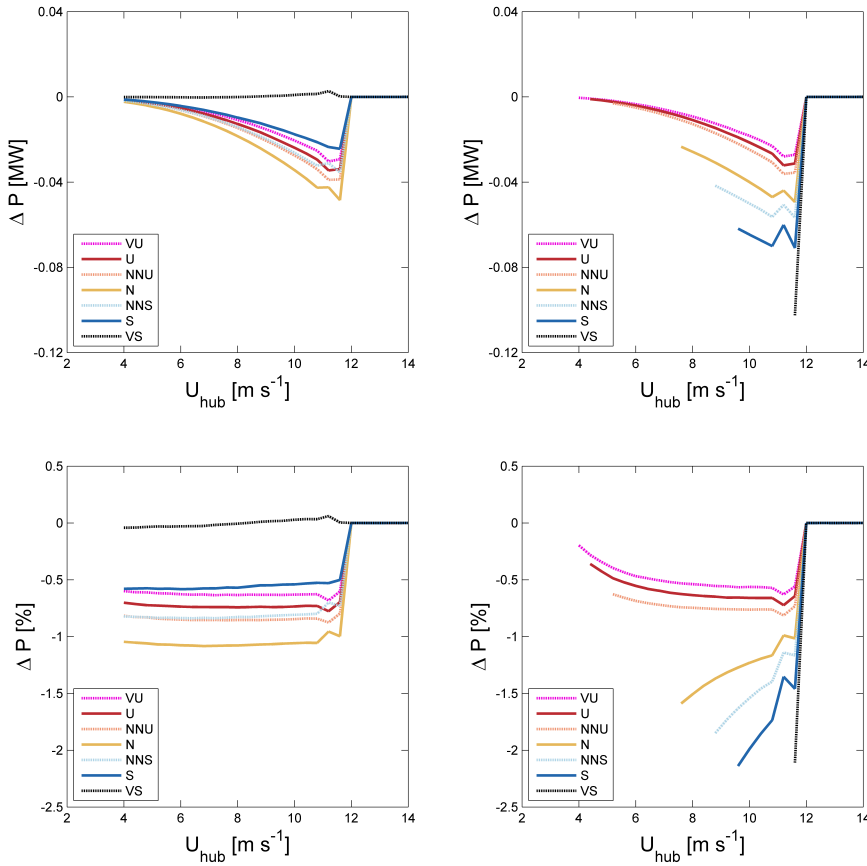


Figure 6.8: Difference in simulated wind turbine power production considering either constant wind speed or wind shear across the rotor disc. The individual panels correspond to the absolute (upper panels) and relative (lower panels) difference when using the surface layer (left panels) or the boundary layer (right panels) shear profile. See Table 6.1 for a clarification of the colours used.

decrease in power production. For stable stratifications (and near rated wind speeds) the boundary layer wind shear profile results in about 2% less power production compared to assuming constant wind speed across the rotor disc. Since the wind profile cannot be determined up to the maximum blade tip height for stable conditions and low hub height wind speeds with the boundary layer wind profile, it is unclear if there is an even stronger reduction in power production for stable conditions and low ($< 10 \text{ m s}^{-1}$) hub height wind speeds. In contrast to the surface layer wind profile, neutral conditions do not result in a minimum power production here. Instead, there appears to be a gradual increase in power production (for a given fixed hub height wind speed) if the atmosphere changes from stable to neutral or from neutral to unstable stratification. Do note as well that, for the stabilities considered, there always is a decrease in power production com-

pared to using a constant wind speed across the rotor disc. It is thus very well possible that the expected lifetime power production for offshore wind turbines (assuming the dimensions of the 5 MW NREL wind turbine) is overestimated for offshore sites.

When specifically comparing the surface layer and boundary layer wind shear profile, notice that for unstable conditions power production is slightly higher when using the boundary layer wind profile as using the surface layer wind profile. For stable conditions power production is higher when using the surface layer wind profile.

6.4.2. DIABATIC WIND PROFILES AND FATIGUE LOADS

Next, the variation in the bending moment of the blade root in flapwise direction is considered. Since in this chapter simulations with constant wind conditions (i.e., no turbulence) are used, there is no need to convert fatigue loads into equivalent loads as done in Chapter 5. Besides, although it is possible to calculate fatigue loads of specific wind turbine components, the simulated loads do not correspond to actual conditions offshore since in reality shear and turbulence combined cause variations in bending moments and subsequently fatigue loads. As such, the variation in the bending moment of the blade root in flapwise direction are considered instead of fatigue loads. The variation of the bending moment, quantified with the standard deviation for a given simulation, provides a first indication if at least the blade root fatigue loads are expected to increase or decrease for prescribed shear conditions. Besides, for the diabatic wind profile it is obvious that an increase in wind shear (i.e., from unstable to neutral and stable conditions) results in a higher variation in the blade root bending moment. For the diabatic shear profiles it is therefore decided to assess the change in the standard deviation of the blade root bending moment instead of the absolute standard deviations. Results are presented in Figure 6.9, where the standard deviation of the blade root flapwise bending moment is shown for specific stability conditions using the boundary layer wind shear profile relative to using the surface layer wind shear profile. As such, positive values indicate the boundary layer wind shear profile results in higher variations in the bending moment as using the surface layer wind shear profile.

The general trend that appears from Figure 6.9 is that the boundary layer wind shear profile results in (slightly) higher variations in the bending moment for unstable conditions (about 0.5-1.5%), and for near neutral conditions (up to 8% higher), while for stable conditions the variations rapidly decrease (by up to 14%). The strong reduction in variations of the blade root bending moment in flapwise directions for stable conditions is obviously caused by the substantial decrease in shear when using the boundary layer wind shear profile (see also the validation of the wind profile in Chapter 3 Figures 3.5 and 3.6).

There is a clear difference in the relative variations of the blade root bending moment for below and above rated wind speeds, depending on stability. For unstable and neutral conditions the relative variations of the bending moment increase with increasing wind speed as long as the hub height wind speed is below rated. Next, for wind speeds of about 11 to 18 m s⁻¹ the relative variations of the bending moment decrease again slightly, and for even higher wind speeds they increase again. For stable conditions there is in general an increase in the relative loads for low wind speeds (say, below rated, though the black line has a maximum at above rated wind speed), and for all higher wind speeds

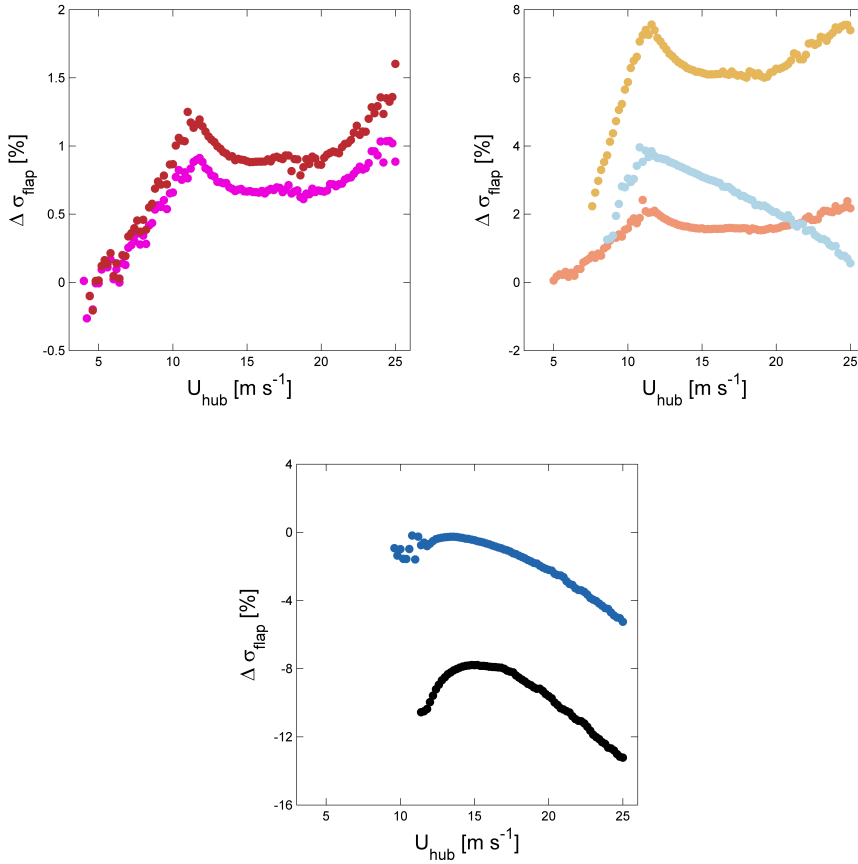


Figure 6.9: Relative difference in the standard deviation of the blade root bending moment in flapwise direction when using the surface layer and boundary layer wind shear profiles for various stability conditions (see Table 6.1 for details). The upper left panel shows very unstable (magenta) and unstable (dark red) conditions, the upper right panel shows near neutral unstable (light red), neutral (yellow) and near neutral stable (light blue) conditions, and the lower panel shows stable (dark blue) and very stable (black) conditions.

the relative variations of the bending moment decreases with increasing wind speed.

6.4.3. LOW-LEVEL JET WIND PROFILES AND POWER PRODUCTION

The influence of low-level jets on the simulated power production is assessed in terms of the hub height wind speed as well as the equivalent wind speed since it has previously been found that there is a substantial difference between both wind speeds for the low-level jet model. First the traditional assessment is adopted and wind turbine power production is assessed as a function of hub height wind speed. Results are shown in Figure 6.10. It is decided to assess the influence of the jet height and the influence of the model parameters P_1 and P_2 to the power curve. The simulations are run with a low-

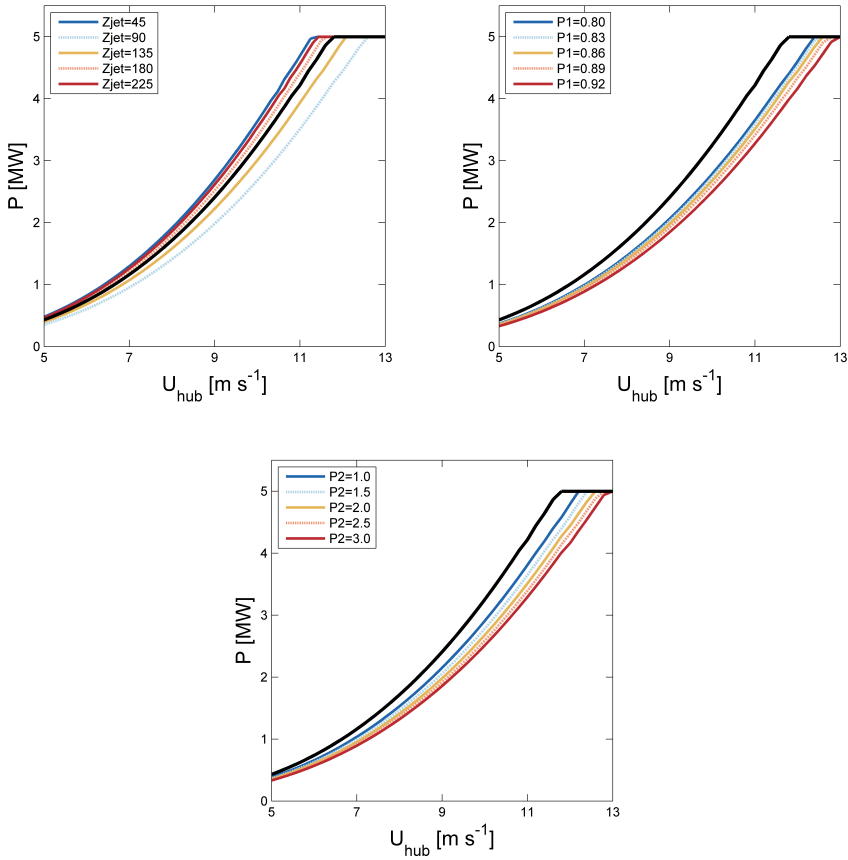


Figure 6.10: Sensitivity of the wind turbine power curve (as a function of hub height wind speed) to specific model parameters of the low-level jet. The individual panels show the sensitivity to the jet height (upper left panel), the model parameter P_1 (upper right panel) and the model parameter P_2 .

level jet fixed at the hub (i.e., $z_j = 90$ m), $P_1 = 0.86$ and $P_2 = 2$, and these parameters are altered as shown in the legends of Figure 6.10. The solid black line shown in each panel corresponds to the power curve in absence of wind shear.

First, it is assessed how the power curve depends on the height of the low level jet. It is found that if the low-level jet occurs exactly at the hub, there is a severe decrease in power production compared to the expected (dashed line) power curve assuming no shear. Since the power production at a given wind speed is thus reduced, also the power at the expected rated wind speed is not yet equal to the rated power. When the jet height increases to higher altitudes, either within or above the upper half of the wind turbine rotor disc, the power production starts to increase and can be higher compared to the reference constant wind speed power curve. In general it is found that wind turbine power production increases if the the jet height is located at higher altitudes. The power

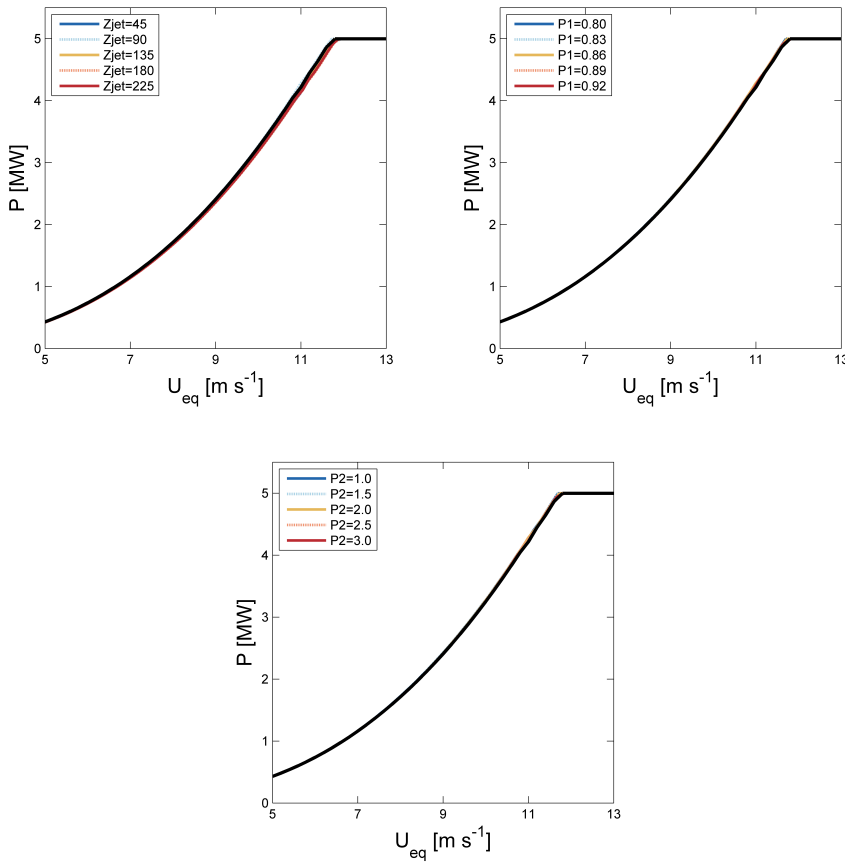


Figure 6.11: Power curve assessment similar as Figure 6.10 but as a function of the equivalent wind speed.

production also rapidly increases if the jet height decreases to heights in between the surface and the hub height, In the upper left panel of Figure 6.10 it can be seen that the highest power production (for a given hub height wind speed) occurs when the jet height is well below the hub height at 45 m height.

Next, let us consider how the model parameter P_1 influences wind turbine power production. The power production is for all simulates less then the reference power curve since a constant jet height of 90 m is considered. It is found that there is a gradual decrease in power production when P_1 increases. This shows that the higher the difference between the jet speed and the background wind profile (and thus the higher the wind shear above and below the jet height), the lower the power production. For decreasing values of P_1 the deficit between the low-level jet power curve and the reference power curve decreases.

When the model parameter P_2 is altered, results are similar as found for P_1 , and again

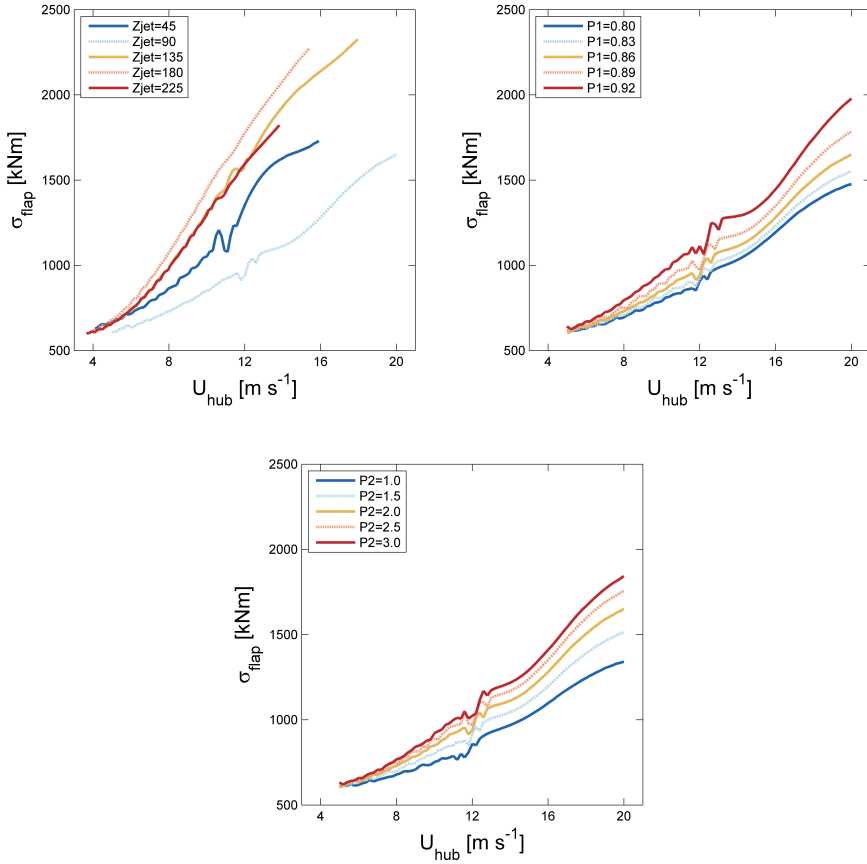


Figure 6.12: Sensitivity of the variation in the blade root bending moment in flapwise direction to specific model parameters of the low-level jet. The individual panels correspond to those presented in Figure 6.10.

the higher P_2 the lower the power production of the wind turbine becomes. Since a change in P_2 corresponds to changing the width of the low-level jet, it is expected that for very low P_2 the width of the jet increases and approaches eventually a uniform wind speed across the rotor disc. For such conditions the reference power curve shown would thus be approached.

The differences between the expected reference power curve and the numerous low-level jet power curves, in combination with the previously obtained result that substantial differences occur for the low-level jet model between the hub height wind speed and the equivalent wind speed (i.e., Figure 6.7), provide an argument to assess if the power curves are more uniform when power production is considered as a function of the equivalent wind speed. As such, Figure 6.11 shows the power curves as a function of the equivalent wind speed instead of as a function of the hub height wind speed. It is found that all power curves agree very well. This shows, in line with the results presented

in [Wagner et al. \(2011\)](#), that the equivalent wind speed is a much more representative wind speed when assessing wind turbine power production.

6.4.4. LOW-LEVEL JET WIND PROFILES AND FATIGUE LOADS

The variations of the blade root bending moment in flapwise direction are assessed for specific low-level jet conditions. Here however only the absolute variations of the blade root bending moment are considered, since it is on forehand not clear how the blade root bending moment depends on jet characteristics. Results are shown in [Figure 6.12](#).

It is found that if the jet height equals the hub height, the variations in the bending moment is substantially smaller as when the jet is located either below or above the hub. The variation of the bending moment increases rapidly when the jet is located above or below the hub height, but within the rotor disc (i.e., at either 45 or 135 m height). If the jet is positioned above the wind turbine, variations in the blade root bending moment remain high, but they will decrease. This is also expected, since if the jet is located very far above the hub, the wind profile across the rotor disc will start to correspond to the neutral logarithmic wind profile. For such conditions it is found (though not explicitly shown) that the variations are substantially less (around 1200 kNm for a hub height wind speed of 20 m s^{-1}). The influence of both parameters P_1 and P_2 is straightforward: if either P_1 or P_2 increases, the jet is sharper defined with more shear across the rotor disc (assuming the jet is located at hub height), hence variations in the blade root bending moment increase.

In all three panels of [Figure 6.12](#) it is found that the variation in the blade root bending moment increases smoothly for increasing wind speeds unless the wind speed is approximately 12 m s^{-1} where the profiles appear to be distorted. The wind turbine starts to operate at rated power at this specific wind speed (i.e., see [Figure 6.10](#)), hence the controller switches from aiming for ideal tip speed ratio to aiming for constant torque. This change in control behaviour causes the sudden variation in σ_{flap} when the wind turbine starts to operate at rated power.

6.5. DISCUSSION

The influence of diabatic shear profiles on wind turbine power production can be compared to results presented in literature, and the obtained results deviate substantially from [Wagner et al. \(2011\)](#) and [Wharton & Lundquist \(2012\)](#) who find higher power production for stable conditions compared to unstable conditions. Both studies consider wind shear in terms of a power law, hence it is likely that exact results differ, however it is possible to make a qualitative comparison in terms of "low shear" (low coefficient for the power law profile or unstable conditions for diabatic profiles) or "high shear" (high coefficient for the power law profile or stable conditions). In [Wagner et al. \(2011\)](#) it is shown that there is a minimum in the flux of kinetic energy through a wind turbine rotor disc for low wind shear conditions, with an increase in the kinetic energy flux if wind shear either vanishes or increases substantially. This is in line with the results presented in this chapter for the surface layer wind shear profile, where the kinetic energy flux and the wind turbine power production have a minimum for near neutral conditions, and both increase for unstable (decreasing wind shear) and stable (increasing wind shear)

conditions. However, for the boundary layer wind shear profile different results are obtained. As explained, this is caused by the decrease in wind shear when using the boundary layer wind shear profile. In Wharton & Lundquist (2012) observed power curves are assessed as a function of atmospheric stability, and it is found that power production increases for stable conditions, and decreases for unstable conditions. This is the exact opposite of the results presented in this chapter when using the boundary layer wind profile. Do note first of all however that since Wharton & Lundquist (2012) considers observation data, the effect of both wind shear and turbulence is included in the power curves, whereas in this chapter turbulence is neglected. Besides, and this is expected to be of more importance, it is mentioned in Wharton & Lundquist (2012) that they "found a higher rotor-averaged wind speed than hub-height wind speed under stable conditions, and consequently greater energy production". Since in this study the hub height wind speed is kept constant (and thus the equivalent wind speed differs for stable and unstable conditions), results will by definition differ from those presented in Wharton & Lundquist (2012).

If the results presented for the impact of low-level jets on wind turbine performance are considered in more detail, it has to be noted that in this chapter a wide range of conditions in terms of the jet speed and jet height has been considered. This includes some conditions that are highly unlikely to occur: jets close to the surface with very high jet speeds, and jets higher up in the atmosphere with very low jet speeds (see also the dependence shown in Chapter 4 Figure 4.3). As such, in practice not all combinations occur, and it would be valuable to assess the actual impact of LLJ on wind turbine performance based on observed jet characteristics. Also, it is frequently assumed that low-level jets have a possible beneficial influence on wind turbine power production due to high wind speeds, while causing increased fatigue loads due to the occurrence of high wind shear. Based on the results presented in this chapter, this reasoning is not necessarily true, and in principle it is a subjective reasoning as well since it depends on what you compare the resulting wind turbine performance to. As shown in Figure 6.10, a jet that occurs at hub height in fact causes a decrease in wind turbine power production compared to the theoretic power curve of the considered wind turbine. At the same time, the resulting blade root bending moment decreases, and the combined effect is thus the exact opposite of what is frequently assumed. One therefore has to be careful with conclusions.

6.6. CONCLUSIONS

In this chapter the influence of specific wind shear profiles on wind turbine performance is assessed. The wind shear profiles considered are two diabatic wind profiles, and low-level jet wind profiles with various jet characteristics. In absence of a simple engineering low-level jet model, it has been decided to first formulate a new low-level jet model that can be used for wind energy purposes. It is assumed that the low-level jet can be considered a superposition of a local wind maximum on top of a standard neutral logarithmic wind profile. Besides, one can define a specific jet height and jet speed for the low-level jet model, which is an advantageous characteristic for wind energy assessment.

The influence of the specific shear profiles on wind turbine performance is assessed in terms of theoretic quantities (the rotor disc kinetic energy flux, and the rotor disc

equivalent wind speed), as well as simulation data (power production and variation of the blade root bending moment in flapwise direction). For the diabatic shear profiles it is found that both the surface layer wind profile and the boundary layer wind profile frequently result in a reduction in the flux of kinetic energy through the rotor disc compared to uniform wind speed across the rotor disc. The simulation results confirm this, and wind turbine power production for sheared wind conditions is reduced compared to uniform wind conditions by up to 2.5%, depending on the exact wind shear (i.e., atmospheric stability). With respect to the blade root bending moment, it is found that for unstable and (near) neutral conditions the boundary layer wind shear profile results in higher variations in the bending moment, up to 2% for unstable conditions and up to 8% for neutral conditions. For stable conditions however the boundary layer shear profiles results in substantial lower variations in the bending moment, by up to 15%. The results are in line with the behaviour of the wind profiles shown in Chapter 3, where it was shown that the boundary layer wind profile results in slightly higher shear for unstable and near neutral conditions, but substantial lower shear for (very) stable conditions.

For the low-level jet model it is found that the hub height wind speed is not necessarily a representative wind speed any longer for power production assessment, and the kinetic energy flux through the rotor disc can differ up to 25% from uniform wind conditions. This is also found when assessing the power curves obtained with simulation data. When considering the power curves obtained with simulation data, it is found that wind turbine power production strongly diminishes when the low-level jet is located exactly at hub height. The hub height wind speed however is no representative wind speed for low-level jet shear profiles, and if instead power curves are considered as a function of the rotor disc equivalent wind speed all power curves obtained with numerical simulations virtually collapse onto each other. For the blade root bending moment in flapwise direction it is found that low level jets that occur exactly at hub height cause lowest variations. Besides, the height at which the low-level jet occurs is found to be of much higher importance than the strength or width of the low-level jet.

It is clear based upon the obtained results that especially for resource assessment and wind turbine power forecasting wind shear should be taken into account. The hub height wind speed is obviously no representative wind speed, especially for low-level jet conditions. Especially on shore, though not the scope of this thesis, jets can occur frequently and for long periods of time (Baas et al. (2009)), and neglecting wind shear is expected to cause a severe error both in day-ahead power forecasting as well as in lifetime power estimations.

7

WIND TURBINE PERFORMANCE AS A FUNCTION OF TURBULENCE SCALES

Forecasting is very difficult especially if it is about the future...

Niels Bohr

The majority of research carried out in the field of wind energy aims to reduce the cost of energy, typically by increasing wind turbine efficiency, reducing construction costs or reducing wind turbine downtime in case of malfunctioning. However, even if a turbine is operating at the intended efficiency and failures do not occur, there is the inherent difficulty that wind power cannot be regulated as easily as conventional power production without operating at sub-optimal levels. Besides, for wind power forecasting one not only has to deal with the uncertainty in weather forecasts, but also with variations in power production for given mean wind speeds. Part of these variations have been explained in Chapter 6, where it was found that wind shear influences wind turbine power production. Similarly, turbulence might also cause variations in power production, hence in this chapter the impact of turbulence on power production is assessed in more detail.

It is recognised that both the amount of turbulent energy, as well as the size of turbulent structures, may influence wind turbine performance. With aid of numerical simulations it is possible to control inflow conditions of a wind turbine, which will be useful for the assessment. Although simulation simplifications do pose restrictions in quantitative conclusions, the qualitative interpretation of results should lead to fundamental understanding how and why wind turbine performance varies for given mean wind conditions.

This chapter will be submitted for publication as: Holtslag, M. C. & Bos, R (2016), 'Wind turbine performance as a function of turbulence scales'.

7.1. INTRODUCTION

Wind energy has established itself as one of the most economically viable renewable energy sources. For 2020, the European Wind Energy Association (EWEA) has estimated that wind energy will supply between 12.8% and 16.9% of the EU's total electricity demand ('EWEA' 2014). But since large-scale energy storage is still not realised, a plant operator has to be able to forecast the intended power generation (e.g., for the next day) in order to compete with other energy sources. Wind power forecasts are made with statistical models of wind farms, which require meteorological input parameters obtained from numerical weather prediction models. Not only does the need for weather forecast data introduce uncertainty in the power forecast, but actual power production may deviate from the expected theoretic power production based upon power curves for known mean wind speeds. This deviation is, apart from mechanical issues (e.g., yaw misalignment), primarily caused by turbulence and wind shear: two mechanisms that influence power production on short time scales that are typically not included in power curves. As a result wind power forecasts will always contain some uncertainty, which is a disadvantage of wind power compared to conventional, regulated power production.

There have been many attempts to quantify the short-term variations in wind power. Full scale tests indicate that higher turbulence levels generally lead to an increase in energy production, at least for below rated wind speed (Bleiber et al. 2006, Elliott & Cadoogan 1990, Milan et al. 2013, Muljadi et al. 1997, Sumner & Masson 2006). Near and above rated wind speed, the opposite effect is sometimes found as well (Gottschall & Peinke 2008, Honrubia et al. 2012). However, as wind shear and turbulence intensity are both dependent on the stability of the atmosphere as shown in Chapter 2, it is difficult to understand the role of each mechanism separately based on field tests alone. The impact of wind shear on wind turbine power production has been discussed in Chapter 6. The effect of turbulence is not straightforward, as it involves a wide range of eddy scales that each interact differently with a turbine. Wind tunnel tests, where scale models are placed behind a grid, are either inconclusive (Sicot et al. 2006) or show a decrease in power with increasing turbulence levels (Mikkelsen 2013). However, it is questionable whether such effects can be accurately quantified with wind tunnel models, since the performance of airfoils is known to be sensitive to turbulence at low Reynolds numbers (Devinant et al. 2002).

The aim of this chapter is to develop a better understanding of the role of turbulence in wind power generation. In contrast to field studies or wind tunnel models, here a numerical approach is adopted by modelling the 5 MW NREL reference turbine in a turbulent wind field, without including wind shear. By filtering the wind fields over a range of wave numbers (i.e., scales of turbulent structures) and recalculating the power production for each step, it is possible to find out which eddy scales are relevant and which are simply ignored by the turbine.

7.2. THEORY

The traditional way to determine the power coefficient, C_p , is by assuming the power production of a wind turbine equals

$$\bar{P}_s = \frac{1}{2} C_p \rho A \bar{U}_h^3 \quad (7.1)$$

where \overline{P}_s is the average (low-speed) shaft power in a given time interval, ρ is the air density (assumed to be constant in space and time), A is the rotor disc area, and \overline{U}_h is the mean hub height wind speed. Let us consider the derivation of Equation (7.1) but now including turbulence. First, the total kinetic energy in the wind, per unit mass¹, is on average

$$KE = \frac{1}{V(B)} \iiint_B \frac{1}{2} (\mathbf{u}(\mathbf{x}) \cdot \mathbf{u}(\mathbf{x})) \, dx \, dy \, dz = \frac{1}{2} (\overline{u^2 + v^2 + w^2}) \quad (7.2)$$

where $\mathbf{u}(\mathbf{x}) = [u, v, w]^T$ is the wind speed vector, $\mathbf{x} = [x, y, z]^T$ is a position vector, B is a three-dimensional domain with a volume $V(B)$, and the overbar is used to denote averaging. In scope of the turbulence assessment of this chapter, the wind vector is decomposed using Reynolds decomposition. Assuming absence of subsidence (i.e., $\overline{W} = 0$) and a coordinate system aligned with the mean horizontal wind (i.e., $\overline{V} = 0$), one obtains

$$KE = \frac{1}{2} (\overline{U^2} + \overline{u'^2} + \overline{v'^2} + \overline{w'^2}) \quad (7.3)$$

Under Taylor's hypothesis, turbulence is considered frozen (i.e., $d/dt = 0$) and is advected with the mean wind speed \overline{U} . In that case, the average power flowing through an area A is given by

$$\overline{P} = \frac{1}{2} \rho \overline{U} A (\overline{U^2} + \overline{u'^2} + \overline{v'^2} + \overline{w'^2}) \quad (7.4)$$

If the definitions of mean kinetic energy per unit mass (MKE) and turbulent kinetic energy per unit mass (TKE) are introduced as in [Stull \(1988\)](#),

$$MKE = \frac{1}{2} (\overline{U^2} + \overline{V^2} + \overline{W^2}) \quad (7.5)$$

$$TKE = \frac{1}{2} (\overline{u'^2} + \overline{v'^2} + \overline{w'^2}) \quad (7.6)$$

it should be easy to see that the average power in the wind is a function of both the mean kinetic energy as well as the turbulent kinetic energy:

$$\overline{P} = \rho A \overline{U} (MKE + TKE) \quad (7.7)$$

since it is assumed that $\overline{V} = \overline{W} = 0$. Hence, the power production of a wind turbine may vary depending on the amount of TKE present in the atmosphere. With the above set of equations, the power coefficient of a wind turbine can be expressed as

$$C_P = \frac{\overline{P}_s}{\rho A \overline{U} (MKE + TKE)} \quad (7.8)$$

This is different from the classical definition of Equation 7.1, which only takes into account the MKE. However, since TKE only consists of quadratic terms, its contribution to

¹Since it is common to treat mean kinetic energy (MKE) and turbulence kinetic energy (TKE) as mean properties, this is extended to the total kinetic energy (KE) as well to avoid confusion.

the total kinetic energy is always positive. The question is if this is also converted into useful power.

In addition, with aid of turbulence spectra, it is also possible to investigate the effect of the scales of motion on wind power production. A turbulence spectrum describes how TKE is distributed over wave number, k :

$$TKE = \int_0^{\infty} E(k) dk \quad (7.9)$$

where $E(k)$ is the energy spectrum. Commonly used spectral models in wind energy include the Mann model (Mann 1994) and the Kaimal model (Kaimal et al. 1972). Because a wind turbine has a certain response time, but also because smaller velocity fluctuations cancel out over the length of a blade, it is expected that large coherent structures are converted into power more efficiently than smaller structures.

7.3. METHODOLOGY

7.3.1. SIMULATION SET-UP

The impact of turbulence scales on wind turbine performance is analysed based on numerical simulations to control inflow conditions as much as possible. All simulations are carried out with the 5 MW NREL reference turbine in FAST v7. Specifications of the 5 MW NREL turbine have been presented in Chapter 5, and Table 5.1. In order to only take into account the effect of turbulence on the rotor disc, the calculations are done without tower shadow effects and with zero shaft tilt, and drive train losses are not considered. Furthermore, the first minute of every simulation is discarded to avoid any start-up transients.

Since the effect of wind shear falls outside the scope of this research, all simulations are carried out with a mean horizontal wind speed that is constant with height. Superimposed on the mean wind speed, a turbulent velocity field is generated through a 3D FFT, leading to

$$\mathbf{u}(\mathbf{x}) = \begin{bmatrix} \bar{U} \\ 0 \\ 0 \end{bmatrix} + \sum_{\mathbf{k}} \mathbf{C}(\mathbf{k}) \mathbf{n}(\mathbf{k}) e^{i\mathbf{k} \cdot \mathbf{x}} \quad (7.10)$$

where $\mathbf{k} = [k_x, k_y, k_z]^T$ is the wave number vector, \mathbf{C} is a matrix of coefficients, and \mathbf{n} is a complex white noise vector with zero mean and unit variance. For a domain with N_i elements and a length L_i in the i th dimension, the wave numbers are given by

$$k_i = \frac{2\pi m}{L_i} \quad (7.11)$$

for the integers $m = N_i/2, \dots, N_i/2 - 1$. The matrix \mathbf{C} can be derived from the spectral tensor $\Phi(\mathbf{k})$ by

$$\mathbf{C}^*(\mathbf{k}) \mathbf{C}(\mathbf{k}) \approx \Phi(\mathbf{k}) \Delta k_x \Delta k_y \Delta k_z \quad (7.12)$$

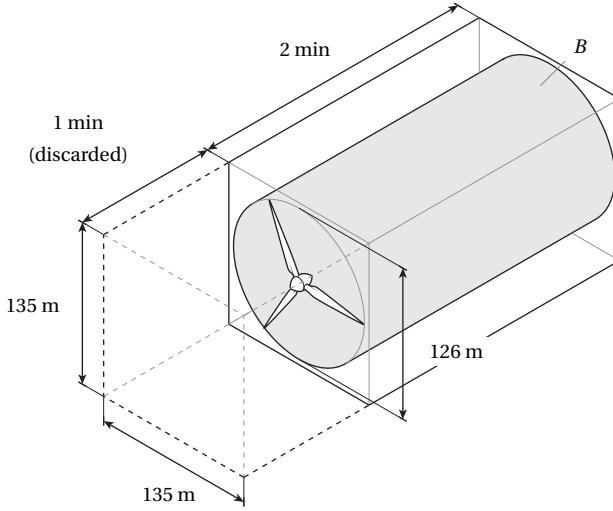


Figure 7.1: Sketch of the wind field. The TKE inside the cylinder (B) is controlled for every wind field.

with $*$ denoting a conjugate transpose (Mann 1998). It is assumed that turbulence is incompressible and isotropic with the spectral tensor given by Batchelor (Batchelor 1953):

$$\Phi_{ij}(\mathbf{k}) = \frac{E(k)}{4\pi k^2} \left(\delta_{ij} - \frac{k_i k_j}{k^2} \right) \quad (7.13)$$

where $k = \|\mathbf{k}\| = \sqrt{k_x^2 + k_y^2 + k_z^2}$ and δ_{ij} is the Kronecker delta. Moreover, for $E(k)$, the isotropic energy spectrum by Von Kármán (von Kármán 1948) is adopted:

$$E(k) = \frac{4\Gamma(\frac{17}{6})}{\sqrt{\pi}\Gamma(\frac{1}{3})} \frac{\sigma_{\text{iso}}^2 k^4 l^5}{(1 + k^2 l^2)^{17/6}} \quad (7.14)$$

where l is the turbulent length scale, $\Gamma(x)$ is the gamma function, and

$$\sigma_{\text{iso}}^2 = \overline{u'^2} = \overline{v'^2} = \overline{w'^2} = \frac{2}{3} TKE \quad (7.15)$$

is the isotropic variance.

From Equations 7.12 and 7.13, the matrix \mathbf{C} can be defined as:

$$\mathbf{C}(\mathbf{k}) = \sqrt{\frac{2\pi^2 E(k)}{L_x L_y L_z k^4}} \begin{bmatrix} 0 & k_z & -k_y \\ -k_z & 0 & k_x \\ k_y & -k_x & 0 \end{bmatrix} \quad (7.16)$$

where $L_x \times L_y \times L_z$ is the total domain size. The downside of using a 3D FFT is that the domain has to be large enough to properly fit the largest eddies (Mann 1998). For this reason, the grid size is increased to 128×128 ($\approx 540 \times 540$ m) in the lateral and vertical

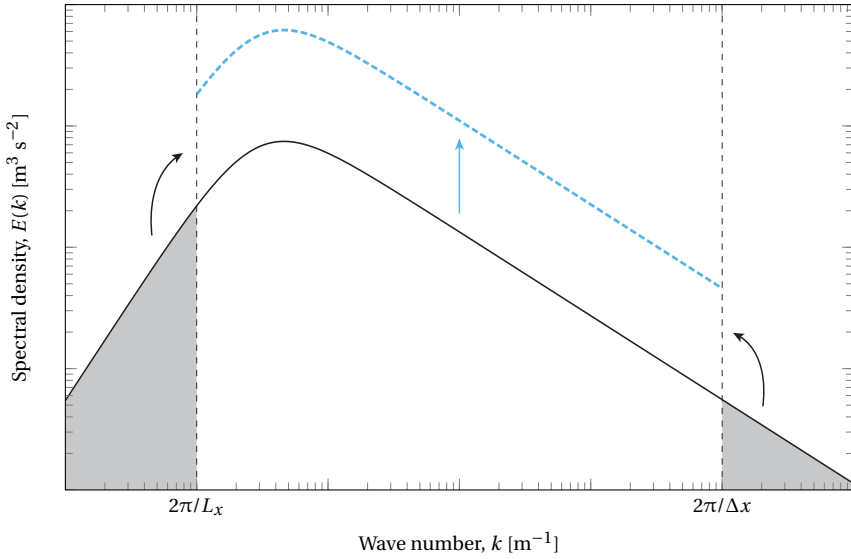


Figure 7.2: Effect of incorrectly scaling the velocities to meet a target variance. Because the largest and smallest eddies in a numerical simulation are determined by respectively the size of the domain L_x and the grid spacing Δx , some TKE (indicated in gray) is not resolved. The variance in the velocity field is thus less than expected. If one erroneously corrects the velocities (blue line), this TKE is added to the medium sized eddies.

directions to perform the FFT, but only a 32×32 ($\approx 135 \times 135$ m) subvolume is ultimately fed to the aeroelastic model to reduce computational demand of the simulations. At a longitudinal sampling frequency of 10 Hz, the total domain length could be increased to 3 minutes before running into memory problems ($\approx 3 \cdot 10^7$ grid points). A sketch of the domain is shown in Figure 7.1.

7.3.2. FILTERING FOR EDDY SIZES

In order to assess the role of different eddy sizes on wind turbine performance, an ideal low-pass filter is used:

$$G(k) = H(k_0 - k) \quad (7.17)$$

where $G(k)$ is the spectral window, k_0 is the cut-off wave number, and $H(k)$ is the Heaviside step function. To control the amount of TKE, each velocity field is corrected after filtering to ensure that

$$\frac{1}{V(B)} \iiint_B \frac{1}{2} (\mathbf{u}(\mathbf{x}) \cdot \mathbf{u}(\mathbf{x})) \, dx \, dy \, dz = \int_{2\pi/L_x}^{k_0} E(k) \, dk \quad (7.18)$$

where the triple integral is carried out over the cylinder depicted in Figure 7.1 with a volume of $V(B) = \frac{1}{4} \pi D^2 \cdot 120 \bar{U}$. This takes into account that the TKE lost by filtering in the wave number domain is correctly translated to the spatial domain. Also, any TKE

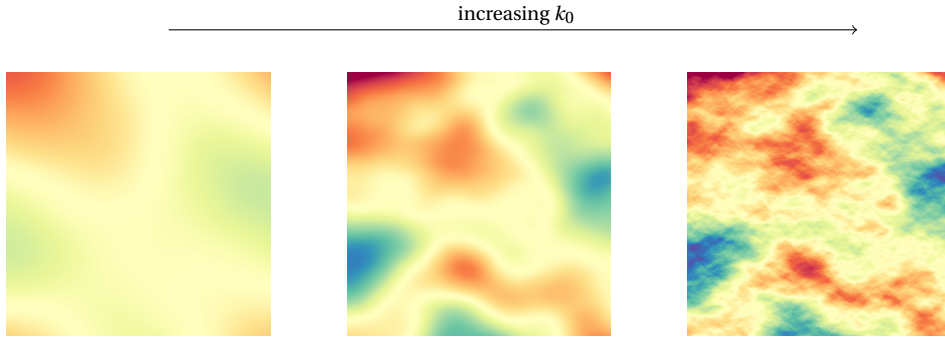


Figure 7.3: Effect of the low-pass filter on an arbitrary velocity field.

stored in very low wave numbers ($k < 2\pi/L_x$) or in the subgrid ($k > 2\pi/\Delta x$) is discarded to make sure it is not incorrectly redistributed as shown in Figure 7.2.

The filter wave number k_0 is moved from low to high wave numbers, meaning that the TKE is added to the largest turbulent structures first (see Figure 7.3 for clarification). The filtering procedure is executed for each turbulence seed separately to directly compare the effect of adding smaller eddies for a given stochastic wind field. With aid of the filter it is possible to investigate the effect of turbulent structures of a specific scale on wind turbine performance. In the following section, the behaviour of various parameters (i.e., power production, power coefficient, etc.) will be expressed as a function of k_0 .

7.4. RESULTS

7.4.1. CASE DESCRIPTION

First, a set of simulations is run to obtain the (shaft) power curve at different turbulence intensities (see Figure 7.4), where turbulence intensity is defined as

$$TI = \frac{\sigma_{\text{iso}}}{\bar{U}} \quad (7.19)$$

Below rated wind speed, a higher turbulence intensity (i.e., more TKE) clearly leads to an increase in shaft power, even beyond the “classical” Betz limit (i.e., $\frac{16}{27}$ of the power available from MKE, excluding turbulence). However, the pitch controller, which limits power production to rated power for high wind speeds, reverses this effect at near rated and above rated wind speeds. For such wind speeds, the controller imposes an upper limit on the generator torque, and the net effect of generator torque fluctuations caused by turbulence will be a decrease in power production. For the wave number filter assessment simulations are performed for mean wind speeds of 7.5 m s^{-1} (below rated) and 15 m s^{-1} (above rated). For these wind speeds the controller should aim for the ideal tip speed ratio and a constant torque, respectively.

Four separate simulation cases are defined to assess the response of a wind turbine to varying atmospheric conditions (see Table 7.1). A reference case (case-R) is defined with a mean hub height wind speed of $\bar{U} = 7.5 \text{ m s}^{-1}$ (i.e., well above cut-in wind speed

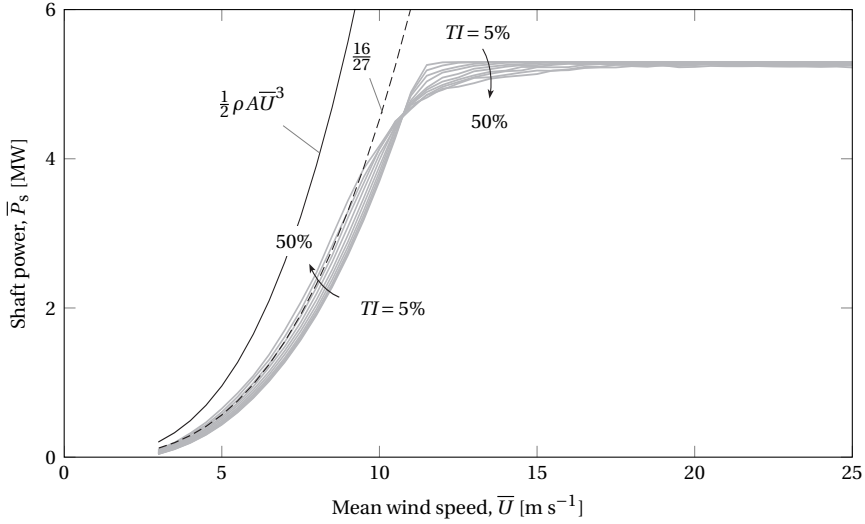


Figure 7.4: Shaft power of the 5 MW NREL at different turbulence levels, where the turbulence intensity (TI) is increased in steps of 5% from 5% to 50%. The rated wind speed is $\bar{U} = 11.4 \text{ m s}^{-1}$. Added in black is the power available from the mean kinetic energy (MKE), together with $\frac{16}{27}$ of that amount (dashed line); i.e., the Betz limit.

Table 7.1: Simulation settings for the difference cases.

case	\bar{U} [m s^{-1}]	TI [%]	l [m]	$L_x \times L_y \times L_z$ [m]	$\Delta x \times \Delta y \times \Delta z$ [m]
case-R	7.5	14	33.6	$1,350 \times 537.6 \times 537.6$	$0.75 \times 4.2 \times 4.2$
case-U	15.0	14	33.6	$2,700 \times 537.6 \times 537.6$	$1.50 \times 4.2 \times 4.2$
case-TI	7.5	28	33.6	$1,350 \times 537.6 \times 537.6$	$0.75 \times 4.2 \times 4.2$
case-L	7.5	14	67.2	$1,350 \times 537.6 \times 537.6$	$0.75 \times 4.2 \times 4.2$

and below rated wind speed). Furthermore, the turbulence intensity is set to $TI = 14\%$ and the turbulence length scale is taken as $l = 33.6 \text{ m}$, comparable to an IEC class B site for which the reference turbine was originally designed (Jonkman et al. 2009). The three remaining cases are defined by doubling either \bar{U} , TI , or l . First, in case-U, the hub height wind speed is multiplied by a factor 2, which will show the effect of turbulence on wind turbine performance for above rated wind speeds. The turbulence intensity is kept constant, meaning that the TKE will increase by a factor 4 compared to the reference case. Second, in case-TI, the turbulence intensity is increased by a factor 2 while keeping the hub height wind speed constant (again resulting in an increase in TKE by a factor 4) to investigate the effect of injecting more TKE into the system for similar mean wind speeds. Lastly, in case-L, the turbulence length scale is increased by a factor 2, which redistributes the TKE over the wave numbers (i.e., there will be relatively more energy contained in large structures). To increase the statistical certainty of the results, each case is executed with 100 turbulence seeds.

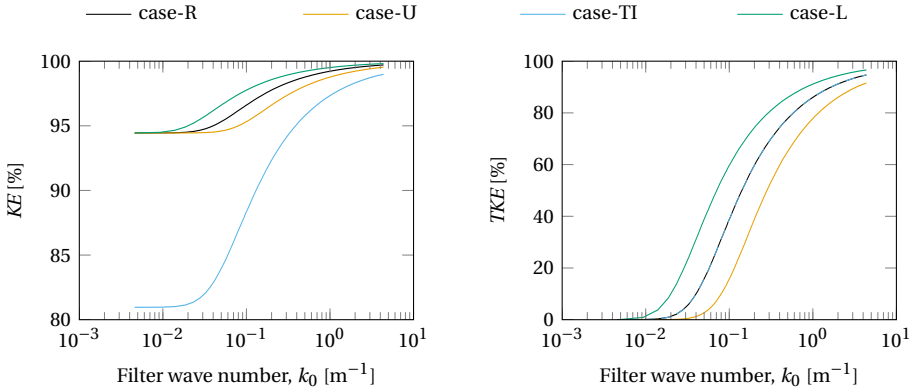


Figure 7.5: Amount of kinetic energy (KE, left panel) and turbulence kinetic energy (TKE, right panel) included in the simulations as a function of the filter wave number k_0 , relative to the theoretical maximum (i.e., $TKE_{\max} = \frac{3}{2}\sigma_{\text{iso}}$ and $KE_{\max} = \frac{1}{2}\bar{U}^2 + \frac{3}{2}\sigma_{\text{iso}}$).

7.4.2. EFFECT OF TURBULENCE SCALES ON POWER PRODUCTION

Figure 7.5 shows that the total kinetic energy KE and the turbulent kinetic energy TKE change as a function of filtering wave number k_0 . It is found that in absence of turbulence (i.e., by filtering at the smallest wave number), the total kinetic energy is reduced by 5 to 19% (depending on the case), meaning that the majority of KE originates from the mean flow. Even if only the largest turbulent structures are included (i.e., k_0 is small), there is virtually no TKE present in the flow. This indicates that the domain is sufficiently large, and that all the relevant scales at the lower wave numbers are included. When all turbulent structures are included (i.e., k_0 is large), at least 90% of all TKE (and at least 98% of the KE) is resolved. The remaining TKE is present in subgrid scale turbulent structures and is thus not resolved.

Although one could easily calculate the relative contribution of TKE to the total KE for isotropic conditions as

$$KE = MKE(1 + 3Tl^2) \quad (7.20)$$

the relative importance of turbulent structures of specific scales is not obvious. As seen in Figure 7.5, both the mean wind speed and the turbulent length scale determine how TKE is distributed over turbulent scales. However, the amount of TKE (i.e., case-TI) does not change the shape of the distribution, shown by the overlapping lines of case-R and case-TI. The mean wind speed influences the distribution since the wave number k_i (and thus the filter wave number k_0 as well) depends on the domain length as shown in Equation 7.11, which is given as $L_x = t \cdot \bar{U}$. The dependence of the turbulence spectrum on the turbulence length scale follows from Equation 7.14

Next, let us consider in more detail wind turbine characteristics as a function of turbulent scales. Table 7.2 provides an overview of the main results. Figure 7.6 shows the power production as a function of k_0 for each case. In absence of turbulence, the three

Table 7.2: Overview of simulation results, showing the result of the medians of 100 seeds. Differences are taken between the simulations without TKE and with all TKE. See Figures 7.5, 7.6 and 7.7 for details.

case	ΔKE [%]	ΔTKE [%]	$\overline{\Delta P_s}$ [kW]	$\overline{\Delta P_s}$ [%]	$\Delta C_P(KE)$ [-]
case-R	5.3	94.6	37.3	2.4	-0.015
case-U	5.1	91.5	0.3	0.0	-0.011
case-TI	18.0	94.6	151.7	9.7	-0.050
case-L	5.4	96.6	43.8	2.8	-0.013

cases with $\overline{U} = 7.5 \text{ m s}^{-1}$ obviously show the same power production ($\approx 1.56 \text{ MW}$). At $k_0 \approx 10^{-2} \text{ m}^{-1}$, the individual simulations start to deviate from each other, and power production generally increases when higher wave numbers are included. This corresponds, at least for case-R and case-TI, to the wave number where TKE is starting to appear (see the right panel of Figure 7.5). For case-L, TKE is already present at lower wave numbers. One would therefore expect that the increase in power production already starts at $k_0 < 10^{-2} \text{ m}^{-1}$, though this is not found in Figure 7.6. The increase in power production occurs at a frequency that corresponds to $k_0 = 2\pi/L_y$ (with $L_y = L_z \approx 540 \text{ m}$) $= 1.17 \cdot 10^{-2} \text{ m}^{-1}$. For lower wave numbers turbulence is not well defined since isotropic turbulence is considered, and thus the coherent structures do not fit the domain in the lateral and vertical directions. It is expected that if the domain would be expanded in lateral and vertical direction, the increase in power production of specifically case-L (but possibly also case-R and case-TI) would occur at slightly lower wave numbers. For case-U, the variation in power production between turbulence seeds occurs at higher wave numbers compared to the other three cases, since TKE is introduced at higher wave numbers (i.e., at low frequencies there is simply no TKE, thus no change in power production). Do note that the change in power production is very small compared to the change found for the other cases, and the median of all simulations of case-U is approximately constant for all k_0 .

For case-R the total increase in power production due to the presence of turbulence is about 37 kW (2.4%). The panel corresponding to case-TI shows a significant increase in power production of more than 100 kW before the power production starts to flatten around $k_0 \approx 10^0 \text{ m}^{-1}$. For case-L the total increase in power production is only slightly higher compared to case-R, and the increase occurs primarily at low wave numbers of $10^{-2} \text{ m}^{-1} \leq k_0 \leq 10^{-1} \text{ m}^{-1}$ since the change in turbulence length scale redistributes TKE to larger turbulence structures. The change in power production for case-U is negligible since the turbine operates at rated power.

It is also found that there is a substantial increase in the spread of the simulation results for case-L compared to case-R. However, a detailed analyses of the 100 individual turbulence seeds showed that the spread between seeds of one specific case originates from the smaller wave numbers (i.e., the larger coherent structures), while at $k_0 \geq 10^{-1} \text{ m}^{-1}$ the difference between individual simulations and the median of all simulations is more or less constant. The effect of these small turbulent structures is for all simulations similar: there is a minor increase in power production for all individual seeds, and this has very little effect on the spread observed amongst simulations of a specific case. This effect however is not found for case-U, where the higher wave numbers do

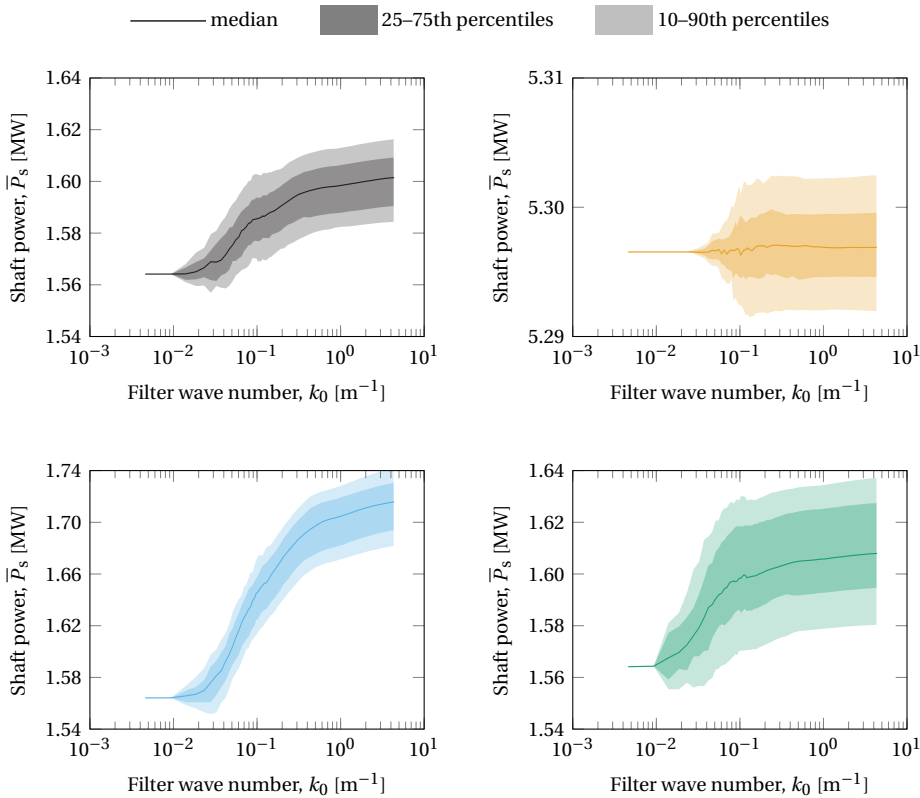


Figure 7.6: Shaft power as a function of filter wave-number for case-R (upper left panel), case-U (upper right panel), case-TI (lower left panel) and case-L (lower right panel).

not influence power production at all. The corresponding small turbulence structures do produce torque (i.e., see the small increase in power production for the other three cases). As such, the controller appears to be able to react to these structures, and keeps power production constant, while the largest structures do result in minor changes in power production that the controller cannot account for.

So far, power production is assessed as a function of turbulent scales. With aid of Equation 7.8 it is recognised that it might very well be that the power coefficient of a turbine is a function of turbulence characteristics as well. Let us first consider the traditional way to determine C_p with Equation 7.1 to assess the increase in C_p due to turbulence. Results are shown in the left panels of Figure 7.7. Since part of the TKE is converted into power by the turbine while MKE is by definition constant, C_p increases for below rated wind speeds once turbulence is included in the simulations. For case-U, C_p is approximately constant since power production is nearly constant and the mean wind speed does not change by adding turbulence. For the three other cases, it is found that C_p increases by approximately 0.01 to 0.05, depending on turbulence characteris-

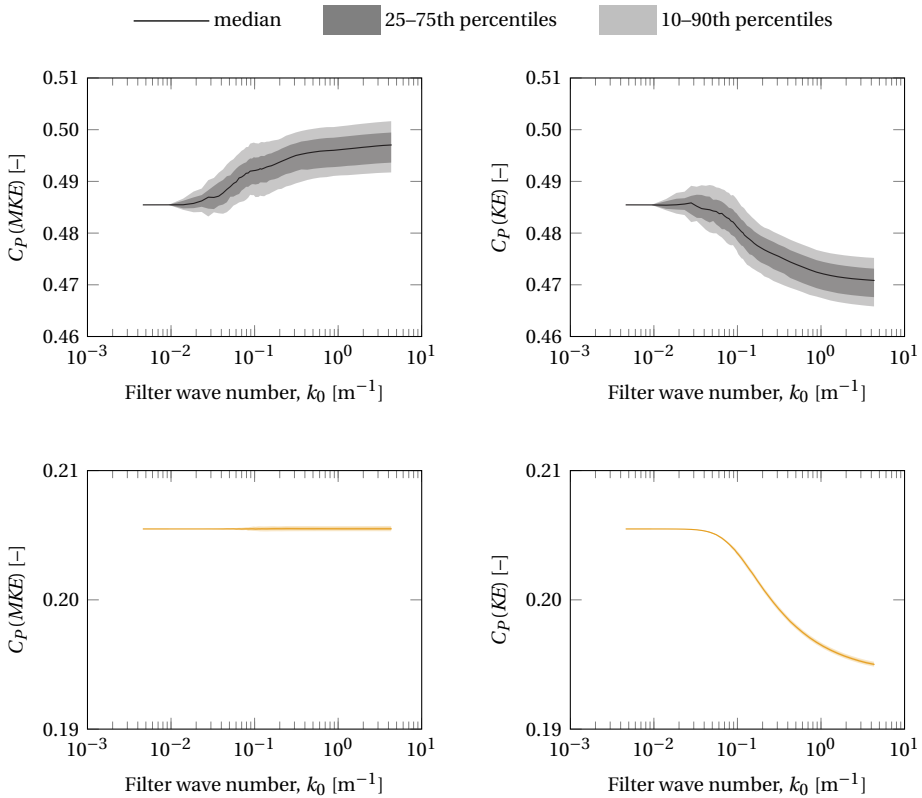


Figure 7.7: Power coefficient based on MKE (left column) and on KE (right column) as a function of filter wave number for case-R (upper panels) and case-U (lower panels).

tics. The results are similar to Figure 7.6 since in Equation 7.1 only \overline{P}_s increases. As such a similar assessment is done for C_p but then calculated as a function of the combination of MKE and TKE (i.e., Equation 7.8; see the right panels of Figure 7.7).

For case-R, it is found that C_p is constant at low k_0 . A first interpretation would be that the wind turbine thus has a similar efficiency in converting steady state conditions as well as the largest turbulent structures into power. Do note from Figure 7.5, however, that for these large structures virtually no TKE is added to the simulations, and from Figure 7.6 that there is also virtually no change in power production of the turbine. As a consequence, C_p at very low wave numbers ($k_0 < 10^{-2} \text{ m}^{-1}$) is still nearly fully related to the MKE and power production of the mean flow. It is thus not clear if a turbine can convert large turbulence structures efficiently into power. Once higher wave numbers are added, C_p starts to decrease, but this decrease levels off for high k_0 . The result of case-R is more or less the inverse of the previous power production results, and this is also found for case-TI and case-L. For case-U, results again differ though the general shape is again observed (i.e., constant C_p for low wave numbers and decrease C_p for

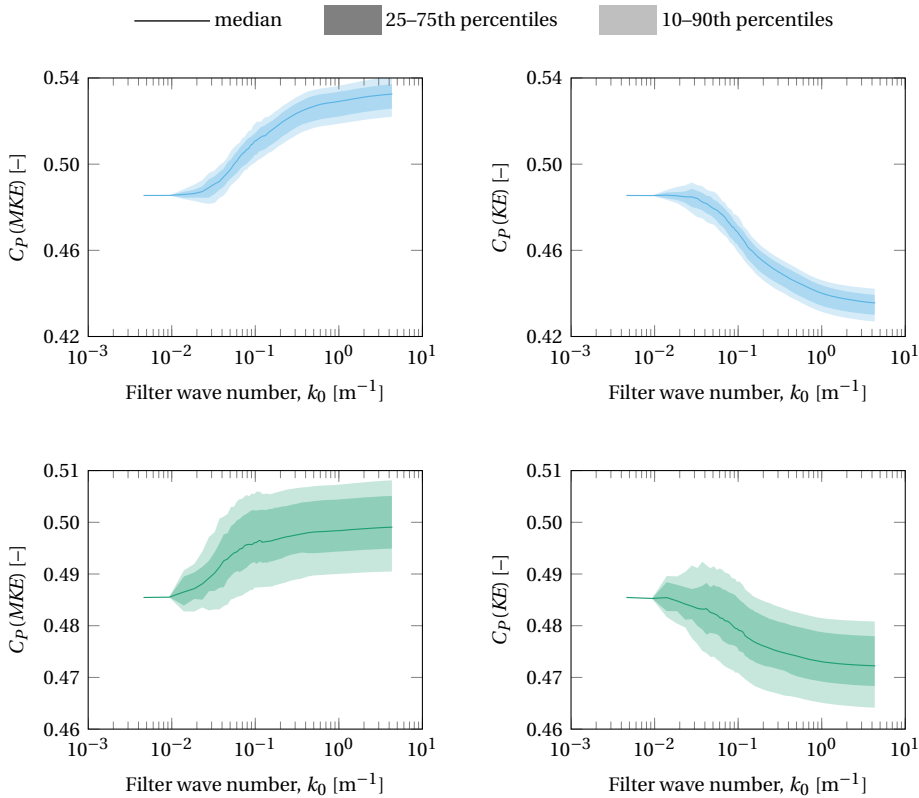


Figure 7.7 (cont.): Power coefficient based on MKE (left column) and on KE (right column) as a function of filter wave-number for case-TI (upper panels) and case-L (lower panels).

higher wave numbers). The absolute values however are substantially lower compared to the relatively high values found for the other three cases since the wind turbine operates at above rated power. Besides, there is virtually no spread in C_p between the individual simulations for case-U.

For below rated power conditions, it is found that C_p in principle decreases when turbulence is introduced to the simulations. This can only be the case if TKE is converted less efficient into power than MKE.

7.4.3. EFFECT OF TURBULENCE SCALES ON BLADE ROOT BENDING MOMENT

The emphasis of this research is the impact of turbulence on power production. However, it is recognised that, since turbulence is of major importance for wind turbine fatigue loads, it is a sensible extension to also assess bending moments. Due to the simplified representation of the wind turbine, only blade root bending moments are considered, although one could in principle execute similar research for other components as well. The wave number filter used in this research allows to assess if, as is frequently stated, a wind turbine acts as a low-pass filter. If this is the case, adding small turbu-

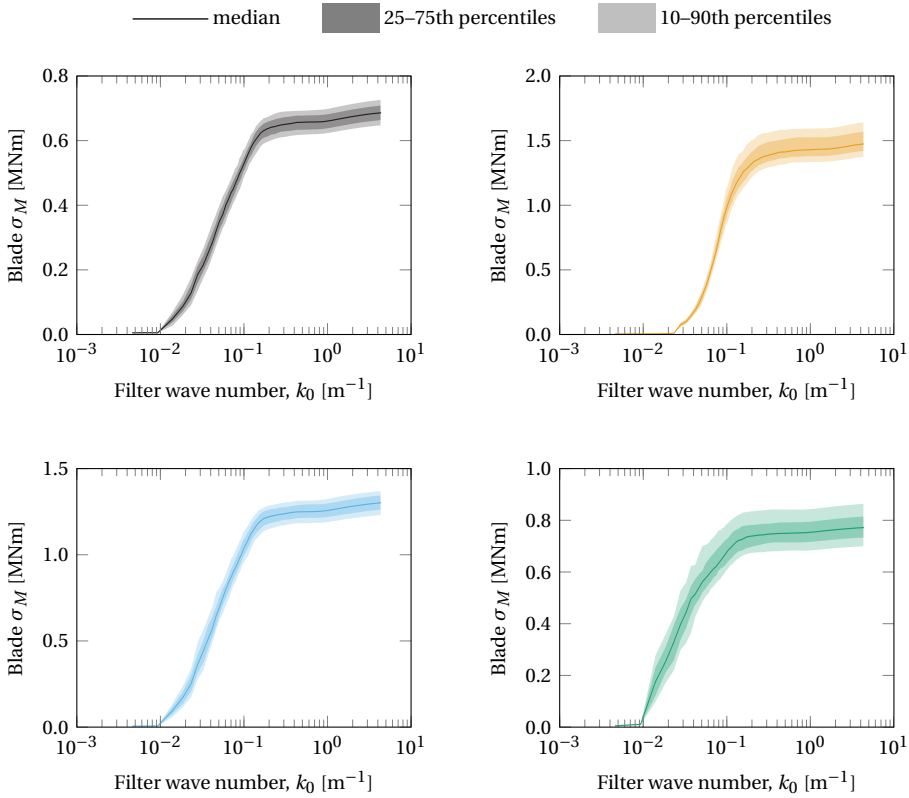


Figure 7.8: Standard deviation of the blade root flapwise bending moment, σ_M for case-R (upper left panel), case-U (upper right panel), case-TI (lower left panel) and case-L (lower right panel).

lent structures to simulations should not influence the resulting blade root bending moments. Since variations in the bending moments are the driving cause of fatigue, it is expected that the standard deviation of the bending moment σ_M is a more useful parameter for study than the mean bending moment for a given simulation. Besides, although large variations in bending moments contribute substantially more to fatigue compared to small variations, the maximum bending moment was not considered. This is because a very large number of simulations have to be run in order to obtain a reliable trend for the extreme loads.

Results are shown in Figure 7.8, where for all four simulations cases and all turbulence seeds it is very clear that the wind turbine acts as a low-pass filter. In absence of turbulence, the blade root bending moment is approximately constant, hence $\sigma_M = 0$ MNm by definition for low k_0 . Once TKE is introduced to the simulations (thus at a similar k_0 as was found for the shaft power, Figure 7.6, and for C_P , Figure 7.7), σ_M rapidly increases. The strong increase in σ_M for low wave numbers differs in shape from the results found for the shaft power where the increase was more gradual at low k_0 . This is

an indication that large turbulent structures have a significant impact on the blade root bending moment, despite containing little TKE and contributing little to wind turbine power production. The increase continues up to a filter wave number of approximately $k_0 = 2 \cdot 10^{-1} \text{ m}^{-1}$, and for higher wave numbers simulations σ_M starts to become independent of k_0 . Despite the addition of TKE at high wave numbers, the blade root bending moment hardly shows an increase in variation, which indicates the low-pass filter behaviour of a wind turbine. Since all four cases have a constant σ_M at similar k_0 , there appears to be a specific turbulent structure size for which the turbine acts as a low-pass filter. This structure size (or low-pass filter wave number) is independent of atmospheric conditions, otherwise the flattening found in Figure 7.8 would occur at different k_0 for the four individual cases. Instead, it is expected that the low-pass filter wave number is closely related to the dimensions of the wind turbine (especially blade length), the controller response time, and dynamic wake effects. Another striking result found for all four cases is that σ_M shows very little variation between the 100 turbulence seeds of a given case. For the variation in bending moment that occurs in the simulation, it is thus not of importance how turbulence structures are placed in the stochastic wind field (i.e., the seed number).

7.5. DISCUSSION

Based on the results one can conclude that turbulence has a pronounced impact on wind turbine performance, both with respect to experienced fatigue loads but also on power production. Since only a simplified situation has been treated so far, here it is aimed to place the results in perspective of more realistic conditions.

7.5.1. IMPLICATIONS FOR OPERATING WIND TURBINES

It is expected that the actual power production of offshore wind turbines should differ less from theoretic power curves than the power production of onshore wind turbines. As shown, turbulence influences wind turbine power production, hence for a given mean wind speed turbulence characteristics will result in scatter when validating wind turbine power production with the theoretic power curve. Offshore, the turbulence intensity is typically less than 10% (Türk & Emeis 2010). The simulations executed for the reference case with a turbulence intensity of 14% resulted in a 2.4% increase in power production. As such, it is expected that for offshore wind turbines the variation in power production for a given mean wind speed is reasonably small, assuming one knows exact wind conditions. Onshore however, substantially higher turbulence intensities occur, hence the deviation from theoretic power curves is likely to be large as well. As such, it is expected that the certainty and accuracy of wind power forecasting offshore should be higher than onshore.

Turbulence characteristics are highly dependent on the stability of the atmosphere as shown in Chapter 2. Therefore, one can generally assume that for unstable atmospheric conditions the amount of TKE increases and is predominantly present in large structures. For stable conditions, on the other hand, there is little TKE and turbulence is present in small structures. The results shown in this chapter thus indicate that the influence of turbulence on power production will be substantially higher for unstable

conditions compared to stable conditions. This should be valid both onshore as well as offshore.

It is not expected that the obtained results have a significant impact on the design or construction of a wind turbine, though the results indicate that load simulations can be optimised in terms of domain and grid characteristics. For power curve validation, however, it is clear that the efficiency of a turbine is highly dependent on turbulence characteristics. Besides, for practical purposes such as power forecasting the results indicate that at least the amount of TKE present in the atmosphere has a substantial influence on wind turbine performance. This can serve as an argument to consider atmospheric models that resolve turbulence (i.e., LES-models) in wind power forecasting.

7.5.2. DESIGN OF SIMULATIONS AND EXPERIMENTS

The results also provide insight in how to design wind fields for wind turbine simulations. It is imperative that at all scales turbulence has to be properly represented in simulations. The chosen domain size, grid spacing, and number of turbulence seeds thus all depend on turbulence characteristics imposed into the simulations. It has been shown that the response of a wind turbine to TKE differs depending on the scale of the turbulent structures. As such, it is of importance that one does not artificially redistribute TKE from scales outside the simulation domain (or at scales smaller than the grid resolution) into scales that actually are present in the stochastic wind field, as was indicated in Figure 7.2. Similarly, one should be careful to execute simulations with the exact same turbulence intensity as found in resource assessment. In meteorology, turbulence intensities are typically determined for 10-minute periods. Hence, if one executes simulations at much shorter domains (say, several minutes) with similar turbulence intensities, one will redistribute large scale TKE into smaller scales. Similarly, even if one considers a 10-minute wind field in wind turbine simulations, the operating frequency of wind sensors might not coincide with the grid resolution of the simulation. This could result in the redistribution of TKE over turbulence scales as shown in Figure 7.2.

The results obtained in this chapter appear to differ from the wind tunnel experiments of Mikkelsen (2013), who showed a decrease in wind turbine performance if turbulence is introduced in a wind tunnel. This can be explained by conservation of energy. It is obvious that the amount of TKE will increase behind a grid placed in a wind tunnel, and the law of conservation of energy thus implies that, since KE is constant, MKE (and thus the mean wind speed) will have to decrease behind the grid. For similar free stream conditions (i.e., in front of the grid), a wind turbine placed behind the grid will thus experience a reduced mean wind speed compared to an experiment where no grid is placed in the wind tunnel. It would be more accurate to keep mean wind speeds experienced by the wind turbine constant, which would imply a change in reference wind speed of the wind tunnel between both experiments.

7.6. CONCLUSIONS

Real life wind turbine power production may deviate substantially from certified power curves, and in this chapter it is analysed if power production depends on turbulence characteristics of the atmosphere. Due to the simplifications imposed on the simula-

tions with respect to atmospheric conditions and wind turbine characteristics, the obtained results should be interpreted as indications.

It is found that indeed turbulence is converted into power by a wind turbine, although turbulent kinetic energy is not converted as efficiently as mean kinetic energy. Whether turbulence is beneficial or hindering the efficiency of a wind turbine depends strongly on the definition of the power coefficient. For situations where mean kinetic energy is partially converted into kinetic energy (as is the case with placing a grid in a wind tunnel), power production will be reduced and the efficiency of a wind turbine will decrease. In contrary, if the mean kinetic energy is constant but turbulence kinetic energy is added on top of the mean kinetic energy, the energy production of a wind turbine will increase. The contribution of turbulence to power production is not considered in the classical definition of C_p , and it appears to be more sensible to define C_p as a function of the total kinetic energy (i.e., the sum of mean and turbulent kinetic energy).

It has been shown that the turbulent kinetic energy present in small turbulent structures is converted less efficiently compared to the energy present in large structures. Similarly, the small turbulent structures have very little impact on the blade root bending moments. Combined, this serves as an indication that a wind turbine acts as a low-pass filter. Spectral characteristics and the distribution of turbulent energy over scales are thus of importance for both power production and loads. This also serves as an argument not to scale the velocities in a turbulent wind field to meet a target turbulence intensity in wind turbine simulations.

The results obtained can be used to better understand a wind turbine's performance in different atmospheric conditions. For unstable conditions, where turbulent structures are larger and turbulence levels are higher, wind turbines should produce more power compared to stable atmospheric conditions. For accurate wind power forecasting turbulence characteristics, especially the amount of turbulent kinetic energy, has to be taken into account. Besides, it is expected that the quality of wind power forecasts is higher for offshore conditions. Not only are wind speeds higher (i.e., a wind turbine operates more often at or above rated wind speed), but turbulence levels are low, which means smaller deviations from the theoretical power curve.

8

CONCLUSIONS AND RECOMMENDATIONS

There is only one good: knowledge, and one evil: ignorance

Socrates

In this thesis the interdisciplinary field of offshore wind energy meteorology has been studied. Offshore atmospheric conditions have been defined and specified, and their influence on wind turbine performance has been assessed. Due to the interdisciplinary nature of this research, the work and results have been split into meteorological aspects and wind energy related implications. In this chapter the overarching conclusions of the individual chapters are presented, and recommendations both for future research but also for best practices in wind energy applications are discussed. Both the conclusions of this research and the subsequent recommendations will be discussed with respect to offshore atmospheric conditions and wind energy implications separately.

8.1. CONCLUSIONS

8.1.1. OFFSHORE ATMOSPHERIC CONDITIONS

Wind shear, turbulence intensity and turbulence spectra are relevant for wind energy purposes and a framework has been defined in which these conditions are coupled and all depend on atmospheric stability. The applicability of Monin-Obukhov theory for the offshore site considered in this research was validated. This has the advantage that wind shear and turbulence characteristics all depend on only one additional parameter: stability. For stable conditions it is found that wind shear increases and turbulence levels (as well as the spectral length scale) decrease, while for unstable conditions wind shear decreases while turbulence levels (as well as the turbulence length scale) increase. Obtained relations that can be used to quantify wind shear and turbulence are found to work well for unstable and neutral conditions. For stable conditions scatter was found

in observed wind shear and observed turbulence characteristics. Two possible explanations for the scatter in wind shear (and potentially turbulence) are the shallowness of stable boundary layers (i.e., part of the observations have been obtained above the surface layer where MO-theory is applicable), and the occurrence of low-level jets.

Given the size of state of the art wind turbines, commonly used wind profiles are no longer valid to describe wind shear up to maximum blade tip heights. As such a wind shear profile is derived based on theoretic arguments in line with the wind profile proposed by Gryning (Gryning et al. 2007). The boundary layer wind shear profile includes several extra parameters not considered in commonly used surface layer wind profiles, such as the resistance functions and the boundary layer height h . One can parametrize these additional parameters as a function of the friction velocity and Obukhov length. As such the derived extended wind profile has the same amount of independent variables as surface layer wind profiles. The accuracy of the wind profile is compared to the accuracy of other commonly used wind profiles in wind energy based on LIDAR observation data. For unstable and neutral conditions it is found that the proposed extended wind profile performs equal or better, and substantially better for (very) stable conditions compared to other wind profiles. It is found that for stable conditions the boundary layer height is frequently estimated to be less than 150 m, which poses problems when adopting this shear model in simulations of very large wind turbines. For such conditions the wind profile cannot be computed up to the maximum blade tip height.

All wind profiles used in wind energy have in common that the wind speed increases with height, hence specific situations with local wind maxima close to the surface cannot be simulated properly. The occurrence and the characteristics of these local wind maxima close to the surface, called low-level jets, was studied. It is known that low-level jets occur frequently onshore, but there is little knowledge about offshore low-level jets. Based on two years of observation data it is found that low-level jets also occur offshore. The frequency of occurrence of offshore low-level jets ranges from 3 to 10% of the time depending on the criteria used to detect low-level jets. The jet speed of the detected low-level jets is found to typically vary from 5 to 15 m s⁻¹, and the wind maximum occurs in the lowest 200 m of the atmosphere. These characteristics indicate that offshore low-level jets could very well be relevant for wind energy purposes, which has been studied in more detail in this thesis as well. In contrast to onshore low-level jets, offshore low-level jets are found to persist for short periods of time, typically less than an hour. Although onshore one typically can contribute the occurrence of low-level jets to a site specific phenomenon, the offshore low-level jet is related to a variety of formation causes. These include the inertial oscillation, synoptic scale baroclinicity, nearby coastal surface changes and the presence of frontal systems.

8.1.2. IMPLICATIONS FOR WIND ENERGY PURPOSES

The proposed framework in which wind shear, the turbulence intensity and the turbulence length scale depend on atmospheric stability has been applied to wind energy. Equivalent loads of the blade root, the rotor and the tower are determined for a reference wind turbine using wind turbine design software. Wind shear turns out to have the most influence on blade root flapwise loads and rotor out of plane loads, while turbulence is predominantly causing tower loads (both fore-aft and side-side) and rotor in plane loads.

If commonly used standards are followed and atmospheric stability is neglected, equivalent loads of the specific components considered are overestimated up to approximately 30%. This is not caused by conservatism in either wind shear or turbulence levels in guidelines, but by a missing coupling between both conditions. In reality the combination of high wind shear and high turbulence simply does not occur simultaneously. It is found that the joint probability distribution of wind speed and atmospheric stability has a profound influence on the simulated equivalent loads. As such, it is imperative that in resource assessment stability is measured accurately. Including atmospheric stability in wind turbine design results in a substantial computational demand. An equivalent stability is therefore introduced, which reduces computational demand while increasing the accuracy of load simulations. The simulation data and subsequent analyses provide a better understanding of the influence of stability on wind turbine loads. However, it is difficult to quantify the importance of wind shear and turbulence on wind turbine performance based on simulations where both atmospheric conditions are incorporated. As such, the influence of both processes separately on wind turbine performance has been studied.

For wind shear the influence of specific diabatic wind profiles as well as low-level jet wind profiles on wind turbine power production and blade root loads in flapwise direction was studied. A simplified low-level jet model is derived, which can be used for wind energy purposes, and in which one can set specific jet characteristics. With respect to wind turbine power production, it is found that the flux of kinetic energy through the wind turbine rotor disc is shear dependent. Discarding this shear dependency results in overestimation of the kinetic energy flux experienced by a wind turbine compared to considering the boundary layer wind shear profile. The hub height wind speed does not appear to be representative for wind turbine power production assessment, and instead one should consider the rotor disc equivalent wind speed. Especially in the presence of a low-level jets, the difference in wind turbine power curves is substantial. The influence of wind shear on blade root fatigue loads has been assessed in terms of the variation of the blade root bending moment in flapwise direction. The extended wind profile causes a slight increase in variations in the blade root bending moment for unstable and neutral conditions and a substantial decrease for stable conditions compared to adopting the surface layer wind profile. For low-level jets the jet height has a significant influence on the resulting wind turbine response, and both wind turbine power production and variations in the blade root bending moment rapidly decrease if a low-level jet occurs exactly at hub height.

Besides wind shear, turbulence is important for wind turbine design, however, there is little known on the effect of coherent turbulence structures of specific scales on wind turbine performance. With aid of spectral filters it has been assessed how turbulence influences wind turbine power production and variations in the blade root bending moment. Although one typically only considers the influence of mean kinetic energy on wind turbine power production, the flux of kinetic energy through the rotor disc also depends on turbulent kinetic energy. In fact, a wind turbine converts part of the turbulent kinetic energy into electrical power, though at lower efficiency compared to the conversion of mean kinetic energy. It is therefore suggested to include turbulence by separately considering mean kinetic energy (MKE) and turbulent kinetic energy (TKE) in

the definition of the power coefficient C_p . Application of the spectral filters has shown that small turbulent structures have little influence on wind turbine power production and the blade root bending moment, which serves as an indication that a wind turbine acts as a low-pass filter. One should thus be careful when scaling turbulence kinetic energy in wind turbine simulations, since one should not redistribute turbulent energy over various turbulent scales. It is expected that for unstable conditions, where both the amount of turbulent kinetic energy and the size of turbulent structures increases, wind turbine power production should increase compared to stable conditions (at similar mean hub height wind speeds). As such turbulence characteristics should be considered in wind turbine power forecasting. Offshore wind turbines will likely show less deviations from theoretical power curves, since turbulence levels offshore are reduced compared to onshore conditions. This provides an additional argument why offshore conditions are favourable for wind energy purposes.

8.2. RECOMMENDATIONS

8.2.1. OFFSHORE METEOROLOGY FOR WIND ENERGY PURPOSES

The recommendations presented in this section are formulated based on research executed for offshore sites, however, several recommendations are applicable for onshore sites as well. The recommendations are formulated in general, without mentioning specifically the applicability onshore and offshore.

First of all, with Monin-Obukhov similarity theory a framework has been formulated that can be used to define the surface layer. However in scope of the shallow boundary layer offshore and the increasing size of state of the art wind turbines, it is needed to formulate a framework for the entire boundary layer. For wind shear a methodology was provided to extend the surface layer wind profile up to the top of the boundary layer. A similar methodology has not been provided to accurately describe the change in turbulence intensity and spectral characteristics with height. It is thus recommended to formulate height dependent relations for the turbulence intensity and for spectral characteristics with scaling arguments. With aid of observation and simulation data these relations can be parametrized, which extends the surface layer framework of Chapter 2 into a boundary layer framework.

As an extension of the previous recommendation, it is recognised that in this entire thesis it is assumed that the Obukhov length L is constant with height. For surface layer scaling this should not pose a problem as long as the atmosphere is not very (un)stable stratified (i.e., potential temperature gradients will influence the Obukhov length as well, besides the turbulent fluxes of heat and momentum). For the entire boundary layer however, turbulent fluxes have to change with height, and it is only logical that the Obukhov length also changes with height. This has not been considered for example in the derivation of the boundary-layer wind shear profile. Incorporating a height dependent Obukhov length in formulations and derivations should result in a more accurate description of atmospheric conditions.

It is found that the stable atmosphere is radically different compared to the neutral and unstable atmosphere, and the description of turbulence (Chapter 2) and wind shear (Chapters 2 and 3) for heights relevant for wind energy purposes is not accurate for stable

conditions. Discarding scaling arguments used in this research, and either considering different scaling principles (local scaling for example) or different scaling parameters to define the stable atmosphere might lead to a substantially more accurate description of wind shear and turbulence in the stable atmospheric boundary layer. In scope of the importance of wind shear and turbulence for wind energy purposes, this is not only recommended for meteorological purposes but also for wind energy.

With respect to wind shear, it is needed to combine wind profiles within and above the boundary layer. It has been shown that the extended wind profile of Gryning is more accurate as surface layer wind profiles, however, for stable conditions the wind profile cannot be computed up to the maximum blade tip height of state of the art wind turbines. Extending wind profiles above the boundary layer is therefore a necessity to accurately incorporate wind shear in fatigue load and power production assessment.

Lastly, it is of crucial importance to extend atmospheric measurements for wind energy purposes with the observation of turbulent fluxes. Not only does atmospheric stability depend on the turbulent fluxes of heat and momentum, but also the vertical transport of heat and momentum are important for wind shear and turbulence conditions within the boundary layer. As such, the observation of turbulent fluxes aids substantially in the formulation of boundary layer wind conditions, and the height dependence of the Obukhov length. To achieve such extension of atmospheric measurements it is required that at several heights in the atmosphere the three components of the wind vector are observed at high frequency (i.e., discarding the use of cup anemometers). At the exact same height one also has to observe the air temperature, relative humidity and air pressure at the same frequency as the wind observations. Due to the increase in high frequency signals, the data storage capacity would have to increase as well. In scope of the total costs involved in resource assessment, extension of the measurements as suggested would result in only a minor increase in costs, while improving the accuracy of expected lifetime wind conditions for the wind energy site of interest.

8.2.2. WIND ENERGY ASPECTS

First and foremost, based on the results obtained throughout this thesis, one can no longer discard the importance of atmospheric stability for wind turbine purposes. It should become standard in wind energy to consider atmospheric stability in resource assessment, wind turbine design and wind power forecasting. Simply said, the influence of atmospheric stability on wind turbine performance is too obvious to be ignored.

Atmospheric conditions can be defined as accurate (and complicated) as possible, however, for wind turbine design purposes this will nearly always result in an increase in computational expenses. As such it is needed to convert an elaborate physics based description of atmospheric conditions into wind turbine design simulations without excessively increasing computational costs. This has been achieved in this thesis for turbulence levels by defining a stability dependent equivalent turbulence. Similarly, it is proposed to adopt an equivalent stability in wind turbine load simulations. It appears however, that the equivalent stability is wind turbine component specific, which does pose limitations to the applicability of the equivalent stability in wind turbine design. As such it is recommended to assess the dependence of the equivalent stability on wind turbine characteristics (i.e., wind turbine dimensions and material characteristics) and

site characteristics (i.e., onshore and offshore difference, and sensitivity to the probability distribution of wind speed and stability). This can be used subsequently to define an equivalent stability for a given site and a given wind turbine, which allows for a computational efficient and accurate physics based description of atmospheric conditions in wind turbine design.

In scope of wind turbine simulations, it is nearly always assumed that the standard deviations of wind vector components are constant in space (for example in Bladed and FAST one defines a characteristic turbulence intensity). In reality however, both the turbulence intensity and the standard deviation of the horizontal wind components decrease rapidly with height at least in the lower half of the boundary layer (see also Figure 4 of Sullivan et al. (1998) and Figure 5 of Caughey et al. (1979)). Similar to wind shear, one can define relations for the change in the standard deviation of the wind with height up to the top of the boundary layer, as shown for stable and neutral conditions in Stull (1988). Due to the importance of turbulence for both wind turbine fatigue loads as well as wind turbine power production, it is imperative that the equations that define the height dependence of the standard deviation of the wind are incorporated in wind turbine simulations.

Wind turbine performance is nearly always assessed as a function of the hub height wind speed, both if one is interested in wind turbine fatigue loads or wind turbine power production. However, the hub height wind speed does not define atmospheric conditions, and the hub height wind speed alone is not the cause of power production or fatigue. Instead, it is much more sensible to assess wind turbine power production as a function of the rotor disc kinetic energy flux or the equivalent wind speed. Wind turbine fatigue loads have to be assessed as a function of wind shear and turbulence. This provides much more insight in how wind turbine performance depends on atmospheric conditions. Besides, one can argue that the hub height wind speed itself is also the result, not the cause, of the state of the atmosphere.

In wind energy resource assessment, it is crucial to assess accurately all relevant atmospheric parameters at sufficient spatial and temporal resolutions. In scope of the limited design of the meteorological mast used in this thesis (only one observation of the horizontal wind speed in the lowest 50 m of the atmosphere, only turbulence observations with sonic anemometers (i.e., three wind vector separately) at one height far above the surface, and no observations of the turbulent heat flux at all) it is questionable if stability and turbulence characteristics have been observed in sufficient detail. This clearly compromises the precision with which one can estimate needed parameters for wind turbine design. In scope of costly offshore measurement campaigns, the questioned capability of LIDARs to observe turbulence (Sathe 2012), tower distortion effects (Wessels 1983), and the uncertainty in converting observed signals into useful parameters (i.e., from the Richardson number to ζ for example), it is recommended to complement actual local field observations with numerical simulations. With aid of LES simulation data, validated with local observations, one can not only extend the spatial resolution of observations, but also include a hindcast to substantially extend the range of data included when assessing atmospheric conditions for the lifetime of a wind turbine. This will reduce the uncertainty in lifetime atmospheric conditions experienced by wind turbines and the subsequent lifetime power production, thereby contributing

to reducing the cost of (offshore) wind energy. Besides, the cost of offshore measurement campaigns can be reduced, since the use of a floating LIDAR with temperature sensors is sufficient to validate a LES model. Combined, this should reduce both the uncertainty of estimated atmospheric design parameters as well as the costs involved in resource assessment.

A

SURFACE LAYER WIND PROFILES

For the derivation of the stability corrected logarithmic wind profile one considers Equation 2.6 in combination with stability dependent functions of Φ_M . In this appendix the derivation is shown for the commonly used Businger-Dyer equations as well as the Free Convection relation for unstable conditions, and the relation of Holtslag for stable conditions. To keep the derivation as general as possible all coefficients are not specified since the coefficients vary in literature.

A.1. THE LOG-PROFILE FOR UNSTABLE CONDITIONS

The Businger-Dyer relation for Φ_M is considered first for unstable conditions, which equals

$$\Phi_M = [1 - \gamma\zeta]^{-1/4} \quad (\text{A.1})$$

Incorporating Equation A.1 into Equation 2.6 results in

$$\bar{U}(z) = \frac{u_{*0}}{\kappa} \int_{z_0}^z \frac{[1 - \gamma\zeta]^{-1/4}}{z} dz \quad (\text{A.2})$$

which with integration by substitution can be rewritten as

$$\bar{U}(z) = \frac{u_{*0}}{\kappa} \left[\int_{z_0}^z \frac{1}{z} dz - \int_{\zeta_0}^{\zeta} \frac{1 - [1 - \gamma\zeta]^{-1/4}}{\zeta} d\zeta \right] \quad (\text{A.3})$$

where $\zeta_0 = z_0/L$. The first integral on the right hand side corresponds to neutral logarithmic wind profile, the second integral is the added stability correction. As such one can also find in literature (do note the on purpose omitted minus sign, in consistency with literature)

$$\Psi(\zeta) = \int_{\zeta_0}^{\zeta} \frac{1 - \Phi_M}{\zeta} d\zeta \quad (\text{A.4})$$

The second integral on the right hand side of Equation A.3 is rewritten with integration by substitution of $x = [1 - \gamma\zeta]^{1/4}$ as

$$\int_{\zeta_0}^{\zeta} \frac{1 - \Phi_M}{\zeta} d\zeta = \int_{[1 - \gamma\zeta_0]^{1/4}}^{[1 - \gamma\zeta]^{1/4}} \frac{4x^3 - 4x^2}{x^4 - 1} dx = \int_{[1 - \gamma\zeta_0]^{1/4}}^{[1 - \gamma\zeta]^{1/4}} \frac{2x - 2}{x^2 + 1} + \frac{2}{x + 1} dx \quad (\text{A.5})$$

With the aid of the following standard integrals

$$\int \frac{1}{z} dz = \ln(z) \quad (\text{A.6})$$

$$\int \frac{2x-2}{x^2+1} dx = \ln(1+x^2) - 2\arctan(x) \quad (\text{A.7})$$

$$\int \frac{1}{x+1} dx = \ln(1+x) \quad (\text{A.8})$$

it is found for Equation A.3 (where $x_0 = [1 - \gamma\zeta_0]^{1/4}$ is used)

$$\begin{aligned} \bar{U}(z) = \frac{u_{*0}}{\kappa} \left[\ln\left(\frac{z}{z_0}\right) - 2\ln(1+x) - \ln(1+x^2) + 2\arctan(x) \right. \\ \left. + 2\ln(1+x_0) + \ln(1+x_0^2) - 2\arctan(x_0) \right] \end{aligned} \quad (\text{A.9})$$

which can be written as

$$\bar{U}(z) = \frac{u_{*0}}{\kappa} \left[\ln\left(\frac{z}{z_0}\right) - \Psi(\zeta) + \Psi(\zeta_0) \right] \quad (\text{A.10})$$

$$\Psi(\zeta) = 2\ln(1+x) + \ln(1+x^2) - 2\arctan(x) \quad (\text{A.11})$$

which is the same as Equation 2.9 apart from a different integration constant, which does not influence the logarithmic wind profile as long as one strictly considers both $\Psi(\zeta)$ as well as $\Psi(\zeta_0)$.

Next, the free convective formulation for the dimensionless wind gradient is considered

$$\Phi_M = [1 - \gamma\zeta]^{-1/3} \quad (\text{A.12})$$

As mentioned in Chapter 2 as well, the coefficient γ differs here in value from the coefficient in Equation A.1. Equation 2.6 it further derived integration by substitution as

$$\bar{U}(z) = \frac{u_{*0}}{\kappa} \left[\int_{z_0}^z \frac{1}{z} dz - \int_{\zeta_0}^{\zeta} \frac{1 - [1 - \gamma\zeta]^{-1/3}}{\zeta} d\zeta \right] \quad (\text{A.13})$$

Applying the second substitution (thus $y = [1 - \gamma\zeta]^{1/3}$) to the second integral on the right hand side of Equation A.13 results in

$$\int_{\zeta_0}^{\zeta} \frac{1 - \Phi_M}{\zeta} d\zeta = \int_{[1-\gamma\zeta_0]^{1/3}}^{[1-\gamma\zeta]^{1/3}} \frac{3y}{y^2 + y + 1} dy \quad (\text{A.14})$$

Next the following two standard integrals are considered

$$\int \frac{y}{y^2 + y + 1} dy = \frac{1}{2} \ln(1 + y + y^2) - \frac{1}{2} \int \frac{1}{y^2 + y + 1} dy \quad (\text{A.15})$$

$$\int \frac{1}{y^2 + y + 1} dy = \frac{2}{\sqrt{3}} \arctan\left(\frac{2y+1}{\sqrt{3}}\right) \quad (\text{A.16})$$

to find for the wind shear profile, in combination with $y_0 = [1 - \gamma\zeta_0]^{1/3}$

$$\begin{aligned} \bar{U}(z) = \frac{u_{*0}}{\kappa} \left[\ln\left(\frac{z}{z_0}\right) - \frac{3}{2}\ln(1+y+y^2) + \sqrt{3}\arctan\left(\frac{2y+1}{\sqrt{3}}\right) \right. \\ \left. + \frac{3}{2}\ln(1+y_0+y_0^2) - \sqrt{3}\arctan\left(\frac{2y_0+1}{\sqrt{3}}\right) \right] \end{aligned} \quad (\text{A.17})$$

This can be written as

$$\bar{U}(z) = \frac{u_{*0}}{\kappa} [\ln - \Psi(\zeta) + \Psi(\zeta_0)] \quad (\text{A.18})$$

$$\Psi(\zeta) = \frac{3}{2}\ln(1+y+y^2) - \sqrt{3}\arctan\left(\frac{2y+1}{\sqrt{3}}\right) \quad (\text{A.19})$$

Where again the different notation is found compared to Equation 2.11, however this can be explained similarly as is done for the Businger-Dyer equation before.

A.2. THE LOG-PROFILE FOR STABLE CONDITIONS

For stable conditions the derivation is less complicated than for unstable conditions, especially if one considers the Businger-Dyer equation for the dimensionless wind gradient

$$\Phi_M = 1 + \beta\zeta \quad (\text{A.20})$$

Combined with Equation 2.6 and considering the integration bounds, this results in

$$\bar{U}(z) = \frac{u_{*0}}{\kappa} \left[\int_{z_0}^z \frac{1}{z} dz - \int_{\zeta_0}^{\zeta} \frac{1 - [1 + \beta\zeta]}{\zeta} d\zeta \right] \quad (\text{A.21})$$

Which is easy to integrate to obtain

$$\bar{U}(z) = \frac{u_{*0}}{\kappa} \left[\ln\left(\frac{z}{z_0}\right) + \beta\zeta - \beta\zeta_0 \right] \quad (\text{A.22})$$

This can be written as

$$\bar{U}(z) = \frac{u_{*0}}{\kappa} [\ln - \Psi(\zeta) + \Psi(\zeta_0)] \quad (\text{A.23})$$

$$\Psi(\zeta) = -\beta\zeta \quad (\text{A.24})$$

It is decided to take the derivative of the wind profile instead of integrating the local wind gradient to obtain the Ψ -function of Holtslag. According to [Holtslag & de Bruin \(1988\)](#) the wind profile equals

$$\bar{U}(z) = \frac{u_{*0}}{\kappa} \left[\ln\frac{z}{z_0} + a\zeta + b \left[\zeta - \frac{c}{d} \right] \exp(-d\zeta) + \frac{bc}{d} \right] \quad (\text{A.25})$$

Rewriting $\zeta = z/L$ and taking the derivative of Equation A.25 with respect to height, the

A

dimensionless wind gradient is found to equal

$$\begin{aligned}
 \Phi_M &= \frac{\kappa z}{u_{*0}} \frac{d\bar{U}}{dz} \\
 &= z \frac{d}{dz} \left[\ln \frac{z}{z_0} + a\zeta + b \left[\zeta - \frac{c}{d} \right] \exp(-d\zeta) + \frac{bc}{d} \right] \\
 &= z \left[\frac{1}{z} + a \frac{1}{L} + b \frac{1}{L} \exp\left(-d \frac{z}{L}\right) - b \frac{1}{L} \left[d \frac{z}{L} - c \right] \exp\left(-d \frac{z}{L}\right) \right] \\
 &= 1 + \frac{z}{L} \left[a + b \left[1 + c - d \frac{z}{L} \right] \exp\left(-d \frac{z}{L}\right) \right]
 \end{aligned} \tag{A.26}$$

which is the same equation as shown in [Vickers & Mahrt \(1999\)](#).

B

SCALING ARGUMENTS FOR UNSTABLE CONDITIONS

The concepts of free convection scaling with Monin-Obukhov theory and dimensional scaling are explained in more detail here for clarification purposes. Besides, the applicability of both scaling techniques is discussed.

B.1. FREE CONVECTIVE SCALING WITH MO-THEORY

The behaviour of the wind gradient $d\bar{U}/dz$ and the second-order moments σ_x is assessed as a function of stability for the unstable atmosphere. The limiting conditions in the unstable atmosphere occur when conditions approach neutral stratification ($L \rightarrow -\infty$) or when conditions approach so called free convective conditions ($L \rightarrow 0$). In these limiting conditions the four state variables defined for Monin-Obukhov theory in Chapter 2 reduce to three, since respectively the heat flux H and the surface shear stress τ_0 vanish for neutral and free convective conditions. As a consequence the non-dimensional stability parameter is no longer properly defined (that is, it is a function of both the heat flux and the shear stress, hence when either vanishes it is no longer a valid non-dimensional scaling parameter). It is expected that the wind gradient is independent of the heat flux for neutral conditions (Stull 1988), thus

$$\frac{d\bar{U}}{dz} = \frac{u_{*0}}{z} C_1 \quad (\text{B.1})$$

where by definition $C_1 = 1/\kappa$. For free convective conditions the wind gradient is independent of the surface shear stress, hence

$$\frac{d\bar{U}}{dz} = \frac{u_f}{z} C_2 \quad (\text{B.2})$$

where the constant C_2 has to be obtained from experimental observation data. In between both velocity scales u_{*0} and u_f are appropriate, hence the convention is followed to scale the wind gradient with the friction velocity. As such for unstable conditions in

non-limiting conditions it is found that

$$\frac{d\bar{U}}{dz} = \frac{u_{*0}}{z} f(\zeta) \quad (\text{B.3})$$

The function f again has to be found from experimental data, however, it is expected that for unstable conditions the wind gradient is proportional to the friction velocity squared since it is known from first order closure conditions that

$$u_{*0}^2 = -\overline{u'w'}_s = K_M \frac{d\bar{U}}{dz} \quad (\text{B.4})$$

where K_M is the eddy viscosity. This was already proposed by Prandtl in 1932, in combination with $d\bar{U}/dz \propto z^{-4/3}$ (Prandtl 1932). If the definition of the Obukhov length is considered it is found that

$$(-\zeta)^{-1/3} = \left(\frac{z\kappa g \left[\overline{w'\theta'_v} \right]_s}{u_{*0}^3 \overline{\theta_v}} \right)^{-1/3} = u_{*0} \left(\kappa z \frac{g}{\theta_v} \left[\overline{w'\theta'_v} \right]_s \right)^{-1/3} \quad (\text{B.5})$$

Thus the expected proportionality of $d\bar{U}/dz \propto u_{*0}^2$ can only hold if

$$\begin{aligned} \frac{d\bar{U}}{dz} &\propto \frac{u_{*0}}{z} (-\zeta)^{-1/3} \\ &\propto u_{*0}^2 z^{-4/3} \left(\kappa \frac{g}{\theta_v} \left[\overline{w'\theta'_v} \right]_s \right)^{-1/3} \end{aligned} \quad (\text{B.6})$$

and hereby both of the expected scaling relations of Prandtl are obtained.

For very unstable conditions it is expected that the second-order moments are independent of u_{*0} , which is indeed found if the second-order moments are scaled with u_f . As a consequence the non-dimensional second-order moments should scale to stability as

$$\begin{aligned} \sigma_x &\propto u_f \\ &\propto \left[z \frac{g}{\theta_v} \overline{w'\theta'_v}_s \right]^{1/3} \end{aligned} \quad (\text{B.7})$$

which can only hold if

$$\sigma_x \propto u_{*0} \left(-\frac{z}{L} \right)^{1/3} \quad (\text{B.8})$$

Hence for the second-order moments the expected 1/3 scaling for free convective conditions is obtained.

B.2. DIRECTIONAL SCALING FOR UNSTABLE CONDITIONS

It is argued by Kader & Yaglom (1990) that Monin-Obukhov theory is a simplification of the atmosphere, and that in fact experimentally obtained relations for wind shear and second-order moments are only valid for moderate unstable conditions. Instead, an extension of the dimensional analyses is suggested in which directional scaling is applied,

in which the length scale is decomposed into orthogonal components. This directional scaling has been first proposed by Williams (1892). For simplicity reasons two directions are considered and the longitudinal and lateral length scale are combined into one horizontal scale, while separately a vertical length scale is considered. This directional scaling is controversial (see Kader & Yaglom (1990) for a discussion), however it is found that at least for the second-order moments the results presented in Chapter 2 might suggest validity of directional scaling.

It is stated in Betchov & Yaglom (1971) that directional scaling is only applicable if there is no coupling of energy in the horizontal and vertical direction. In other words, if the horizontal second-order moments originate primarily from mechanical production of turbulence by shear stress while the vertical second-order moments originate primarily from thermal production of turbulence, and there is little exchange of energy between the horizontal and vertical second-order moments, then directional scaling is applicable. In contrary, if all turbulent energy is completely produced mechanically or completely produced thermally, then directional scaling is no longer applicable. In the unstable atmosphere one can differentiate between three cases

- The atmosphere is nearly neutral stratified, and buoyancy is absent. There is mechanical production of turbulence in the horizontal wind components, and the vertical component receives turbulent energy from the mechanical production due to pressure perturbations that redistribute turbulent energy. This regime is called the dynamic sublayer by Kader & Yaglom (1990). Since all turbulent energy is produced mechanically directional scaling is not applicable.
- The atmosphere is unstable stratified, and there is both buoyancy as well as shear stress. As such there is both mechanical and thermal production of turbulence, and thermal production causes the vertical second-order moments while mechanical production causes the horizontal second-order moments. At the same time there is some exchange of energy from the horizontal to the vertical second-order moments and vice versa by pressure perturbations, however the exchange is approximately in balance. A first order approximation is therefore that there is no horizontal turbulence caused directly by buoyancy, and there is no vertical turbulence directly caused by shear stress. This regime is called the dynamic-convective sublayer by Kader & Yaglom (1990). Since the horizontal and vertical second-order moments are decoupled directional scaling is applicable.
- The atmosphere is very unstable, and shear stress vanishes. As such all turbulent energy is produced by buoyancy in the vertical direction, and the horizontal components receive energy from the vertical component by pressure perturbations. This regime is called the free convective sublayer by Kader & Yaglom (1990), and directional scaling is not applicable.

As a consequence there are also three different scaling relations expected for the wind gradient and the second-order moments.

In the dynamic sublayer buoyancy is absent and since no dimensionless group can be formed with the remaining scaling variables any proper non-dimensionalized variable (i.e. wind shear or second order moments) have to be constant similar as proposed

by Monin-Obukhov theory. For the wind gradient and the second-order moments it is thus found (on purpose the horizontal and vertical second-order moments are separately shown)

B

$$\frac{d\bar{U}}{dz} \propto \frac{u_{*0}}{z} \quad (\text{B.9})$$

$$\sigma_{u,v} \propto u_{*0} \quad (\text{B.10})$$

$$\sigma_w \propto u_{*0} \quad (\text{B.11})$$

In the dynamic-convective sublayer the energetic scales are decoupled and directional scaling is adopted. The dimensions of the considered variables are

$$\frac{d\bar{U}}{dz} = [l_x l_z^{-1} t^{-1}] \quad (\text{B.12})$$

$$\sigma_{u,v} = [l_x t^{-1}] \quad (\text{B.13})$$

$$\sigma_w = [l_z t^{-1}] \quad (\text{B.14})$$

Next, it is necessary to obtain scaling variables with proper dimensions. One can easily show that the dimensions of u_{*0} correspond to $[l_x^{1/2} l_z^{1/2} t^{-1}]$. The scaling variable u_f has dimensions $[l_z t^{-1}]$. Combined a horizontal velocity scale is found as u_{*0}^2 / u_f , which equals

$$\frac{u_{*0}^2}{u_f} = u_{*0}^2 \left[z \frac{g}{\theta_v} \overline{w'\theta'_{vs}} \right]^{-1/3} \quad (\text{B.15})$$

Based on dimensional scaling the following relations are expected

$$\frac{d\bar{U}}{dz} \propto u_{*0}^2 z^{-4/3} \left[\frac{g}{\theta_v} \overline{w'\theta'_{vs}} \right]^{-1/3} \quad (\text{B.16})$$

$$\sigma_{u,v} \propto u_{*0}^2 \left[z \frac{g}{\theta_v} \overline{w'\theta'_{vs}} \right]^{-1/3} \quad (\text{B.17})$$

$$\sigma_w \propto \left[z \frac{g}{\theta_v} \overline{w'\theta'_{vs}} \right]^{1/3} \quad (\text{B.18})$$

If the definition of ζ would be incorporated this would equal

$$\frac{d\bar{U}}{dz} \propto \frac{u_{*0}}{z} [-\zeta]^{-1/3} \quad (\text{B.19})$$

$$\sigma_{u,v} \propto u_{*0} [-\zeta]^{-1/3} \quad (\text{B.20})$$

$$\sigma_w \propto u_{*0} [-\zeta]^{1/3} \quad (\text{B.21})$$

which also shows in fact the risk of self similarity if one would assess the relation between non-dimensional second-order moments (non-dimensionalized with u_{*0}) and ζ . Here it is found that in the unstable regime the horizontal second-order moments should in fact not scale with a +1/3 power law relation to stability as proposed by Monin-Obukhov

theory (see Equation B.8), but with a $-1/3$ power law relation. The wind gradient and vertical second-order moment scale similarly as is proposed in Monin-Obukhov theory.

For the free convective sublayer the energetic scales are coupled again, hence directional scaling is not applicable. In absence of shear stress the only relevant velocity scale is u_f , hence it is found that

$$\frac{d\bar{U}}{dz} \propto z^{-2/3} \left[\frac{g}{\theta_v} \overline{w'\theta'_{vs}} \right]^{1/3} \quad (\text{B.22})$$

$$\sigma_{u,v} \propto \left[z \frac{g}{\theta_v} \overline{w'\theta'_{vs}} \right]^{1/3} \quad (\text{B.23})$$

$$\sigma_w \propto \left[z \frac{g}{\theta_v} \overline{w'\theta'_{vs}} \right]^{1/3} \quad (\text{B.24})$$

And thus all non-dimensional parameters should be proportional to ζ as

$$\frac{d\bar{U}}{dz} \propto \frac{u_{*0}}{z} [-\zeta]^{1/3} \quad (\text{B.25})$$

$$\sigma_{u,v} \propto u_{*0} [-\zeta]^{1/3} \quad (\text{B.26})$$

$$\sigma_w \propto u_{*0} [-\zeta]^{1/3} \quad (\text{B.27})$$

And here the unexpected result is obtained that the wind gradient should not decrease but increase with increasing unstable conditions when the free convective limit is approached. The $+1/3$ scaling relations for all three second-order moments are in line with Monin-Obukhov theory as shown in Equation B.8.

There are two obvious differences between the proposed relations based on Monin-Obukhov similarity theory and the directional scaling theory which will be discussed further. First of all, for wind shear it is found that directional scaling results in an unexpected $+1/3$ power law relation with respect to ζ . For extreme unstable conditions it is evident that $\bar{U} \rightarrow 0$, $d\bar{U}/dz \rightarrow 0$, and $u_{*0} \rightarrow 0$. Integration of Equation B.22 however would result in a shear profile where

$$\bar{U} \propto \left[z \frac{g}{\theta_v} \overline{w'\theta'_{vs}} \right]^{1/3} \quad (\text{B.28})$$

And thus the wind speed would increase with height, and more importantly it would not vanish. As such directional scaling is not suitable to describe the mean flow when the atmosphere approaches free convective conditions. As mentioned in Businger (1973), it is questionable if the average of fixed-point observations can be used to analyse the free convective boundary layer. Due to large turbulent structures and pressure perturbations one might find locally some horizontal wind (even averaged over larger time scales), however for a sufficiently large horizontal area that approaches free convective conditions the mean horizontal wind speed does vanish. The local fixed-point observations are thus not representative for free convective conditions, which might explain the apparent $+1/3$ scaling between Φ_M and ζ shown in Figure 1 of Kader & Yaglom (1990).

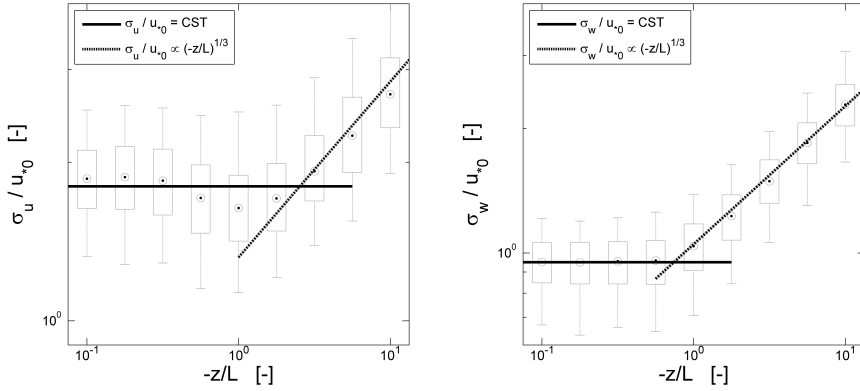


Figure B.1: Close up of the longitudinal (left) and vertical (right) non-dimensional second order moments for unstable conditions (see Figure 2.6 for the full figure).

For the second-order moments however differences in expected scaling laws were not found for the free convective limit but for the dynamic-convective regime (i.e. moderate unstable conditions where turbulence is produced both by shear stress as well as by buoyancy). The theoretic difference might very well explain some peculiar detailed result shown in Figure 2.6. Figure B.1 shows a close up of the longitudinal and vertical second-order moments for unstable conditions. For weak unstable conditions both second-order moments are constant, in line with Monin-Obukhov theory and directional scaling. For moderate unstable conditions Monin-Obukhov theory states that both second-order moments would increase with increasing unstable conditions. In Figure B.1 however it is shown that the longitudinal second-order moment decreases slightly with increasing unstable conditions at $0.5 \leq -\zeta \leq 1$. For nearly similar conditions the vertical second-order moments do increase slightly (seen between $0.75 \leq -\zeta \leq 1$). As such there is a regime where the scaling of both second-order moments with stability differs. This is not obtained with Monin-Obukhov theory, however it does correspond well to directional scaling theory. It has to be emphasized that the decrease is far from a $-1/3$ scaling with ζ . As mentioned in Kader & Yaglom (1990) however directional scaling is probably only valid in more strict conditions compared to general Monin-Obukhov theory, and in Figures 2.6 and B.1 it is likely that conditions have been included where directional scaling is not valid. It is therefore concluded that based on the observation data obtained with meteorological mast IJmuiden directional scaling can neither be validated nor discarded, and a carefully designed field experiment would be required to validate the applicability of directional scaling for second-order moments.

C

THE RELATION BETWEEN RI AND ζ

As shown in [Businger et al. \(1971\)](#) ζ and the gradient Richardson number (note, not the bulk Richardson number), are related as

$$\zeta = a\Phi_M RI \quad (\text{C.1})$$

where the relation between the friction velocity and the turbulent momentum flux is adopted and the following definitions are used

$$\zeta = -\frac{z\kappa g \overline{w'\theta'_{vs}}}{\overline{\theta_v} u_{*0}^3} \quad (\text{C.2})$$

$$a = \frac{\overline{w'\theta'_{vs}} \frac{d\overline{U}/dz}{u'w'_s \frac{d\overline{\theta_v}/dz}}{\quad} \quad (\text{C.3})$$

$$\phi_M = \frac{\kappa z}{u_{*0}} \frac{d\overline{U}}{dz} \quad (\text{C.4})$$

$$RI = \frac{g}{\overline{\theta_v}} \frac{d\overline{\theta_v}/dz}{\left(\frac{d\overline{U}}{dz}\right)^2} \quad (\text{C.5})$$

Here a is the ratio of the eddy viscosity coefficients of heat and momentum, also known as the Prandtl number. Although the Prandtl number is often considered the inverse of the formulation shown here (i.e. the eddy diffusivity of momentum divided by the eddy diffusivity of heat), it is decided to follow here the formulation of [Businger et al. \(1971\)](#). One can rewrite a as

$$a = \frac{\Phi_M}{\Phi_H} \quad (\text{C.6})$$

where Φ_H is the non-dimensional temperature gradient. Combining Equations [C.1](#) and [C.6](#) results in

$$\zeta = \frac{\Phi_M^2}{\Phi_H} RI \quad (\text{C.7})$$

and thus one only needs a description of the non-dimensional heat and momentum gradients to find a proper relation between ζ and the gradient Richardson number.

For stable conditions Equation C.1 is in fact most useful, which in combination with the Businger-Dyer relation results in

$$\begin{aligned}\zeta &= a [1 + \beta\zeta] RI \\ &= \frac{aRI}{1 - a\beta RI}\end{aligned}\tag{C.8}$$

Which is a general form of Equation 2.29, where the difference of a factor 10 is explained by the fact that in practice one considers finite differences (with the bulk Richardson number) instead of local gradients.

For unstable conditions either the Businger-Dyer equations or the relations following from free-convective scaling could be assumed to be valid. In general form, without specifying coefficients, this results with aid of Equation C.7 in

$$\zeta \frac{(1 - \gamma_M \zeta)^{1/2}}{(1 - \gamma_H \zeta)^{1/2}} = RI\tag{C.9}$$

$$\zeta \frac{(1 - \gamma_M \zeta)^{2/3}}{(1 - \gamma_H \zeta)^{1/3}} = RI\tag{C.10}$$

where the first relation follows the Businger-Dyer equations and the second relation follows free convective scaling. Note that both of these results differ substantially from Equation 2.30. The assumption of a linear dependence however is quite well obtained with the Businger-Dyer equations (see Figure 5 in [Businger et al. \(1971\)](#)), which is in practice true if $\gamma_M \approx \gamma_H$. In absence of accurate observations of fluxes and local gradients validation of any of the proposed relations is not possible.

D

DERIVING THE BOUNDARY LAYER WIND PROFILE

In Chapter 3 the boundary layer wind shear profile is derived, and here the majority of the derivation will be shown in more detail for clarification purposes. The derivation of the wind profile and the derivation of the resistance functions will be shown.

D.1. DERIVATION OF THE GENERAL WIND PROFILE

As a starting point of the derivation, Equation 3.3 is considered and rewritten to obtain

$$\frac{\partial \bar{U}}{\partial z} = \frac{u_{*0}}{\kappa} \left[\frac{\phi_M}{z} + \frac{1 - \phi_M}{h} + \frac{1}{l_{ML}} \left[1 - \frac{z}{h} \right] \right] \quad (D.1)$$

Integration of the wind gradient $\partial \bar{U} / \partial z$ with respect to height thus results in three integrals on the right hand side of Equation D.1. The integral of the first term on the right hand side can be rewritten with integration by substitution to obtain

$$\int_{z_0}^z \frac{\phi_M}{z} dz = \int_{z_0}^z \frac{1}{z} dz - \int_{\zeta_0}^{\zeta} \frac{1 - \phi_M}{\zeta} d\zeta \quad (D.2)$$

which equals

$$\int_{z_0}^z \frac{\partial \bar{U}}{\partial z} dz = \frac{u_{*0}}{\kappa} \left[\int_{z_0}^z \frac{1}{z} dz - \int_{\zeta_0}^{\zeta} \frac{1 - \phi_M}{\zeta} d\zeta + \frac{1}{h} \int_{z_0}^z [1 - \phi_M] dz + \frac{1}{l_{ML}} \int_{z_0}^z \left[1 - \frac{z}{h} \right] dz \right] \quad (D.3)$$

Since $\bar{U}(z_0) = 0$ by definition, and not solving the integrals of ϕ_M yet, it is found that

$$\bar{U}(z) = \frac{u_{*0}}{\kappa} \left[\ln \left(\frac{z}{z_0} \right) - \int_{\zeta_0}^{\zeta} \frac{1 - \phi_M}{\zeta} d\zeta + \frac{1}{h} \int_{z_0}^z [1 - \phi_M] dz + \frac{1}{2 l_{ML}} \left[\left[1 - \frac{z_0}{h} \right]^2 - \left[1 - \frac{z}{h} \right]^2 \right] \right] \quad (D.4)$$

Next, the integration of the ϕ_M -terms for stable and unstable conditions is considered separately. For stable conditions the Businger-Dyer equation $\phi_M = 1 + \beta_{BD}\zeta$ is considered, and for unstable conditions the Free-Convection formulation $\phi_M = (1 - \gamma_{FC}\zeta)^{-1/3}$

is used. The first integral on the right hand side of Equation D.4 by definition results in (Paulson 1970)

$$-\int_{\zeta_0}^{\zeta} \frac{1-\phi_M}{\zeta} d\zeta = -\Psi(\zeta) + \Psi(\zeta_0) \quad (\text{D.5})$$

with the Ψ -functions shown in Chapter 3. The second integral differs for stable and unstable conditions. For stable conditions it is found that

$$\begin{aligned} \frac{1}{h} \int_{z_0}^z [1-\phi_M] dz &= -\frac{1}{2} \frac{z}{h} \beta_{BD} \frac{z}{L} + \frac{1}{2} \frac{z_0}{h} \beta_{BD} \frac{z_0}{L} \\ &= \frac{1}{2} \frac{z}{h} \Psi(\zeta) - \frac{1}{2} \frac{z_0}{h} \Psi(\zeta_0) \end{aligned} \quad (\text{D.6})$$

and for unstable conditions it is found that

$$\begin{aligned} \frac{1}{h} \int_{z_0}^z [1-\phi_M] dz &= \frac{1}{h} \left[\left[z + \frac{3}{2} \frac{x^2 L}{\gamma_{FC}} \right] - \left[z_0 + \frac{3}{2} \frac{x_0^2 L}{\gamma_{FC}} \right] \right] \\ &= \frac{z}{h} - \frac{z_0}{h} - \frac{3}{2} \frac{z}{h} \frac{x^2 - x_0^2}{x^3 - 1} \end{aligned} \quad (\text{D.7})$$

Combining Equations D.5 and D.6, and considering the linearity of the Businger-Dyer equation (see Equation 3.12), results for stable conditions in

$$-\int_{\zeta_0}^{\zeta} \frac{1-\phi_M}{\zeta} d\zeta + \frac{1}{h} \int_{z_0}^z [1-\phi_M] dz = -\frac{1}{2} \Psi\left(\frac{h}{L}\right) \left[\left[1 - \frac{z_0}{h} \right]^2 - \left[1 - \frac{z}{h} \right]^2 \right] \quad (\text{D.8})$$

which can be incorporated into Equation D.4 to obtain the following wind profile for stable conditions

$$\bar{U}(z) = \frac{u_{*0}}{\kappa} \left[\ln\left(\frac{z}{z_0}\right) + \frac{1}{2} \left[\left[1 - \frac{z_0}{h} \right]^2 - \left[1 - \frac{z}{h} \right]^2 \right] \left[\frac{h}{l_{ML}} - \Psi\left(\frac{h}{L}\right) \right] \right] \quad (\text{D.9})$$

The wind profile shown in Chapter 3 Equation 3.13 is found if it is assumed that $z_0/h = 0$. Equations D.5 and D.7 are incorporated into Equation D.4 in combination with $z_0/h = 0$ to obtain the wind profile shown in Chapter 3 Equation 3.14.

D.2. DERIVATION OF THE RESISTANCE FUNCTION B

Only the derivation of the resistance function B is considered, since A is defined without the requirement of derivatives or integrals. As a starting point the definitions of B as shown in Chapter 3 Equation 3.24 are considered

$$B = \frac{p+1}{p} - \Psi\left(\frac{z_0}{L}\right) - \frac{\Psi\left(\frac{h}{L}\right)}{p} + \frac{p+1}{p \frac{h}{L}} \left[\Gamma\left(\frac{h}{L}\right) - \Gamma\left(\frac{z_0}{L}\right) \right] \quad (\text{D.10})$$

as well as the definition of Γ (Equation 3.25)

$$\Gamma\left(\frac{h}{L}\right) = \int \Psi\left(\frac{h}{L}\right) d\frac{h}{L} \quad (\text{D.11})$$

The derivation for stable conditions is considered first. With the Businger-Dyer equation for stable conditions Equation 3.26 is easily obtained, hence Equation D.10 for stable conditions equals

$$B = \frac{p+1}{p} - \Psi\left(\frac{z_0}{L}\right) - \frac{\Psi\left(\frac{h}{L}\right)}{p} + \frac{p+1}{p \frac{h}{L}} \left[\frac{1}{2} \frac{h}{L} \Psi\left(\frac{h}{L}\right) - \frac{1}{2} \frac{z_0}{L} \Psi\left(\frac{z_0}{L}\right) \right] \quad (\text{D.12})$$

This can be rewritten as

$$B = \frac{p+1}{p} - \Psi\left(\frac{z_0}{L}\right) - \frac{1}{p} \Psi\left(\frac{h}{L}\right) + \frac{1}{2} \frac{p+1}{p} \left[\Psi\left(\frac{h}{L}\right) - \left(\frac{z_0}{h}\right)^2 \Psi\left(\frac{h}{L}\right) \right] \quad (\text{D.13})$$

and since $(z_0/h)^2 \ll 1$ it is found that

$$B = \frac{p+1}{p} + \frac{1}{2} \frac{p-1}{p} \Psi\left(\frac{h}{L}\right) - \Psi\left(\frac{z_0}{L}\right) \quad (\text{D.14})$$

For unstable conditions the derivation is more complicated, and first the Ψ -function is integrated, which is required in Equation D.11. The Free Convection formulation is considered for unstable conditions

$$\Psi\left(\frac{z}{L}\right) = \frac{3}{2} \ln\left(\frac{x^2 + x + 1}{3}\right) - \sqrt{3} \arctan\left(\frac{2x+1}{\sqrt{3}}\right) + \frac{\pi}{\sqrt{3}} \quad (\text{D.15})$$

Which is rewritten as

$$\Psi\left(\frac{z}{L}\right) = \frac{3}{2} \ln(x^2 + x + 1) - \sqrt{3} \arctan\left(\frac{2x+1}{\sqrt{3}}\right) + \frac{\pi}{\sqrt{3}} - \frac{3}{2} \ln(3) \quad (\text{D.16})$$

where $x = [1 - \gamma z/L]^{1/3}$. The derivation of $\Gamma(h/L)$ is shown here, hence h/L is considered everywhere instead of z/L . There are three integrals to solve since $\Psi(h/L)$ is has to be integrated

$$\begin{aligned} \Gamma\left(\frac{h}{L}\right) &= \int \frac{3}{2} \ln(x_h^2 + x_h + 1) d\frac{h}{L} - \\ &\quad \int \sqrt{3} \arctan\left(\frac{2x_h+1}{\sqrt{3}}\right) d\frac{h}{L} + \\ &\quad \int \frac{\pi}{\sqrt{3}} - \frac{3}{2} \ln(3) d\frac{h}{L} \end{aligned} \quad (\text{D.17})$$

First integration by substitution is used to rewrite Equation D.17 as

$$\begin{aligned} \Gamma\left(\frac{h}{L}\right) &= - \int \frac{3}{2} \frac{3x_h^2}{\gamma} \ln(x_h^2 + x_h + 1) dx_h \\ &\quad + \int \frac{3\sqrt{3}}{\gamma} x_h^2 \arctan\left(\frac{2x_h+1}{\sqrt{3}}\right) dx_h \\ &\quad + \int \frac{\pi}{\sqrt{3}} - \frac{3}{2} \ln(3) d\frac{h}{L} \end{aligned} \quad (\text{D.18})$$

Next, the integrals are solved one by one separately for clarity purposes. The first integral on the right hand side of Equation D.18 is solved with integration by parts as

$$\begin{aligned}
 & -\frac{3}{2\gamma} \int 3x_h^2 \ln(x_h^2 + x_h + 1) dx_h = -\frac{3}{2\gamma} x_h^3 \ln(x_h^2 + x_h + 1) + \frac{3}{2\gamma} \int x_h^3 \frac{2x_h + 1}{x_h^2 + x_h + 1} dx_h \\
 & = -\frac{3}{2\gamma} x_h^3 \ln(x_h^2 + x_h + 1) + \frac{3}{2\gamma} \int \frac{[2x_h^2 - x_h - 1][x_h^2 + x_h + 1] + [2x_h + 1]}{x_h^2 + x_h + 1} dx_h \\
 & = -\frac{3}{2\gamma} x_h^3 \ln(x_h^2 + x_h + 1) + \frac{3}{2\gamma} \left[\frac{2}{3} x_h^3 - \frac{1}{2} x_h^2 - x_h + \ln(x_h^2 + x_h + 1) \right] \\
 & = \frac{3}{2\gamma} [1 - x_h^3] \ln(x_h^2 + x_h + 1) + \frac{x_h^3}{\gamma} - \frac{3x_h^2}{4\gamma} - \frac{3x_h}{2\gamma} \tag{D.19}
 \end{aligned}$$

The second integral on the right hand side of Equation D.18 is first rewritten with the substitution $y = 2x_h + 1$ as

$$\int \frac{3\sqrt{3}}{\gamma} x_h^2 \arctan\left(\frac{2x_h + 1}{\sqrt{3}}\right) dx_h = \frac{3\sqrt{3}}{\gamma} \int \frac{y^2 - 2y + 1}{8} \arctan\left(\frac{y}{\sqrt{3}}\right) dy \tag{D.20}$$

The right hand side of Equation D.20 can be split up into three integrals that can all be solved with standard integrals. The following standard integrals are used

$$\int y^2 \arctan\left(\frac{y}{C}\right) dy = \frac{1}{3} y^3 \arctan\left(\frac{y}{C}\right) + \frac{1}{6} C^3 \ln\left(\frac{y^2}{C^2} + 1\right) - \frac{1}{6} C y^2 \tag{D.21}$$

$$\int y \arctan\left(\frac{y}{C}\right) dy = \frac{1}{2} y^2 \arctan\left(\frac{y}{C}\right) + \frac{1}{2} C^2 \arctan\left(\frac{y}{C}\right) - \frac{1}{2} C y \tag{D.22}$$

$$\int \arctan\left(\frac{y}{C}\right) dy = y \arctan\left(\frac{y}{C}\right) - \frac{1}{2} C \ln\left(\frac{y^2}{C^2} + 1\right) \tag{D.23}$$

with $C = \sqrt{3}$. With aid of these three standard integrals Equation D.20 equals

$$\begin{aligned}
 \int \frac{3\sqrt{3}}{\gamma} x_h^2 \arctan\left(\frac{2x_h + 1}{\sqrt{3}}\right) dx_h & = \frac{3\sqrt{3}}{8\gamma} \left[\frac{1}{3} y^3 - y^2 + y - 3 \right] \arctan\left(\frac{y}{\sqrt{3}}\right) + \\
 & \quad \frac{3\sqrt{3}}{8\gamma} \left[\frac{1}{2} \sqrt{3} - \frac{1}{2} \sqrt{3} \right] \ln\left(\frac{y^2}{3} + 1\right) + \\
 & \quad \frac{3\sqrt{3}}{8\gamma} \left[\sqrt{3} y - \frac{\sqrt{3}}{6} y^2 \right] \tag{D.24}
 \end{aligned}$$

The second-term on the right hand side including the logarithm thus becomes 0. If now $y = 2x_h + 1$ is substituted back it is found that

$$\begin{aligned} \int \frac{3\sqrt{3}}{\gamma} x_h^2 \arctan\left(\frac{2x_h+1}{\sqrt{3}}\right) dx_h &= \frac{3\sqrt{3}}{8\gamma} \left[\frac{8}{3} x_h^3 - \frac{8}{3} \right] \arctan\left(\frac{2x_h+1}{\sqrt{3}}\right) - \\ &\quad \frac{3\sqrt{3}}{8\gamma} \left[\frac{2\sqrt{3}}{3} x_h^2 - \frac{4\sqrt{3}}{3} x_h - \frac{5\sqrt{3}}{6} \right] \\ &= \frac{\sqrt{3}}{\gamma} [x_h^3 - 1] \arctan\left(\frac{2x_h+1}{\sqrt{3}}\right) - \\ &\quad \frac{3}{4} \frac{x_h^2}{\gamma} + \frac{3}{2} \frac{x_h}{\gamma} + \frac{15}{16\gamma} \end{aligned} \quad (\text{D.25})$$

As such only the last integral of Equation D.18 remains, which is easily found to be

$$\int \frac{\pi}{\sqrt{3}} - \frac{3}{2} \ln(3) d\frac{h}{L} = \frac{\pi}{\sqrt{3}} \frac{h}{L} - \frac{3}{2} \frac{h}{L} \ln(3) \quad (\text{D.26})$$

If now Equations D.19, D.25 and D.26 are incorporated into Equation D.18, it is found for Γ that

$$\begin{aligned} \Gamma\left(\frac{h}{L}\right) &= \frac{3}{2\gamma} [1 - x_h^3] \ln(x_h^2 + x_h + 1) + \frac{x_h^3}{\gamma} - \frac{3x_h^2}{4\gamma} - \frac{3x_h}{2\gamma} + \\ &\quad \frac{\sqrt{3}}{\gamma} [x_h^3 - 1] \arctan\left(\frac{2x_h+1}{\sqrt{3}}\right) - \frac{3x_h^2}{4\gamma} + \frac{3x_h}{2\gamma} + \frac{15}{16\gamma} + \\ &\quad \frac{\pi}{\sqrt{3}} \frac{h}{L} - \frac{3}{2} \frac{h}{L} \ln(3) \end{aligned} \quad (\text{D.27})$$

Besides, notice that $x_h^3 = 1 - \gamma h/L$, hence

$$\begin{aligned} \Gamma\left(\frac{h}{L}\right) &= \frac{3}{2} \frac{h}{L} \ln(x_h^2 + x_h + 1) + \frac{1}{\gamma} - \frac{h}{L} - \frac{3x_h^2}{4\gamma} - \frac{3x_h}{2\gamma} - \\ &\quad \sqrt{3} \frac{h}{L} \arctan\left(\frac{2x_h+1}{\sqrt{3}}\right) - \frac{3x_h^2}{4\gamma} + \frac{3x_h}{2\gamma} + \frac{15}{16\gamma} + \\ &\quad \frac{\pi}{\sqrt{3}} \frac{h}{L} - \frac{3}{2} \frac{h}{L} \ln(3) \end{aligned} \quad (\text{D.28})$$

Now the definition of the Ψ -function for unstable conditions is considered, Equation D.16, to obtain

$$\Gamma\left(\frac{h}{L}\right) = \frac{h}{L} \Psi\left(\frac{h}{L}\right) - \frac{h}{L} - \frac{3x_h^2}{2\gamma} + \frac{31}{16\gamma} \quad (\text{D.29})$$

which equals the equation of Γ for unstable conditions as shown in Chapter 3 (Equation 3.27).

The derivation of Γ for unstable conditions has been shown, but the derivation of B is also briefly assessed. The definition of B is shown in Equation D.10. The last term

including the Γ -functions is further derived first. With aid of Equation D.29 this is written as

$$\frac{p+1}{p \frac{h}{L}} \left[\Gamma \left(\frac{h}{L} \right) - \Gamma \left(\frac{z_0}{L} \right) \right] = \frac{p+1}{p \frac{h}{L}} \left[\frac{h}{L} \left[\Psi \left(\frac{h}{L} \right) - 1 \right] - \frac{z_0}{L} \left[\Psi \left(\frac{z_0}{L} \right) - 1 \right] - \frac{3}{2} \frac{x_h^2 - x_0^2}{\gamma} \right] \quad (\text{D.30})$$

This is first rewritten as

$$\frac{p+1}{p \frac{h}{L}} \left[\Gamma \left(\frac{h}{L} \right) - \Gamma \left(\frac{z_0}{L} \right) \right] = \frac{p+1}{p} \left[\left[\Psi \left(\frac{h}{L} \right) - 1 \right] - \frac{z_0}{h} \left[\Psi \left(\frac{z_0}{L} \right) - 1 \right] - \frac{3}{2} \frac{x_h^2 - x_0^2}{\gamma \frac{h}{L}} \right] \quad (\text{D.31})$$

Next, since $-\gamma h/L = x_h^3 - 1$ and assuming $z_0 / h = 0$ it is found that

$$\frac{p+1}{p \frac{h}{L}} \left[\Gamma \left(\frac{h}{L} \right) - \Gamma \left(\frac{z_0}{L} \right) \right] = \frac{p+1}{p} \left[\left[\Psi \left(\frac{h}{L} \right) - 1 \right] + \frac{3}{2} \frac{x_h^2 - x_0^2}{x_h^3 - 1} \right] \quad (\text{D.32})$$

Incorporating this into Equation D.10 results for unstable conditions in

$$B = \frac{p+1}{p} - \Psi \left(\frac{z_0}{L} \right) - \frac{\Psi \left(\frac{h}{L} \right)}{p} + \frac{p+1}{p} \left[\left[\Psi \left(\frac{h}{L} \right) - 1 \right] + \frac{3}{2} \frac{x_h^2 - x_0^2}{x_h^3 - 1} \right] \quad (\text{D.33})$$

Which equals after some rewriting Equation 3.29.

BIBLIOGRAPHY

- Akylas, E. & Tombrou, M. (2005), 'Interpolation between businger-dyer formulae and free convection forms: a revised approach', *Boundary-Layer Meteorology* **115**, 381–398.
- Andreas, E. L., Claffey, K. J. & Makshtas, A. P. (2000), 'Low-level atmospheric jets and inversions over the western weddel sea', *Boundary-Layer Meteorology* **97**, 459–486.
- Baas, P., Bosveld, F. C., Baltink, H. K. & Holtslag, A. A. M. (2009), 'A climatology of nocturnal low-level jets at cabauw', *Journal of applied meteorology and climatology* **48**, 1627–1642.
- Baas, P., Steeneveld, G. J., van de Wiel, B. J. H. & Holtslag, A. A. M. (2006), 'Exploring self-correlation in stably stratified conditions', *Journal of the Atmospheric Sciences* **63**, 3045–3054.
- Barthelmie, R. J., Semprevia, A. M. & Pryor, S. C. (2010), 'The influence of humidity fluxes on offshore wind speed profiles', *Annales Geophysicae* **28**, 1043–1052.
- Batchelor, G. K. (1953), *The theory of homogeneous turbulence*, Cambridge University Press.
- Beljaars, A. C. M. & Holtslag, A. A. M. (1991), 'Flux parameterization over land surfaces for atmospheric models', *Journal of Applied Meteorology* **30**, 327–341.
- Betchov, R. & Yaglom, A. M. (1971), 'Comments on the theory of similarity as applied to turbulence in an unstably stratified fluid', *Izv. Akad. Nauk SSSR, Ser. Fiz. Atmosf. i Okeana* **7**, 1270–1279.
- Bhaganagar, K. & Debnath, M. (2015), 'The effects of mean atmospheric forcings of the stable atmospheric boundary layer on wind turbine wake', *Journal of Renewable and Sustainable Energy* **7**, 013124.
- Blackader, A. K. (1957), 'Boundary layer wind maxima and their significance for the growth of nocturnal inversions', *Bulletin American Meteorological Society* **38**, 283–290.
- Blackader, A. K. (1962), 'The vertical distribution of wind and turbulent exchange in a neutral atmosphere', *Journal of Geophysical Research* **67**, 3095–3102.
- Blackader, A. K. & Tennekes, H. (1968), 'Asymptotic similarity in neutral barotropic planetary boundary layers', *Journal of the Atmospheric Sciences* **25**, 1015–1020.
- Bleiber, K., Kramkowski, T., Cosack, N. & Braun, K. (2006), 'The influence of meteorological parameters on the operational behavior of multi-megawatt wec', in 'Germanic Wind Energy Conference, Bremen, Germany'.
- Bonner, W. (1968), 'Climatology of the low level jet', *Monthly Weather Review* **96**, 833–850.
- Busch, N. E. (1973), 'The surface boundary layer', *Boundary-Layer Meteorology* **4**, 213–240.

- Businger, J. A. (1973), 'A note on free convection', *Boundary-Layer Meteorology* **4**, 323–326.
- Businger, J. A., Wyngaard, J. C., Izumi, Y. & Bradley, E. F. (1971), 'Flux-profile relationships in the atmospheric boundary layer', *Journal of the atmospheric sciences* **28**, 181–189.
- Byun, D. W. (1991), 'Determination of similarity functions of the resistance laws for the planetary boundary layer using surface-layer similarity functions', *Boundary-Layer Meteorology* **57**, 17–48.
- Carl, D. M., Tarbell, T. C. & Panofsky, H. A. (1973), 'Profiles of wind and temperature from towers over homogeneous terrain', *Journal of the Atmospheric Sciences* **30**, 788–794.
- Caughey, S. J. (1977), 'Boundary-layer turbulence spectra in stable conditions', *Boundary-Layer Meteorology* **11**, 3–14.
- Caughey, S. J., Wyngaard, J. C. & Kaimal, J. C. (1979), 'Turbulence in the evolving stable boundary layer', *Journal of the atmospheric sciences* **36**, 1041–1052.
- Charnock, H. (1955), 'Wind stress on a water surface', *Quarterly Journal of the Royal Meteorological Society* **81**, 639.
- Cheng, Y. & Brutsaert, W. (2005), 'Flux-profile relationships for wind speed and temperature in the stable atmospheric boundary layer', *Boundary-Layer Meteorology* **114**, 519–538.
- Christakos, K., Varlas, G., Reuder, J., Katsafados, P. & Papadopoulos, A. (2014), 'Analysis of a low-level coastal jet off the western coast of Norway', *Energy Procedia* **53**, 162–172.
- Coelingh, J. P., van Wijk, A. J. M. & Holtslag, A. A. M. (1996), 'Analysis of wind speed observations over the north sea', *Journal of Wind Engineering* **61**, 51–69.
- Devinant, P., Laverne, T. & Hureau, J. (2002), 'Experimental study of wind-turbine airfoil aerodynamics in high turbulence', *Journal of Wind Engineering and Industrial Aerodynamics* **90**, 689–707. doi:10.1016/S0167-6105(02)00162-9.
- Dimitrov, N., Natarajan, A. & Kelly, M. (2014), 'Model of wind shear conditional on turbulence and its impact on wind turbine loads', *Wind Energy* p. doi: 10.1002/we.1797.
- Dörenkämper, M., Optis, M., Monahan, A. & Steinfeld, G. (2015), 'On the offshore advection of boundary-layer structures and the influence on offshore wind conditions', *Boundary-Layer Meteorology* **155**, 459–482.
- Doyle, J. & Warner, T. (2010), 'A Carolina coastal low-level jet during GALE IOP 2', *Monthly Weather Review* **138**, 2385–2404.
- Dyer, A. J. (1974), 'A review of flux-profile relationships', *Boundary-Layer Meteorology* **7**, 363–372.
- Elliot, D. L. & Cadogan, J. B. (1990), Effects of wind shear and turbulence on wind turbine power curves, in 'Proceedings of the 1990 European Community Wind Energy Conference and Exhibition'.
- Elliott, D. L. & Cadogan, J. B. (1990), Effects of wind shear and turbulence on wind turbine power curves, in 'European Community Wind Energy Conference and Exhibition, Madrid, Spain'.
- 'EWEA' (2014), Wind energy scenarios for 2020, Technical report, European Wind Energy

Association.

- Fairall, C. W., Bradley, E. F., Rogers, D. P., Edson, J. B. & Young, G. S. (1996), 'Bulk parameterization of air-sea fluxes for tropical ocean global atmosphere coupled-ocean atmosphere response experiment', *Journal of Geophysical Research* **101**, 3747–3764.
- Galmarini, S. & Attié, J. L. (2010), 'Turbulent transport at the thermal internal boundary-layer top: wavelet analysis of aircraft measurements', *Boundary-Layer Meteorology* **94**, 175–196.
- Garratt, J. R. (1990), 'The internal boundary layer - a review', *Boundary-layer Meteorology* **50**, 171–203.
- Gerhardt, J. R. (1963), 'Mesoscale association of a low-level jet stream with a squall-line cold front situation', *Journal of Applied Meteorology* **2**, 49–55.
- Gontier, H., Schaffarczyk, A. P., Kleinhans, D. & Friedrich, R. (2007), 'A comparison of fatigue loads of wind turbine resulting from a non-gaussian turbulence model vs. standard ones', *Journal of Physics: Conference Series* **75**, 012070. doi: 10.1088/1742-6596/75/1/012070.
- Gottschall, J. & Peinke, J. (2008), 'How to improve the estimation of power curves for wind turbines', *Environmental Research Letters* **3**, 015005. doi:10.1088/1748-9326/3/1/015005.
- Grachev, A. A. & Fairall, C. W. (1997), 'Dependence of the Monin-Obukhov stability parameter on the bulk Richardson number over the ocean', *Journal of Applied Meteorology* **36**, 406–414.
- Gryning, S., Batchvarova, E., Brümmer, B., Jorgensen, H. & Larsen, S. (2007), 'On the extension of the wind profile over homogeneous terrain beyond the surface boundary layer', *Boundary-Layer Meteorology* **124**, 251–268.
- Hansen, K. S. & Larsen, G. C. (2005), 'Characterising turbulence intensity for fatigue load analysis of wind turbines', *Wind Engineering* **29**, 319–329.
- Hansen, K. S., Larsen, G. C. & Ott, S. (2014), 'Dependence of offshore wind turbine fatigue loads on atmospheric stratification', *Journal of Physics: Conference Series* **524**, 012165. doi: 10.1088/1742-6596/524/1/012165.
- Haugen, D. A., Kaimal, J. C. & Bradley, E. F. (1971), 'An experimental study of Reynolds stress and heat flux in the atmospheric surface layer', *Quarterly Journal of the Royal Meteorological Society* **97**, 168–180.
- He, Y. (2014), A new LLJ model and its application to wind turbine power analysis, PhD thesis, Technical University Delft.
- Hedde, T. & Durand, P. (1994), 'Turbulence intensities and bulk coefficients in the surface layer above the sea', *Boundary-Layer Meteorology* **71**, 415–432.
- Högström, U. (1988), 'Non-dimensional wind and temperature profiles in the atmospheric boundary layer: a re-evaluation', *Boundary-Layer Meteorology* **42**, 55–78.
- Högström, U. (1990), 'Analysis of turbulence structure in the surface layer with a modified similarity formulation for near neutral conditions', *Journal of the Atmospheric Sciences* **47**, 1949–1972.

- Holton, J. R. (1972), *An introduction to dynamic meteorology*, Academic Press, NY.
- Holtslag, A. A. M. (1984), 'Estimates of diabatic wind speed profiles from near-surface weather observations', *Boundary-Layer Meteorology* **29**, 225–250.
- Holtslag, A. A. M. & de Bruin, H. A. R. (1988), 'Applied modeling of the nighttime surface energy balance over land', *Journal of Applied Meteorology* **27**, 689–704.
- Honrubia, A., Viguera-Rodríguez, A. & Gómez-Lázaro, E. (2012), *Progress in Turbulence and Wind Energy IV. Chapter 4: The influence of turbulence and vertical wind profile in wind turbine power curve*, Springer.
- Hsu, S. A. (1979), 'Mesoscale nocturnal jetlike winds within the planetary boundary layer over flat, open coast', *Boundary-Layer Meteorology* **17**, 485–494.
- IEC (2005), IEC 61400-1 ed.3: Wind-turbines - part 1: Design requirements, Technical report, International Electrotechnical Commission.
- IEC (2009), IEC 61400-3 ed.1: Wind-turbines - part 3: Design requirements for offshore wind turbines, Technical report, International Electrotechnical Commission.
- Jonkman, J., Butterfield, S., Musial, W. & Scott, G. (2009), Definition of a 5-MW reference wind turbine for offshore system development, Technical report, National Renewable Energy Laboratory.
- Kader, B. A. & Yaglom, A. M. (1990), 'Mean fields and fluctuation moments in unstably stratified turbulent boundary layers', *Journal of Fluid Mechanics* **212**, 637–662.
- Kaimal, J. C. (1973), 'Turbulence spectra, length scales and structure parameters in the stable surface layer', *Boundary-Layer Meteorology* **4**, 289–309.
- Kaimal, J. C. & Wyngaard, J. C. (1990), 'The kansas and minnesota experiments', *Boundary-layer Meteorology* **50**, 31–47.
- Kaimal, J. C., Wyngaard, J. C., Izumi, Y. & Coté, O. R. (1972), 'Spectral characteristics of surface-layer turbulence', *Quarterly Journal of the Royal Meteorological Society* **98**, 563–589.
- Kelley, N., Shirazi, M., Jager, D., Wilde, S., Adams, J., Buhl, M., Sullivan, P. & Patton, E. (2004), Lamar low-level jet project interim report, Technical report, National Renewable Energy Laboratory.
- Kelly, M. & Gryning, S. E. (2010), 'Long-term mean wind profiles based on similarity theory', *Boundary-Layer Meteorology* **136**, 377–390.
- KNMI (2015), 'Weerkaarten archief europa'. Online; accessed 23-October-2015.
URL: <http://www.knmi.nl/nederland-nu/klimatologie/daggegevens/weerkaarten>
- Kotroni, V. & Lagouvardos, K. (1993), 'Low-level jet streams associated with atmospheric cold fronts: seven case studies from the FRONTS87 experiment', *Geophysical research letters* **20**, 1371–1374.
- Kottmeier, C., Palacio-Sese, P., Kalthoff, N., Corsmeier, U. & Fiedler, F. (2000), 'Sea breezes and coastal jets in southeastern Spain', *International Journal of Climatology* **20**, 1791–1808.
- Kraus, H., Malcher, J. & Schaller, E. (1985), 'A nocturnal low level jet during PUKK', *Boundary-Layer Meteorology* **31**, 187–195.

- Lange, B., Larsen, S., Hojstrup, J. & Barthelmie, R. (2004), 'The influence of thermal effects on the wind speed profile of the coastal marine boundary layer', *Boundary-Layer meteorology* **112**, 587–614.
- Lu, H. & Porté-Agel, F. (2011), 'Large-eddy simulation of a very large wind farm in a stable atmospheric boundary layer', *Physics of Fluids* **23**, 065101.
- Mann, J. (1994), 'The spatial structure of neutral atmospheric surface-layer turbulence', *Journal of Fluid Mechanics* **273**, 141–168.
- Mann, J. (1998), 'Wind field simulation', *Prob. Engng. Mech.* **13**, 269–282.
- Mikkelsen, K. (2013), Effect of free stream turbulence on wind turbine performance, Master's thesis, Norwegian University of Science and Technology.
- Milan, P., Wächter, M. & Peinke, J. (2013), 'Turbulent character of wind energy', *Physical Review Letters* **110**, 138701. doi:10.1103/PhysRevLett.110.138701.
- Monin, A. S. & Obukhov, A. M. (1954), 'Basic laws of turbulent mixing in the ground layer of the atmosphere', *Tr. Akad. Nauk SSSR Geophys. Inst.* **151**, 163–187.
- Morales, A., Wächter, M. & Peinke, J. (2011), 'Characterization of wind turbulence by higher-order statistics', *Wind Energy* p. doi: 10.1002/we.478.
- Mücke, T., Kleinhans, D. & Peinke, J. (2011), 'Atmospheric turbulence and its influence on the alternating loads on wind turbines', *Wind Energy* **14**, 301–316.
- Muljadi, E., Butterfield, C. P. & Jr., M. L. B. (1997), Effects of turbulence on power generation for variable-speed wind turbines, in '35th Aerospace Scientific Meeting Exhibition, Reston, VA, United States: AIAA'.
- Nunalee, C. G. & Basu, S. (2014), 'Mesoscale modeling of coastal low-level jets: implications for offshore wind resource estimation', *Wind Energy* **17**, 1199–1216.
- Obukhov, A. M. (1946), 'Turbulence in the atmosphere with inhomogeneous temperature', *Tr. Geofiz. Inst. Akad. Nauk SSSR* **1**, 95–115.
- Obukhov, A. M. (1971), 'Turbulence in the atmosphere with a non-uniform temperature', *Boundary-Layer Meteorology* **2**, 7–29.
- Parish, T. & Oolman, L. (2010), 'On the role of sloping terrain in the forcing of the great plains low-level jet', *Journal of the Atmospheric Sciences* **67**, 2690–2699.
- Paulson, C. A. (1970), 'The mathematical representation of wind speed and temperature profiles in the unstable atmospheric surface layer', *Journal of applied meteorology* **9**, 857–861.
- Peña, A. & Gryning, S. (2008), 'Charnock's roughness length model and non-dimensional wind profiles over the sea', *Boundary-Layer Meteorology* **128**, 191–203.
- Peña, A., Gryning, S. & Hasager, C. B. (2010a), 'Comparing mixing-length models of the diabatic wind profile over homogeneous terrain', *Theoretical and Applied Climatology* **100**, 325–335.
- Peña, A., Gryning, S., Mann, J. & Hasager, C. B. (2010b), 'Length scales of the neutral wind profile over homogeneous terrain', *Journal of Applied Meteorology and Climate* **49**, 792–806.

- Prandtl, L. (1932), 'Meteorologische anwendungen der stromungslehre', *Beitraege zur Physik der Atmosphaere* **19**, 188–202.
- Sathe, A. & Bierbooms, W. (2007), 'Influence of different wind-profiles due to varying atmospheric stability on the fatigue life of wind turbines', *Journal of Physics: Conference Series* **75**, 012056. doi: 10.1088/1742-6596/75/1/012056.
- Sathe, A., Gryning, S. & Peña, A. (2011), 'Comparison of the atmospheric stability and wind profiles at two wind farm sites over a long marine fetch in the north sea', *Wind Energy* **14**, 767–780.
- Sathe, A., Mann, J., Barlas, T., Bierbooms, W. A. A. M. & van Bussel, G. J. W. (2013), 'Influence of atmospheric stability on wind turbine loads', *Wind Energy* **16**, 1013–1032.
- Sathe, A. R. (2012), Influence of wind conditions on wind turbine loads and measurement of turbulence using lidars, PhD thesis, Technical University Delft.
- Shapiro, A. & Fedorovich, E. (2010), 'Analytical description of a nocturnal low-level jet', *Quarterly Journal of the Royal Meteorological Society* **136**, 1255–1262.
- Sicot, C., Devinant, P., Laverne, T., Loyer, S. & Hureau, J. (2006), 'Experimental study of the effect of turbulence on horizontal axis wind turbine aerodynamics', *Wind Energy* **9**, 361–370. doi:10.1002/we.184.
- Sim, C., Basu, S. & Manual, L. (2009), 'The influence of stable boundary layer flows on wind turbine fatigue loads', *AIAA 2009-1405*.
- Sim, C., Manual, L. & Basu, S. (2010), 'A comparison of wind turbine load statistics for inflow turbulence fields based on conventional spectral methods and large eddy simulation', *AIAA 2010-829*.
- Smedman, A., Bergström, H. & Högström, U. (1995), 'Spectra, variances and length scales in a marine stable boundary layer dominated by a low level jet', *Boundary-Layer Meteorology* **76**, 211–232.
- Stull, R. B. (1988), *An introduction to boundary layer meteorology*, Kluwer Academic Publishers.
- Stull, R. B. (2000), *Meteorology for Scientists and Engineers*, second edn, Gary Garlson.
- Sullivan, P. P., Moeng, C. H., Stevens, B., Lenschow, D. H. & Mayor, S. D. (1998), 'Structure of the entrainment zone capping the convective atmospheric boundary layer', *Journal of the Atmospheric Sciences* **55**, 3042–3064.
- Sumner, J. & Masson, C. (2006), 'Influence of atmospheric stability on wind turbine power performance curves', *Journal of Solar Energy Engineering* **128**, 531. doi:10.1115/1.2347714.
- Türk, M. & Emeis, S. (2010), 'The dependence of off shore turbulence intensity on wind speed', *Journal of Wind Engineering and Industrial Aerodynamics* **98**, 466–471.
- van de Wiel, B. J. H., Moene, A. F., Steeneveld, G. J., Baas, P., Bosveld, F. C. & Holtslag, A. A. M. (2010), 'A conceptual view on inertial oscillations and nocturnal low-level jets', *Journal of the Atmospheric Sciences* **67**, 2679–2689.
- van Wijk, A. J. M., Beljaars, A. C. M., Holtslag, A. A. M. & Turkenburg, W. C. (1990), 'Evaluation of stability corrections in wind speed profiles over the north sea', *Journal of Wind*

- Engineering and Industrial Aerodynamics* **33**, 551–566.
- Vanderwende, B. J. & Lundquist, J. K. (2012), 'The modification of wind turbine performance by statistically distinct atmospheric regimes', *Environmental Research Letters* **7**, 034035 (7pp).
- Veldkamp, H. F. (2006), Chances in Wind Energy; A probabilistic approach to wind turbine fatigue design, PhD thesis, Technical University Delft.
- Vickers, D. & Mahrt, L. (1999), 'Observations of non-dimensional wind shear in the coastal zone', *Quarterly Journal of the Royal Meteorological Society* **125**, 2685–2702.
- von Kármán, T. (1948), 'Progress in the statistical theory of turbulence', *Proc. Natl. Acad. Sci.* **34**, 530–539.
- Wagner, R., Courtney, M., Gottschall, J. & Lindelöw-Marsden, P. (2011), 'Accounting for the speed shear in wind turbine power performance measurement', *Wind Energy* **14**, 993–1004.
- Werkhoven, E. J. & Verhoef, J. P. (2012), *Offshore meteorological mast IJmuiden - Abstract of instrumentation report*, ECN. ECN-WindMemo-12-010, ECN project nr.:5.1008.
- Wessels, H. R. A. (1983), Distortion of the wind field by the cabauw meteorological tower, Technical report, Royal Dutch meteorological Institute.
- Wharton, S. & Lundquist, J. K. (2012), 'Atmospheric stability affects wind turbine power collection', *Environmental Research Letters* **7**, 014005 (9pp).
- Whiteman, C. D., Bian, X. & Zhong, S. (1987), 'Low-level jet climatology from enhanced rawinsonde observations at a site in the southern great plains', *Journal of Applied Meteorology* **36**, 1363–1376.
- Williams, W. (1892), 'On the relation of the dimensions of physical quantities to directions in space', *Philosophical Magazine Series 5* **34**, 234–271.
- Wyngaard, J. C., Coté, O. R. & Izumi, Y. (1971), 'Local free convection, similarity, and the budgets of shear stress and heat flux', *Journal of the Atmospheric Sciences* **28**, 1171–1182.
- Zemba, J. & Friehe, C. A. (1987), 'The marine atmospheric boundary layer jet in the coastal ocean dynamics experiment', *Journal of Geophysical Research* **92**, 1489–1496.
- Zilitinkevich, S. S. & Dardorff, J. W. (1974), 'Similarity theory for the planetary boundary layer of time-dependent height', *Journal of the Atmospheric Sciences* **31**, 1449–1452.

ACKNOWLEDGEMENT

Doing PhD-research can at times be a lonely challenge: you have to read literature, perform simulations or experiments, interpret results, present research at conferences, publish papers and write a thesis, and in the end you have to do the majority of this work on your own. I am grateful however that numerous people have helped me out when needed, either directly or indirectly, and I would like to take this opportunity to express my gratitude to some of you.

First of all, I have been able to work on this thesis only since my promotor and supervisor, Gerard van Bussel and Wim Bierbooms, decided to hire a meteorologist instead of an engineer for their PhD vacancy. I am grateful for the opportunity you gave me, and whereas for many PhD students their research is an extension of their MSc program, you gave me the opportunity to work in a complete different field of research. Due to the interdisciplinary nature of the research I have been able to work on two distinct different domains, one related to physics and one related to engineering, which allowed me to further develop my knowledge and skills in an interdisciplinary manner. I appreciate the confidence you gave me when I had doubts about the academic quality of my work, and you convinced me several times that there is a need for the research I was doing, which encouraged me to further pursue research that eventually is presented in this thesis.

Over the course of my PhD I had to move several times from one office to another, but by far most of the time I was in the fortunate surrounding of my office mates in room 5.11. Etana, Lars, Ricardo and Ye: the four of you have been great company, and we have had countless discussion both work related but also on a variety of random topics, ranging from sports to politics, food, society, religion, culture, science and whatever more. Ricardo, as you were sitting opposite of me, I bothered you far too often with simple questions on wind energy, especially related to Bladed, fatigue loads and eigen-frequencies. You always took the time to patiently explain me things that should have been common knowledge for a PhD-student in wind energy, and in return I hope I have aided you in obtaining better understanding of meteorology. In coming years, whenever I bump my foot I probably still raise my arm out of habit as you understand.

Besides the colleagues with which I have had the pleasure to share an office, I also would like to express my gratitude to Rene and Ashim. Both of you started a PhD on a meteorological related project, and with the two of you I have had by far most in-depth discussions about meteorological aspects related to wind energy. It has been great working with you guys, trying to enlighten those stubborn enough to think meteorology can be simplified with power laws and a variety of other empirical relations. Rene, besides the discussions we have had about meteorology, we also collaborated for a journal publication, and you frequently helped me out with creating figures, posters and presentations. Whereas I have been able to show you the need to consider physics in meteorology and wind energy, you have shown to me that both statistics as well as engineering simplifications at times are a necessity.

I would also like to express my gratitude to Stephan de Roode. Although no direct colleague, we have had several very useful meetings in the first two years of my PhD, in which I could discuss a bit more fundamental meteorological problems I encountered in my research. Later on we have been able to discuss student projects, and you sparked my interest in using LES-models for wind energy purposes.

I would not have finished this PhD in any way whatsoever if I would not have had the support and distractions of work provided by friends and family. First of all, I truly am grateful for my family who has always been around for support. Pap & mam, Wouter & Sanne: I am convinced you are looking forward to read what I have been doing for four years. Similarly I would like to thank my family in law for bearing with me through these years. Theo, Ina, Thiemo, Krista, Yuri, Suus and Noah, Levi & Lynn: you have provided a great amount of pleasant distractions from work that are necessary to complete these four years, and I have appreciated the interest you have shown in the work I have been doing during these years. The same also counts for my friends, of which I will name a few specifically. A big thanks to Marvin, Martijn & Marieke, Berry & Sanne, Michel & Linnet: it has been great hanging out in the weekends, going on holidays, cycling nearby or abroad, and of course total distraction from work at Pinkpop! I would like to thank Stefan & Cathy as well for the numerous evenings with diners, games and special beers. And lastly a brief thanks to Bart (I should have come to Hamburg more often, glad you are back in the Netherlands once again!) and to the guys and girl from Twiggy (Casper, Arjen and Wies, we should rehearse more often, or just have a beer!).

And lastly, I would like to end with the one person who stood with me during these years. Tamar, you have pulled me through these four years more often than you realise, and thanks to you I managed to finalize this research. I finished my PhD, besides the defence, more or less in time and this would not have been possible without your support. You have always believed in me, showed me a smile when I was grumpy, and bared with me while I rambled on about the details of my work. I am extremely grateful that I share my life with you, thank you for all that you do, and simply for being around.

LIST OF PUBLICATIONS

Peer-Reviewed journal publication

Holtslag, M. C., Bierbooms, W. A. A. M. & van Bussel, G. J. W. (2014), 'Estimating atmospheric stability from observations and correcting wind shear models accordingly', *Journal of Physics: Conference series* **555** 012052.

Holtslag, M. C., Bierbooms, W. A. A. M. & van Bussel, G. J. W. (2014), 'Definition of the equivalent stability for wind turbine fatigue load assessment', *Journal of Physics: Conference series* **524** 012110.

Holtslag, M. C., Bierbooms, W. A. A. M. & van Bussel, G. J. W. (2015), 'Validation of surface layer similarity theory to describe far offshore marine conditions in the Dutch North Sea in scope of wind energy research', *Journal of Wind Engineering and Industrial Aerodynamics* **136** 180-191.

Holtslag, M. C., Bierbooms, W. A. A. M. & van Bussel, G. J. W. (2016), 'Wind turbine fatigue loads as a function of atmospheric conditions offshore', *Wind Energy* doi: 10.1002/we.1959.

Holtslag, M. C., Bierbooms, W. A. A. M. & van Bussel, G. J. W. (2016), 'Extending the diabatic surface layer wind shear profile for offshore wind energy', *Submitted for publication to Renewable Energy*

Holtslag, M. C., He, Y., Bierbooms, W. A. A. M. & van Bussel, G. J. W. (2016), 'On the occurrence and characteristics of low-level jets in the Dutch North Sea', *Submitted for publication to Journal of Wind Engineering and Industrial Aerodynamics*

Holtslag, M. C., He, Y., Bierbooms, W. A. A. M. & van Bussel, G. J. W. (2016), 'Derivation and implementation of an empirical low-level jet wind shear model for wind energy purposes', *To be submitted*

Holtslag, M. C. & Bos, R (2016), 'Wind turbine performance as a function of turbulence scales', *To be submitted*.

Non-academic publication

Holtslag, M. C. & Bos, R (2015), 'Putting the wind in wind turbines', *Leonardo Times – Magazine of study association “Leonardo da Vinci”*.

CURRICULUM VITÆ

Maarten Christiaan HOLTSLAG

- 10-07-1985 Born in Zoetermeer, the Netherlands
- 1997–2004 VWO, het Alfrink College, Zoetermeer
- 2006–2010 BSc Bodem, Water en Atmosfeer, Wageningen University
Bachelor thesis: *Fog forecasting: "old fashioned" semi-empirical methods from radio sounding observations versus "modern" numerical models*
- 2010–2011 MSc Meteorology and Air Quality, Wageningen University
Master thesis: *A scale analysis of turbulence in a convective boundary layer based on spectral analysis of LES data*
Internship: *Impact of aerosols on boundary layer clouds and precipitation*
- 2011-2015 PhD Research at TU-Delft
Thesis *Far offshore wind conditions in scope of wind energy*
Promotor: prof. dr. G. J. W. van Bussel
Supervisor: dr. W. A. A. M. Bierbooms